

FABRICATION, STRUCTURE, AND PROPERTIES OF
 $\text{Bi}_{1-x}\text{A}_x\text{FeO}_3$ (A = La, Ba, Sm) MATERIALS



A Thesis Submitted in Partial Fulfillment of the Requirements for the
Degree of Doctor of Philosophy in Physics
Suranaree University of Technology
Academic Year 2016

การประดิษฐ์ โครงสร้างและสมบัติของวัสดุ $\text{Bi}_{1-x}\text{A}_x\text{FeO}_3$ (A = La, Ba, Sm)



วิทยานิพนธ์นี้เป็นส่วนหนึ่งของการศึกษาตามหลักสูตรปริญญาวิทยาศาสตรดุษฎีบัณฑิต

สาขาวิชาฟิสิกส์

มหาวิทยาลัยเทคโนโลยีสุรนารี

ปีการศึกษา 2559

FABRICATION, STRUCTURE, AND PROPERTIES OF

$\text{Bi}_{1-x}\text{A}_x\text{FeO}_3$ (A = La, Ba, Sm) MATERIALS


Suranaree University of Technology has approved this thesis submitted in partial fulfillment of the requirements for the Degree of Doctor of Philosophy.

Thesis Examining Committee



(Asst. Prof. Dr. Worawat Meevasana)

Chairperson



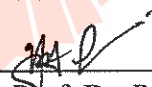
(Prof. Dr. Santi Maensiri)

Member (Thesis Advisor)



(Assoc. Prof. Dr. Rattikorn Yimnirun)

Member



(Asst. Prof. Dr. Prasit Thongbai)

Member




(Dr. Pinit Kidkhunthod)

Member



(Prof. Dr. Sukit Limpijunnong)

Vice Rector for Academic Affairs
and Innovation



(Prof. Dr. Santi Maensiri)

Dean of Institute of Science

เบญจพร ขสมบูรณ์ : การประดิษฐ์ โครงสร้างและสมบัติของวัสดุ $\text{Bi}_{1-x}\text{A}_x\text{FeO}_3$ (A = La, Ba, Sm) (FABRICATION, STRUCTURE, AND PROPERTIES OF $\text{Bi}_{1-x}\text{A}_x\text{FeO}_3$ (A = La, Ba, Sm) MATERIALS) อาจารย์ที่ปรึกษา : ศาสตราจารย์ ดร.สันติ แม่นศิริ, 285 หน้า

งานวิจัยนี้ได้ทำการสังเคราะห์สารแม่เหล็กเฟอร์โรอิก $\text{Bi}_{1-x}\text{A}_x\text{FeO}_3$ (เมื่อ x มีค่าเท่ากับ 0, 0.05, 0.1, 0.2, และ 0.3) ที่เจือด้วย Ba, La, และ Sm ด้วยวิธีตกตะกอน จากผลการทดลองพบว่าวัสดุโครงสร้างระดับนาโนเมตรของ BiFeO_3 เมื่อมีการเจือด้วยสารกลุ่มแรเอิร์ทและโลหะแอลคาไลน์เอิร์ทขนาดอนุภาคมีค่าลดลงตามปริมาณการเจืออยู่ในช่วง 19–79 นาโนเมตร จากผลการตรวจสอบเฟสด้วยเทคนิคการเลี้ยวเบนด้วยรังสีเอกซ์ (XRD) พบว่าวัสดุ BiFeO_3 มีโครงสร้างหลักสอดคล้องกับสารมาตรฐาน BiFeO_3 ซึ่งมีโครงสร้างแบบเพอโรฟสไกต์บิดเบี้ยวเป็นรอม โบฮีครอล มี space group เป็น $R3c$ สำหรับ BiFeO_3 มีเฟสเจือปนของเฟสอื่นๆ เช่น Bi_2O_3 และ $\text{Bi}_2\text{Fe}_4\text{O}_{13}$ เกิดขึ้นซึ่งสอดคล้องกับภาพ BSE ที่มีสีของเกรนแตกต่างกัน แต่พบว่าการเจือสารกลุ่มแรเอิร์ท La สามารถกำจัดปริมาณของการเกิดเฟสเจือปนได้ ผลการศึกษาโครงสร้างจุลภาคพบว่าเมื่อเพิ่มปริมาณการเจือไอออนของ Ba, La, และ Sm ขนาดของเกรนเฉลี่ยลดลงตามปริมาณการเจือเป็นผลมาจากการยับยั้งการโตของเกรน ผลการทดลองด้วยเทคนิค XANES แสดงให้เห็นว่าเลขออกซิเดชันของ Fe ไอออนในตัวอย่าง BiFeO_3 และในสารกลุ่มที่เจือด้วย Ba, La, และ Sm มีค่าเท่ากับ +3 และจากการศึกษาสมบัติการดูดกลืนของแสงด้วยเทคนิค UV–Vis พบว่าอนุภาคนาโนสามารถดูดกลืนแสงในย่านที่ตามองเห็นได้เป็นอย่างดีนั้นคือช่วงความยาวคลื่น 490–700 นาโนเมตร และพบว่ามีช่องว่างแถบพลังงานของตัวอย่างมีค่าลดลง เมื่อเจือสารกลุ่มแรเอิร์ทและแอลคาไลน์เอิร์ทในช่วง 1.91–2.12 eV สำหรับการศึกษาสมบัติทางแม่เหล็กของวัสดุ BiFeO_3 แสดงพฤติกรรมทางแม่เหล็กแบบแอนติเฟอร์โรที่อุณหภูมิห้อง และสังเกตเห็นว่าวงฮิสเทอรีซิสของ BiFeO_3 ที่เจือด้วย Ba ยังคงแสดงพฤติกรรมทางแม่เหล็กแบบแอนติเฟอร์โร สำหรับการเจือด้วยแรเอิร์ท สามารถปรับปรุงสมบัติทางแม่เหล็กของสาร BiFeO_3 โดยพบว่าสารตัวอย่างที่เจือด้วยแรเอิร์ทแสดงพฤติกรรมทางแม่เหล็กแบบเฟอร์โรแบบอ่อนที่อุณหภูมิห้อง จากการศึกษาด้วย Curie–Weiss law พบว่าค่าอุณหภูมิ Curie–Weiss ของตัวอย่าง BiFeO_3 และที่เจือด้วย Ba มีค่าติดลบซึ่งแสดงว่าเกิดอันตรกิริยาแม่เหล็กแบบแอนติเฟอร์โรอันเนื่องมาจากการจับคู่ของไอออนเดี่ยว แต่สำหรับตัวอย่างที่เจือด้วยแรเอิร์ทนั้นแสดง

ค่าอุณหภูมิ Curie–Weiss เป็นบวก แสดงว่าสมบัติทางแม่เหล็กของตัวอย่างเป็นแบบเฟอร์โร ผลการวัดสมบัติไดอิเล็กทริกของเซรามิก BiFeO_3 พบว่ามีค่าคงที่ไดอิเล็กทริกที่สูงมากในช่วงความถี่ต่ำๆ ($< 10^4$ Hz) และอุณหภูมิสูง สำหรับพฤติกรรมการมีค่าคงที่ไดอิเล็กทริกสูงของเซรามิก BiFeO_3 มีสาเหตุมาจากกลไกการโพลาไรเซชันแบบ Maxwell–Wagner ที่บริเวณรอยต่อระหว่างเกรน มีการตรวจสอบพบว่าเกิดกระบวนการผ่อนคลายทางไดอิเล็กทริกในวัสดุเซรามิกกลุ่มที่เจือด้วย Ba, La, และ Sm พบว่าค่าคงที่ไดอิเล็กทริกมีแนวโน้มลดลงเมื่อปริมาณการเจือเพิ่มขึ้น ซึ่งสอดคล้องกับการลดลงของขนาดเกรนเฉลี่ย ผลการศึกษาสมบัติไดอิเล็กทริกที่เป็นฟังก์ชันของการปรับแรงดันกระแสตรง สามารถระบุถึงการตอบสนองทางไดอิเล็กทริกของพื้นผิวขั้วไฟฟ้า ขอบเกรนและเกรน พบว่าการการตอบสนองที่ความถี่ต่ำ มีผลมาจากการตอบสนองของโพลาไรเซชันบริเวณพื้นผิวของขั้วไฟฟ้าและขอบเกรน ในขณะที่บริเวณความถี่สูงขึ้นสารตัวอย่างทุกตัวแสดงพฤติกรรมไม่ขึ้นอยู่กับการปรับแรงดันกระแสตรง สำหรับการศึกษาสมบัติความไม่เป็นเชิงเส้นทางไฟฟ้า พบว่าวัสดุเซรามิกทั้งหมดแสดงพฤติกรรมความไม่เป็นเชิงเส้นทางไฟฟ้า ซึ่งพบว่าการเจือสามารถลดการรั่วไหลของกระแสไฟฟ้าได้ และยังพบว่าค่าสัมประสิทธิ์ของความไม่เป็นเชิงเส้นทางไฟฟ้าสามารถนำไปประยุกต์ในงานด้านวาริสเตอร์ในช่วงแรงดันไฟฟ้าต่ำๆ ที่อุณหภูมิห้อง นอกจากนี้ยังพบว่าการนำไฟฟ้าในวัสดุเซรามิกทั้งหมด เป็นผลมาจากความร้อนที่ปล่อยออกมาสูงกว่าชั้นกำแพงศักย์ชอตต์กี ที่บริเวณรอยต่อระหว่างเกรน

สาขาวิชาฟิสิกส์

ปีการศึกษา 2559

ลายมือชื่อนักศึกษา เบญจพร ขจรบุษ

ลายมือชื่ออาจารย์ที่ปรึกษา ส.ก.

BENJAPORN YOTBURUT : FABRICATION, STRUCTURE, AND
PROPERTIES OF $\text{Bi}_{1-x}\text{A}_x\text{FeO}_3$ (A = La, Ba, Sm) MATERIALS.

THESIS ADVISOR : PROF. SANTI MAENSIRI, D.Phil. 285 PP.

BISMUTH FERRITE/MULTIFERROIC/MAGNETIC PROPERTIES/OPTICAL
PROPERTIES/DIELECTRIC CONSTANT/DIELECTRIC RELAXATION/DC
BIAS/NONLINEAR BEHAVIOR/SCHOTTKY EMISSION


In this thesis, the series of multiferroic $\text{Bi}_{1-x}\text{A}_x\text{FeO}_3$ ($x = 0, 0.05, 0.1, 0.2,$ and 0.3) with A is Ba, La, and Sm elements have been synthesized by a co-precipitation method. The average particle size has been decreased as increase doping levels in the range of 19–79 nm, which suggests that these doping ions inhibit the crystal growth. It is clearly seen that the diffraction peaks of all samples can be identified to main phase of rhombohedrally distorted structure BiFeO_3 with $R3c$ space group. Some low intense secondary phases such as Bi_2O_3 , $\text{Bi}_2\text{Fe}_4\text{O}_9$ were observed in the XRD pattern of BiFeO_3 , Sm- and Ba-doped BiFeO_3 samples associated with different color of grain in BSE images. The addition of La ions has eliminated the impurity phases found for undoped BiFeO_3 . It can be seen that the average grain size is gradually decreased with increasing dopant content due to the inhibited grain growth by doping ions. XANES spectra of all samples measured at Fe K-edge are very similar to Fe_2O_3 , indicating that the oxidation number of Fe ion corresponds to Fe^{3+} . Pure BiFeO_3 nanoparticle exhibits the absorption peak at around 490–700 nm and the band gap values for all samples were decreased gradually with increase doping contents in the range of 1.91–2.12 eV. The M–H loop for pure BiFeO_3 and Ba-doped samples

indicates antiferromagnetic behavior at room temperature. In case of La and Sm doping, the M–H curve exhibits clear weak ferromagnetic behavior. The Curie–Weiss temperature value of the BiFeO₃ and Ba–doped is negative value indicating that the antiferromagnetic characteristic of these ceramics. While we obtained positive value of θ for some of La– and Sm–doped samples, which is probably due to a manifest FM component. The dielectric constant spectra show highest value at low–frequency range (below 10⁴ Hz) and high temperatures. It shows a large dielectric curves attributed to the Maxwell–Wagner polarization or interfacial space charge polarization. All of BiFeO₃ and doped ceramics exhibit the dielectric relaxation behavior. In case of doped BiFeO₃ samples, the dielectric constant decrease as substituted by Ba, La, and Sm ions which corresponds to the slightly reduction of the average grain sizes in the microstructure. The applied dc bias was used to analyze the electrical response of electrode surface, grain boundary, and the grain. It was found that the interfacial polarizations of the electrode surface and grain boundaries could be suppressed by an applied bias voltage at low–frequency, but not for the grain polarization at high–frequency. All of ceramics display non–Ohmic behaviors at various temperatures and show the leakage current density decreases for all doped compositions. The obtained nonlinear coefficient values of all samples suggest the applicability of the varistor in the low voltage range at room temperature. It can be found that the electrical conduction in pure and doped samples is contributed to the thermally emitted over a Schottky potential barrier at grain boundary.

School of Physics

Student's Signature Benjaporn Yotbuent

Academic Year 2016

Advisor's Signature 

ACKNOWLEDGMENTS

I would like to express my sincere gratitude to my supervisor, Prof. Dr. Santi Maensiri, School of Physics for his effective scientific supervision, motivation, instructive guidance, generous personal encouragement and support. I benefited from his guidance in every aspect during my Ph.D research. I wish to thank Advance Materials Physics Laboratory (AMP), the Center for Scientific and Technological Equipment, Suranaree University of Technology for research facilities supporting. I would like to thank specially the Royal Golden Jubilee (RGJ) Ph.D. Programme scholarship for my PhD study and financial support both for research presentation outside the country and funding for overseas travel. I would like to thank NANOTEC-SUT Center of Excellence on Advanced Functional Nanomaterials from Suranaree University of Technology for the financial support, and School of Physics, Institute of science, Suranaree University of Technology for having very good laboratory facilities. I specially thank Department of Physics, Faculty of Science, Khon Kaen University for magnetic properties measurement, National Metal and Materials Technology Center (MTEC) for dielectric and electric properties measurement. I would like to thank AMP group members whose direct and indirect support helped and guided me during work and for their friendship.

Finally, I would like to thank my family for their understanding, endless love throughout my life, to bring me up and give me the good life.

Benjaporn Yotburut

CONTENTS

	Page
ABSTRACT IN THAI	I
ABSTRACT IN ENGLISH.....	III
ACKNOWLEDGEMENTS	V
CONTENTS	VI
LIST OF TABLES	X
LIST OF FIGURES	XII
LIST OF ABBREVIATIONS	XXIII
CHAPTER	
I INTRODUCTION.....	1
1.1 Background and motivation.....	1
1.2 Objectives of research.....	4
1.3 Limitations of study.....	5
1.4 Location of the research.....	5
1.5 Expected results	6
1.6 Outline of thesis	6
II LITERATURE REVIEWS.....	7
2.1 Multiferroics	7
2.2 Multiferroic BiFeO ₃	11

CONTENTS (Continued)

	Page
2.2.1 Properties of BiFeO ₃	11
2.2.2 The synthesis methods.....	17
2.2.3 Magnetism in BiFeO ₃	22
2.2.4 Electrical properties of BiFeO ₃	24
2.2.5 General doping concepts	29
III RESEARCH METHODOLOGY.....	32
3.1 BiFeO ₃ -based powders and ceramic samples preparation.....	32
3.2 Powder and ceramic sample characterization	37
3.2.1 X-ray diffraction (XRD).....	37
3.2.2 Transmission electron microscopy (TEM).....	40
3.2.3 Scanning electron microscopy (SEM).....	40
3.2.4 X-ray absorption spectroscopy (XAS).....	41
3.2.5 Fourier transform infrared spectroscopy (FTIR).....	44
3.2.6 UV-Visible spectroscopy (UV-Vis).....	45
3.2.7 Magnetic measurements	46
3.3 Dielectric properties	47
3.4 Current-voltage characteristics	50
IV RESULTES AND DISCUSSION.....	52
4.1 Structural characterization and morphology of BiFeO ₃ and Ba-, La- and Sm-doped BiFeO ₃ nanopowders.....	52

CONTENTS (Continued)

	Page
4.1.1 Structural and morphology of the BiFeO ₃ nanopowders	52
4.1.2 Effects of Ba, La and Sm doping on the morphologies and crystal structure of BiFeO ₃ nanopowders	56
4.1.3 X-ray absorption spectroscopy study of the Fe K-edge in Bi _{1-x} A _x FeO ₃ (A = La, Sm, and Ba) nanopowders	79
4.1.4 Fourier transform infrared spectrometer (FTIR).....	84
4.2 Optical properties (UV-Vis).....	88
4.3 Magnetic hysteresis (M-H) properties.....	97
4.3.1 Magnetic hysteresis (M-H) properties of the pure BiFeO ₃ and Ba-doped BiFeO ₃ nanopowders at room temperature.....	97
4.3.2 Magnetic hysteresis (M-H) properties of La-doped BiFeO ₃ nanopowders	99
4.3.3 Magnetic hysteresis (M-H) properties of Sm-doped BiFeO ₃ nanopowders	102
4.3.4 Temperature dependence of magnetization for the pure BiFeO ₃ and doped BiFeO ₃ nanopowders.....	106
4.4 Ceramic characterization: crystal structure and morphologies	120
4.4.1 Crystal structure and phase formation	120
4.4.2 Surface morphology.....	126
4.5 Frequency and temperature dependence on dielectric properties	142

CONTENTS (Continued)

	Page
4.5.1 Dielectric properties as a function of frequency for doped BiFeO ₃ ceramics at room temperature	142
4.5.2 Dielectric properties as a function of frequency for doped BiFeO ₃ ceramics at various temperatures	149
4.5.3 The temperature dependence of dielectric properties of doped BiFeO ₃ ceramics	173
4.5.4 Effect of dc conductivity on dielectric behavior	181
4.5.5 Impedance spectroscopy	191
4.6 Effect of DC bias voltage on dielectric response	213
4.7 Current–voltage characteristic	230
V CONCLUSION AND SUGGESTION	253
5.1 The structure and surface morphology characterization	253
5.2 Optical properties	255
5.3 Magnetic properties	256
5.4 Dielectric properties	257
5.5 Current–voltage characteristics	259
5.6 Suggestion for future work	260
REFERENTES	261
APPENDIX	282
CURRICULUM VITAE	285

LIST OF TABLES

Table	Page
2.1 Summarizes of several of multiferroic materials	10
2.2 Summarizes the most important structural and physical properties of BiFeO ₃	11
2.3 Lists of reports of electric and magnetic properties	29
3.1 List of materials used as starting raw materials for BiFeO ₃ -based powder preparation, and their source and purity	35
4.1 Details of Rietveld refined XRD parameters for Bi _{1-x} A _x FeO ₃ (A = Ba, La, and Sm) with x = 0.0, 0.1, 0.2, and 0.3 samples	54
4.2 Summary of crystallite size of pure BiFeO ₃ , Ba-, La-, and Sm-doped BiFeO ₃ nanopowders calcined at 600 °C for 3 h	76
4.3 Summary of band gap energy (E_g) of undoped BiFeO ₃ and Ba-, La-, and Sm-doped BiFeO ₃ nanopowders calcined at 600 °C for 3h	96
4.4 Summary of magnetization of Ba-, La-, and Sm-doped BiFeO ₃ at room temperature	106
4.5 Effective magnetic moment (μ_{eff}), Curie-Weiss temperature (θ) obtained from Curie-Weiss law fitting results for doped BiFeO ₃	112
4.6 Relative densities and average grain size of undoped BiFeO ₃ and Ba-, La-, and Sm-doped BiFeO ₃ sintered at 800 °C for 3 h	141

LIST OF TABLES (Continued)

Table	Page
4.7 Summarizing of fitting parameters corresponding to equivalent circuits in temperature range 50–170 °C and at different compositions of Ba-doped BiFeO ₃ ceramics	206
4.8 Summarizing of fitting parameters corresponding to equivalent circuits in temperature range 50–170 °C and at different compositions of La-doped BiFeO ₃ ceramics	207
4.9 Summarizing of fitting parameters corresponding to equivalent circuits in temperature range 50–170 °C and at different compositions of Sm-doped BiFeO ₃ ceramics	208
4.10 Activation energy of conductivity at grain and grain boundary for pure BiFeO ₃ and doped BiFeO ₃ ceramics	212
4.11 The current–voltage characteristics of various Ba-, La-, and Sm-doped BiFeO ₃ samples	243

LIST OF FIGURES

Figure	Page
2.1 The relationship between multiferroic and magnetoelectric materials	9
2.2 Schematic views of BiFeO ₃ perovskite unit cells, (a) a rhombohedral unit cell of BiFeO ₃ in the ferroelectric phase and (b) accommodation of two perovskite unit cells into one rhombohedral structure	13
2.3 Phase diagram for Bi _{1-x} Tb _x FeO ₃ (0 ≤ x ≤ 0.20) and remnant magnetization (M _r) as a function of the Tb concentration x (inset).....	14
2.4 Schematic of the 64 nm of antiferromagnetic spin circular cycloid structure of BiFeO ₃	16
2.5 Phase diagram of system of Bi ₂ O ₃ and Fe ₂ O ₃	18
2.6 The dielectric behaviors and microstructure of BiFeO ₃ ceramic prepared by a simple co-precipitation method	21
2.7 Magnetization hysteresis loops of Eu-doped BiFeO ₃ samples.....	23
2.8 Schematic presentation of antiferromagnetic ordering in BiFeO ₃ (G-type) structure	24
2.9 The current-voltage characteristics and (b) the dielectric properties of Bi _{1-x} Ba _x FeO ₃ (x = 0.00-0.25) at room temperature	26

LIST OF FIGURES (Continued)

Figure	Page
2.10 The frequency dependence of the capacitance and complex impedance of the In/BFO/LSMO capacitor under applied biases 0–2 V	27
2.11 Impedance spectra and dielectric properties of CuO ceramics under applied dc bias (a) sintered at 900 °C and (b) sintered at 950 °C	28
2.12 M–H loops of $\text{Bi}_{1-x}\text{A}_x\text{FeO}_{3-x/2}$ samples and (inset) M_s as a function of the average ionic radius of the A–site ions	31
3.1 Calcination and sinter diagrams of BiFeO_3 –based samples	35
3.2 Diagram showing the preparation and characterization of BiFeO_3 –based powder and ceramics	36
3.3 Schematic principle of XRD equipment and description of Bragg’s diffraction law	39
3.4 Schematic diagram of the vibrating sample magnetometer (VSM).....	47
3.5 Schematic of parallel plate capacitor with electrodes on both sides of the dielectric	48
3.6 Diagram presenting measuring dielectric parameters of the BiFeO_3 –based ceramic samples using a Hewlett Packard 4194A impedance gain phase analyzer	50
4.1 Rietveld refinement of the XRD pattern of pure BiFeO_3 nanopowders	54

LIST OF FIGURES (Continued)

Figure	Page
4.2 TEM bright field images (left) with the corresponding SAED pattern (right) of (a) pure BiFeO ₃ , (b)–(e) Bi _{1-x} Ba _x FeO ₃ , (f)–(i) Bi _{1-x} La _x FeO ₃ , and (j)–(m) Bi _{1-x} Sm _x FeO ₃ , with x = 0.05, 0.1, 0.2, and 0.3 respectively.....	64
4.3 The XRD patterns of undoped BiFeO ₃ and Bi _{1-x} Ba _x FeO ₃ samples with x = 0.05, 0.1, 0.2, and 0.3, respectively (b) Enlarged view of the diffraction peaks in the 2θ ~32° range	69
4.4 The XRD patterns of undoped BiFeO ₃ and Bi _{1-x} La _x FeO ₃ samples with x = 0.05, 0.1, 0.2, and 0.3, respectively (b)–(c) Enlarged view of the diffraction peaks in the 2θ ~32° and 51° range	70
4.5 The XRD patterns of undoped BiFeO ₃ and Bi _{1-x} Sm _x FeO ₃ samples with x = 0.05, 0.1, 0.2, and 0.3, respectively (b) Enlarged view of the diffraction peaks in the 2θ ~32°	71
4.6 Rietveld refinement of XRD data for Bi _{1-x} Ba _x FeO ₃ powder (a) x = 0.05 and (b) x = 0.3.....	72
4.7 Rietveld refinement of XRD data for Bi _{1-x} La _x FeO ₃ powder (a) x = 0.05 and (b) x = 0.3.....	73
4.8 Rietveld refinement of XRD data for Bi _{1-x} Sm _x FeO ₃ powder (a) x = 0.05 and (b) x = 0.3.....	74
4.9 An average crystallite size of undoped BiFeO ₃ , Ba–, La–, and Sm–doped samples calcined at 600 °C for 3 h.....	77

LIST OF FIGURES (Continued)

Figure	Page
4.10 Lattice constant of undoped BiFeO ₃ sample, (a) a, (b) c parameter, and (c) Volume of Ba-, La-, and Sm-doped BiFeO ₃ nanopowders	79
4.11 Fe K-edge X-ray absorption near-edge structure (XANES) for Ba-doped BiFeO ₃ (x = 0, 0.05, 0.1, 0.2, and 0.3) samples, Fe ₂ O ₃ and Fe ₃ O ₄ are reference materials for Fe ²⁺ and Fe ³⁺ , the first derivative of Fe K-edge XANES spectrum in BiFeO ₃ (b)	83
4.12 FT-IR Spectra for (a) Bi _{1-x} Ba _x FeO ₃ , (b), Bi _{1-x} La _x FeO ₃ , and (c) Bi _{1-x} Sm _x FeO ₃ powders calcined at 600 °C for 3 h as a function of Ba, La, and Sm content with x = 0.05, 0.1, 0.2, and 0.3	87
4.13 Room-temperature optical absorbance spectra of undoped BiFeO ₃ and doped BiFeO ₃ nanoparticles; (a) Ba-, (b) La-, and (c) Sm-doped BiFeO ₃ , respectively and (d) Schematic representation of the crystal-field effect lowering the symmetry from octahedral O _h to rhombohedral C _{3v}	91
4.14 Plot of as a function of photon energy (ahv) ^{1/2} for undoped BiFeO ₃ nanorods prepared in air at 600 °C for 3 h (a) Ba-doped BiFeO ₃ , (b) La-doped BiFeO ₃ , and (c) Sm-doped BiFeO ₃ nanopowders, respectively and (d) the schematic diagram of the possible mechanism for electronic energy band	95

LIST OF FIGURES (Continued)

Figure	Page
4.15 Band gap versus doping concentration of undoped BiFeO ₃ and Ba-, La-, and Sm-doped BiFeO ₃ nanopowders calcined at 600 °C for 3 h	96
4.16 The magnetization magnetic measurement (M) versus applied magnetic field (H) were performed on undoped BiFeO ₃ , (a) Ba-doped, (b) La-doped, and (c) Sm-doped BiFeO ₃ powders with different compositions obtained at 293 K from VSM measurement	105
4.17 (a), (b), (c), (d), and (e) display the temperature-dependent magnetization (M-T) curves of pure BiFeO ₃ and Ba-doped BiFeO ₃ samples, respectively. Inset: the Curie-Weiss fitting to the data between 150 and 300 K under 1 kOe as a function of temperature and fitting result using the Curie-Weiss law	115
4.18 (a), (b), (c), and (d) display the temperature-dependent magnetization (M-T) curves of La-doped BiFeO ₃ samples, respectively. Inset: the Curie-Weiss fitting to the data between 150 and 300 K under 1 kOe as a function of temperature and fitting result using the Curie-Weiss law	117
4.19 (a), (b), (c), and (d) display the temperature-dependent magnetization (M-T) curves of Sm-doped BiFeO ₃ samples, respectively. Inset: the Curie-Weiss fitting to the data between 150 and 300 K under 1 kOe as a function of temperature and fitting result using the Curie-Weiss law	119

LIST OF FIGURES (Continued)

Figure	Page
4.20 (a) X-ray diffraction patterns of $\text{Bi}_{1-x}\text{Ba}_x\text{FeO}_3$ with $x = 0, 0.05, 0.1, 0.2,$ and 0.3 ; (* and # indicates the secondary phase Bi_2O_3 and $\text{Bi}_2\text{Fe}_4\text{O}_9$) and (b) show the enlarged view of diffraction peaks at $2\theta \sim 32^\circ$	123
4.21 X-ray diffraction patterns of $\text{Bi}_{1-x}\text{La}_x\text{FeO}_3$ with $x = 0, 0.05, 0.1, 0.2,$ and 0.3 ; (* and # indicates the secondary phase Bi_2O_3 and $\text{Bi}_2\text{Fe}_4\text{O}_9$), (b) show the enlarged view of diffraction peaks at $2\theta \sim 32^\circ$, and (c) at $2\theta \sim 39^\circ$, and $\sim 51^\circ$	124
4.22 X-ray diffraction patterns of $\text{Bi}_{1-x}\text{Sm}_x\text{FeO}_3$ with $x = 0, 0.05, 0.1, 0.2,$ and 0.3 ; (* and # indicates the secondary phase Bi_2O_3 and $\text{Bi}_2\text{Fe}_4\text{O}_9$) and (b) shows the enlarged view of diffraction peaks at $2\theta \sim 32^\circ$	125.
4.23 SEM micrographs for $\text{Bi}_{1-x}\text{Ba}_x\text{FeO}_3$ powders calcined at 800°C for 3 h as a function of Ba content: (a) $x = 0$, (b) $x = 0.05$, (c) $x = 0.1$, (d) $x = 0.2$, and (e) $x = 0.3$	131
4.24 SEM micrographs for $\text{Bi}_{1-x}\text{La}_x\text{FeO}_3$ powders calcined at 800°C for 3 h as a function of La content: (a) $x = 0$, (b) $x = 0.05$, (c) $x = 0.1$, (d) $x = 0.2$, and (e) $x = 0.3$	136
4.25 SEM micrographs for $\text{Bi}_{1-x}\text{Sm}_x\text{FeO}_3$ powders calcined at 800°C for 3 h as a function of Sm content: (a) $x = 0$, (b) $x = 0.05$, (c) $x = 0.1$, (d) $x = 0.2$, and (e) $x = 0.3$	140

LIST OF FIGURES (Continued)

Figure	Page
4.26 Frequency dependence of dielectric properties (dielectric constant (ϵ'), loss tangent ($\tan \delta$) at room temperature for $\text{Bi}_{1-x}\text{Ba}_x\text{FeO}_3$ ceramics sintered at 800 °C for 3 h	146
4.27 Frequency dependence of dielectric properties (dielectric constant (ϵ'), loss tangent ($\tan \delta$)) at room temperature for $\text{Bi}_{1-x}\text{La}_x\text{FeO}_3$ ceramics sintered at 800 °C for 3 h	147
4.28 Frequency dependence of dielectric properties (dielectric constant (ϵ'), loss tangent ($\tan \delta$)) at room temperature for $\text{Bi}_{1-x}\text{Sm}_x\text{FeO}_3$ ceramics sintered at 800 °C for 3 h	148
4.29 Frequency dependence of dielectric properties (dielectric constant (ϵ'), loss tangent ($\tan \delta$), and dielectric loss (ϵ'')) at the temperature range of -50 to 200 °C for BiFeO_3 ceramics sintered at 800 °C	151
4.30 (a) Dielectric constant (ϵ') and (b) loss tangent ($\tan \delta$) in the temperature range -50–30 °C for the $\text{Bi}_{1-x}\text{Ba}_x\text{FeO}_3$ ceramics sintered at 800 °C .	154
4.31 Frequency dependence of dielectric properties (dielectric constant (ϵ') and loss tangent ($\tan \delta$)) in the temperature range of -50 to 200 °C for $\text{Bi}_{1-x}\text{La}_x\text{FeO}_3$ ceramics	160
4.32 Frequency dependence of dielectric properties (dielectric constant (ϵ') and loss tangent ($\tan \delta$)) at the temperature range of -50 to 200 °C for $\text{Bi}_{1-x}\text{Sm}_x\text{FeO}_3$ ceramics	167

LIST OF FIGURES (Continued)

Figure	Page
4.33 Low–frequency relaxation (LFR) and high–frequency relaxation (HFR) of (a) pure BiFeO ₃ and (b)–(e) Bi _{1-x} Ba _x FeO ₃ ceramics at various temperatures; the solid and dotted curves are the best fit to the Cole–Cole relaxation model for the LFR and HFR, respectively.....	171
4.34 Arrhenius plots of the LFR and HFR of (a) the pure BiFeO ₃ and Ba–doped BiFeO ₃ ceramics and (b) Bi _{0.9} Sm _{0.1} FeO ₃ ceramic	172
4.35 Temperature dependence of dielectric constant (ϵ') and loss tangent ($\tan \delta$) at the frequency range of 10 ² –10 ⁶ Hz for the pure BiFeO ₃ ceramics...	176
4.36 Temperature dependence of dielectric constant (ϵ') and loss tangent ($\tan \delta$) at the frequency range of 10 ² –10 ⁶ Hz for the doped BiFeO ₃ ceramics	180
4.37 Dielectric loss and fitted results of Bi _{1-x} Ba _x FeO ₃ sintered at 800 °C for 3 h for (a) x = 0.05 and (b) x = 0.3	186
4.38 Dielectric loss and fitted results of Bi _{1-x} La _x FeO ₃ sintered at 800 °C for 3 h for (a) x = 0.05 , (b) x = 0.1 and (c) x = 0.2.....	188
4.39 Dielectric loss and fitted results of Bi _{1-x} Sm _x FeO ₃ sintered at 800 °C for 3 h for (a) x = 0.05 and (b) x = 0.3	189
4.40 Temperature dependence of DC conductivity for (a) Ba-doped BiFeO ₃ , (b) La-doped BiFeO ₃ , and (c) Sm-doped BiFeO ₃	191

LIST OF FIGURES (Continued)

Figure	Page
4.41 Complex impedance plane plot (Z' versus Z'') in the temperature range -50 to -10 °C of the pure BiFeO ₃ ceramic (a) and (b) the complex impedance plot in the temperature range 120–200 °C.....	194
4.42 Complex impedance plane plot (Z' versus Z'') in the temperature range 120–200 °C of the pure BiFeO ₃ and Ba-doped BiFeO ₃ ceramics ; inset is inset is complex impedance plot at 50 and 60 °C.....	197
4.43 Complex impedance plane plots (Z' versus Z'') in the temperature range 120–200 °C of the pure BiFeO ₃ and La-doped BiFeO ₃ ceramics; the inset is the complex impedance plots in the temperature range -50 to -10 °C	201
4.44 Complex impedance plane plots (Z' versus Z'') in the temperature range 120–200 °C of the pure BiFeO ₃ and Sm-doped BiFeO ₃ ceramics; the inset is the complex impedance plots in the temperature range -50 to -20 °C	205
4.45 Temperature dependence of grain and grain boundary conductivity for the pure BiFeO ₃ sample	210
4.46 Temperature dependence of grain (a) and (b) grain boundary conductivity for the Ba-doped BiFeO ₃ samples.....	211
4.47 Temperature dependence of grain (a) and (b) grain boundary conductivity for the La-doped BiFeO ₃ samples	211
4.48 Temperature dependence of grain (a) and (b) grain boundary conductivity for the Sm-doped BiFeO ₃ samples	212

LIST OF FIGURES (Continued)

Figure	Page
4.49 The dielectric constant (ϵ') and loss tangent ($\tan \delta$) for the pure BiFeO ₃ ceramics sintered at 800 °C for 3 h under various applied voltages DC bias as a function of frequency at room temperature	217
4.50 The dielectric constant (ϵ') and loss tangent ($\tan \delta$) at for Ba-doped BiFeO ₃ ceramics sintered at 800 °C for 3 h under various applied voltages DC bias as a function of frequency at room temperature	219
4.51 The dielectric constant (ϵ') and loss tangent ($\tan \delta$) at for La-doped BiFeO ₃ ceramics sintered at 800 °C for 3 h under various applied voltages DC bias as a function of frequency at room temperature	221
4.52 The dielectric constant (ϵ') and loss tangent ($\tan \delta$) at for Sm-doped BiFeO ₃ ceramics sintered at 800 °C for 3 h under various applied voltages DC bias as a function of frequency at room temperature	223
4.53 Complex impedance spectra of the undoped BiFeO ₃ ceramic sintered at 800 °C for 3 h as a function of DC bias voltage	226
4.54 Complex impedance spectra of the Ba-doped BiFeO ₃ ceramic sintered at 800 °C for 3 h as a function of DC bias voltages	227
4.55 Complex impedance spectra of the La-doped BiFeO ₃ ceramic sintered at 800 °C for 3 h as a function of DC bias voltages	228
4.56 Complex impedance spectra of the Sm-doped BiFeO ₃ ceramic sintered at 800 °C for 3 h as a function of DC bias voltages	229

LIST OF FIGURES (Continued)

Figure	Page
4.57 (a)–(c) Current–voltage curves of doped BiFeO ₃ samples at room temperature and (inset) current leakage and breakdown field as a function of doping content for the BiFeO ₃ ceramics	234
4.58 Logarithmic plots of dependence of J as a function of E measured at room temperature for BiFeO ₃ ceramics sintered at 800 °C for 3 h.....	237
4.59 Logarithmic plots of dependence of J as a function of E measured at room temperature for (a) Bi _{1-x} Ba _x FeO ₃ , (b) Bi _{1-x} La _x FeO ₃ , and (c) Bi _{1-x} Sm _x FeO ₃ ceramics sintered at 800 °C for 3 h	239
4.60 Nonlinear characteristics (J – E curves) of the pure BiFeO ₃ (a) and (b)–(e) Ba–doped BiFeO ₃ ceramics at various temperatures and (inset) plots of $\ln J$ versus $E^{1/2}$	246
4.61 Nonlinear characteristics (J – E curves) of the pure BiFeO ₃ (a) and (b)–(e) La–doped BiFeO ₃ ceramics at various temperatures.....	248
4.62 Nonlinear characteristics (J – E curves) of the Sm–doped BiFeO ₃ ceramics at various temperatures; (a) $x = 0.05$, (b) $x = 0.1$, and (c) $x = 0.2$	250
4.63 Plots of $\ln J_0$ vs $1/T$ for pure BiFeO ₃ and (a) Ba– (b) La–, and (c) Sm–doped BiFeO ₃ samples and the estimated potential barrier height, ϕ_B	252

LIST OF ABBREVIATIONS

FTIR	=	Fourier transform infrared spectroscopy
SEM	=	Scanning electron microscopy
TEM	=	Transmission electron microscopy
VSM	=	Vibrating sample magnetometer
XANES	=	X-ray absorption near edge structure
XAS	=	X-ray absorption spectroscopy
XRD	=	X-ray diffraction
UV-Vis	=	UV-Visible spectroscopy
SAED	=	Selected area electron diffraction

CHAPTER I

INTRODUCTION

1.1 Background and motivation

In recent years, multiferroic materials which show a coupling between electrical and magnetic properties in a material have attracted a great deal of attention due to their fascinating fundamental physics and potential applications. In these materials, the coexistence of ferroelectricity and ferromagnetism and their coupling, as well as their influences on static and dynamic phenomena have led to the discovery of next generation actuators, sensors, and memory devices. Moreover, these materials have significant potential for the manufacture of MRAMs (Magnetoelectric Random Access Memory) (Bibes and Barthélémy, 2008; Béa *et al.*, 2006) that provide several benefits over the traditional RAM currently in use, i.e., higher reading and speed of writing, non-volatile nature, reduce energy consumption, and high density storage. However, the present demand for ever-decreasing size of transistors and other necessary electronic parts in electronic devices has led to a greater interest in advanced functional materials. A possible way of meeting this challenge is to use multiferroic materials instead of single-ferroic materials. Multiferroic materials are very rare in nature since ferroelectricity and ferro/antiferromagnetism tend to be mutually exclusive and interact weakly with each other when they coexist. YMnO_3 ,

TbMnO₃, BiMnO₃, BiFeO₃, etc. are some of the multiferroic materials which were discovered in the past and which have low electric and magnetic polarization with a large leakage current density. This is particularly the case among the few known multiferroic materials, for example perovskite bismuth ferrite (BiFeO₃) with rhombohedrally distorted perovskite structure (R3c space group). BiFeO₃ exhibits both ferroelectric and antiferromagnetic (AFM) order simultaneously above room temperature (Ghosh *et al.*, 2005; Maurya *et al.*, 2008). It exhibits antiferromagnetic ordering with high Neel temperature ($T_N \sim 643$ K) and ferroelectric behavior with high Curie temperatures ($T_c \sim 1103$ K) (Kumar *et al.*, 2000; Pradhan *et al.*, 2005). The ferroelectricity in BiFeO₃ is attributed to the $6s^2$ lone pair electrons of Bi³⁺ that may hybridize with empty p-orbital in materials to form a localized segment causing a structural distortion, while magnetism is believed to originate from partially filled d-orbital of Fe ions. According to first principle calculation, it has been reported that BiFeO₃ shows a large spontaneous polarization (P_s) of about $\sim 90\text{--}100 \mu\text{C}/\text{cm}^2$ for a rhombohedral distorted structure with R3c space group and around $\sim 150 \mu\text{C}/\text{cm}^2$ for the tetragonal phase. The magnetism of BiFeO₃ is G-type antiferromagnetic, where spin is given by the transition metal of Fe³⁺ ions. The antiferromagnetic G-type structure is long range modulated as it has a spiral spin-modulated cycloidal magnetic structure of the length of 62 nm in the (110) spiral direction. The BiFeO₃ bulk undergoes weak magnetization due to its antiferromagnetic behavior and modulated spin spiral structure which inhibit linear magnetoelectric properties. However, its rhombohedral distorted structure gives rise to the canting of the magnetic spins leading to a localized weak ferromagnetism which is locked in the period length of 62 nm. Moreover, high permittivity dielectric behavior is observed in BiFeO₃-based

which can be affected by the existence of interfacial polarization at grain boundaries in inhomogeneous microstructures.

However, it should be noticed that the dielectric response and electric conductivity of BiFeO₃ ceramics have been investigated by studying the processing conditions, which are responsible not only for the drawbacks and the existence of Fe²⁺, but also for the formation of various parasitic phases. Conductivity increases suddenly with activation energy of 1.26 eV at temperatures higher than ~350 °C and its low frequency values become larger than those of the high frequency range. As is well known, in polycrystalline ceramics, the grain and grain boundary structure play important roles in the microstructure, which have an impact on the dielectric response and the electrical properties of the ceramics. Interesting dielectric behavior with three relaxation processes have been reported for the BiFeO₃-based ceramics sintered at 700 °C for 4 h and obtained from precipitation-synthesized powder. They found that the low-temperature relaxation with E_a of 0.34 eV can be attributed to the hopping conduction of the localized charge carriers, whilst the middle-temperature relaxation process of E_a 0.77 eV was likely affected by the grain boundary effect, and the high-temperature relaxation process with E_a 0.95 eV contributed to the defects dipole and/or conduction defects. However, practical applications of BiFeO₃ have been restricted because of the high leakage current induced by defects, low electrical resistivity linked to the presence of impurities, a low magnetic moment and a very weak magnetoelectric coupling. In order to circumvent these inconsistencies, attempts to improve BiFeO₃ properties have been made by doping it with trivalent rare earth elements (La³⁺, Dy³⁺, Gd³⁺, Tb³⁺, Sm³⁺), divalent cation (Bi²⁺, Ca²⁺, Sr²⁺), transition metal elements (Cu³⁺, Mn^{3+/4+}, Cr³⁺, Ti^{2+/4+}) or by optimizing the preparation

parameters. Great increases in multiferroic properties have been found in several research works. The doping has resulted in changes to the cycloidal spin structure of pure BiFeO_3 which changes to a canting spin structure which can be the cause of the the improvement in ferromagnetic properties at room temperature. Moreover, decreases in leakage current density using proper dopants can be attributed to the enhancement of room temperature ferroelectric properties in doped materials. However, studies on the properties of BiFeO_3 ceramics are rare in the literature, especially the effects of DC bias voltage on the dielectric response, and on the temperature dependence of current–voltage characteristics. The purpose of this study is to prepare dense, single phase BiFeO_3 powders and ceramics using a co-precipitation method by adding Ba, La and Sm as dopants. The effects of the substitution on the structural, phase formation, and magnetic, optical, dielectric and electric properties are reported and discussed.

1.2 Objectives of research

The main objectives of this Ph.D. thesis are

1.2.1 To synthesize pure BiFeO_3 and isovalent ions (La^{3+} and Sm^{3+}) and divalent ion (Ba^{2+}) substitution at A–site in BiFeO_3 nanopowders.

1.2.2 To fabricate pure BiFeO_3 and Ba^{2+} –, La^{3+} – and Sm^{3+} –doped BiFeO_3 ceramics.

1.2.3 To study the effect of doping concentration on the structure, phase formation, morphology of pure BiFeO_3 and doped– BiFeO_3 powders and ceramics.

1.2.4 To study the optical and magnetic properties of synthesized pure BiFeO_3 and doped- BiFeO_3 nanopowders.

1.2.5 To investigate the dielectric and electrical properties of pure fabricated BiFeO_3 and doped- BiFeO_3 ceramics under different temperatures, frequencies and with DC bias voltages.

1.3 Limitations of the study

1.3.1 Preparation of $\text{Bi}_{1-x}\text{A}_x\text{FeO}_3$ powders by a simple co-precipitation method.

1.3.2 This study focuses on the fabrication of the $\text{Bi}_{1-x}\text{A}_x\text{FeO}_3$ ceramics (where $\text{A} = \text{Ba}, \text{La}, \text{Sm}$) and ($x = 0, 0.05, 0.1, 0.2, \text{ and } 0.3$).

1.3.3 The calcination is carried out only at $600\text{ }^\circ\text{C}$ and sintering at $800\text{ }^\circ\text{C}$ for 3 h, and the concentration of doping is varied from 5 to 30 mol.%.

1.3.4 Investigation of the magnetic properties of $\text{Bi}_{1-x}\text{A}_x\text{FeO}_3$ powders and $\text{Bi}_{1-x}\text{A}_x\text{FeO}_3$ ceramics at a temperature range of 50 to 350 K.

1.3.5 Investigations of the dielectric and electrical properties of $\text{Bi}_{1-x}\text{A}_x\text{FeO}_3$ ceramics.

1.4 Location of the research

1.4.1 Advanced Materials Physics (Amp.) Laboratory, School of Physics, Institute of Science and the Center of Scientific and Technology equipment, Suranaree University of Technology, Nakhon Ratchasima, Thailand.

1.4.2 Faculty of Science, Chang Mai University.

1.4.3 National Metal and Materials Technology Center (MTEC).

1.4.4 Faculty of Science, Khon Kaen University.

1.5 Expected results

1.5.1 Skill and expertise for fabrication and characterization techniques of the BiFeO₃-based ceramics with improved properties for electrical devices.

1.5.2 Understanding of the structure, dielectric and electrical properties of the BiFeO₃-based ceramics

1.5.3 Publications in ISI journals

1.6 Outline of thesis

The thesis is organized as follows:

1.6.1 Chapter I gives an introduction to the background and the research motivations.

1.6.2 Chapter II provides a literature review of information concerning the structure, synthesis method and applications of bismuth ferrite-based materials. The basic physics concerning the optical, magnetic, dielectric and electrical properties of BiFeO₃-based compounds are also detailed in this chapter.

1.6.3 Chapter III describes the experimental procedures and characterization method of BiFeO₃-based materials.

1.6.4 Chapter IV presents the experimental results and discussion.

1.6.5 Chapter V contains the conclusions and recommendations of this thesis.

CHAPTER II

LITERATURE REVIEWS

The chapter II reviews the literature on the structure, preparation, and potential applications of BiFeO₃-based powder and ceramic materials, and some recent studies about their properties. A simple explanation of the theoretical background of the dielectric properties, magnetic properties, optical properties and related electrical properties in the BiFeO₃-based powder and ceramic materials are also given in detailed in this chapter.

2.1 Multiferroics

Single phase multiferroic materials have been formally defined as materials that possesses two of the three ferroic properties i.e. ferroelectricity, ferromagnetism and ferroelasticity coexisting in the same phase. This term was first used by H. Schmid in 1994. In general, the notion is extended nowadays to exclude the requirement for ferroelastic properties in practice. The field of research that will be described typically involves the terms multiferroic and magnetoelectric, whose overlap is incomplete. Multifunctional materials have had a wide research interest due to both the fundamental physics and the amount of potential multifunctional applications in modern technology. The coexistence of ferroelectricity and

ferromagnetism might allow an additional degree of freedom in the development of novel devices, for example, actuators, transducers, optical diodes, and storage devices.

The relationship between multiferroic and magnetoelectric properties is shown in Figure 2.1 (Eerenstein *et al.*, 2006). The figure refers to magnetically polarisable materials that form the superset of ferromagnetic materials such as antiferromagnets (paraelectrics and antiferroelectrics). Table 2.1 summarizes electrical and magnetic properties of several of multiferroic materials. The intersection between them represents materials that are multiferroic. Obtaining single-phase multiferroic materials is made even more difficult by the condition that most multiferroics are not naturally-occurring materials. Most multiferroic materials have low magnetic moment ordering and a ferroelectric transition temperature. This can be partly enhanced by introducing dopant (for example, rare earth elements) into the parent material. Moreover, the formation of magnetism can be explained as the presence of localized electrons, mainly in the partly filled d-orbitals making a corresponding localized spin or magnetic moment. On the other hand, ferroelectricity requires transition metal ions with empty d-orbitals. The mutual exclusivity of ferroelectricity and magnetism is often referred to as a problem called “ d^0 VS d^n ” which has been studied (Hill, 2000). However, many materials showing multiferroic properties have been reported in the current literature. We can see the classification of multiferroic materials into different groups. There are two groups of multiferroic materials which Van den Brink *et al.* have mentioned (Van Den Brink and Khomskii, 2008). The first group contains materials with independently originating ferroelectricity and magnetism, which have different origins and are often due to different active subsystems of a material. The second group of multiferroics includes

materials in which ferroelectricity occurs only in the magnetically ordered state. In order for the coexistence of ferroelectricity and magnetism to arise, both elements and structures need to be discussed. In the perovskite structure (ABO_3) of multiferroics, the A-site element is selected its ferroelectricity while the magnetism is associated with the element at the B-site. For example the $BiFeO_3$ perovskite, the ferroelectricity of $BiFeO_3$ mainly occur from the lone pair of $6s^2$ electrons of Bi^{3+} which tend to hybridize with $2s$ and $2p$ of oxygen to form a space-filling localized segment, which in turn pushes away its neighboring atoms causing a structure distortion.

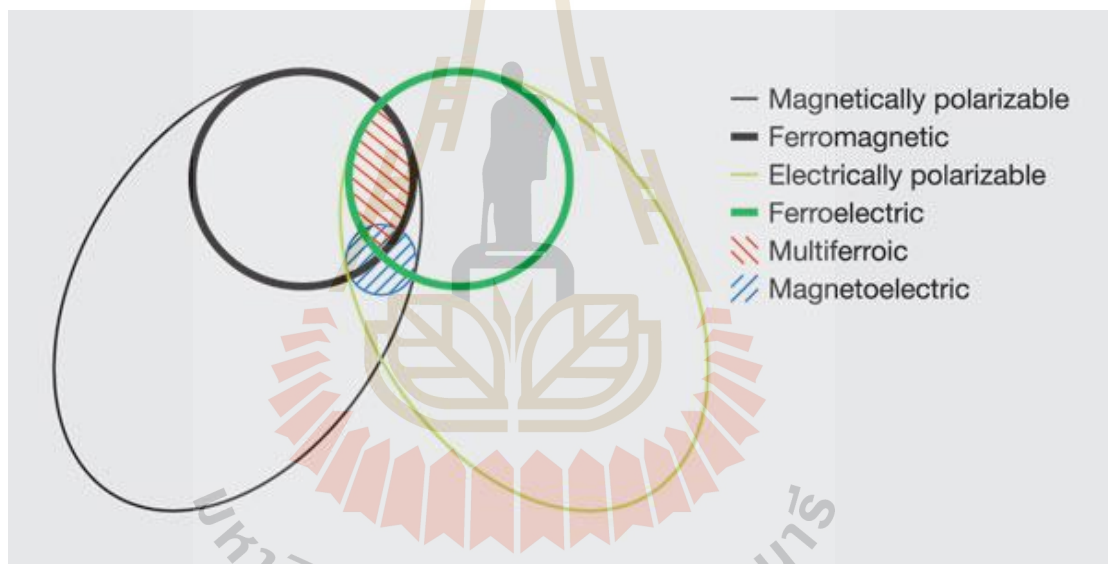


Figure 2.1 The relationship between multiferroic and magnetoelectric materials (Adapted from Eerenstein *et al.*, 2006).

Table 2.1 Summary of several multiferroic materials (Adapted from Smolenskii *et al.*, 1980).

Materials	Electric properties	Magnetic properties	T _c (K)	T _N (K)
Pb(Fe _{2/3} W _{1/3})O ₃	Ferroelectric	Antiferromagnetic	178	363
Pb(Fe _{1/2} Nb _{1/2})O ₃	Ferroelectric	Antiferromagnetic	387	143
Pb(Co _{1/2} W _{1/2})O ₃	Ferroelectric	Weak ferromagnetic	68	9
Pb(Mn _{2/3} W _{1/3})O ₃	Antiferroelectric	Antiferromagnetic	473	203
Pb(Fe _{2/3} Ta _{1/2})O ₃	Ferroelectric	Antiferromagnetic	233	180
BiFeO ₃	Ferroelectric	Antiferromagnetic	1123	650
BiMnO ₃	Antiferroelectric	Ferromagnetic	773	103
YMnO ₃	Ferroelectric	Antiferromagnetic	913	80
YbMnO ₃	Ferroelectric	Antiferromagnetic/ Weak ferromagnetic	983	87.3
HoMnO ₃	Ferroelectric	Antiferromagnetic	873	76
ErMnO ₃	Ferroelectric	Antiferromagnetic	833	79
Ni ₃ B ₇ O ₁₃ I	Ferroelectric	Weak ferromagnetic	64	64

2.2 Multiferroic BiFeO₃

2.2.1 Properties of BiFeO₃

Table 2.2 Summarises the most important structural and physical properties of BiFeO₃.

Property	Value	References
Crystal structure ^a	$a_{rh} = 5.63 \text{ \AA}$, $\alpha_{rh} = 59.4^\circ$ $a_h = 5.571 \text{ \AA}$, $c_h = 13.858 \text{ \AA}$	(Kubel and Schmid, 1990)
Space group	R3c	
Tolerance factor ^b	0.89	(Xi <i>et al.</i> , 2014)
Density	82%	(Ilić <i>et al.</i> , 2016)
Thermal expansion	Non-linear and anisotropic	(IG, 1966)
Ferroelectricity	$T_c = 1103 \text{ K}$	(Eerenstein <i>et al.</i> , 2006)
Polarisation	$125 \mu\text{C}/\text{cm}^2$	(Priya <i>et al.</i> , 2016)
Dielectric constant	10^3 – 10^6	(Hunpratub <i>et al.</i> , 2009)
Antiferromagnetism	Canted G-type, $T_N = 645 \text{ K}$	(Vijayanand <i>et al.</i> , 2009)
Piezoelectricity	$D_{33} = 15$ – 60 pm/V	(Wang <i>et al.</i> , 2003)

^aTrigonal crystals can be represented with rhombohedral, hexagonal or pseudocubic unit cell axes and lattice parameters.

^bAssuming six-coordinated high spin Fe³⁺ and eight-coordinated Bi³⁺ with ionic size from Shannon.

Bismuth ferrite (BiFeO_3 or BFO) is one of a few multiferroic materials that has Curie and Neel temperatures above room temperature. The initial research of perovskite BiFeO_3 was carried out by Smolenskii in 1960 and this is the typical multiferroic material that has been widely studied in recent years. In 1967, Achenbach successfully synthesized a single-phase BiFeO_3 and after a few years the XRD analysis was also adopted to examine the monodomain single-phase by Kubel and Schmid in 1990. Later in 2003, thin film BiFeO_3 revealed large remnants of polarization 15 times larger than that of the bulk BiFeO_3 and together with strong ferromagnetism on BiFeO_3 thin films were also observed (Kubel and Schmid, 1990). Until recently, increasing efforts have been made to focus on the synthesis and characterization of BiFeO_3 in terms of bulk, film, and nanostructure. The structure of a single-phase BiFeO_3 has a rhombohedrally distorted perovskite structure belonging to the $R3c$ space group symmetry at room temperature. The structure of perovskite BiFeO_3 is shown in Figure 2.2 which consists of Bi ions placed in the corner positions, and at the center of the cubic lies the transition Fe ion and the face centers are occupied by six oxygen ions (Naganuma, 2011). BiFeO_3 has long been known to exhibit, in its bulk form, antiferromagnetic, ferroelectric multiferroic characteristics with an antiferromagnetic order of Neel temperature at $T_N = 645$ K (Vijayanand *et al.*, 2009) and a ferroelectric transition temperature of $T_c = 1103$ K (Eerenstein *et al.*, 2006). The perovskite-type lattice parameters of the rhombohedral unit cell have a-axis of 5.63 \AA and a rhombohedral angle, $\alpha = 59.4^\circ$ at room temperature, with ferroelectric polarization along the pseudocubic $[111]$ direction (Kubel and Schmid, 1990).

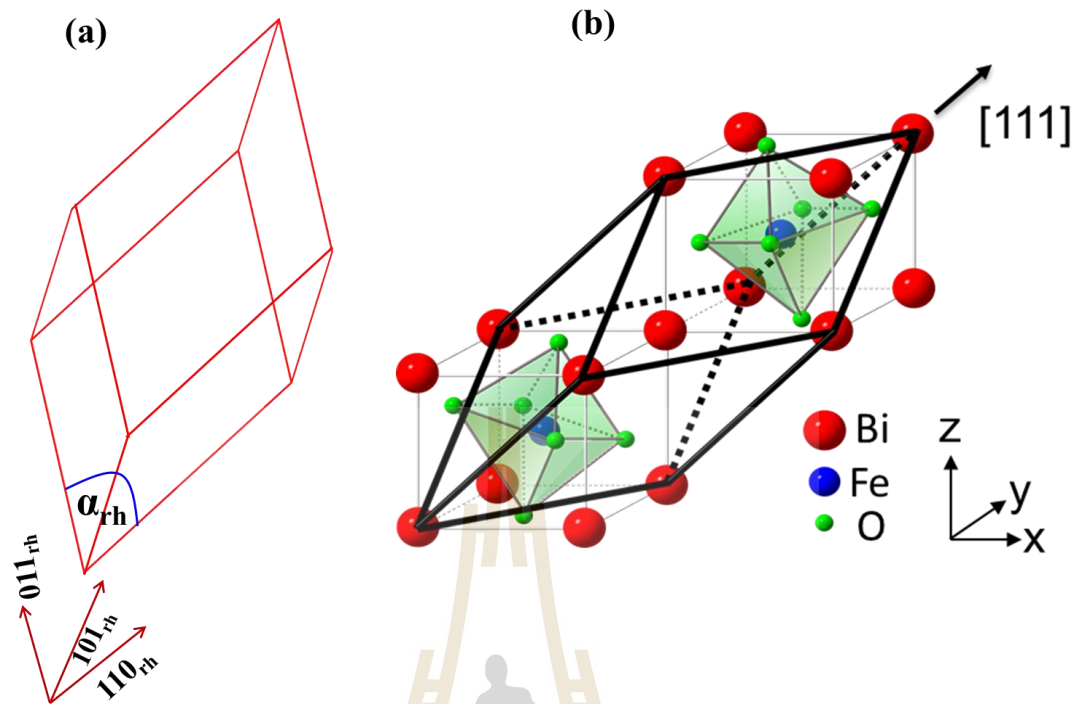


Figure 2.2 Schematic views of BiFeO_3 perovskite unit cells, (a) a rhombohedral unit cell of BiFeO_3 in the ferroelectric phase and (b) accommodation of two perovskite unit cells into one rhombohedral structure (Adapted from Naganuma, 2011).

Early studies of structures of rare earth-doped BiFeO_3 compounds with $x \leq 0.1$ still exhibits the rhombohedrally perovskite structure of BiFeO_3 . Huong and co-worker (Thu Huong *et al.*, 2015) discovered a structural transition from rhombohedral to single orthorhombic phase as the Ho and Sm concentration increases beyond $x \geq 0.2$, while for Pr and Nd, it exists in mixed phase of orthorhombic and tetragonal phases for $x \geq 0.2$. The crystal structure of Tb-doped BiFeO_3 is bi-phasic coexistence of the $R3c$ and $Pnma$ phases for $x \leq 0.15$ whereas a complete modified the orthoehombic $Pnma$ phase for $x = 0.2$. At these critical doping, the BiFeO_3 -based compounds have features of a morphotropic phase boundary (MPB) solid solution. Zhang and co-worker (Zhang *et al.*, 2013) reported structural transition of well Tb-

doped BiFeO_3 powder. They found that the a -axis less changes in the rhombohedral $R3c$ phase while increases in the orthorhombic $Pnma$ phase. For the c -axis value slightly decreases in the $R3c$ structure, whereas greatly drops in the $Pnma$ structure. Therefore, the structural phase transition from the rhombohedral $R3c$ structure to orthorhombic $Pnma$ phase between $x = 0.10$ and 0.125 . The significant enhanced magnetic properties of $\text{Bi}_{0.9}\text{Tb}_{0.1}\text{FeO}_3$ sample is in good agreement with structural transformation of Tb-doped BiFeO_3 near the MPB. Karpinsky and co-worker also studied an evolution of the $\text{Bi}_{1-x}\text{La}_x\text{FeO}_3$ structures across the morphotropic phase boundary as a function of the dopant and a temperature. The structural phase diagram exhibits distinct increase of the remanent magnetization near the rhombohedral-orthorhombic phase boundary.

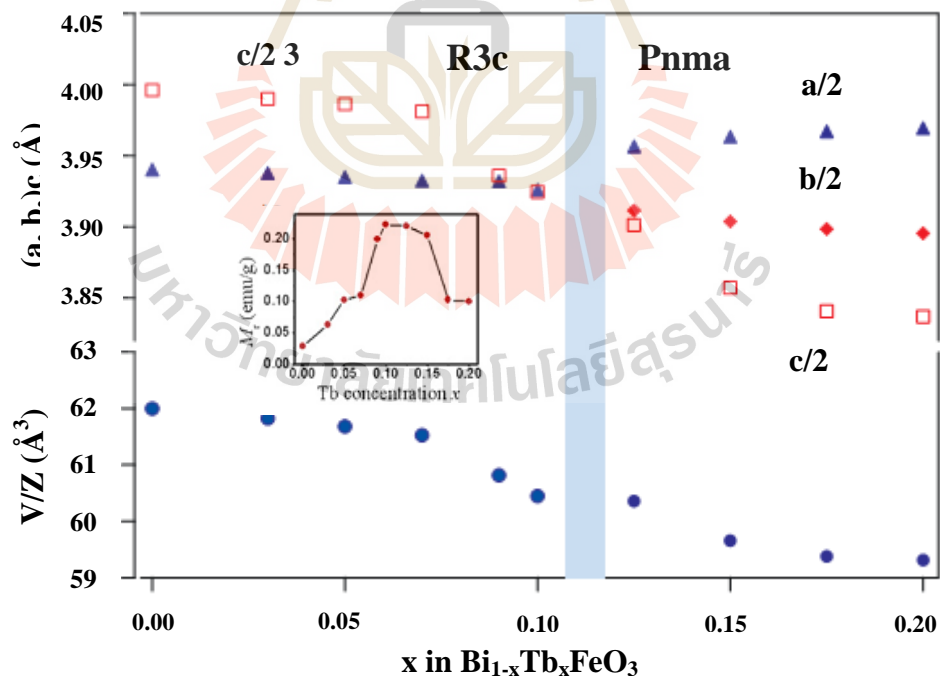


Figure 2.3 Phase diagram for $\text{Bi}_{1-x}\text{Tb}_x\text{FeO}_3$ ($0 \leq x \leq 0.20$) and remnant magnetization (M_r) as a function of the Tb concentration x (inset) (Adapted from Zhang *et al.*, 2013).

The FeO_6 angle is important because it indicates both magnetic ordering and orbital overlap between Fe and O ions and it controls magnetic ordering temperature and conductivity. The large displacement of the Bi cation along the pseudocubic axis relative to the FeO_6 octahedral brings about a non-centrosymmetric polarization resulting in the ferroelectric state. The reason for this structure is due to two important considerations. First, the ferroelectric polarization of BiFeO_3 lies along the [111] direction, resulting in the formation of eight possible polarization variants, (positive and negative orientations along the four cube diagonals) corresponding to four structural variants. Second, the antiferromagnetic ordering of BiFeO_3 is a G-type, in which each Fe^{3+} spin is surrounded by six antiparallel spins on the nearest Fe neighbors. This means that the Fe magnetic moments are aligned ferromagnetically within the pseudocubic [111] direction and antiferromagnetically between adjacent planes. In addition, BiFeO_3 is a G-type antiferromagnetic material which is modulated to a spin cycloid structure in the bulk and ordered with a G-type spin configuration along the [111] direction, perpendicular to the ferroelectric polarization direction with six equivalent axes within that plane. Therefore, antiferromagnetic ordering is coupled to the ferroelectric polarization. However, it was also found that the antiferromagnetic BiFeO_3 is modulated to a cycloidal spiral structure with a period 64 nm length with $[-110]$ as a spiral modulated spin structure (SMSS) with a spiral propagation direction and spin rotation within [110], as displayed in Figure 2.4 (Fang *et al.*, 2010). The domain walls of BiFeO_3 might reveal a weak ferromagnetic moment if the moment is aligned in a direction perpendicular to [111] direction according to Dzyaloshinski–Moriya theory.

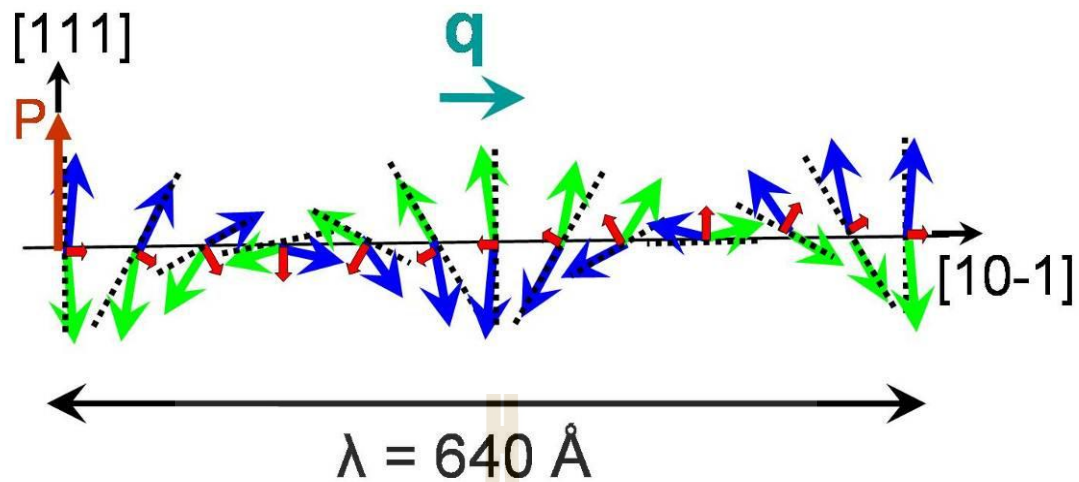


Figure 2.4 Schematic of the 64 nm of antiferromagnetic spin circular cycloid structure of BiFeO₃ (Adapted from Fang *et al.*, 2010).

The structure of perovskite BiFeO₃ is occupied by trivalent Bi³⁺ cations on A-site, but most of the perovskites are dominated by divalent rare earth ions on A-site. The rare earth ions have partly filled 4f-shells which are spatially placed closer to the core region and are protected by outer shells of inert 5s and 5p orbitals. Accordingly, rare earth ions are non-reactive and cannot produce strong chemical bonds with the surrounding oxygen ions. The important roles are to occupy the empty spaces between FeO₆ octahedra influencing the physical properties by controlling the bond angle and to affect band filling by donating electrons into the B-site ions. In contrast, Bi³⁺ rare earth ions have 6s electrons in the valence shell which are reactive in nature in terms of spatial positions and electron energy levels, which may either produce covalent bonding with oxygen ions in its neighbors (Bi 6s–O 2p) or make 6s lone pairs. These 6s lone pairs generate cation off-centering distortion, resulting in ferroelectric spontaneous polarization (Yang *et al.*, 2012). Kumar and Varshney (Kumar and Varshney, 2012) reported the preparation of Nd-doped BiFeO₃ ($x = 0.0$,

0.175, and 0.20) powders by chemical co-precipitation method and found that the FeO_6 is perturbed due to Nd^{3+} doping at Bi^{3+} -site lead to changes in both bond lengths and bond angles. The ferroelectric–paraelectric transformation shows in 20% of Nd doping content which explained by the change of Bi–O covalent bond as a result of weakens of stereochemical activity. The ferromagnetism demands electron in the d orbitals of the Fe ions. When a Fe^{3+} ion is placed at the center of an oxygen six-fold octahedral, the 3d orbitals will split into a t_{2g} triplet state and double degenerate e_g orbitals will be separated by splitting energy in the crystal field. All of five electrons in d orbitals have parallel spins generating 5 per μ_B Fe^{3+} ions.

2.2.2 The synthesis methods

BiFeO_3 is usually prepared from an equal ratio of Bi_2O_3 and Fe_2O_3 . The processing of single phase BiFeO_3 is difficult because of the metastable nature of BiFeO_3 in air, as well as the volatility of Bi_2O_3 resulting in the formation of several phases of impurity, such as $\text{Bi}_2\text{Fe}_4\text{O}_9$, $\text{Bi}_{36}\text{Fe}_{24}\text{O}_{57}$, and $\text{Bi}_{25}\text{FeO}_{40}$. There are reports in the literature about the difficulties in obtaining single-phase BiFeO_3 without the formation of secondary phases. Therefore, it is a challenge to synthesize a single phase formation of BiFeO_3 . The phase diagram of Bi_2O_3 and Fe_2O_3 has been mapped out and is shown below in Figure 2.5 (Palai *et al.*, 2008). It can be clearly seen from the phase diagram that the stoichiometry is an important variant to get a single phase, because unequal amounts of Bi_2O_3 and Fe_2O_3 bring about impurity phases. It is also found that the calcination temperature and melting point of BiFeO_3 are very close to each other since BiFeO_3 can decompose back into these original materials, as shown in the equation below:



However, in practice, it has proven challenging to obtain a single phase and there are many major issues yet to be resolved. These are (i) difficulty in fabricating/growing a single-phase BiFeO_3 material, (ii) difficulty in low temperature synthesis/growth that is compatible with semiconductor processing, (iii) weak magnitude of magnetization at room temperature, and (iv) the presence of impurity phase and high defect concentration resulting in large leakage current density and dielectric loss.

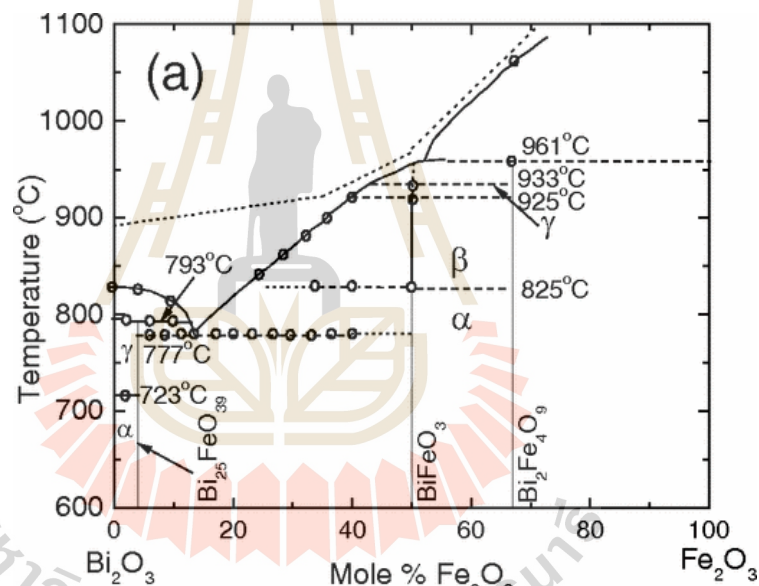


Figure 2.5 Phase diagram of system of Bi_2O_3 and Fe_2O_3 (Adapted from Palai *et al.*, 2008).

Several techniques have been developed to prepare pure phase BiFeO_3 , for example, a rapid liquid phase sintering technique, the modified solid state method, low temperature chemical methods such as sol-gel, hydrothermal, auto combustion, and co-precipitation. Moreover, the material in a nano regime is due to their size dependent properties compared to bulk samples. Nanosized BiFeO_3 prepared samples

have been reported to indicate weak ferromagnetism at room temperature. It is important to notice that the synthesis of single-phase and nanoparticles is of key importance for potential applications. Basu and co-worker (Basu *et al.*, 2008) reported the preparation of BiFeO₃ nanoparticles by hydrothermal technique and found that at low-temperature magnetic measurements exhibited ferromagnetic behavior of the samples with maximum coercivity is about 226 Oe at temperature below 5 K. They found that the magnetization values were significantly reduced when the samples having larger diameters. This result is due to a reduction of an amount of uncompensated spins associated with Fe³⁺ ions with increasing particle diameter. Jia and co-worker (Jia *et al.*, 2009) synthesized a single phase BiFeO₃ powders by a simple sol-gel route at the temperature as low as 450 °C. It was found that the BiFeO₃ powders show room temperature weak ferromagnetism and strong size-dependent magnetic properties. The ferroelectric phase transformation of BiFeO₃ was detected to be around 827 °C. Wang and co-worker (Wang *et al.*, 2010) modified the synthesis of the BiFeO₃ nanoparticles through the tartaric acid-assisted sol-gel route at low temperature. They found that the magnetic state of BiFeO₃ nanoparticles indicates the weak ferromagnetic behavior at room temperature, this may be due to the effect of size confinement. Dai and co-worker (Dai *et al.*, 2011) prepared the BiFeO₃ ceramic powders by a solid state reaction method. They found that the dielectric constant of BiFeO₃ rapid decrease from 2.83×10^4 to 986 with increasing frequency range from 100 Hz to 1 kHz and the observation of the high dispersion in dielectric constant in low frequency range caused by the macroscopic separation of space charges and electrode polarization. The materials have been fabricated using a novel chemical precipitation method purposed at the generation of nanoparticles. In general, co-

precipitation method is a cheap and simple method with the significant reduction in synthesizing temperature. Comyn and co-worker synthesized $\text{BiFeO}_3\text{-PbTiO}_3$ material by chemical co-precipitation and found the pure phase could be calcined at $800\text{ }^\circ\text{C}$ which lower than that reported using conventional mixed oxide synthesis (Comyn *et al.*, 2008). The morphology of SEM and TEM images exhibited a fine particle size distribution of 20 and 75 nm. This co-precipitation method can be used to synthesize dense phase pure of $\text{BiFeO}_3\text{-PbTiO}_3$ which considerably lower calcination and sintering temperature than other previously work reported. Moreover, the dielectric and magnetic properties of the co-precipitation powder samples were measured at room temperature (Shami *et al.*, 2011). With increasing the frequency, the sudden decrease in the dielectric constant was observed at a low frequency which corresponding to the existence of the peak of loss tangent. Dense samples revealed dielectric constant of about 520 and very low $\tan\delta \sim 0.18$ at low frequency, as depicted in Figure 2.6. The dielectric behavior of BiFeO_3 ceramic prepared by a simple co-precipitation method was ascribed based on the fact that Maxwell-Wagner interfacial type polarization. The sample showed weak magnetization in pure BiFeO_3 and this can be improved either by using dopants or synthesizing its composites.

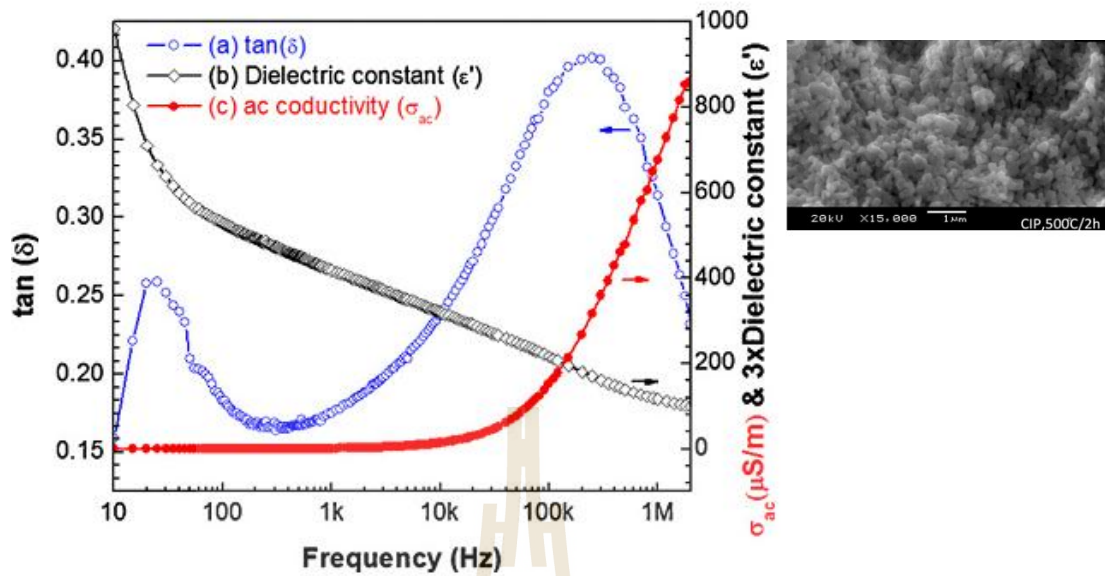


Figure 2.6 The dielectric behaviors and microstructure of BiFeO₃ ceramic prepared by a simple co-precipitation method (Adapted from Shami *et al.*, 2011).

It has been reported that the dielectric constant of the BiFeO₃ ceramic prepared by co-precipitation method and sintered sample at 825 °C could be increased up to the range of 10²–10³ due to its higher density (Shokrollahi, 2013). This reported dielectric constant is larger than that observed in above mentioned work. The increase in both of the dielectric constant and loss tangent by increasing the temperature is indicated to the thermally activated mechanism. However, the nanoparticles (36 nm) show small magnetization (weak ferromagnetism) and they have proposed that this result might be due to canting of the partial antiferromagnetic spiral spin structure and the size effect. As results, it seems that this method shows a high performance for structural and multiferroic properties.

2.2.3 Magnetism in BiFeO₃

The magnetic structure of BiFeO₃ is a G-type antiferromagnetic properties at room temperature, where Fe³⁺ ions magnetic moment due to partially filled 3d-orbital. The arrangement of each Fe spins is surrounded by six antiparallel nearest neighbor Fe spins as shown in Figure 2.8 (Freitas *et al.*, 2013). However, it was found that the BiFeO₃ has a superimposed incommensurate cycloid spin structure with a long periodic wavelength of 620 Å along the [100]_h direction at room temperature. This cycloid spin structure cancels leads to cancellation of the macroscopic magnetization and observed the linear magnetoelectric effect. Li and co-worker (Li *et al.*, 2008) reported sputtering BiFeO₃ thin films on Pt /Ti /SiO₂ /Si substrates show a saturated ferromagnetic loop with saturation magnetization of 21 emu/cm³ at room temperature. Liu and co-worker (Liu *et al.*, 2009) synthesized Bi_{1-x}Eu_xFeO₃ nanoparticles by sol-gel method and found that the remenant magnetization of the Eu-doped BiFeO₃ is found to increase with increasing Eu doping concentrations. The magnetically active Eu³⁺ ions coupled with Fe³⁺ ions is found to be the main reason for such an enhancement in magnetization. The appearance of EuFeO₃ orthoferrite phase may be another reason responsible for the observed high magnetization properties in Bi_{1-x}Eu_xFeO₃ with x = 0.15 compound.

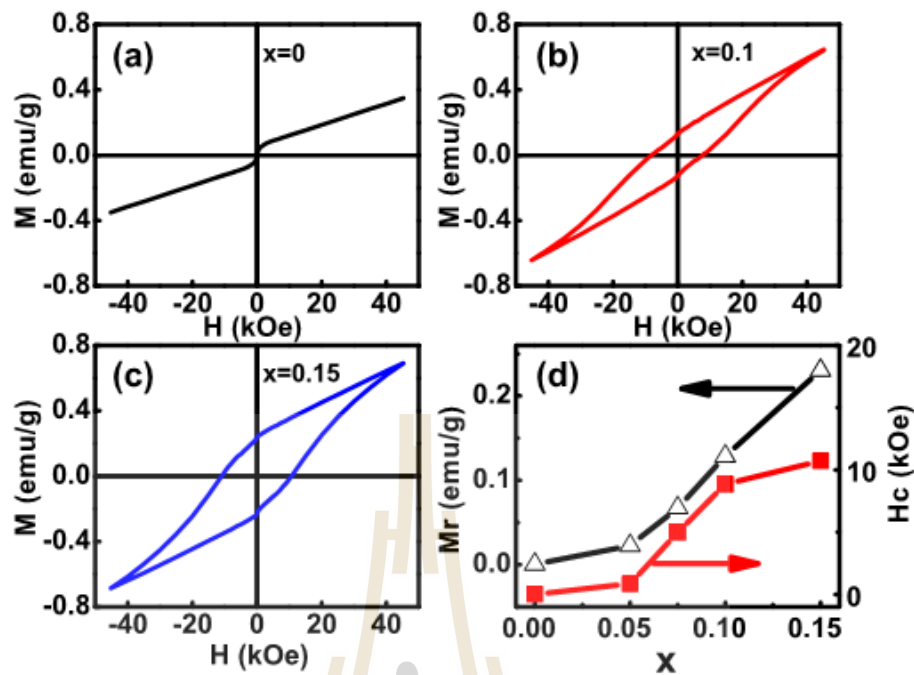


Figure 2.7 Magnetization hysteresis loops of Eu-doped BiFeO_3 samples (Adapted from Liu *et al.*, 2014).

Ramachandran and co-worker (Ramachandran *et al.*, 2012) found that Ca doped and Ba-Ca co-doped BiFeO_3 ceramics show weak ferromagnetic ordering at room temperature. They are also found that the transition temperature in Ca doped and Ba-Ca co-doped BiFeO_3 samples shifts toward to higher temperatures, which is due to the effect of Ca and Ba doping on chemical pressure. Huang and co-worker (Huang *et al.*, 2013) synthesized BiFeO_3 nanoparticles with size from 18 to 248 nm by a sol-gel method. They found that the nonlinear of the initial magnetization curve is only observed for the 62 nm BiFeO_3 particles at the magnetic field below 5 kOe, indicating its different magnetic structure. It is found that a structural anomaly arises for the BiFeO_3 particles with size around 62 nm period of the spiral modulated spin structure, which induces an obviously enhanced ferromagnetic behavior.

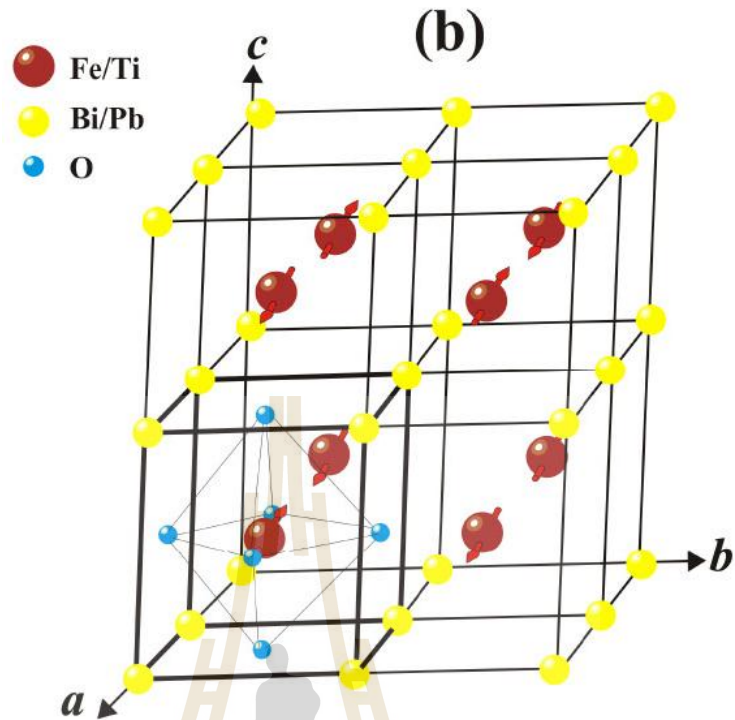


Figure 2.8 Schematic presentation of antiferromagnetic ordering in BiFeO_3 (G-type) structure (Adapted from Freitas *et al.*, 2013).

2.2.4 Electrical properties of BiFeO_3

In the following we will show review of literature of the ferroelectricity, dielectric properties and leakage current characteristics. Bulk BiFeO_3 has ferroelectric ordering below Curie temperature $T_C \sim 1103$ K. Ferroelectricity appears in pure BiFeO_3 due to off centered distortion of Fe^{3+} ions. The polarization is caused by the $6s^2$ lone pair of Bi^{3+} ions in its noncentrosymmetric rhombohedral structure. In theory, the spontaneous polarization of bulk sample of BiFeO_3 could be up to $91.5 \mu\text{C}/\text{cm}^2$ along one of the [111] pseudocubic axes because of its large atomic displacement from their centrosymmetric position and high Curie temperature (Neaton *et al.*, 2005). Dong and co-worker (Dong *et al.*, 2014) synthesized $\text{Bi}_{1-x}\text{Tb}_x\text{FeO}_3$ (BTFO) thin films on FTO (fluorine doped tin oxide) substrates by the sol-

gel spin-coating method. It is found that $\text{Bi}_{1-x}\text{Tb}_x\text{FeO}_3$ $x = 0.10$ thin film obtains the superior electric hysteresis loop and the maximum remanent polarization ($2P_r$) is about $135.1 \mu\text{C}/\text{cm}^2$. Single-phase BiFeO_3 ceramics have been synthesized by a simple conventional solid state reaction and followed immediately by quenching processing. A well-saturated electric hysteresis loop at room temperature with a high remnant polarization $23.5 \mu\text{C}/\text{cm}^2$ is observed, which is attributed to the suppressed formation of impurity phases and the improved resistivity (Zhang *et al.*, 2005).

Makhdoom and co-worker (Makhdoom *et al.*, 2012) reported that the leakage current density of doping of 10% Ba in BiFeO_3 is found to be four orders of magnitude lower than that of the pure BiFeO_3 . The significantly reduced in leakage current density of BiFeO_3 system is attributed to decrease in grain size and reduction in concentration of Fe^{2+} ions and oxygen vacancies related defects. Dielectric properties exhibited that the dielectric constant and dielectric loss obtained their very large values at 5% of Ba doped samples which can be ascribed to large amount of oxygen vacancies in this sample. Interesting dielectric behavior with high dielectric permittivity and three relaxation processes have been reported for the ceramics sintered at 700°C from pure precipitation-synthesized BiFeO_3 powder sample (Hunpratub *et al.*, 2009). The authors suggested that the low-temperature relaxation of the activation energy 0.34 eV was attributed to the carrier hopping process between Fe^{2+} and Fe^{3+} , the middle-temperature relaxation process with the activation energy of 0.77 eV could be due to the grain boundary effect, and the high-temperature relaxation with the highest activation energy (0.95 eV) might be contributed from the defects and/or the conduction.

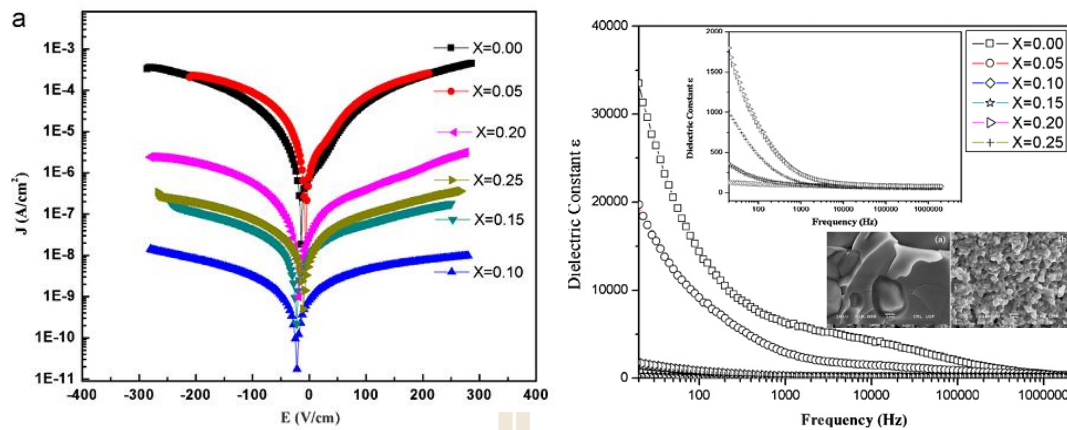


Figure 2.9 (a) The current–voltage characteristics and (b) the dielectric properties of $\text{Bi}_{1-x}\text{Ba}_x\text{FeO}_3$ ($x = 0.00\text{--}0.25$) at room temperature (Adapted from Makhdoom *et al.*, 2012).

Kawae and co-worker (Kawae *et al.*, 2009) reported polycrystalline of Mn and Ti codoped BiFeO_3 thin films deposited on Pt/SrTiO_3 (100) substrate by pulsed laser deposition and found that the leakage current of the BFMT film was much reduced in compared with the other films due to the formation of deep traps. The well-saturated P–E hysteresis loops were observed in the BFMT film and maximum remanent polarization was about $75 \mu\text{C}/\text{cm}^2$ and coercive field of about $310 \text{ kV}/\text{cm}$ at room temperature. $\text{Bi}_{1-x}\text{Dy}_x\text{FeO}_3$ ($x = 0.0\text{--}0.12$) ceramics were synthesized by solid state reaction method. It is found that the values of dielectric constant decreased with increases in Dy doping which indicated dipoles with small effective mass mainly contribute to dielectric response (Van Den Brink and Khomskii, 2008).

Pattanayak and co-worker (Pattanayak *et al.*, 2014) fabricated rare earth-modified BiFeO_3 , $\text{Bi}_{0.95}\text{R}_{0.05}\text{FeO}_3$ ($\text{R} = \text{Nd, Dy}$) (BNFO, BDFO) by a solid-state reaction technique. They found the rare earth-doped BiFeO_3 samples increases the dielectric constant, and the tangent loss decreases as compared to BiFeO_3 . In Nd, Dy-

modified BiFeO₃ has large leakage current density as compared to that of BiFeO₃ which is attributed to the reduction of the defect by the replacing Nd and Dy ions in the Bi site.

Interestingly, Liu and co-worker (Liu *et al.*, 2008) reported epitaxial BiFeO₃/La_{0.7}Sr_{0.3}MnO₃ thin films grown on SrTiO₃ (001) substrates. They found the capacitance of the BiFeO₃/La_{0.7}Sr_{0.3}MnO₃ capacitor decrease with increasing frequency and applied bias voltage in low frequency range. In the impedance spectra the semicircular arc at low frequency range is strongly decrease with the increase of applied bias voltage, while the arc is independent on an applied bias voltage in the higher frequency region. They may the Maxwell–Wagner relaxation term are form at interfaces between film/electric as interfacial polarization and obtain the capacitance of interfacial polarization is higher than that of capacitance of bulk. Therefore, they mentioned that for the epitaxial BFO thin film, there is no grain boundary and contribution of the dielectric relaxations is only bulk and interfaces (film/electrode).

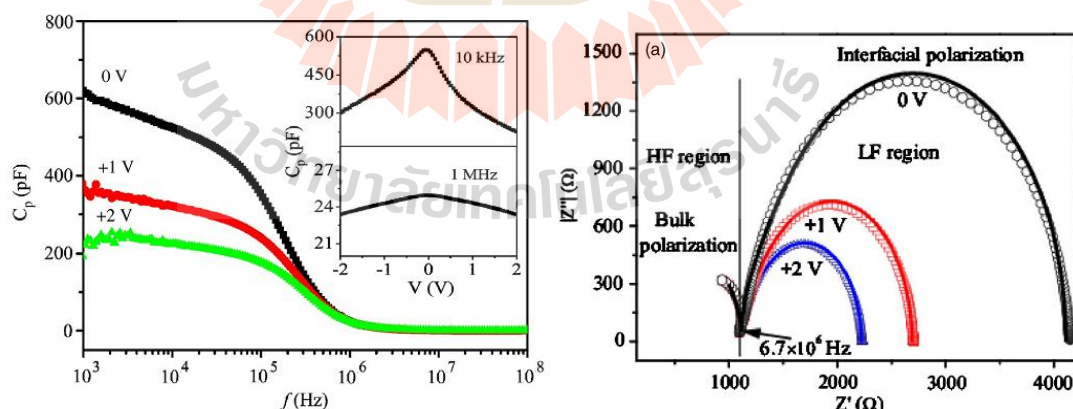


Figure 2.10 The frequency dependence of the capacitance and complex impedance of the In/BFO/LSMO capacitor under applied biases 0–2 V (Adapted from Liu *et al.*, 2008).

Moreover, the influence of dc bias voltage on giant dielectric properties of CuO ceramics was reported Pujuso and co-worker (Putjuso *et al.*, 2011). It is found that the high dielectric constant at room temperature and low frequency range is observed and can be explained by Maxwell–Wagner polarization. The decrease in dielectric constant ceramics with increase dc bias voltage from 0 to 4 V was found in CuO ceramics sintered at 900 °C and 950 °C. The impedance plots show a large semicircle at low frequency which due to the resistance of electrode indicates strongly contributes the electrode on the dielectric behaviour of the CuO ceramics. However, a small semicircle arc remains constant with increases in dc bias suggested that at high frequency range, the effect of dc bias can not affect to the dielectric constant.

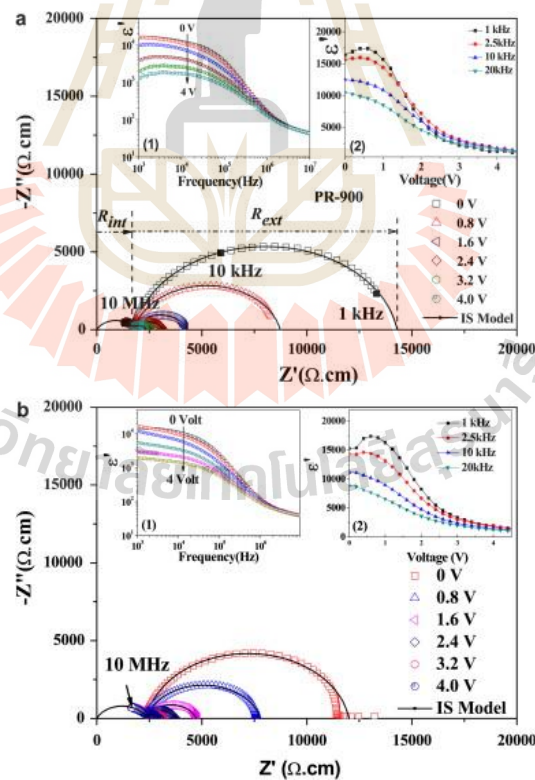


Figure 2.11 Impedance spectra and dielectric properties of CuO ceramics under applied dc bias (a) sintered at 900 °C and (b) sintered at 950 °C (Adapted from Putjuso *et al.*, 2011).

Table 2.3 Lists of reports of electric and magnetic properties.

Materials	Preparation method	P_r ($\mu\text{C}/\text{cm}^2$)	M_r (emu/g)	References
BiFeO ₃ thin film	A cosputtering method	37	21	(Li <i>et al.</i> , 2008)
Bi _{1-x} Eu _x FeO ₃ (x = 0.00–0.15)	Sol-gel method	-	0.23	(Liu <i>et al.</i> , 2009)
BiFeO ₃	Co-precipitation Method	$2P_r = 2.8$	3.8×10^{-4}	(Shami <i>et al.</i> , 2011)
Bi _{1-x} Tb _x FeO ₃ thin film, with $0 \leq x \leq 0.15$	Spin-coating method	$2P_r = 135.1$	0.15–0.45	(Dong <i>et al.</i> , 2014)
Bi _{1-x} A _x FeO _{3-x/2} (A = Ca, Sr, Pb, Ba; x = 0.2, 0.3, 0.005, 0.01, 0.015)	Solid-state reaction method	-	0.75	(Khomchenko <i>et al.</i> , 2009)
BiFeO ₃	Hydrothermal	-	0.01–0.02	(Basu <i>et al.</i> , 2008)

2.2.5 General doping concepts

A-site substitution refers to the case that the Bi³⁺ ions are substituted by the other rare earth or alkaline earth ions. The B-site substitutions are made by replacing the Fe³⁺ ions by other transition metal ions. The A-site and B-site substitution can influence the structural and multiferroic properties. The electrical and

magnetism properties reported in the literature are summarized in Table 2.3. Qian and co-worker (Qian *et al.*, 2009) synthesized Dy-doped BiFeO₃ nanoparticles by an ethylene glycol based sol-gel method and found a high magneto-dielectric coefficient of 4.7% in as-prepared BiFeO₃ nanoparticles. Sharma and co-worker (Sharma *et al.*, 2014) reported Bi_{1-x}Pr_xFeO₃ (x = 0.0, 0.15, 0.25) ceramic samples using solid-state reaction route and they found with increasing doping concentration induce the structural transformation from R3c to P1 is due to Pr substitution at A-site in BiFeO₃. They also reported that the reduced in remanant ferroelectric polarization values for Pr-doped BiFeO₃ samples are attributed to structural change. Zhang and co-worker have been investigated the phase composition, crystal structure, and magnetic properties of rare earth-doped BiFeO₃ ceramics. It was found that the lattice constants decrease slowly with x increasing, which might be due to the larger radius of Bi³⁺ than rare earth. The crystal structure of all rare earth-doped samples shown that the samples are the rhombohedral phase until x = 0.2 and exhibits a structural transformation to the orthorhombic phase between 0.2 ≤ x ≤ 0.4, remains the orthorhombic phase at x = 1. The coercivity as a function of doping content is found the highest values at the middle area of x range which means that the rare earth element contribution to the magnetic properties of these samples. Moreover, A-site substitution with the largest ionic radius ions leads to the effective suppression of the spiral spin structure, hence resulting in an increase value of spontaneous magnetization, as shown in Figure 2.12. (Khomchenko *et al.*, 2009).

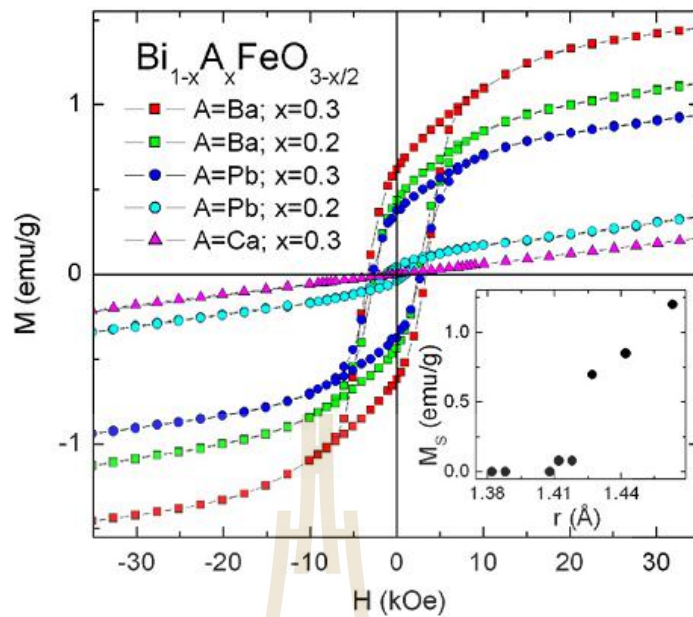


Figure 2.12 M-H loops of $\text{Bi}_{1-x}\text{A}_x\text{FeO}_{3-x/2}$ samples and (inset) M_s as a function of the average ionic radius of the A-site ions (Adapted from Khomchenko *et al.*, 2009).

Mn-doped BiFeO_3 thin films were prepared using sol-gel method (Riaz *et al.*, 2015). The XRD results have been shown that changes in unit cell caused by incorporation of dopant due to the smaller ionic radii as compared to that of Fe ion. Dielectric constant for 0.25 Mn concentrations is found to be 160 at 1 kHz and $\text{BiFe}_{1-x}\text{Mn}_x\text{O}_3$ films showed ferromagnetic behavior with high value of saturation magnetization was found to be 10^2 emu/cm^3 for Mn content of 0.2. Sharif and Muqri synthesized co-doped $\text{Bi}_{1-x}\text{A}_x\text{Fe}_{1-y}\text{B}_y\text{O}_3$, where A = Ca or Gd and B = Ni or Zn using solid state reaction technique. They found the rhombohedral perovskite BiFeO_3 phase accompanied by some impurity phases such as $\text{Bi}_2\text{Fe}_4\text{O}_9$ and $\text{Bi}_{25}\text{FeO}_{40}$ in the XRD patterns. Moreover, doping A-site was found to increase in the coercivity and the remnant magnetization of BiFeO_3 , while doping B-site was found to decrease the coercivity field values.

CHAPTER III

RESEARCH METHODOLOGY

Chapter III describes the experimental procedure of the research, which investigates the dielectric, optical, magnetic and electrical properties of BiFeO₃-based ceramics. The Bi_{1-x}A_xFeO₃ (where A = La, Sm, and Ba, x = 0, 0.05, 0.1, 0.2, and 0.3) powders are synthesized by a simple co-precipitate method and calcined at 600 °C for 3 h and Bi_{1-x}A_xFeO₃ ceramics are sintered at 800 °C for 3 h. The crystal structure and microstructure of BiFeO₃-based powders and ceramics are carried out using X-ray diffraction (XRD) and scanning electron microscopy (SEM). The chemical bonding of BiFeO₃-based powders are observed by FTIR spectroscopic analysis. Room temperature magnetization (M-H) measurement is performed using a vibrating sample magnetometer (VSM). Optical properties are determined UV-Visible diffuse reflectance (UV-vis). The measurement details of the dielectric and electrical properties of Bi_{1-x}A_xFeO₃ systems are also included in this chapter.

3.1 BiFeO₃- based powders and ceramic samples preparation

Bi(NO₃)₃·5H₂O (Kento chemical, 99.99%), Fe(NO₃)₃·9H₂O (Kento chemical, 99.99%), La(NO₃)₃·4H₂O, Sm(NO₃)₃·6H₂O, and BaCO₃ (Sigma) were used

as starting raw materials for the synthesis of the Ba-, La-, and Sm-doped BiFeO₃ powders by a simple co-precipitate method. The source and purity of the starting raw materials are listed in Table 3.1. The BiFeO₃-based powders and ceramics were prepared by the following steps. Firstly, stoichiometric amounts of the high purity starting raw materials, corresponding to any composition of each series BiFeO₃-based powders with different concentrations of the dopant, were dissolved in 20 ml deionized water under constant stirring. Secondly, 16 ml of 65% nitric acid (HNO₃) were added with constant stirring at a temperature of 60 °C for 1 h. There was increasing solubility of the metal salt affected by the addition of nitric acid. Another reason is that the nitric acid reacts with, and removes, other ions that might give a confusing precipitate process. Then polyethylene glycol 20,000 was added to the above solution, and the resulting mixture was stirred continuously at 60 °C for 10 h to obtain gel solution. Next 40 ml of aqueous solution of 25% ammonia solution (NH₄OH) were added to the gel solution with constant stirring to reach pH ~9 in order to certify complete precipitation solution. Then the colour of the solution changed from colourless to brick red. Finally, the precipitate was filtered and washed several times with deionized water for removing anions and dried overnight at 70 °C in an oven. The dried precursors were ground and later calcined at 600 °C for 3 h in air. The calcined powders were pressed into circular shaped pellets in a diameter of 1 cm and 1–2 mm in thickness by a uniaxial pressing method at 200 MPa and sintered at 800 °C for 3 h in air. The calcination and sintering steps are schematically shown in Figure 3.1

The powder X-ray diffraction pattern (XRD, Advance Bruker D8) with Cu K_α radiation and scanning electron microscope (SEM, JEOL, JSM-6010LV) were used

to characterize the phase analysis and microstructure of the BiFeO₃-based powders and ceramics, respectively. The XRD patterns were scanned in the 2θ range of 20–70 degrees and the scan step was 0.02°. Fourier transform infrared spectroscopy (FTIR, Tensor 27) was used to examine the chemical bonding of the BiFeO₃-based powders. The local structure of doped-BiFeO₃ samples was determined by the XANES technique. The optical absorption spectrum was recorded on a Shimadzu, UV-1700, UV-Vis spectrophotometer. The room temperature magnetization-magnetic fields (M-H) of all calcined powders were carried out using the vibrating sample magnetometer (VSM) for the maximum magnetic field of 10 kOe. The dielectric and electrical properties of the pellets were measured using a Hewlett Packard 4194A impedance gain phase analyser over a wide frequency range of 10²–10⁶ Hz and temperatures from -50 to 200 °C at the oscillation voltage of 1.0 V under an applied DC bias voltage 0–20 V. Current-voltage density behaviours were measured at various temperatures using a high voltage measurement unit (Keithley Model 247). The sample preparation route and characterization are summarized in a flowchart diagram as shown in Figure 3.2. And details of BiFeO₃-based powders and ceramic samples characterization are given in section 3.2.

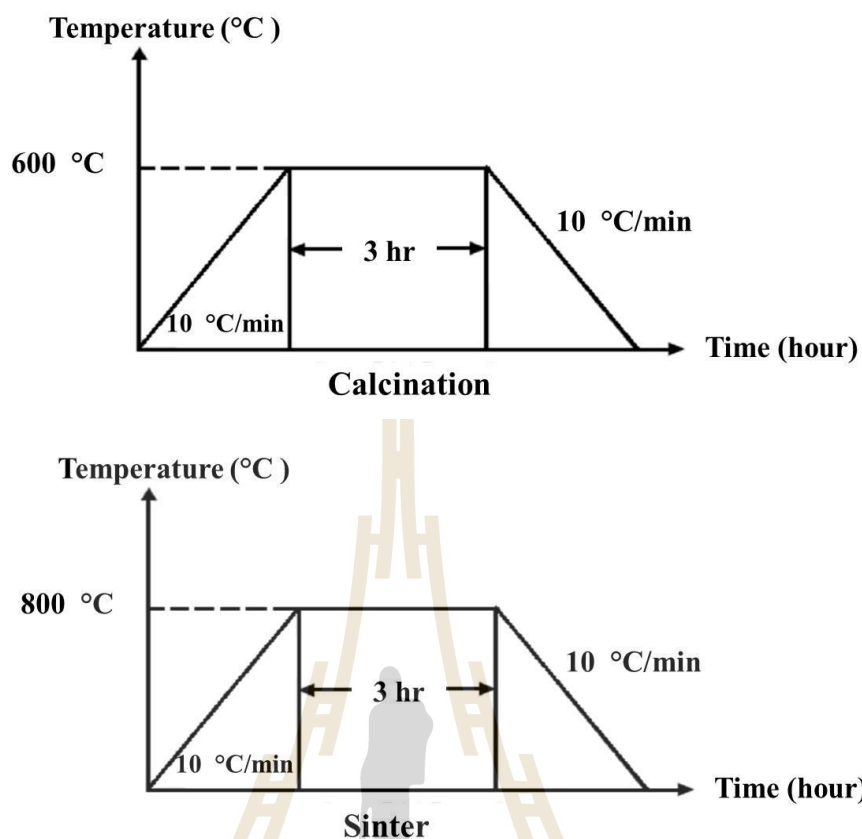


Figure 3.1 Calcination and sinter diagrams of BiFeO_3 -based samples.

Table 3.1 List of materials used as starting raw materials for BiFeO_3 -based powder preparation, and their source and purity.

Materials	Source	Purity
Iron (III) Nitrate Enneahydrate ($\text{Fe}(\text{NO}_3)_3 \cdot 9\text{H}_2\text{O}$)	Kento	99.9%
Lanthanum(III) Nitrate Hexahydrate $\text{La}(\text{NO}_3)_3 \cdot 6\text{H}_2\text{O}$	Kento	99.99%
Samarium(III) Nitrate Hexahydrate $\text{Sm}(\text{NO}_3)_3 \cdot 6\text{H}_2\text{O}$	Kento	99.9%
Barium Carbonate BaCO_3	Sigma–Aldrich	99.999%
Poly(ethylene glycol) average Mw 20,000	Sigma–Aldrich	

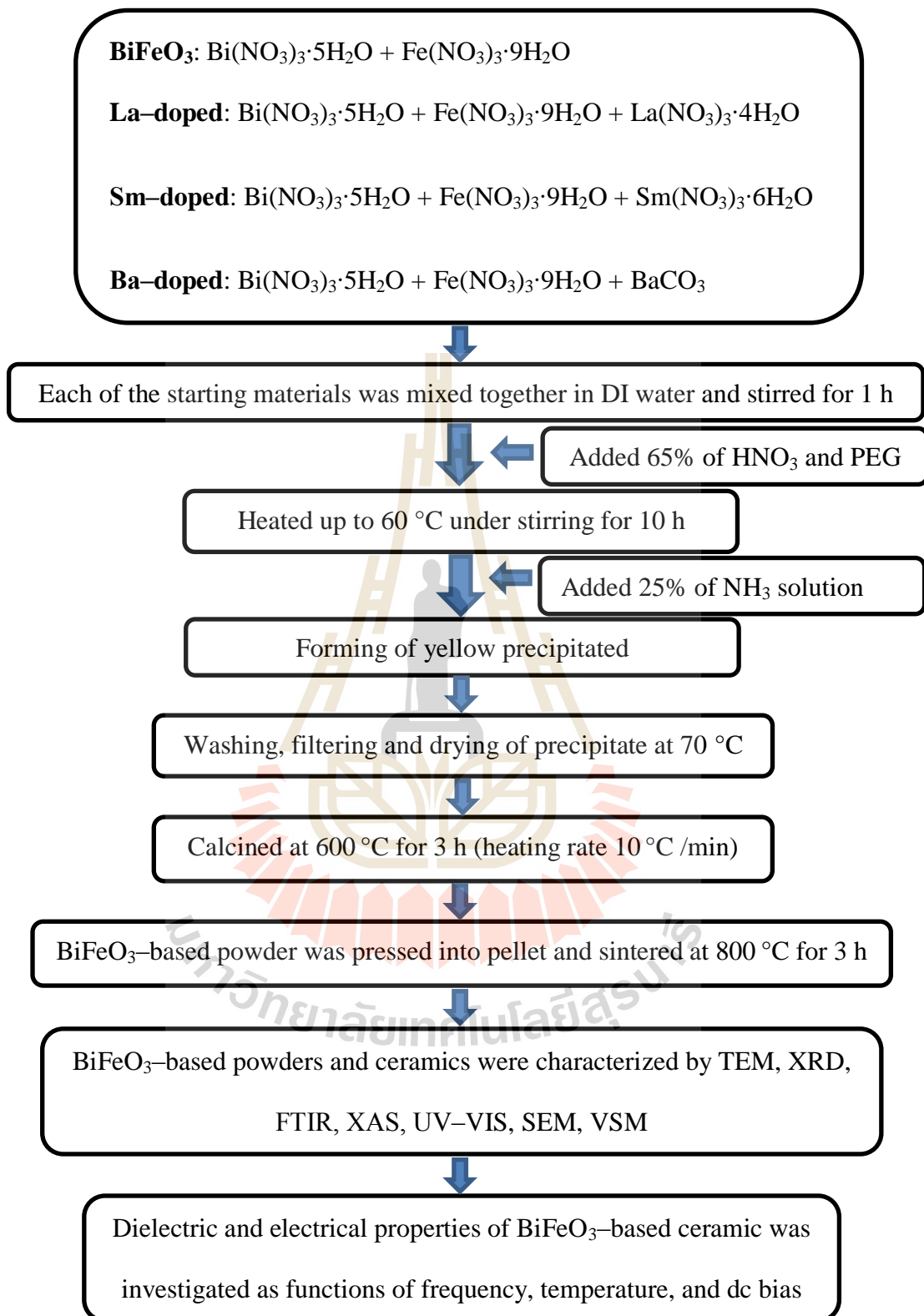


Figure 3.2 Diagram showing the preparation and characterization of BiFeO₃-based powder and ceramics.

3.2 Powder and ceramic samples characterization

The phase analysis and morphology of BiFeO₃-based powders prepared in this work were investigated by XRD and TEM, respectively. The surface microstructure of sintered pellets was studied using the SEM technique. Fourier transform infrared spectroscopy (FTIR) was recorded on a Bruker Tensor 27 FTIR spectrometer within a range of 400–4000 cm⁻¹. The oxidation states of the samples were determined by XANES technique in transmission mode. More details of each characterizations technique used in this work are given as follow.

3.2.1 X-ray diffraction (XRD)

The X-ray diffraction technique is a tool for identifying the arrangement of atoms in a crystalline material. The basic concept of the XRD technique is based on the interference phenomenon of two waves with the same wavelength and incoming in the same direction to the sample. In crystalline materials, the scattered x-rays undergo constructive and destructive interference if a phase difference is $n\lambda$ (in phase) and $n\lambda/2$ (out of phase), respectively. This is the diffraction process which is described by Bragg's Law. Experimentally, a beam of X-ray is incident on a sample and is diffracted by the crystalline phases in the sample corresponding to Bragg's Law (Lipson, 1979)

$$2d \sin \theta = n\lambda \quad (3.1)$$

where d is the lattice interatomic spacing in the crystal plane, θ is the diffraction angle, n is an integer, and λ is the wavelength of the X-ray radiation. The intensity of the X-ray diffraction peak is measured as a function of the diffraction angle (2θ) and the arrangement of a sample. The diffraction peaks of the XRD pattern are directly

related to atomic distance which is on the atomic planes. The diffraction pattern can be considered to identify the crystalline phases of the sample and to determine its crystal structure. Moreover, the lattice parameter, the crystallite size, strain and orientation of crystallite can also be obtained precisely from the diffraction pattern. The diffraction pattern can also determine concentration profiles and film thickness; the atomic arrangement in amorphous materials and multilayers and its defects can be characterized as well. The schematic principle of the XRD instrument is illustrated in Figure 3.3.

In this work, to qualify as a crystal structure, the pure phase and structure of all samples were characterized by the XRD technique (Advance Bruker D8). The XRD patterns were measured with monochromatised Cu- $K\alpha$ radiation ($\lambda = 1.54056 \text{ \AA}$) within a 20° – 70° angle range of 2θ . The data were recorded with a step size of 0.02° and a counting time of 0.2 second per step. To obtain structural and physical information the XRD Rietveld refinement analysis was performed by TOPAS software.

The estimated crystallite size of the powder samples were calculated from the diffraction XRD line broadening peaks at $2\theta \sim 32^\circ$ – 60° by using Scherrer's equation as expressed by (Patterson, 1939)

$$D = \frac{K\lambda}{\beta \cos \theta} \quad (3.2)$$

where D is crystallite size

K is a constant, for this research, K is 0.98.

λ is the wavelength of the X-ray radiation

θ is the Bragg's angle and β is the full-width at half maximum of peak.

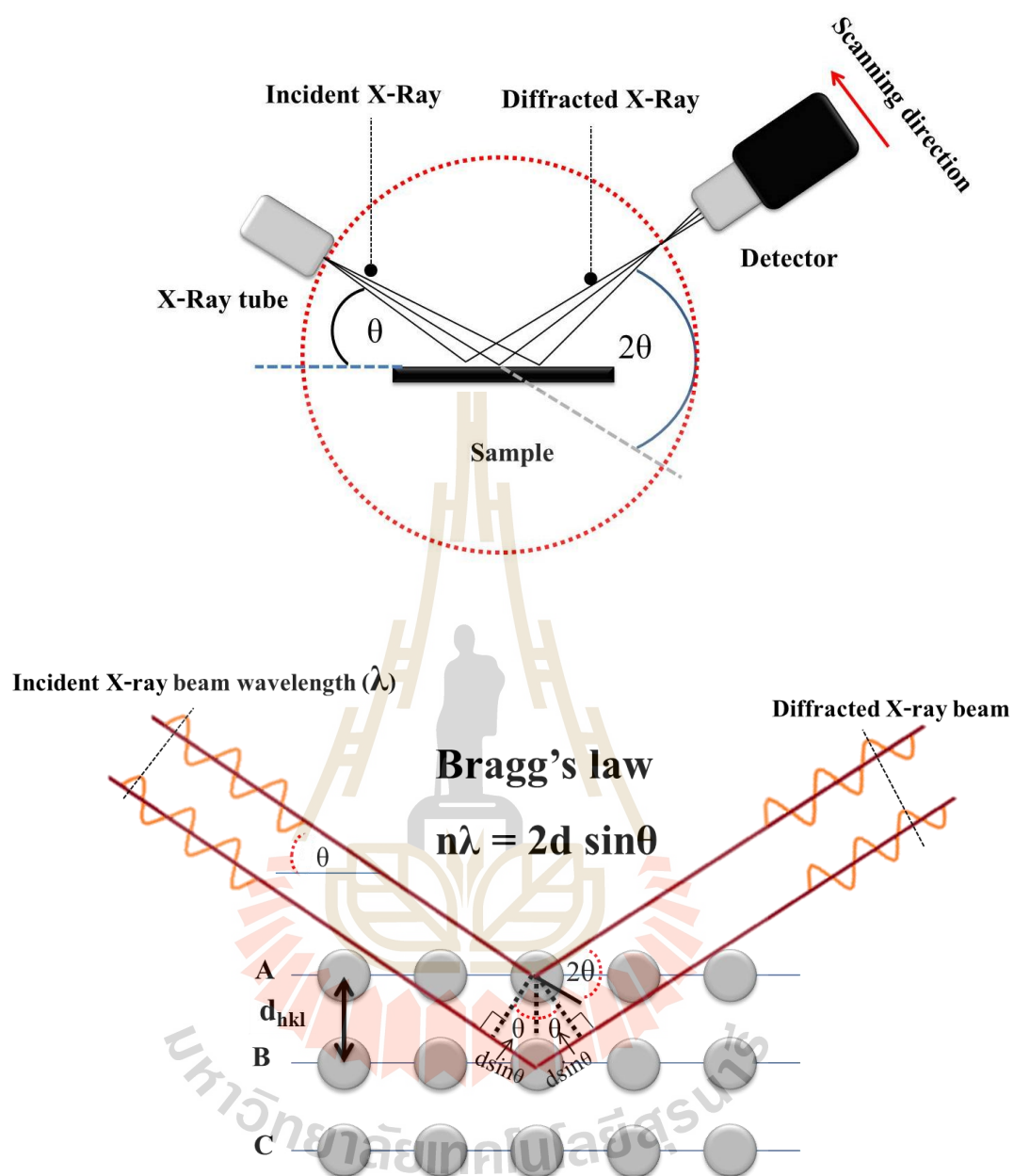


Figure 3.3 Schematic principle of XRD equipment and description of Bragg's diffraction law. (Adapted from <http://lipidlibrary.aocs.org/Biochemistry/content>)

3.2.2 Transmission electron microscopy (TEM)

The transmission electron microscopy (TEM) is a microscopy technique which is a powerful tool for the material sciences. A high energy beam of

electron is transmitted through an ultra-thin sample and interactions between electrons and atoms can be used to observe morphology features. High resolution can be performed to analyse the quality shape, size and density of quantum wells, wires and dots. The preparation sample needs to be thin enough to be transparent for electrons. In this work, all calcined powders were diluted in ethanol and dispersed on a 300 mesh copper grid following by drying in air and then they were measured under an accelerating voltage of 80 kV by TEM (ZEISS (EM902)). The selected-area of electron diffraction (SAED) patterns was also investigated in this research. The BiFeO₃-based nanoparticles and their sizes were analysed by using a combination of TEM bright field image and the ImageJ program.

3.2.3 Scanning electron microscopy

Scanning electron microscopy (SEM) is a characterization technique that is used to image the surface morphology by scanning with a high-energy beam of electrons. This technique is non-destructive, and it is possible to analyse the same materials repeatedly. For these measurements, the image of the sample surface can be obtained by interaction between the electrons and the atoms near or on top of the surface of the specimen. The sample is scanned by the scattered electrons across the sample surface and collects scattered electrons for imaging that contain information of sample surface morphology, chemical composition and electrical conductivity. The most common SEM mode is detection of the backscattered signal the sample does not need electric transparency. Due to the electron beam being very narrow, the observed SEM micrographs have a large depth of three-dimensional appearance. This phenomenon is very helpful for understanding the surface morphology of the sample. For imaging the SEM micrograph, the surface sample must be electrically conductive

to prevent the accumulation of an electrostatic charge at the surface. Therefore, the samples are usually coated with an ultra-thin coating of electrical conducting material, especially gold. In this work, firstly, each appropriate sized pellet was mounted rigidly on the specimen stub. Then, the gold was deposited on the surface to create the conductive surface of the BiFeO₃-based ceramics to increase the signal and resolution. According to the SEM images, the mean grain size of each of the BiFeO₃-based ceramics was directly obtained by measurement of the average diameter of each grain in the micrograph. In this research, the morphology and grain size were characterized by using scanning electron microscopy (SEM, JEOL, JSM-6010LV).

3.2.4 X-ray absorption spectroscopy

X-ray absorption spectroscopy (XAS) is a widely used technique for the local geometric and/or electronic structural study of materials. The experiment is performed by tuning the efficiency photon energy to reject a core electron from an atom. Samples can be in solution, gas-phase or condensed matter (solid). Structure can be determined from samples that are both heterogeneous and amorphous. A parallel monochromatic x-ray beam of intensity I passing through a sample of thickness x will get a reduced intensity I following the equation

$$I = I_0 e^{-\mu x} \quad (3.3)$$

Where μ is the linear absorption coefficient which is the probability that it will be absorbed, I_0 is the incident x-ray intensity. At certain energies the absorption of the x-ray increases dramatically when the energy matches well with the binding energy of the electrons. This is the reason for a decrease in the transmitted x-ray intensity or there is an abrupt increase absorption cross-section of the absorption area. Normally,

each absorption edge occurs when the energy of the incident photon energy is sufficient to cause excitation of a core electron of the absorbing atom to a higher energy unoccupied state or into an unbound state, called the continuum state, i.e. to produce a photoelectron. Three main regions are commonly distinguished in the XAS spectra. First is the region at around 2–50 eV below the absorption edge, namely pre-edge structures. The pre-edge peak caused by the electron transition (mainly dipole allowed) to the lowest empty bound states near the Fermi level. The strengths of the pre-edge peaks provide information about absorber local geometry and electronic state around absorber atom such as a number of neighbour atoms, ligand symmetry and valence state. The second region where the incident x-ray is sufficient to transfer an atomic core of electrons to final states is in the energy region of about 50–100 eV above an absorbed atomic core level of ionization energy which is called the X-ray absorption near edge structure (XANES). Analysis of the absorption edge feature of XANES spectra can be applied for understanding the oxidation state and the coordination number of the absorbing atoms. The name of the absorption edge depends upon excitation of the core electron which corresponds to the principle quantum number, $n = 1$ level refers to K-edge, $n = 2$ level refers to the L-edge and $n = 3$ level corresponds to the M-edge. The final region of the oscillation above the edge, which can extend to 1000 eV or more is referred to as the Extended X-ray Absorption Fine Structure or EXAFS. In this region, the incident photon is able to excite the core electron if its energy is equal or higher than the edge energy. Because there are many other atoms around the absorber atom and these become scattering centers of the photoelectron wave. The final the state of the photoelectron can be explained by the sum of the original and single scattered waves from the nearest

neighbouring atoms. The analysis of the EXAFS part contains information about the interatomic distance, coordination number, and species of neighbours absorbing atom. The EXAFS signal is described as a function of the wave vector k , and the mathematical formula is:

$$\chi(k) = \sum_j \frac{N_j S_0^2 f_j(k) e^{-2R_j/\lambda(k)} e^{-2k^2\sigma_j^2}}{kR_j^2} \sin[2kR_j + \delta_j(k)] \quad (3.4)$$

where $f(k)$ and $\delta_j(k)$ are the scattering amplitude and phase shifts of atoms neighbouring the existing atoms. N is the coordination number of the neighbouring atoms, S_0^2 is called the amplitude reduction, R refers to the distance to the neighbouring atoms, $\lambda(k)$ is the mean free path, and σ_j^2 defines the mean-square disorder of neighbour distance. Though somewhat complicated, the EXAFS equation allows us determine N , R , and σ_j^2 . Moreover, since the scattering amplitude and phase-shifts depend on the atomic number Z of the neighbouring atoms, EXAFS is also sensitive to the atomic type of the neighbouring atoms. The absorption spectra were transposed to the wave vector k -space using the formula $k = \sqrt{2m(E - E_0)/\hbar}$, and Fourier was transformed into the R -space with a k^2 -weight.

In this study, XANES measurement was carried out at the Synchrotron Light Research Institute (SLRI), Nakhon Ratchasima, Thailand. To determine the oxidation states of the Fe K-edge (7112 eV) in BiFeO₃-based samples, XANES spectra were conducted at the SUT-NANOTEC-SLRI XAS beamline 5.2 (electron energy of 1.2 GeV; bending magnet; beam current 80–150 mA; 1.1 to 1.7×10¹¹ photon s⁻¹). All samples were measured in the transmission mode with ionization chamber detectors and were coated in kapton tape between two frame sheets. The normalized XANES

data were performed after background subtraction in the pre-edge and post-edge regime using the ATHENA software.

3.2.5 Fourier transform infrared spectroscopy

Fourier transform infrared (FTIR) spectroscopy is an analytical technique used to identify molecular components and the structure of materials. This technique is used to study the interaction between molecules and the electrostatic field in the IR region. The range of the infrared region is about $12800\text{--}10\text{ cm}^{-1}$ and can be classified into the near-infrared region ($12800\text{--}4000\text{ cm}^{-1}$), the mid-infrared region ($4000\text{--}200\text{ cm}^{-1}$) and the far-infrared region ($50\text{--}1000\text{ cm}^{-1}$). Infrared spectroscopy technique is used to determine the rotational, vibrational and electronic energy levels of molecules with the molecular characteristics absorbed by IR radiation. The IR spectrum has as molecular vibration frequencies spectrum, and the molecules selectively absorb the radiation of specific wavelengths when exposed to IR radiation. Consequently, in this spectral region, a molecule can be excited to a higher vibrational state by absorbing IR radiation. Therefore, a frequency will be strongly absorbed if its photon energy coincides with the vibrational energy level of the molecule. The common frequency range is measured as wavelengths typically over the the range $4000\text{--}400\text{ cm}^{-1}$ because the absorption radiation of most organic materials and inorganic compounds is within this region.

The FTIR spectroscopy (Bruker, tensor 27) is used in this work. This measurement covers all spectra in a wide spectral region from $400\text{--}4000\text{ cm}^{-1}$, i.e., mid-infrared range at room temperature. The evaluation of the FTIR spectra was performed by OPUS software.

3.2.6 UV–Visible spectroscopy (UV–Vis)

Ultraviolet–visible spectroscopy refers to absorption or reflectance spectroscopy in the ultraviolet–visible wavelengths region. This technique is used to measure the amount of UV–Vis light absorbed by matter. The region from 190 to 380 nm is the UV region and 380 to 740 nm refers to the visible light region of the spectrum. Absorption in both radiation regions occurs from electronic transitions within the molecule. When the sample is irradiated with light some of atoms in the molecules will absorb light at various wavelengths of this radiation, depending on their chemical bonds and structure. It is known that a rule energetically favors electrons which are transferred from low–energy to high–energy atomic or molecular orbitals, and the resulting species is known as the excited state. Such electron transfer processes may arise in transition metal ions, i.e., d–d transition and ligand–to–metal or metal–to–ligand charge transfer. This means that they are responsible for the colour of the material. Spectroscopic characterizations of solutions, gas phases and crystals are usually carried out in transmission mode, but it is very hard to fabricate transparent films of powders and solids. Alternatively, diffuse reflected light can be used and this is called diffuse reflectance spectroscopy (DRS).

In this study, the absorption spectra were recorded at room temperature using the UV–Vis spectrophotometer (Shimadzu, UV–1700, $\lambda = 190–900$ nm, Japan). All UV–Vis spectra were recorded over a wavenumber range of $200–800$ cm^{-1} .

3.2.7 Magnetic measurements

A vibrating sample magnetometer or VSM is a scientific instrument that measures magnetic behaviours of materials in several forms such as powder, bulk, or solution. The vibrating component causes a change in the magnetic field of

the specimen, which creates an electrical field in a coil. These changes are based on Faraday's Law of induction. The VSM instrument also includes a device to hold the specimen at the desired angle, a vibrating element, a control unit, and a meter. To obtain a VSM measurement, the sample is placed inside a uniform external static magnetic field and then vibrated sinusoidally to magnetize the sample. If the sample is magnetic, this uniform magnetic field will magnetize the sample by aligning the magnetic domains, or the individual magnetic spin in the direction of the magnetic field. In other words, the magnet is activated before the testing begins and if the sample is magnetic, it will become stronger than the magnetic field that is produced. A magnetic field is present around the material and, once the vibration starts, then the field can be considered as a charge which occurs in relation to the timing of the movement. This creates a corresponding variation in the magnetic flux, inducing a sinusoidal voltage signal. The signal of the AC voltage is proportional to the sample magnetic moment, the vibration amplitude and the vibration frequency. The degree of magnetization is determined by software that uses the strength of the field, how fast the sample vibrates, the data form measurement, and provides the magnetization (M) and value of the magnetic field (H) as a result of vibration. The characteristic M-H curve can be used to classify the kind of magnetic behavior as revealed in Section 2.3.12.

In this study magnetic properties of synthesized powder samples were used to perform a VSM (VersaLab™ PPMS®) at room temperature. The powder sample with a weight of about 20–30 mg was placed into the sample holder, and the magnetization was measured in a varying magnetic field of ± 10 kOe. The parameters, such as

saturation magnetization (M_s), remanent magnetization (M_r) and coercivity field (H_c) were obtained from the hysteresis loop.

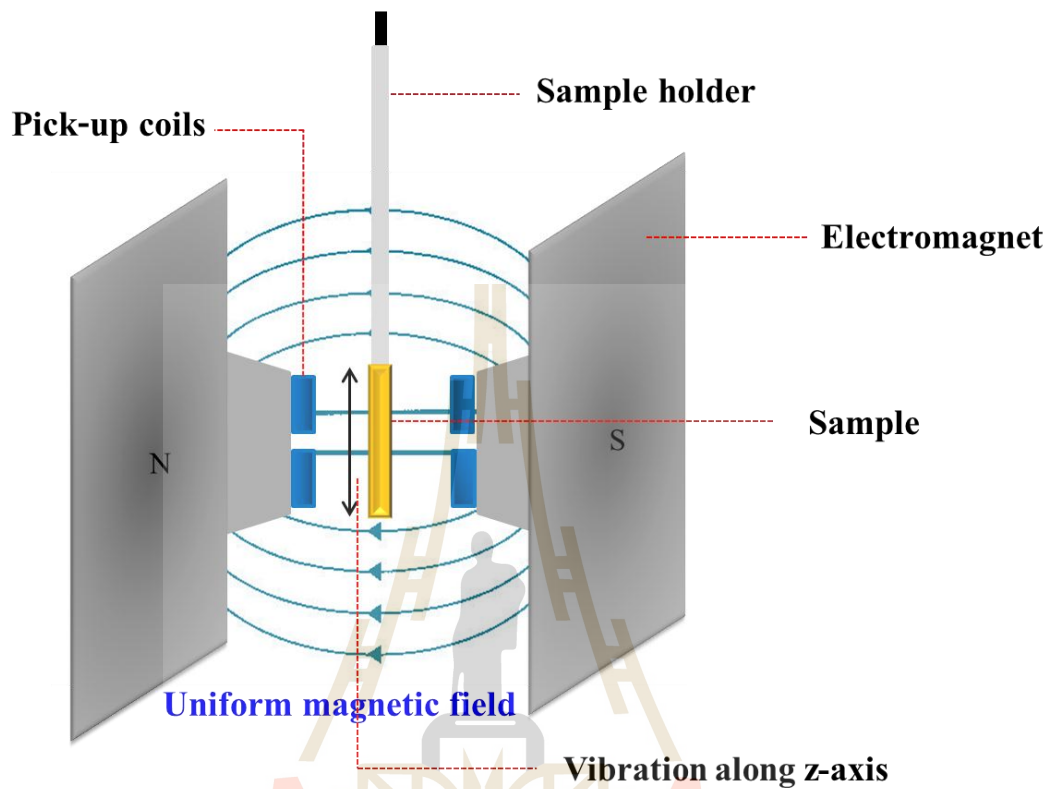


Figure 3.4 Schematic diagram of the vibrating sample magnetometer (VSM) (Adapted from Smith, 1956).

3.3 Dielectric properties

Measurement of dielectric properties can provide design parameter information, for example, the loss of a cable insulator, the complex relative permittivity and the complex relative permeability of the materials. A complex dielectric permittivity includes a real part and an imaginary part. The real part of a complex permittivity is known as the dielectric constant which is the ability to store energy from an external electrical field when it is applied to the material. The

imaginary part is known as the loss factor which represents how much energy is lost from the material due to an external electric field. The term $\tan \delta$ is called loss tangent and it represents the ratio of energy lost to energy stored per cycle. The dielectric constant (ϵ') and dielectric loss (ϵ'') of the materials were determined as the relations:

$$\epsilon' = \frac{C_p d}{\epsilon_0 A} \quad (3.5)$$

$$\epsilon'' = \epsilon' \tan \delta \quad (3.6)$$

where A and d are the area of the electrode and the thickness of the sample (m).

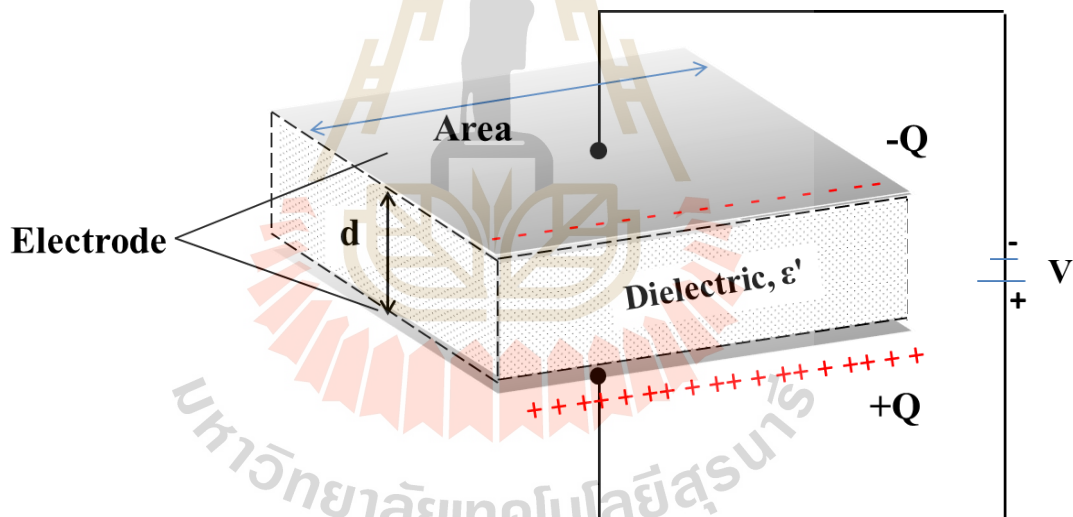


Figure 3.5 Schematic of parallel plate capacitor with electrodes on both sides of the dielectric (adapt from <https://en.wikipedia.org/wiki/Capacitor>).

In this study, the electrical properties of the BiFeO_3 -based ceramics were also investigated through the impedance (Z^*), AC conductivity (σ), and activated energy (E_a). Impedance is an important parameter used to describe electronic circuits and components. The electrical parameters were calculated from the following equations:

$$\varepsilon^* = \varepsilon' - j\varepsilon'' = \frac{1}{j\omega C_0 Z^*}, \quad (3.7)$$

$$\sigma = \varepsilon_0 \omega \varepsilon'', \quad (3.8)$$

Where ω is the angular frequency, and C_0 is the capacitance without dielectric material.

In this research, the dielectric and related electrical measurements, and the sintered BiFeO₃-based pellet samples were electrodes by silver paint on both sides of the disk-shaped samples. The dielectric and related electrical properties of the samples were performed using a Hewlett Packard 4194A impedance gain phase analyser within a wide frequency range 100–1 MHz and temperatures ranging from -50 to 200 °C at the oscillation voltage of 1.0 V. Figure 3.6 shows the flowchart diagram of the measuring dielectric parameters of the BiFeO₃-based ceramics. As illustrated in the flowchart diagram, the values of C_p and $\tan \delta$ at different frequencies and temperatures were obtained directly from the experiment.

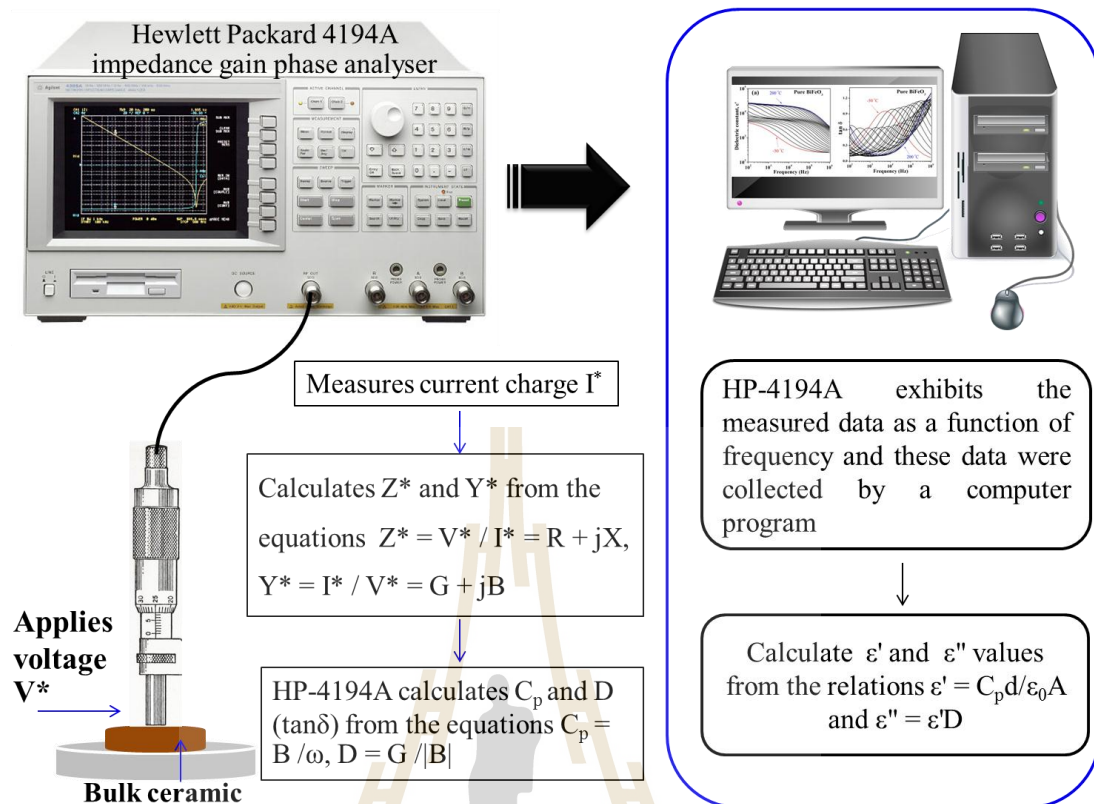


Figure 3.6 Diagram presenting measuring dielectric parameters of the BiFeO_3 -based ceramic samples using a Hewlett Packard 4194A impedance gain phase analyzer.

3.4 Current–voltage characteristics

Current–voltage characteristics are generally used as a tool to investigate and understand the basic parameters of a component, device, and material and which can also be used to model its behaviour within an electronic circuit. The simplest IV characteristic involves a resistor as corresponding to Ohm's Law which presents a linear relationship between the applied voltage and the resulting electric current. If the electrical supply voltage, V , is applied to resistor R and varied, the resulting electric current, I is measured, this current would be carried out as $I = V/R$ according to an

Ohm's Law equation. However, other resistive elements such as thermistors, varistors and even the light bulb, I-V characteristic curves are not straight or linear lines, that is, their V/I ratio is not constant but are curved and shaped and are called non-linear devices. Semiconductor diodes are characterized by non-linear current-voltage behaviours as the current flowing through a forward-biased , silicon diode is limited by the ohmic resistance of the P-N junction. When the forward voltage exceeds the diodes the P-N junctions internal barrier voltage (an avalanche) occurs and the current increases suddenly with a very small increase in voltage promoting a non-linear curve.

In this study, current-voltage measurements were conducted at various temperature ranges from room temperature to 100 °C using a high-voltage measurement unit (Keithley Model 247, Estado St Pasadena, CA). The samples were well polished and sandwiched between two silver electrodes, and current was recorded relative to an increase in the applied voltage. The high source voltage was raised at a rate of 0.45 V/s. The breakdown of the electric field (E_b) was obtained at a current density of 1 mA/cm². The non-linear coefficient (α) values were calculated over the range 1–10 mA/cm² from the equation:

$$\alpha = \frac{\log(J_2 / J_1)}{\log(E_2 / E_1)} \quad (3.9)$$

Where E_1 and E_2 are the electric fields corresponding to J_1 and J_2 at 1 and 10 mA/cm², respectively.

CHAPTER IV

RESULTS AND DISCUSSION

4.1 Structural characterization and morphology of BiFeO₃ and Ba-, La-, and Sm-doped BiFeO₃ nanopowders

4.1.1 Structural characterization and morphology of the pure BiFeO₃ nanopowders prepared by co-precipitation method

The crystal structure and morphology of the parent BiFeO₃ nanopowders calcined in air at 600 °C for 3 h has been investigated by transmission electron microscopy (TEM) and X-ray diffraction (XRD) analysis. Figure 4.1 shows the Rietveld refinement of XRD pattern for pure BiFeO₃ together with the profile obtained from the Rietveld analysis. It can be clearly seen that the diffraction peaks can be indexed to the main phase of the rhombohedral structure BiFeO₃ (JCPDS: 86-1518) with R3c space group as reported in the literature (Hou *et al.*, 2013; Srivastava *et al.*, 2013). In addition, the XRD pattern reveals a small amount of impurity phases according to Bi₂Fe₄O₉. The crystallite size of the calcined BiFeO₃ sample calculated from the diffraction peaks is about 68 nm. The XRD data of BiFeO₃ in 2θ range 20°–60° has been used for refinement and the crystal structure parameters investigated from the refinement are illustrated in Table 4.1. The refinement result of the pure

BiFeO_3 exhibits a rhombohedral structure with R3c space group and goodness of fit (GOF) was found to be ~ 3.87 . The lattice parameters obtained of the pure sample are $a = 5.5791(2) \text{ \AA}$, $b = 13.869(5) \text{ \AA}$, $\alpha, \beta = 90^\circ$ and $\gamma = 120^\circ$ which agree well with the rhombohedral structure R3c symmetry and have been reported by several researchers (Suresh and Srinath, 2013; Rout and Choudhary, 2015).

The morphology of BiFeO_3 nanoparticles was observed by transmission electron microscopy (TEM). The BiFeO_3 nanoparticles have been found to have a similar spherical shape. The particle size of pure BiFeO_3 nanopowder was obtained to be about 67 nm as seen in the inset of Figure 4.1. The particle size obtained from the TEM image is slightly smaller than that obtained from the XRD result. Moreover, in the XRD result, the crystal structure and other phases contained in the compound were investigated by Selected-Area Electron Diffraction (SAED) patterns as shown in the inset of Figure 4.1. The SAED pattern reveals the presence of sharp diffraction rings for the BiFeO_3 nanoparticles, which confirm that it is a polycrystalline structure characteristic of synthesized nanoparticles. The lattice planes of BiFeO_3 are (110), (111), (120), and (202) corresponding to the planes of the rhombohedral structure. This result is in good agreement with the SAED patterns and the results obtained from the XRD data. It should be noted that a small number of impurity phase of $\text{Bi}_2\text{Fe}_4\text{O}_9$ were found but not observed in the SAED patterns.

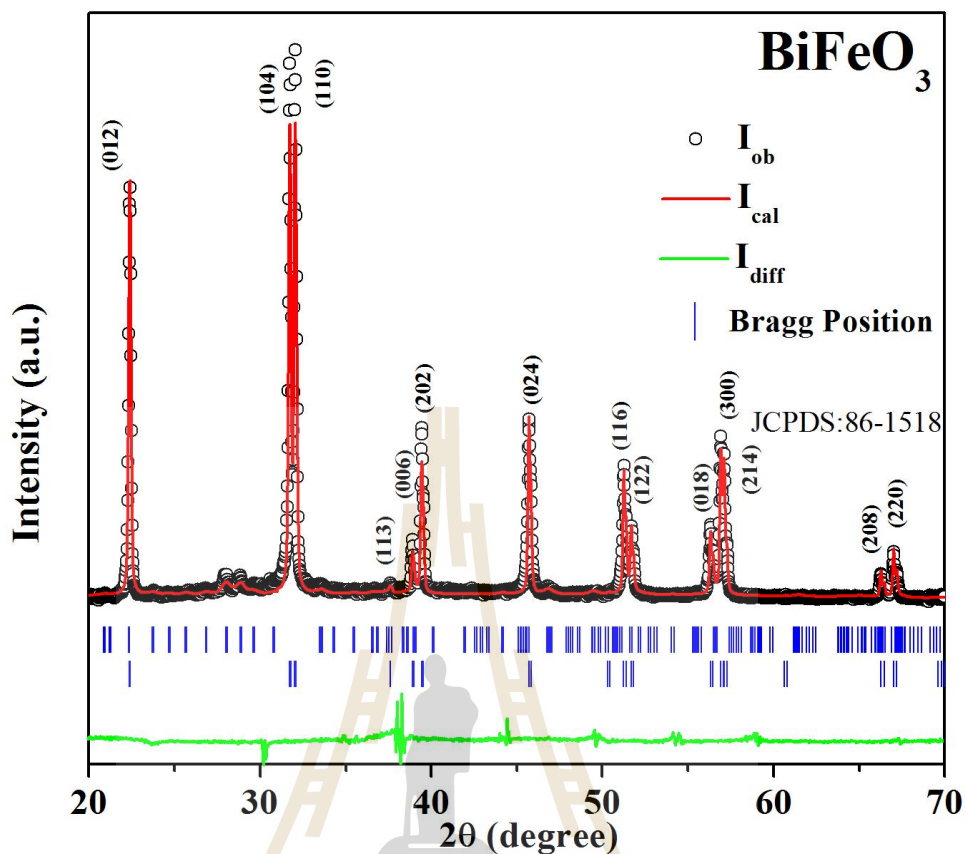


Figure 4.1 Rietveld refinement of the XRD pattern of pure BiFeO_3 nanopowders.

Table 4.1 Details of Rietveld refined XRD parameters for $\text{Bi}_{1-x}\text{A}_x\text{FeO}_3$ (A = Ba, La, and Sm) with $x = 0.0, 0.1, 0.2,$ and 0.3 samples.

Sample	Phase	a (Å)	b (Å)	c (Å)	V (Å ³)	GOF	$R_{wp}\%$
BiFeO_3	R3c	5.5791(2)	5.5791(2)	13.869(5)	373.8731	3.87	16
Ba-doped							
$x = 0.05$	R3c (35.4%),	5.5794(3)	5.5794(3)	13.8698(8)	373.912	3.57	14.52
	Pbam (64.4%)	7.953(3)	8.492(3)	6.024(3)	406.829		
$x = 0.1$	R3c (73%),	5.5791(1)	5.5791(1)	13.8702(4)	373.887	2.01	11.37
	Pbam (27%)	7.968(1)	8.468(1)	6.017(1)	405.963		

Table 4.1 Details of Rietveld refined XRD parameters for $\text{Bi}_{1-x}\text{A}_x\text{FeO}_3$ (A = Ba, La, and Sm) with $x = 0.0, 0.1, 0.2,$ and 0.3 samples (Continued).

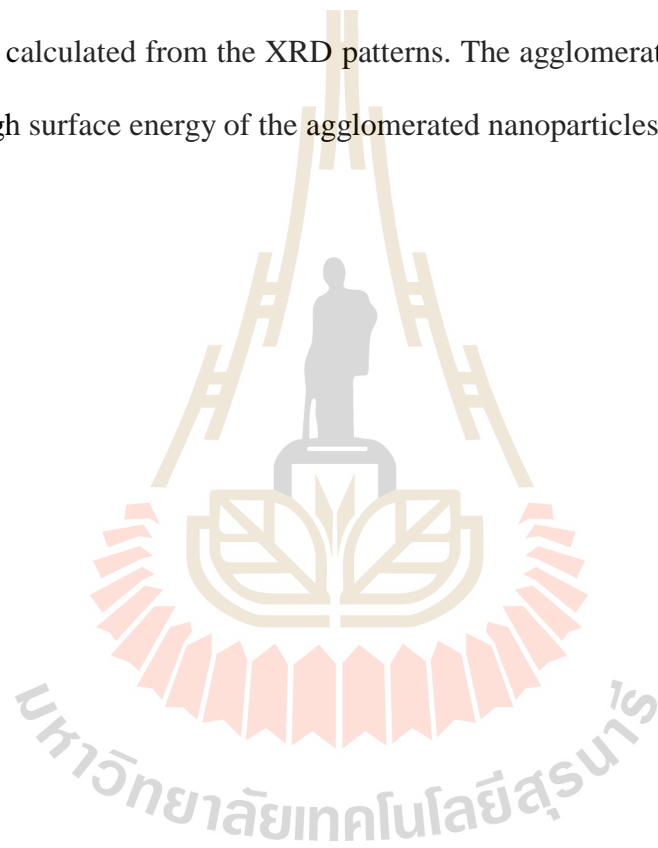
Sample	Phase	a (Å)	b (Å)	c (Å)	V (Å ³)	GOF	$R_{\text{wp}}\%$
$x = 0.2$	R3c (54.1%),	5.5781(1)	5.5781(1)	13.8687(4)	373.719	2.06	10.57
	Pbam (45.9%)	7.9668(7)	8.4616(7)	6.0139(5)	405.409		
$x = 0.3$	R3c (30.8%),	5.5785(2)	5.5785(2)	13.8681(6)	373.752	1.94	10.7
	Pbam (69.2%)	7.9679(5)	8.4643(5)	6.0155(4)	405.702		
La-doped							
$x = 0.05$	R3c	5.578(2)	5.578(2)	13.841(6)	372.986	2.4	12.8
$x = 0.1$	R3c	5.5772(3)	5.5772(3)	13.803(8)	371.828	2.88	13.24
$x = 0.2$	Pnma	5.615(1)	7.884(2)	5.577(1)	246.888	6.28	9.27
$x = 0.3$	Pnma	5.5898(8)	7.8358(9)	5.6125(8)	245.829	5.05	8.40
Sm-doped							
$x = 0.05$	R3c (76.4%),	5.5742(3)	5.5742(3)	13.841(9)	372.454	5.18	11.71
	Pbam (23.6%)	7.946(4)	8.509(4)	6.008(4)	406.237		
$x = 0.1$	R3c (77.3%),	5.5675(6)	5.5675(6)	13.800(2)	370.448	3.26	14.68
	Pbam (22.7%)	7.952(7)	8.561(7)	5.903(7)	401.864		
$x = 0.2$	R3c (26.6%),	5.537(1)	5.537(1)	13.705(4)	363.861	6.07	12.57
	Pnma (48.7),	5.6126(8)	7.816(1)	5.4491(8)	239.036		
	Pbam (24.7%)	7.92(2)	8.80(2)	5.54(2)	385.922		
$x = 0.3$	R3c (18.2%),	5.516(1)	5.516(1)	13.669(6)	360.160	3.46	9.8
	Pnma (60%),	5.6136(6)	7.7996(9)	5.4357(6)	237.995		
	Pbam (21.8%)	7.80(3)	8.89(3)	5.52(2)	382.536		

4.1.2 Effects of Ba, La, and Sm doping on the morphologies and crystal structure of BiFeO₃ nanopowders

The BiFeO₃-based powders were characterized by TEM and XRD techniques in order to analyse and reveal their powder morphologies and phase structure, respectively. The doping effects of doped BiFeO₃ on the microstructure of BiFeO₃ nanoparticles calcined at 600 °C for 3 h are divided into three groups as shown in Figure 4.2(a)–(m). It can be clearly seen, in the first group, the TEM images of La-doped BiFeO₃ nanoparticles are likely to be spherical in shape and are not well separated from each other. The formation of agglomerated nanoparticles having irregular morphology has been observed to increase as the particle size decreases. The nanoparticles were agglomerated by the basic physical force (van der Waals force) of primary particles (Biasotto *et al.*, 2011). In general, smaller primary particles sizes are highly relative to the surface area, and have a tendency to form nearly spherical agglomerates. To minimize their surface energy the nanoparticles create agglomeration. The micrographs show the average particle size of the nanoparticles decreases with increases in the La doping concentrations. As revealed in Figure 4.2, the particle sizes of the nanopowders are found to be in the range of about ~19–67 nm for La substitutions. This is attributed to the fact that the La ions inhibit the grain growth, thus a smaller particle size in La-doped nanopowders may be the cause of increasing the segregation at the surface of nanoparticles by substituting La ions (Qian *et al.*, 2009; Jun *et al.*, 2005). For the second group of morphology, as shown in the Figure 4.2, the morphology of Sm doping is similar to that observed in the TEM images of La-doped BiFeO₃ nanoparticles. Note that the particle sizes of Sm-doped calcined powder are found to be around 22–79 nm which means the average particle

sizes of Sm-doped BiFeO₃ samples are larger than that of La-doped samples. Finally, the observed morphology of the Ba-doped BiFeO₃ samples is likely to have a spherical shape and almost no agglomerated nanoparticles. On the contrary, the morphology images of La- and Sm-doped samples can be clearly seen and the agglomerates of the particles can be observed. It is also observed that the particle sizes of Ba-doped BiFeO₃ nanoparticles tend to decrease with increasing Ba concentration. The particle sizes of the Bi_{1-x}Ba_xFeO₃ system are in the range of 37–66 nm. A significant reduction in particle size upon doping is attributed to inhibited crystal growth caused by the substitution of smaller ionic radii dopants as compared to Bi ions. The decrease in the particle size may be ascribed to the suppression of oxygen vacancy concentration. This may result in slower diffusion of oxygen ions inhibiting the grain growth rate (Song *et al.*, 2012; Srivastava *et al.*, 2013). The selected area electron diffraction (SAED) patterns of these nanoparticles are shown in the insets of TEM micrographs of the respective nanoparticles (Figure 4.2). The indexed electron diffraction patterns also support the rhombohedral and orthorhombic structure of pure and Ba-, La-, and Sm-doped BiFeO₃ nanoparticles, respectively, which corroborate the XRD patterns. For the La-doped BiFeO₃ system, the SAED patterns present sharp diffraction rings in the polycrystalline consisting of diffraction spots. However, it is found that the diffraction rings can be indexed as (120), (402) planes for Bi_{0.95}La_{0.05}FeO₃ and (202), (121), and (310) planes for Bi_{0.9}La_{0.1}FeO₃ corresponding to impurity phases of Bi₂Fe₄O₉. Similarly, for Sm-doped samples, the rhombohedral structure planes are prominent and the Pbam impurity phase planes as (411) are observed for the Bi_{0.95}Sm_{0.05}FeO₃ and Bi_{0.9}Sm_{0.1}FeO₃ samples and (210) for the Bi_{0.8}Sm_{0.2}FeO₃ and the Bi_{0.7}Sm_{0.3}FeO₃ samples. Finally, SAED analysis on Ba

substituting in the BiFeO_3 samples reveals that the structure exists in the R3c rhombohedral structure and can be also observed in the secondary phase planes as (131), (212), and (330) for the $\text{Bi}_{0.95}\text{Ba}_{0.05}\text{FeO}_3$ and the $\text{Bi}_{0.9}\text{Ba}_{0.1}\text{FeO}_3$ samples, (121) and (402) for the $\text{Bi}_{0.8}\text{Ba}_{0.2}\text{FeO}_3$ and the $\text{Bi}_{0.7}\text{Ba}_{0.3}\text{FeO}_3$ samples. These results confirm the impurity phases in these samples that were detected by the XRD analysis. The observed particles size of Sm-doped samples was found to be larger than the particles size that was calculated from the XRD patterns. The agglomeration of the particles is due to the high surface energy of the agglomerated nanoparticles.



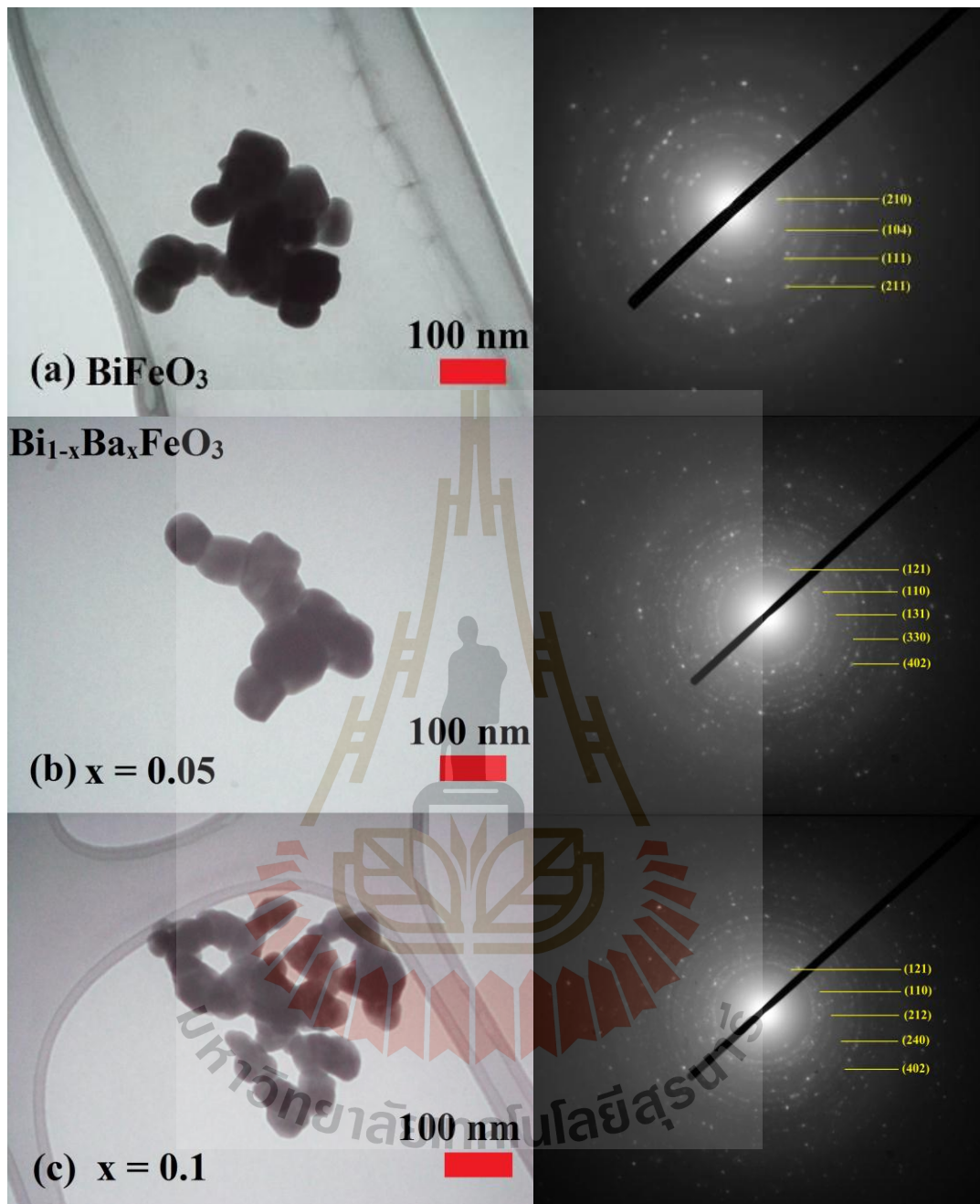


Figure 4.2 TEM bright-field images (left) with the corresponding SAED patterns (right) of (a) pure BiFeO_3 , (b)–(e) $\text{Bi}_{1-x}\text{Ba}_x\text{FeO}_3$, (f)–(i) $\text{Bi}_{1-x}\text{La}_x\text{FeO}_3$, and (j)–(m) $\text{Bi}_{1-x}\text{Sm}_x\text{FeO}_3$, with $x = 0.05, 0.1, 0.2,$ and 0.3 , respectively.

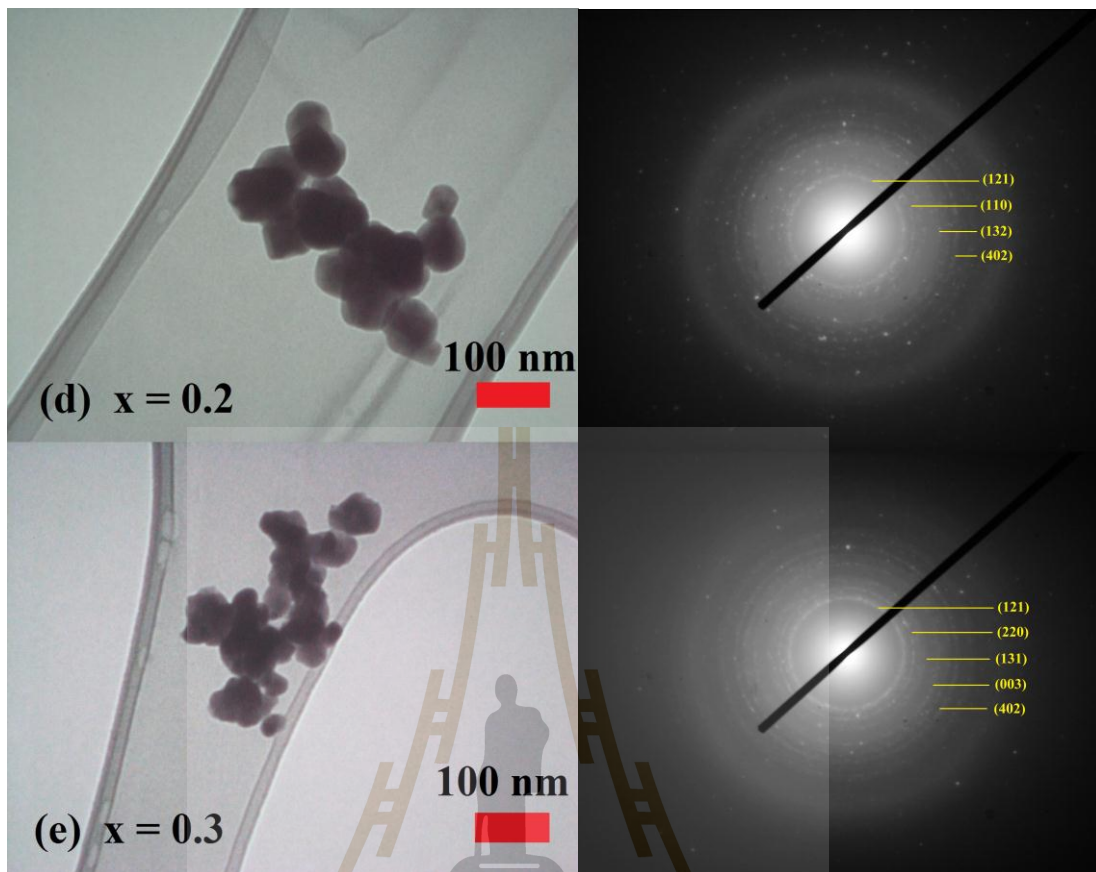


Figure 4.2 TEM bright-field images (left) with the corresponding SAED patterns (right) of (a) pure BiFeO_3 , (b)–(e) $\text{Bi}_{1-x}\text{Ba}_x\text{FeO}_3$, (f)–(i) $\text{Bi}_{1-x}\text{La}_x\text{FeO}_3$, and (j)–(m) $\text{Bi}_{1-x}\text{Sm}_x\text{FeO}_3$, with $x = 0.05, 0.1, 0.2,$ and 0.3 , respectively (Continued).

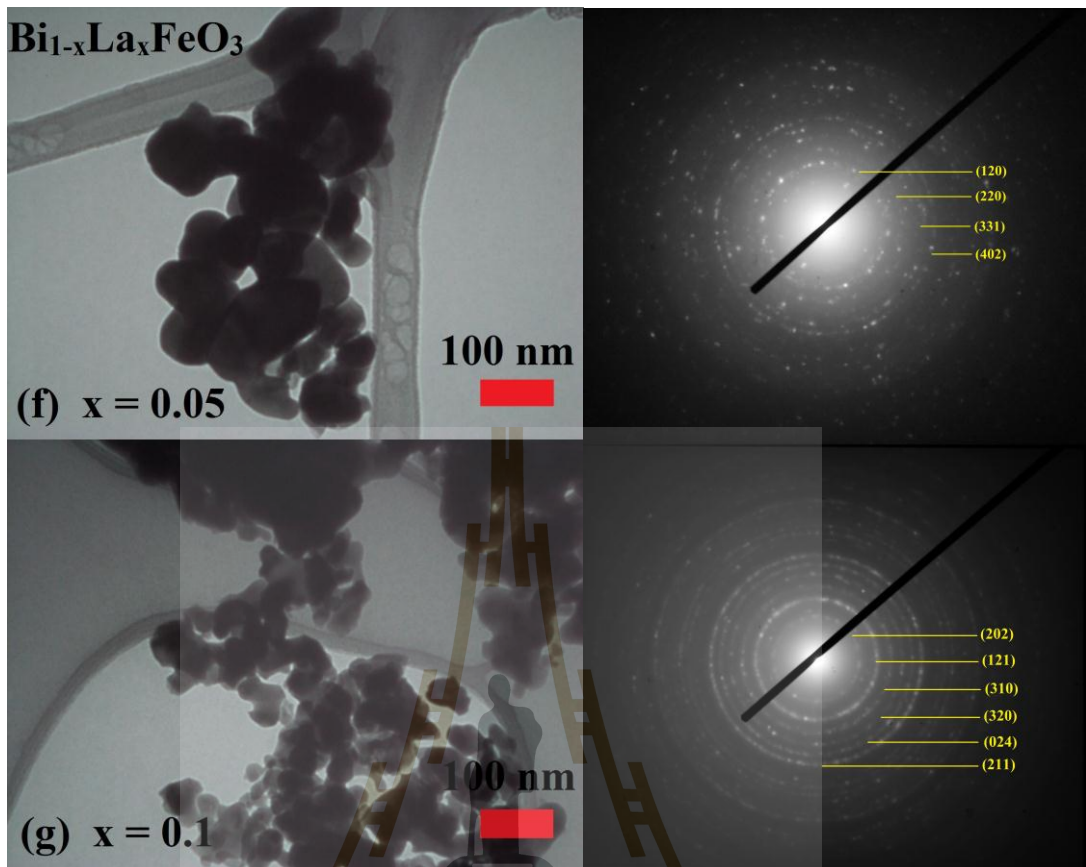


Figure 4.2 TEM bright-field images (left) with the corresponding SAED patterns (right) of (a) pure BiFeO_3 , (b)–(e) $\text{Bi}_{1-x}\text{Ba}_x\text{FeO}_3$, (f)–(i) $\text{Bi}_{1-x}\text{La}_x\text{FeO}_3$, and (j)–(m) $\text{Bi}_{1-x}\text{Sm}_x\text{FeO}_3$, with $x = 0.05, 0.1, 0.2,$ and 0.3 , respectively (Continued).

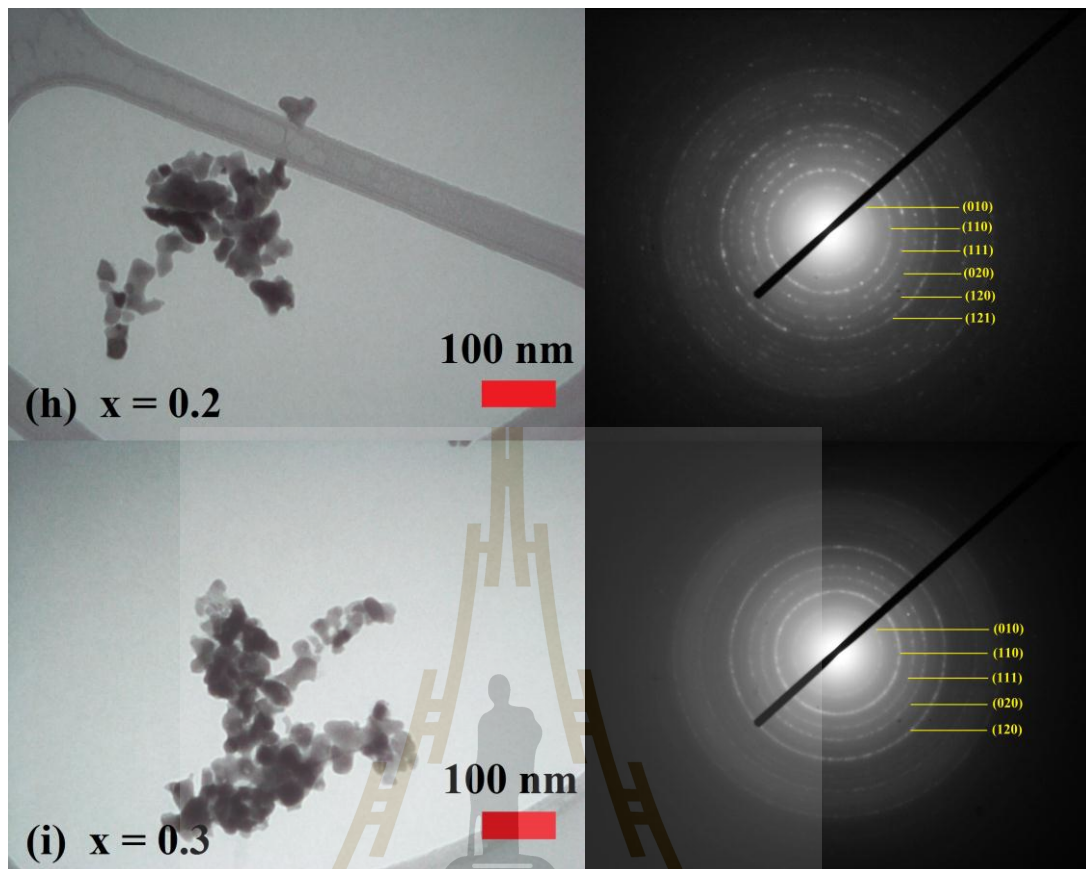


Figure 4.2 TEM bright-field images (left) with the corresponding SAED patterns (right) of (a) pure BiFeO_3 , (b)–(e) $\text{Bi}_{1-x}\text{Ba}_x\text{FeO}_3$, (f)–(i) $\text{Bi}_{1-x}\text{La}_x\text{FeO}_3$, and (j)–(m) $\text{Bi}_{1-x}\text{Sm}_x\text{FeO}_3$, with $x = 0.05, 0.1, 0.2,$ and 0.3 , respectively (Continued).

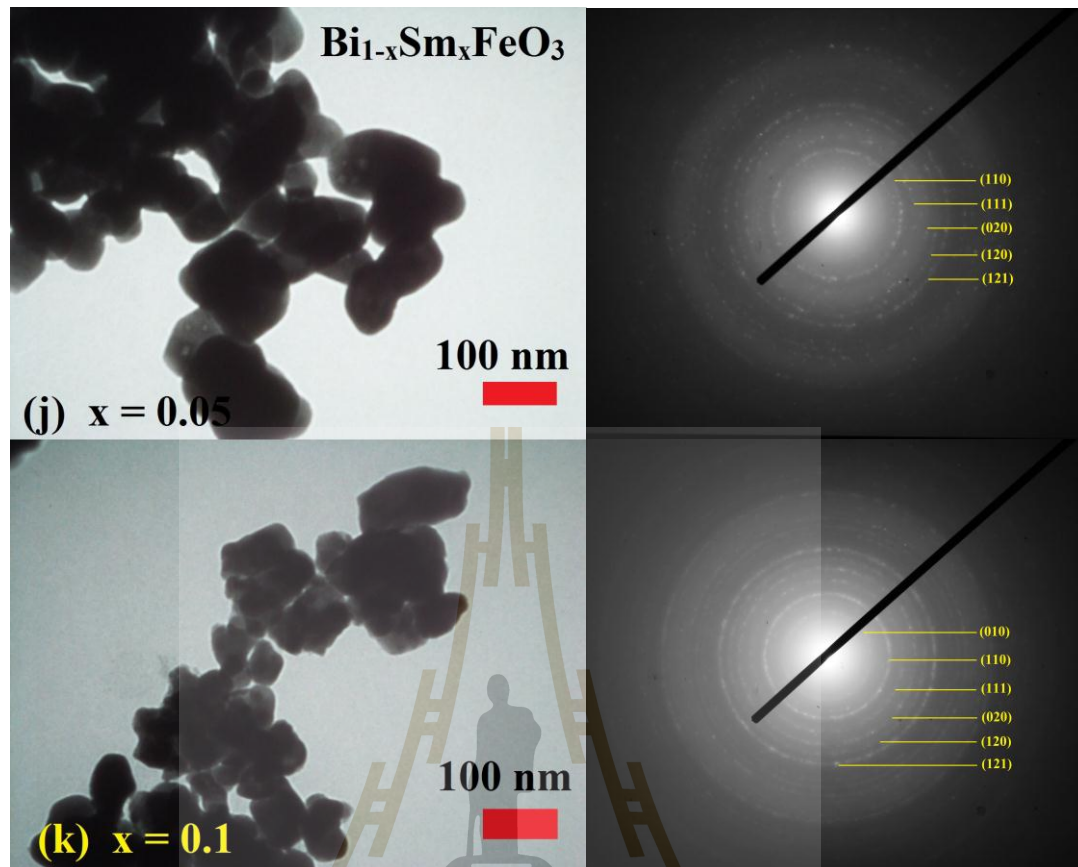


Figure 4.2 TEM bright-field images (left) with the corresponding SAED patterns (right) of (a) pure BiFeO_3 , (b)–(e) $\text{Bi}_{1-x}\text{Ba}_x\text{FeO}_3$, (f)–(i) $\text{Bi}_{1-x}\text{La}_x\text{FeO}_3$, and (j)–(m) $\text{Bi}_{1-x}\text{Sm}_x\text{FeO}_3$, with $x = 0.05, 0.1, 0.2,$ and 0.3 , respectively (Continued).

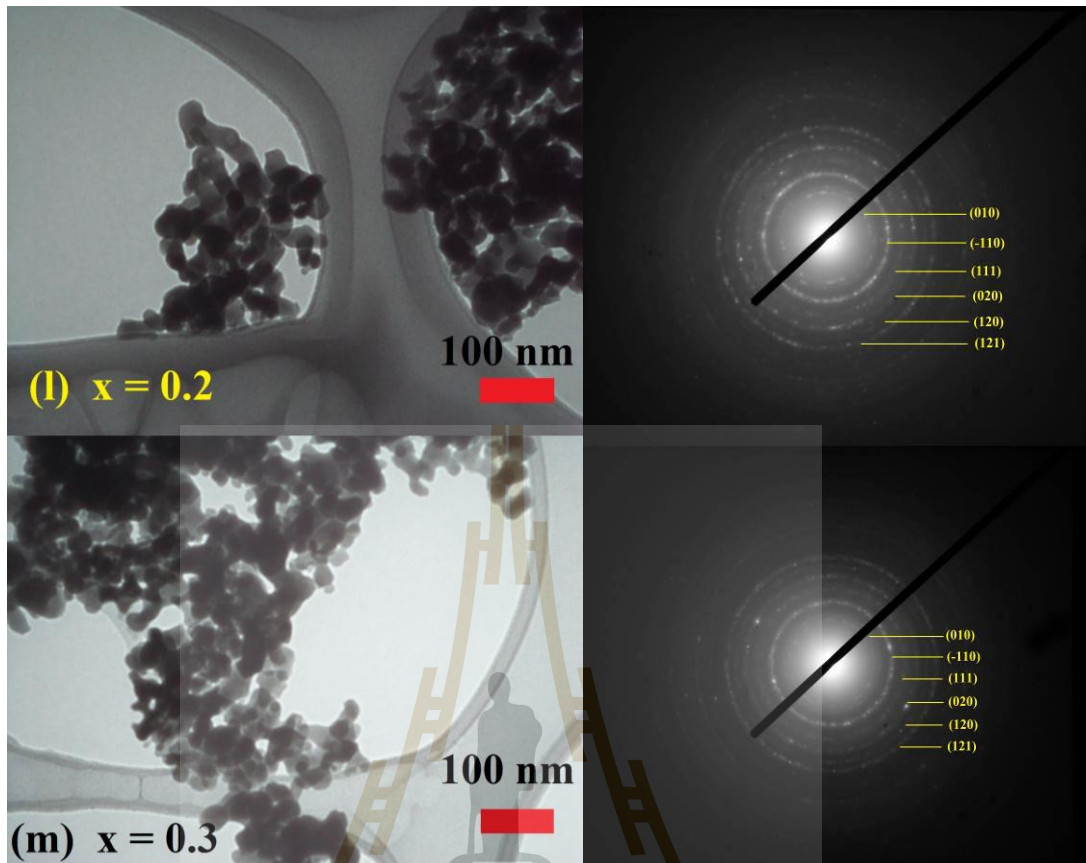


Figure 4.2 TEM bright-field images (left) with the corresponding SAED patterns (right) of (a) pure BiFeO_3 , (b)–(e) $\text{Bi}_{1-x}\text{Ba}_x\text{FeO}_3$, (f)–(i) $\text{Bi}_{1-x}\text{La}_x\text{FeO}_3$, and (j)–(m) $\text{Bi}_{1-x}\text{Sm}_x\text{FeO}_3$, with $x = 0.05, 0.1, 0.2,$ and 0.3 , respectively (Continued).

Crystal structure and phase composition of samples can be analysed by using X-ray diffraction techniques. As can be clearly seen in Figures 4.3–4.5, the XRD patterns of all doping samples can be matched with the rhombohedral structures of BiFeO_3 with space groups $R3c$ (JCPDS no. 86–1518). However, the presence of minor secondary phases from the XRD patterns was observed, for example, with $\text{Bi}_2\text{Fe}_4\text{O}_9$ in the La- and Ba-doped BiFeO_3 samples, while the Sm-doped samples exhibited the SmFeO_3 phase. The formation of impurity phases may be due to compensation for the extra charge or oxygen deficiency for large radii substitutes for

BiFeO₃. As a result of doping, La, Ba, and Sm changes in peak shapes and positions are observed, especially $x \geq 10\%$ doping. These changes are more significant for La and Sm ions doped powders as these two have smaller ionic radii than Ba ions. We start our discussion first with the XRD analyses of Bi_{1-x}Ba_xFeO₃ system which shows the peaks of the secondary phases, which are attributed to the Bi₂Fe₄O₉ phase. The impurity phases are due to the compensation for the extra charges of or oxygen deficiency in Ba²⁺ substitutes for BiFeO₃. It should be noted that the enlarged view of XRD patterns around $\sim 32^\circ$ for Ba-doped BiFeO₃ (Figure 4.3(b)) indicate that the Ba ions do not have an effect on the structural transition of the rhombohedral phase. The double split diffraction peaks in this position do not merge together which is one of the characteristics of the structural phase transition. This indicates that there is no change in the lattice parameters in the Ba substituted system which is similar to previous reports that no structural transitions are available for alkaline rare earth doped in BiFeO₃ (Khomchenko *et al.*, 2009). Compared to parent BiFeO₃, the peaks in the XRD patterns around $\sim 32^\circ$ are found to have slightly shifted to a higher angle with an increase of Ba concentration which confirms the substitution of Ba²⁺ in the BiFeO₃ lattice. The reason may be due to the replacement of Ba²⁺ ($r = 1.42 \text{ \AA}$) having larger ionic radii than the Bi³⁺ ($r = 1.17 \text{ \AA}$) ions (Gautam and Rangra, 2010). The refinement results show that the Ba-doped BiFeO₃ system is found to fit with R3c (35.4, 73, 54.1, and 30.8%) and Pbam (64.4, 27, 45.9, and 69.2%, respectively) in mixed phases for all samples. The Rietveld refinement data shows the percentage of R3c phases decrease with increasing Ba doping. This suggests that the Ba²⁺ substituted in BiFeO₃ has a tendency to enlarge the orthorhombic phase with an increase of Ba concentration.

The substitute of La doping, a magnified view of the XRD patterns, and La^{3+} substitution show gradual variations in peaks when compared with the parent BiFeO_3 . All diffraction peaks of the $\text{Bi}_{0.95}\text{La}_{0.05}\text{FeO}_3$ and $\text{Bi}_{0.9}\text{La}_{0.1}\text{FeO}_3$ samples are similar to that observed in the XRD patterns of the parent BiFeO_3 compound. The Rietveld analysis of BiFeO_3 and La-doped ($\leq 10\%$) samples reveal that the XRD patterns fit well with the standard pattern (JCPDS no. 86–1518), although another impurity phase of $\text{Bi}_2\text{Fe}_4\text{O}_9$ was present. However, the double split diffraction peak near 32° (104) and (110) and near 51° (116) and (122) for $\geq 20\%$ La substitutions slowly merges towards a single diffraction peak. This result means that the lattice unit cell distortion in the rhombohedral structure of pure BiFeO_3 is due to the substitution of La ions into the Bi site. It can be seen that further increases in the quantity of La doping ($x = 0.1$ – 0.3) do not result in any additional peaks corresponding to any impurity phases.

Further the Rietveld refinement is used to estimate the crystal structure profiles of doped samples. The Rietveld refinement of $\text{Bi}_{0.95}\text{La}_{0.05}\text{FeO}_3$ indicates good fits with the rhombohedral structure of R3c space groups. La doping with 10% of the La concentration sample was carried out for the rhombohedral phase belonging to R3c space groups similar to BiFeO_3 with changes in the lattice parameter values. Therefore, with the La doping with $x \leq 10\%$, the main phase R3c still persists as the dominant phase. Moreover, the diffraction peaks are found to shift in their peak positions towards the left with increasing La concentrations, implying an average gradual shrinkage in the unit cells. The peak shift and splitting for these planes in high resolution is given in Figure 4.4. This suggests that there exists some structural distortion taking place on the La substitution at the Bi site (Mishra *et al.*, 2008). For $\geq 20\%$ La substitutions, there is a structural change with La replacing in the Bi site. The

best fit for the experimental data for these two samples are observed using the orthorhombic phase (Pnma space group), suggesting that with 20% La doping the structure of BiFeO₃ is transformed from a distorted rhombohedral R3c to an orthorhombic Pnma. The crystal structure parameters obtained from simulation are detailed in Table 4.1. The lattice parameter values obtained from the refinement profiles decrease with increases in La concentration. Thus La substitution leads to a decrease in the unit cell volume which is a result of the difference in the ionic radius of La³⁺ ($r = 1.22 \text{ \AA}$) being larger than that of Bi³⁺ ($r = 1.17 \text{ \AA}$) (Chen *et al.*, 2012).

Finally, the Sm substituted A-site (Bi³⁺) in BiFeO₃ affects the structure of the parent compound. For Bi_{1-x}Sm_xFeO₃ at $x = 0.05$ and 0.1 the main diffraction peaks can be indexed successfully according to the rhombohedral structure. Some low intensity diffraction peaks of the secondary phase can be also observed in the XRD patterns of Sm-doped BiFeO₃ samples corresponding to Bi₂O₃ and Bi₂Fe₄O₉. The XRD patterns of Bi_{1-x}Sm_xFeO₃ samples in the range of $2\theta = 32^\circ$ show peak broadening together with merging of the double peaks and a shift toward a higher 2θ value. One feature that should be noted is that with increasing the Sm concentration, the intensity of the diffraction peaks in the vicinity of $2\theta \sim 39^\circ$ and 66° become weak. Whereas the diffraction peaks at $2\theta \sim 25.5^\circ$ and 63° begin to appear at the level of Sm $\geq 20\%$ doping. These results mean that the XRD patterns in this case begin close to the orthorhombic phase. Thus, in the case of the Sm-doped system, the maximum level of Sm which takes place in BiFeO₃ occurs somewhere between 10–20% concentration. This indicates that the structural phase transition occurs near $x = 20\%$ which is reported by several authors (Khomchenko *et al.*, 2010; Wu *et al.*, 2013). As confirmation of the structural changes, the Rietveld refinement results of Bi₁₋

$x\text{Sm}_x\text{FeO}_3$ ($x = 0.05$ and 0.1) samples agree well with R3c+Pbam structure model, and the main contribution $\sim 76.4\%$ and 77.3% was analyzed as being related to the rhombohedral phase with R3c space groups and a minor contribution Pbam phase with $\sim 23.6\%$ and 22.7% . At Sm concentrations exceeding 10% i.e. $\text{Bi}_{0.7}\text{Sm}_{0.3}\text{FeO}_3$ and $\text{Bi}_{0.8}\text{Sm}_{0.2}\text{FeO}_3$ samples, the structure models are observed to fit better with R3c (BiFeO_3)+Pnma (SmFeO_3)+Pbam ($\text{Bi}_2\text{Fe}_4\text{O}_9$) symmetry. The refinement result for Sm doping with $x = 0.2$ and 0.3 show the phase of orthorhombic Pbam with 24.7% and 21.8% and rhombohedral R3c (26.6% and 18.2%). The main structural model is observed to fit well with the rhombohedral Pnma of the SmFeO_3 phase with 48.7% and 60% . The structural phase transitions from a rhombohedral to an orthorhombic phase also lead to changes in the lattice unit cells. The a and b-axis unit cell parameters tend to change slightly with increases in Sm doping in the rhombohedral structure, whereas this value significantly increases when the structural transition is to the orthorhombic phase. With increasing Sm doping, the c-axis parameter changes a little in the rhombohedral phase and still decreases in the orthorhombic phase. The variations in the lattice constant values of Sm-doped BiFeO_3 samples lead to decreases in the unit cell volume related to the differences in the ionic radii between Bi^{3+} ($r = 1.17 \text{ \AA}$) and Sm^{3+} ($r = 1.08 \text{ \AA}$) ions. The increasing rare earth substitution in pure BiFeO_3 causes a decrease in the lattice parameter result with decreases in unit cell volume from 373.8731 \AA^3 to 373.752 \AA^3 for Ba-doped, 372.986 \AA^3 to 246.888 \AA^3 for La-doped, and 372.454 \AA^3 to 360.160 \AA^3 for Sm-doped BiFeO_3 samples. This reduction the unit cell volume by increasing rare earth doping is assumed as ionic radii of rare earth ions is slightly lower than that of Bi^{3+} ions.

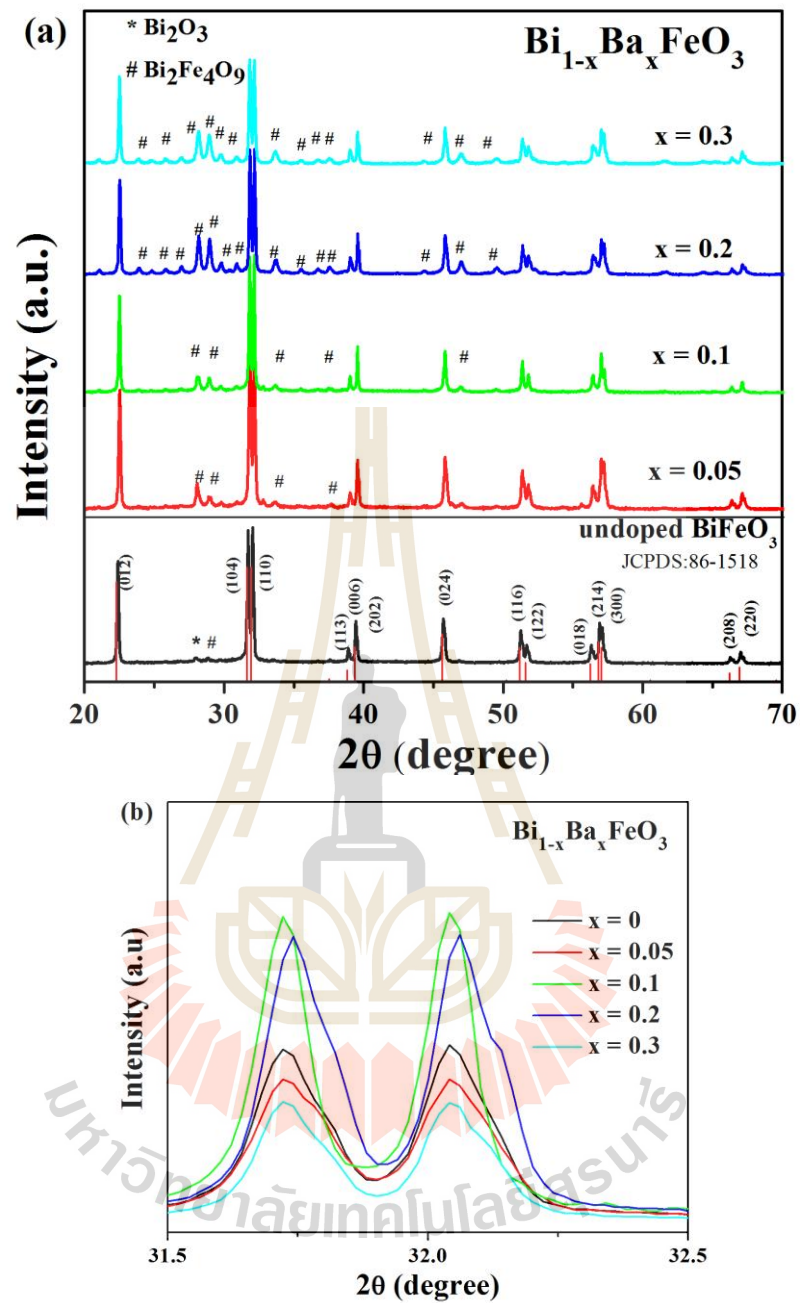


Figure 4.3 The XRD patterns of undoped BiFeO_3 and $\text{Bi}_{1-x}\text{Ba}_x\text{FeO}_3$ samples with $x = 0.05, 0.1, 0.2,$ and $0.3,$ respectively. (b) Enlarged views of the diffraction peaks in the $2\theta \sim 32^\circ$ range.

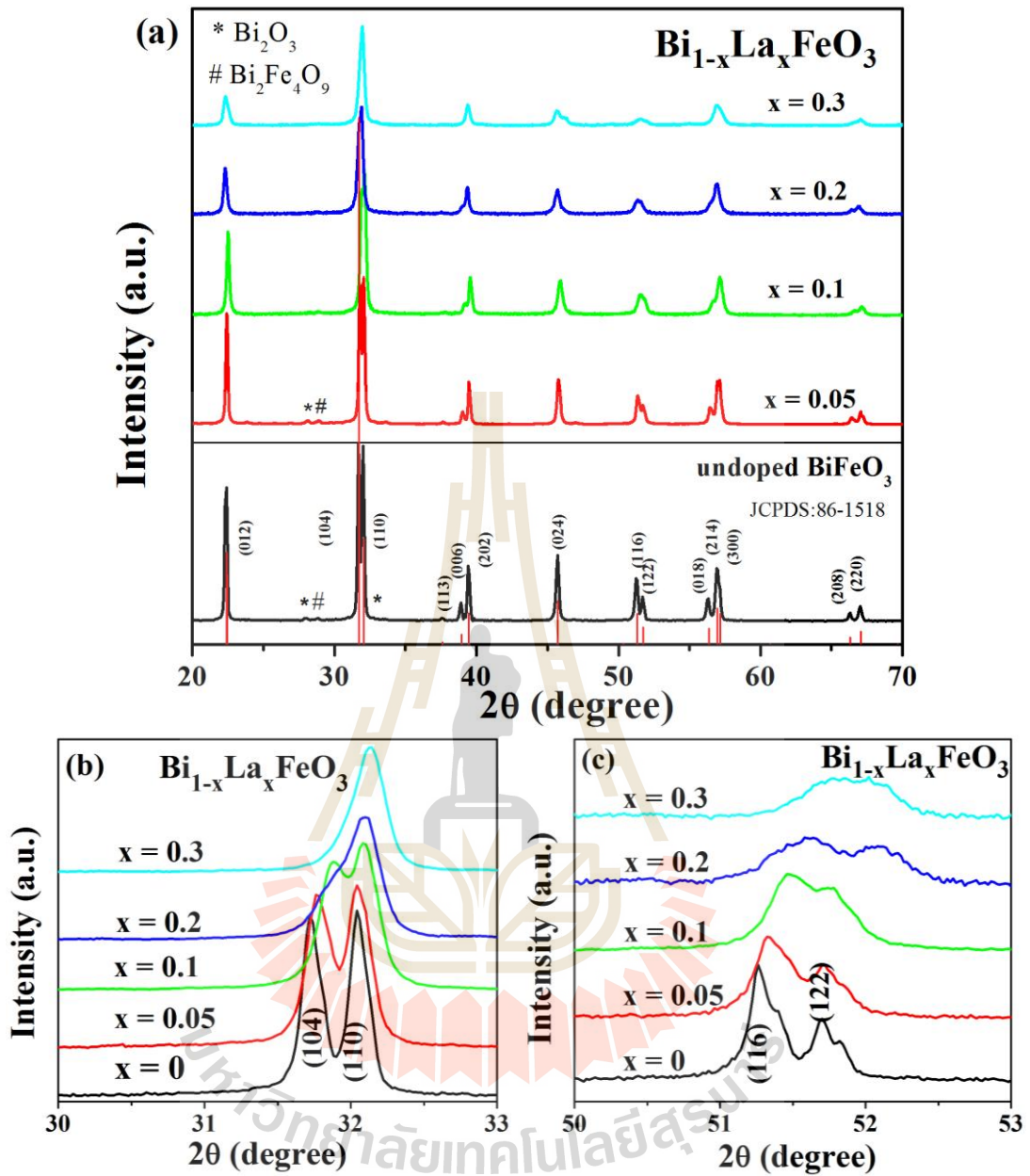


Figure 4.4 The XRD patterns of undoped BiFeO_3 and $\text{Bi}_{1-x}\text{La}_x\text{FeO}_3$ samples with $x = 0.05, 0.1, 0.2, \text{ and } 0.3$, respectively. (b)–(c) Enlarged view of the diffraction peaks in the $2\theta \sim 32^\circ$ and 51° range.

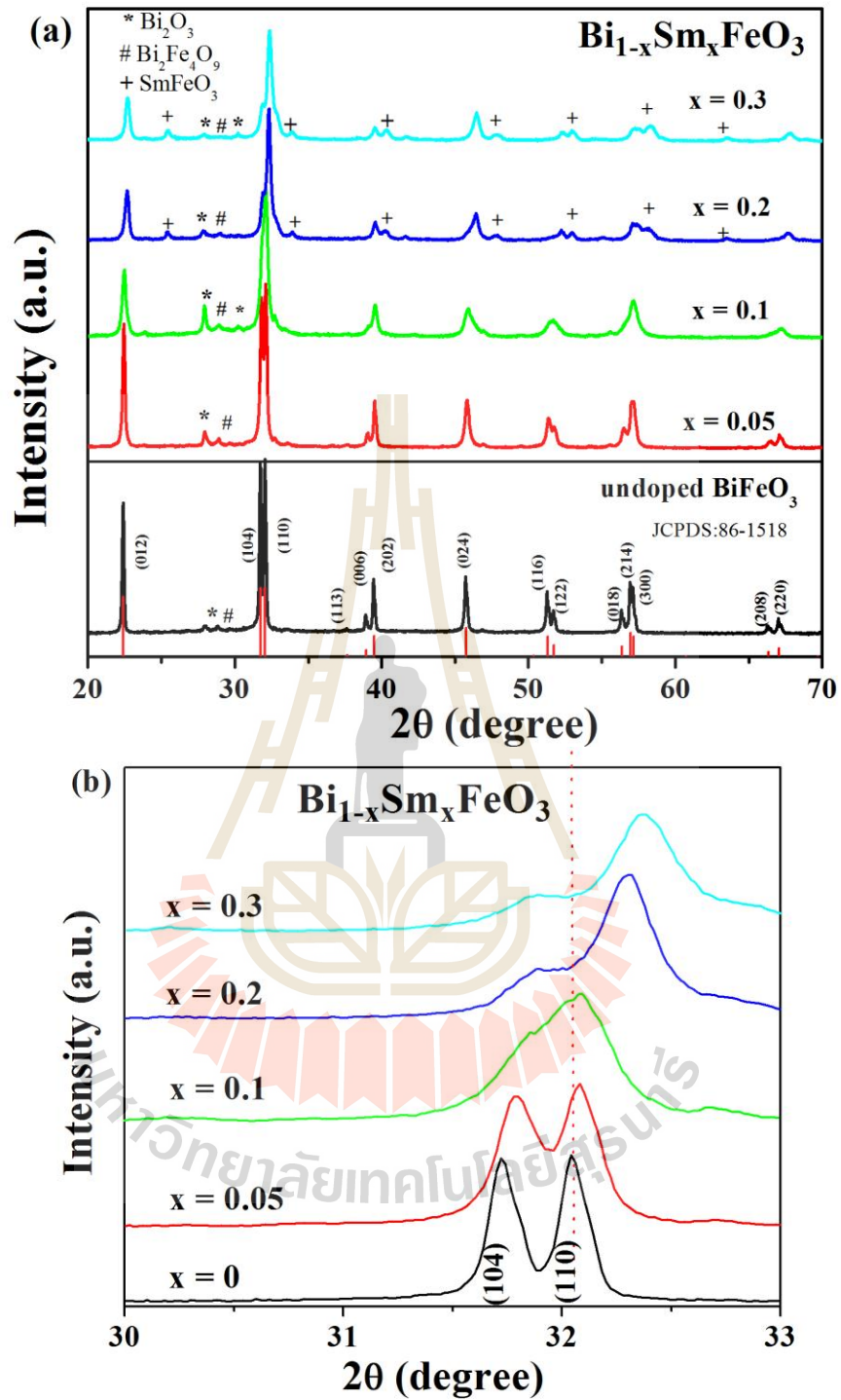


Figure 4.5 The XRD patterns of undoped BiFeO_3 and $\text{Bi}_{1-x}\text{Sm}_x\text{FeO}_3$ samples with $x = 0.05$, 0.1 , 0.2 , and 0.3 , respectively (b) Enlarged view of the diffraction peaks in the $2\theta \sim 32^\circ$.

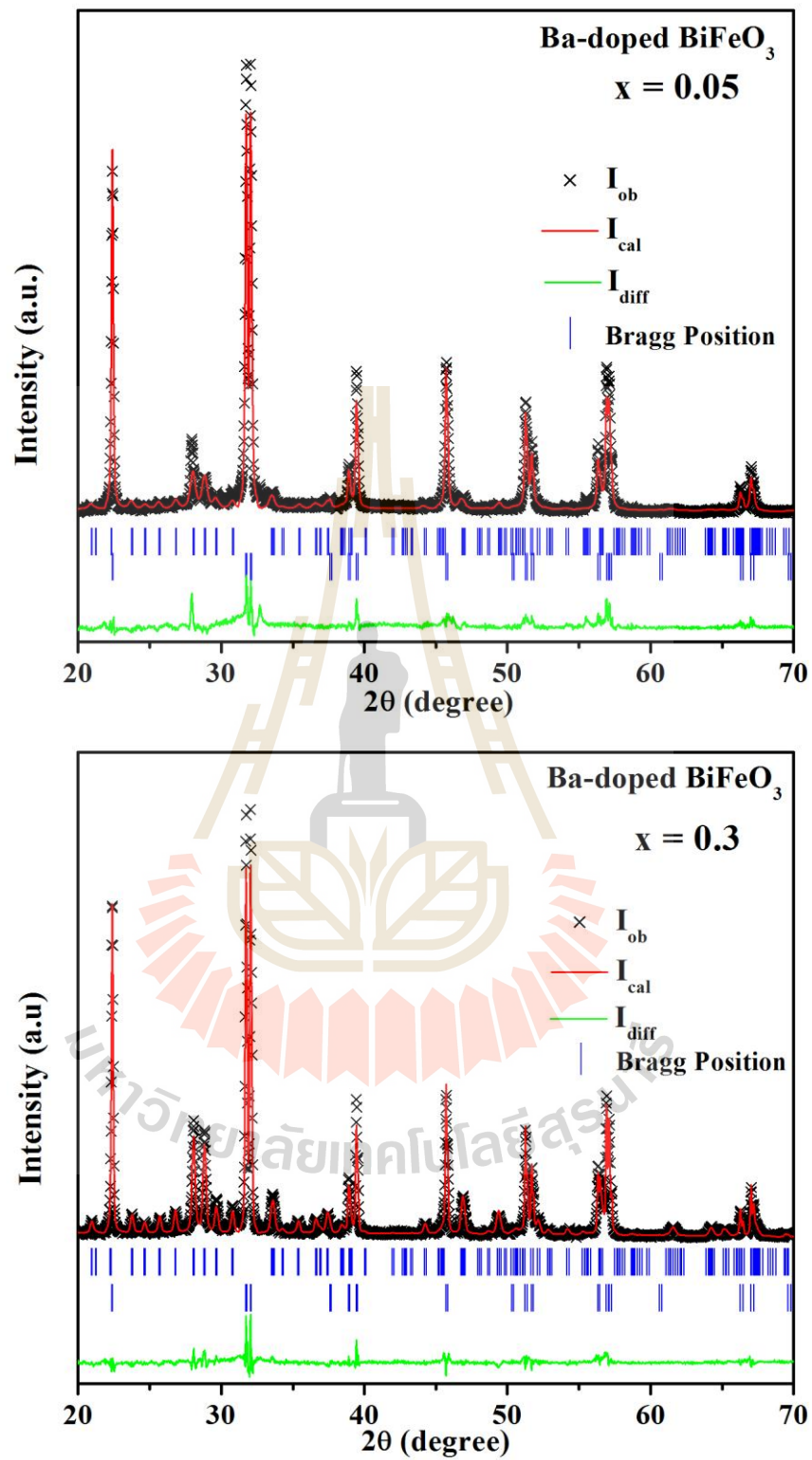


Figure 4.6 Rietveld refinement of XRD data for Bi_{1-x}Ba_xFeO₃ powder (a) $x = 0.05$ and (b) $x = 0.3$.

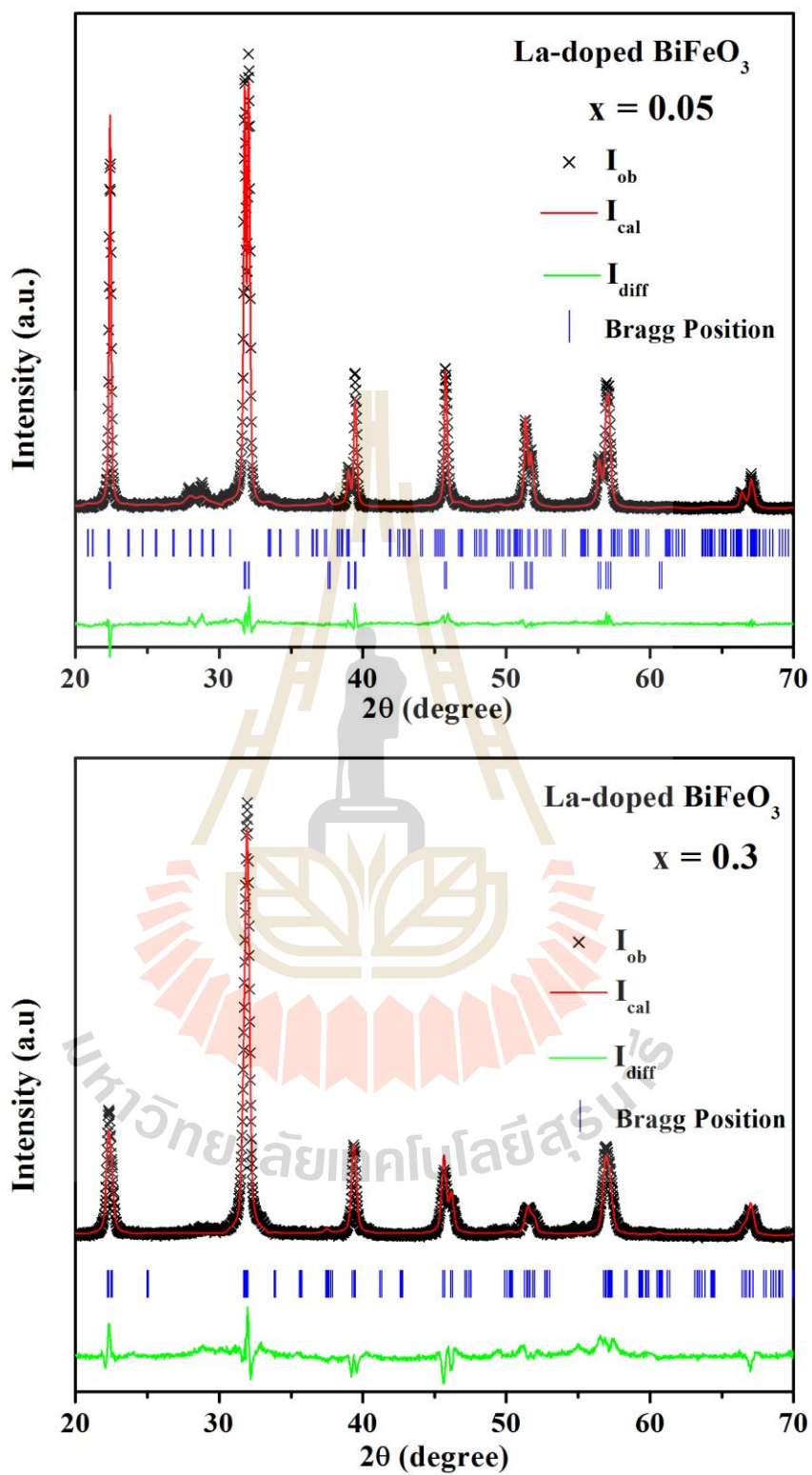


Figure 4.7 Rietveld refinement of XRD data for $\text{Bi}_{1-x}\text{La}_x\text{FeO}_3$ powder (a) $x = 0.05$ and (b) $x = 0.3$.

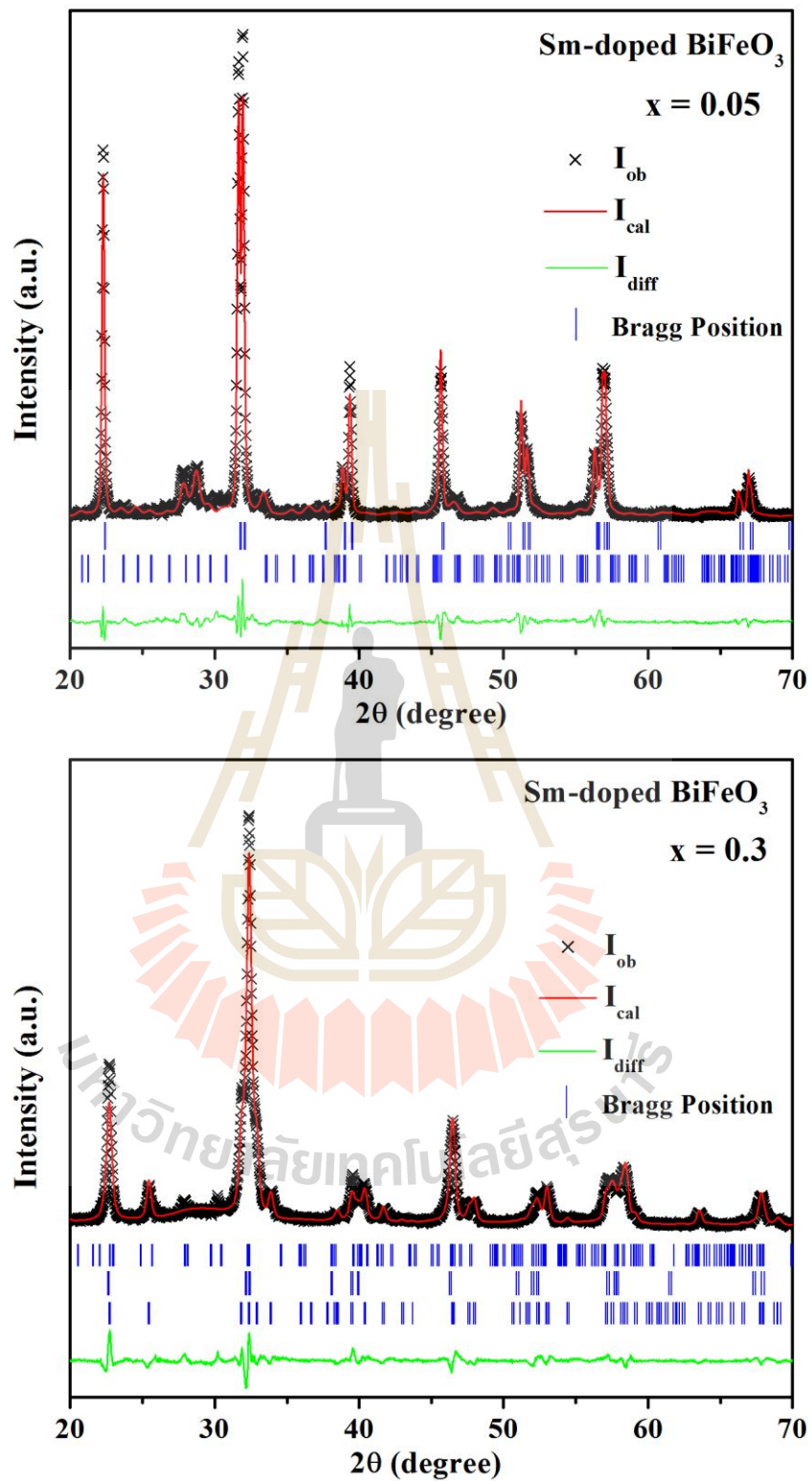


Figure 4.8 Rietveld refinement of XRD data for $\text{Bi}_{1-x}\text{Sm}_x\text{FeO}_3$ powder (a) $x = 0.05$ and (b) $x = 0.3$.

Table 4.1 presents the crystal structure parameters and profile R-factors data derived from the Rietveld refinement program. Within the $\text{Bi}_{1-x}\text{A}_x\text{FeO}_3$ series, it is observed that there are decreases in both “a” and “c” parameters of the unit cells with increases in the ionic radius of the substituted elements which results in reductions in unit cell volume. A similar result was reported for rare earth doped BiFeO_3 (Pradhan *et al.*, 2010; Du *et al.*, 2010; Priyadharsini *et al.*, 2014). This reduction may be due to the replacement of Bi^{3+} by dissimilar ionic radii of Ba^{2+} ($r = 1.42 \text{ \AA}$), La^{3+} ($r = 1.24 \text{ \AA}$), and Sm^{3+} ($r = 1.08 \text{ \AA}$) because all of these ions possess a slightly smaller ionic radii than that of the Bi^{3+} ($r = 1.17 \text{ \AA}$) ions.

The average crystallite size (D) of the samples was calculated from different XRD peaks using the Scherrer equation for all samples as shown in Table 4.2,

$$D = \frac{k\lambda}{\beta \cos \theta} \quad (4.1)$$

where k is a constant ~ 0.89 , λ is the characteristic X-ray wavelength (1.54 \AA), β is the full width at half maxima (in radians) of the most intense peak and θ is Bragg's angle. The average particle size of pure BiFeO_3 was calculated by using Scherrer's equation and the result obtained was $67.15 \pm 1.04 \text{ nm}$. The values obtained were 69.08 ± 1.08 , 67.07 ± 1.78 , 73.83 ± 1.25 , and $75.05 \pm 1.01 \text{ nm}$ for Ba-doped BiFeO_3 with $x = 0.05, 0.1, 0.2,$ and 0.3 , respectively. In the case of La- and Sm-doped BiFeO_3 , the estimated values were 52.78 ± 1.24 , 44.06 ± 1.08 , 27.71 ± 0.78 , and $27.01 \pm 0.9 \text{ nm}$ for La-doped and 55.02 ± 1.46 , 34.33 ± 1.09 , 19.9 ± 0.88 , and $16.41 \pm 1.25 \text{ nm}$ for Sm-substituted BiFeO_3 , respectively. It was found that the average crystal size of the nanopowders decreases as the dopant concentration increases. The reason for the reduction may be attributed to the fact that the dopant ions inhibited crystal growth

caused by ionic radii mismatches between dopant ions in the Bi^{3+} site. It can be seen that the crystallite size of nanopowders obtained from the TEM images is slightly different from that obtained from the XRD calculations. The average crystallite size calculated by the XRD analysis is usually lower than the particle size observed by TEM. These results from the agglomeration of the particles are due to the high surface energy of agglomerated nanoparticles. Moreover, the grains comprise the subgrains which are separated by low-angle grain boundaries. The crystallite size calculated from XRD data is equal to the average size of the domains which scatter X-rays coherently (Besmel *et al.*, 2011; Shokrollahi, 2013).

Table 4.2 Summary of crystallite size of pure BiFeO_3 , Ba-, La-, and Sm-doped BiFeO_3 nanopowders calcined at 600 °C for 3 h.

Doping level	Crystallite size (nm)		
	Ba	La	Sm
x = 0	67.15±1.04	67.15±1.04	67.15±1.04
x = 0.05	69.08±1.08	52.78±1.24	55.02±1.46
x = 0.1	67.07±1.78	44.06±1.08	34.33±1.09
x = 0.2	73.83±1.25	27.71±0.78	19.90±0.88
x = 0.3	75.05±1.01	27.01±0.9	16.41±1.25

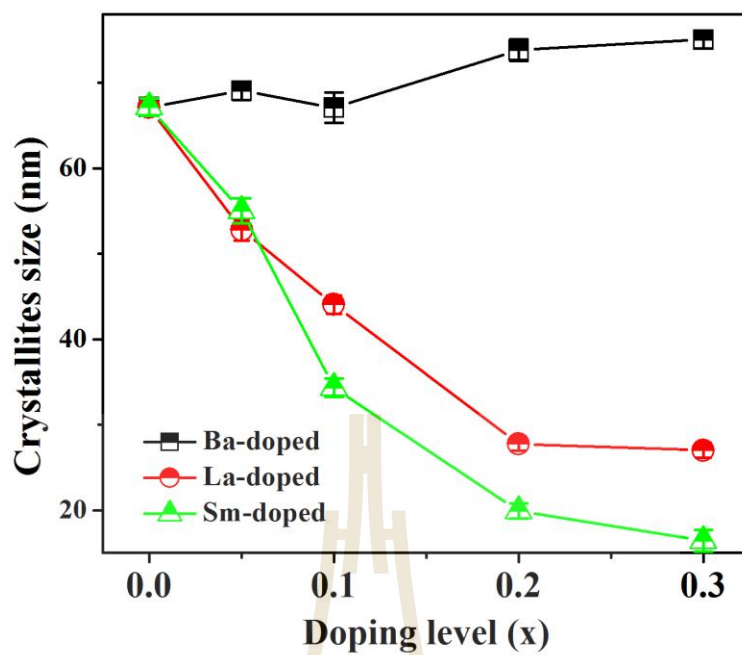


Figure 4.9 An average crystallite size of undoped BiFeO_3 , Ba-, La-, and Sm-doped samples calcined at 600°C for 3 h.

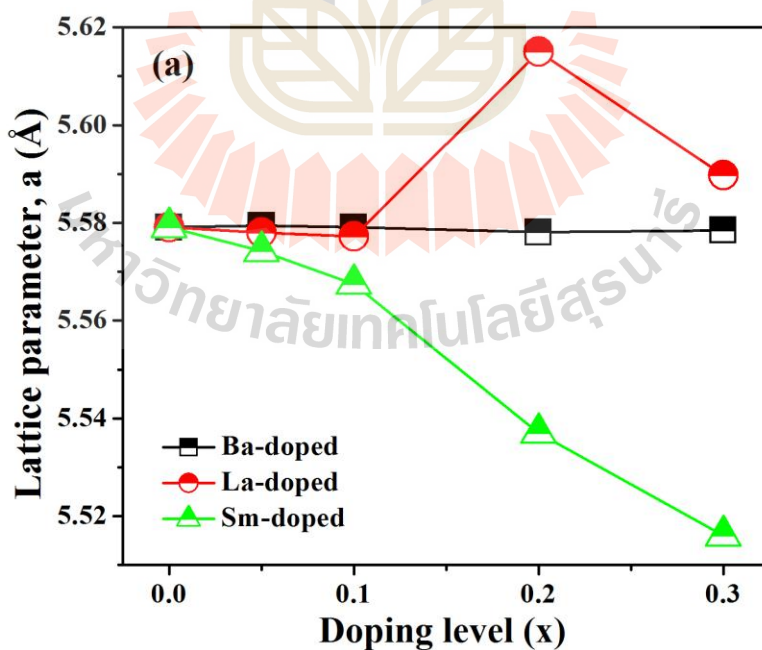


Figure 4.10 Lattice constant of undoped BiFeO_3 sample, (a) a, (b) c parameter, and (c) volume of Ba-, La-, and Sm-doped BiFeO_3 nanopowders.

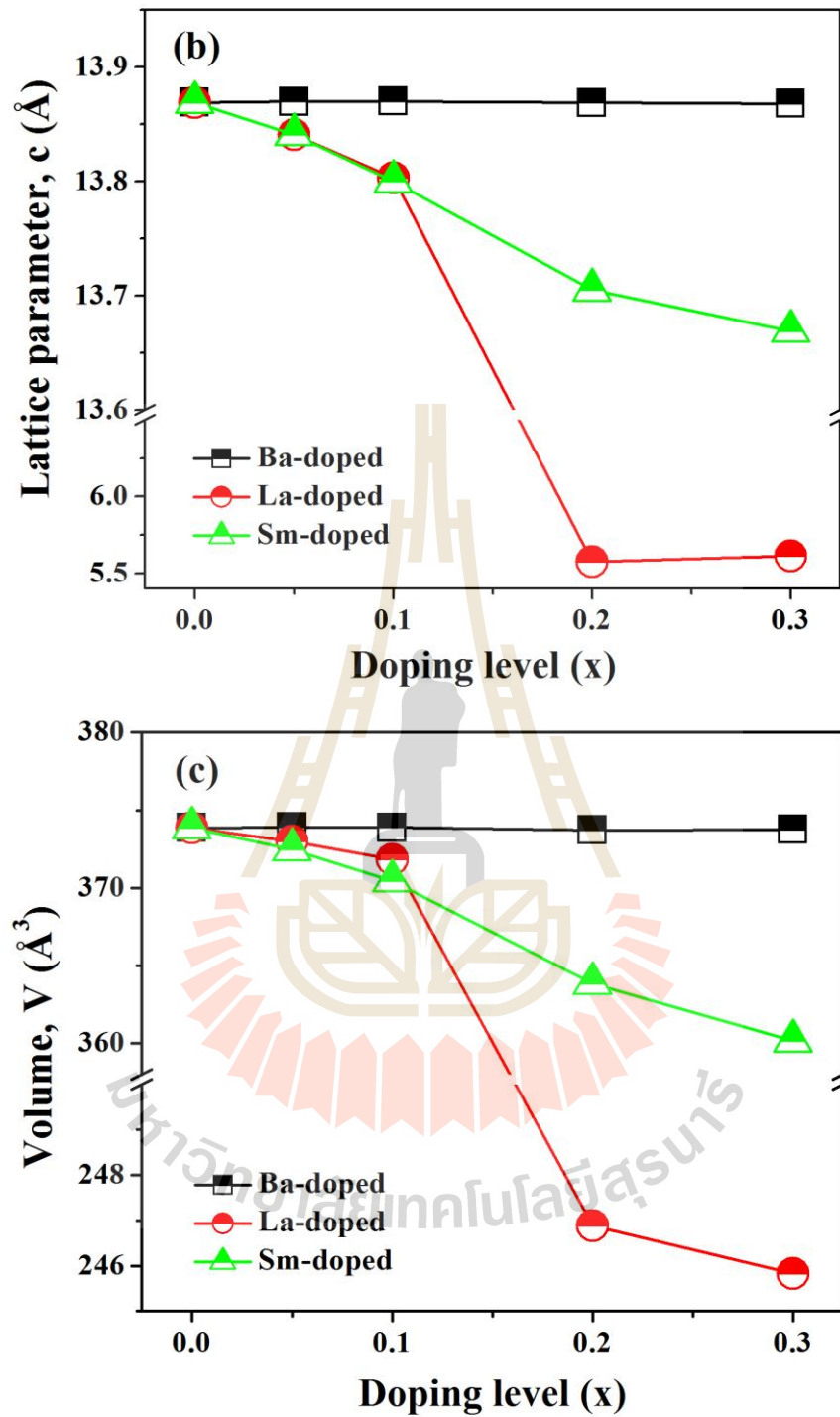


Figure 4.10 Lattice constant of undoped BiFeO₃ sample, (a) a, (b) c parameter, and (c) volume of Ba-, La-, and Sm-doped BiFeO₃ nanopowders (Continued).

4.1.3 X-ray absorption spectroscopy study of the Fe K-edge in $\text{Bi}_{1-x}\text{A}_x\text{FeO}_3$ (A = La, Sm, and Ba) nanopowders

In order to characterize the oxidation states of Fe ion BiFeO_3 , normalized XANES spectra at room temperature were measured at Fe K-edge. The electronic structures of undoped and Ba-, La-, and Sm-doped BiFeO_3 samples have been characterized by XANES in transmission mode. XANES is a fingerprint of the empty electronic structure for the purpose of probing elements. The normalized Fe K-edge spectra and their corresponding first derivatives for $\text{Bi}_{1-x}\text{A}_x\text{FeO}_3$ (A = La, Sm, and Ba) nanopowders at room temperature are shown in Figure 4.11(a)–(f). The oxidation states of Fe in BiFeO_3 -based nanopowders are compared with the spectra of Fe_2O_3 and Fe_3O_4 standard samples. As seen in Figure 4.11, the XANES spectra of pure BiFeO_3 calcined samples measured at Fe K-edge are very similar to Fe_2O_3 , indicating that the oxidation number of Fe in this sample corresponds to Fe^{3+} . Even when Bi is substituted by La, Sm, and Ba ions, there is no noticeable difference in the position of the absorption edge among the prepared samples with changes in the doping content. The excited energy (E_0) for all the samples is around 7124 eV which is determined from the first derivative of the absorption edge, confirming that the oxidation state of Fe^{3+} does not change into Fe^{2+} as the dopant concentration increases. These E_0 values are close to the E_0 value of standard spectra Fe_2O_3 which is characteristic of Fe^{3+} and related to the 1s to 4s electrical transitions. Moreover, the integral amplitude of the pre-edge peaks which are a sign of dipole forbidden transitions (Vedrinskii *et al.*, 1998; Asokan *et al.*, 2001) are quite similar at around 7114 eV. The weak pre-edge (denoted as A) appears at around ~5 eV below the major absorption level that is attributed to the 1s to 3d electric dipole-forbidden

transitions. This weak pre-edge feature is associated with 4p mixing with the 3d orbital configuration around the Fe site. Because of a partially occupied p-orbital character by the 3d-4p hybridization, the intensity of this forbidden peak is not strictly zero. The observation of the post-edge peak (peak C) in all the doped samples can be seen which is attributed to the 1s to 4p dipole-allowed transitions (empty orbital 4p). On the other hand, peak B is known to be a shoulder peak, which corresponds to a partial transition from the 2p electrons in the oxygen 2p orbital to the unoccupied Fe 3d orbital, which is known as the ligand-to-metal charge transfer process. The most pronounced difference in the Sm-doped BiFeO₃ samples is the relative peak position of peak B. It is seen that with an increase in the concentration of the Sm samples are quite different from the La- and Ba-doped samples as they show broader shoulder peaks (B) and disappear as compared to pure BiFeO₃ samples. This result might suggest that there is no observed charge transfer in the high doping content of Sm ions.

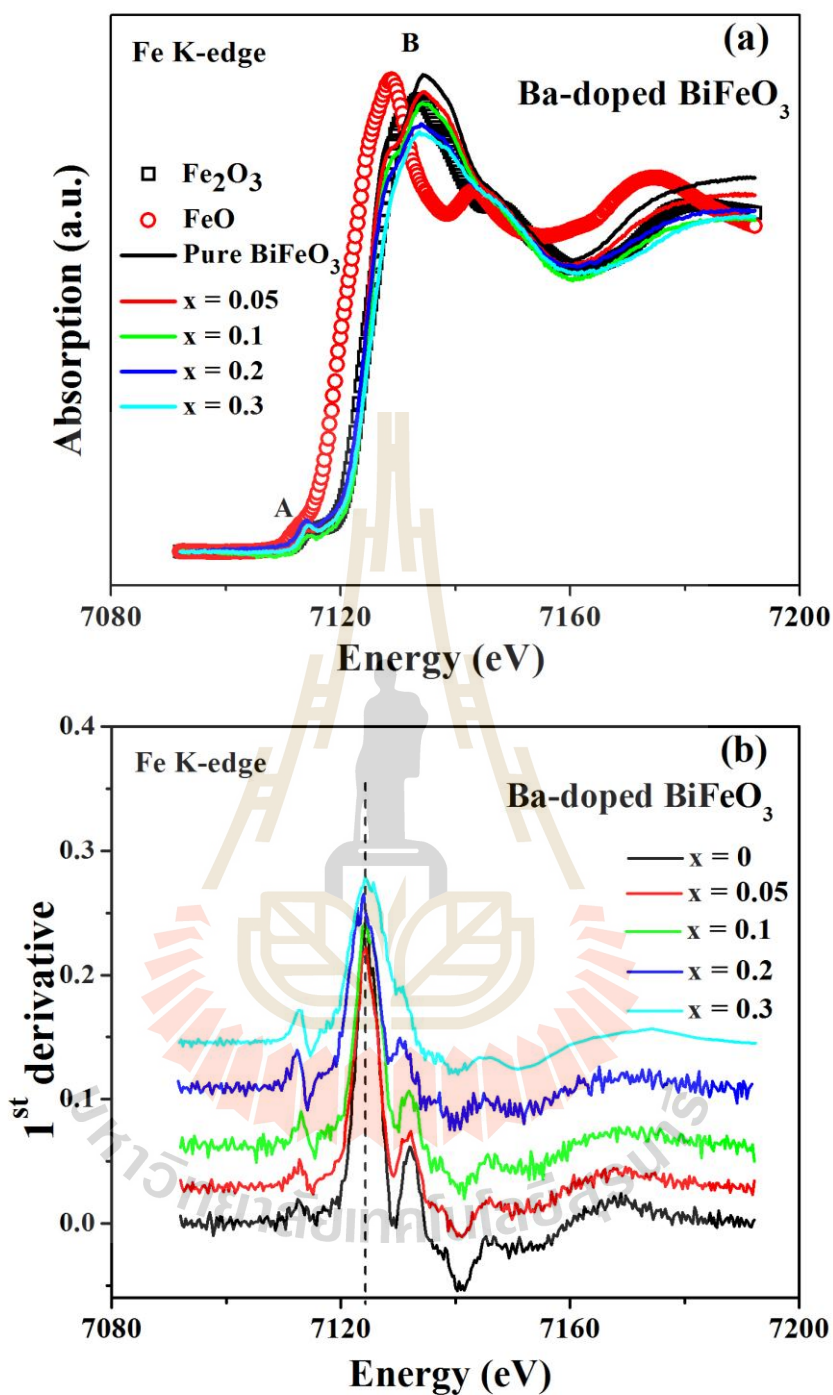


Figure 4.11 Fe K-edge of XANES for Ba-doped BiFeO₃ (x = 0, 0.05, 0.1, 0.2, and 0.3) samples, Fe₂O₃ and Fe₃O₄ are reference materials for Fe²⁺ and Fe³⁺, the first derivative of Fe K-edge XANES spectrum in BiFeO₃ (b).

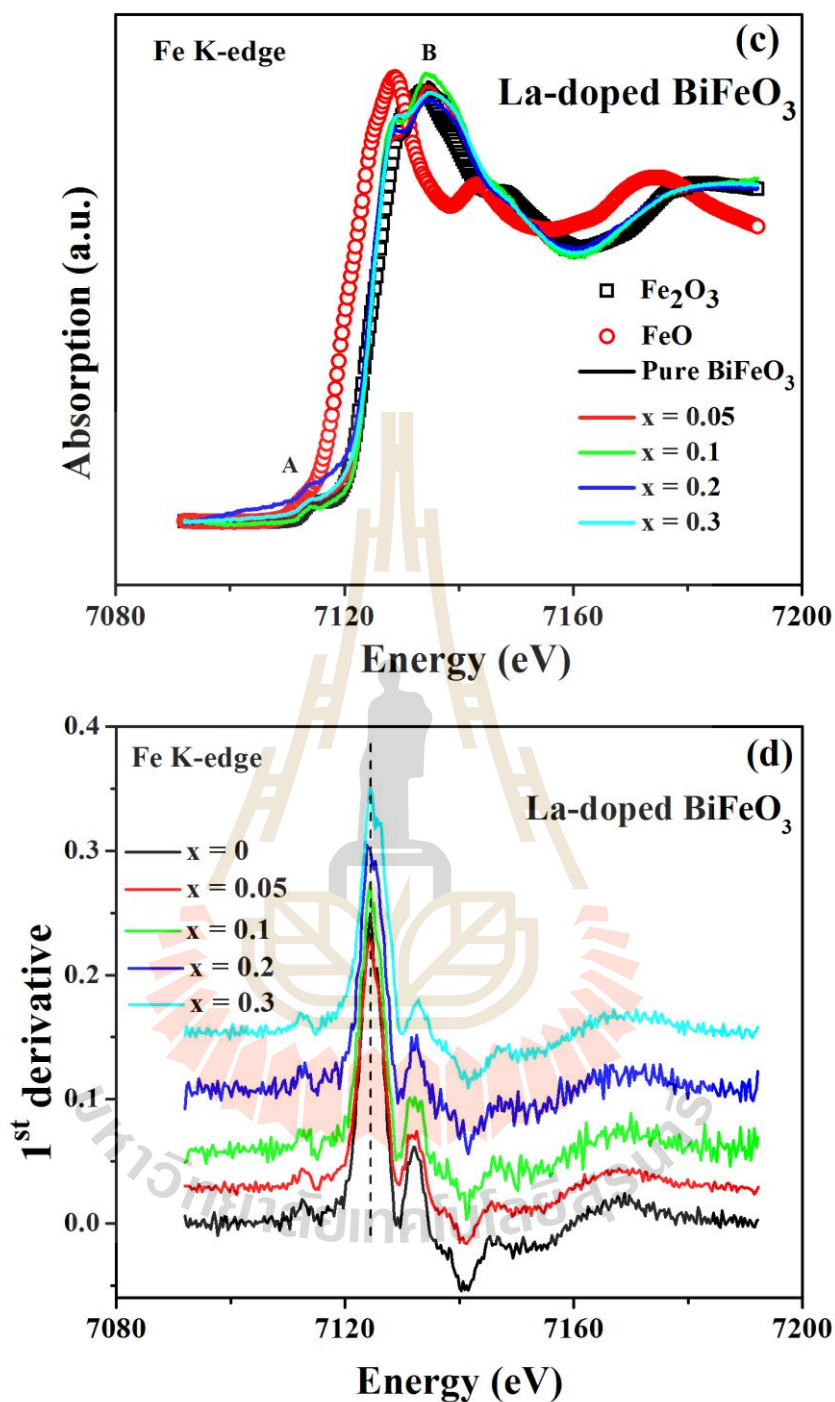


Figure 4.11 (c) Fe K-edge of XANES for La-doped BiFeO₃ (x = 0, 0.05, 0.1, 0.2, and 0.3) samples, Fe₂O₃ and Fe₃O₄ are reference materials for Fe²⁺ and Fe³⁺, the first derivative of Fe K-edge XANES spectrum in BiFeO₃ (d) (Continued).

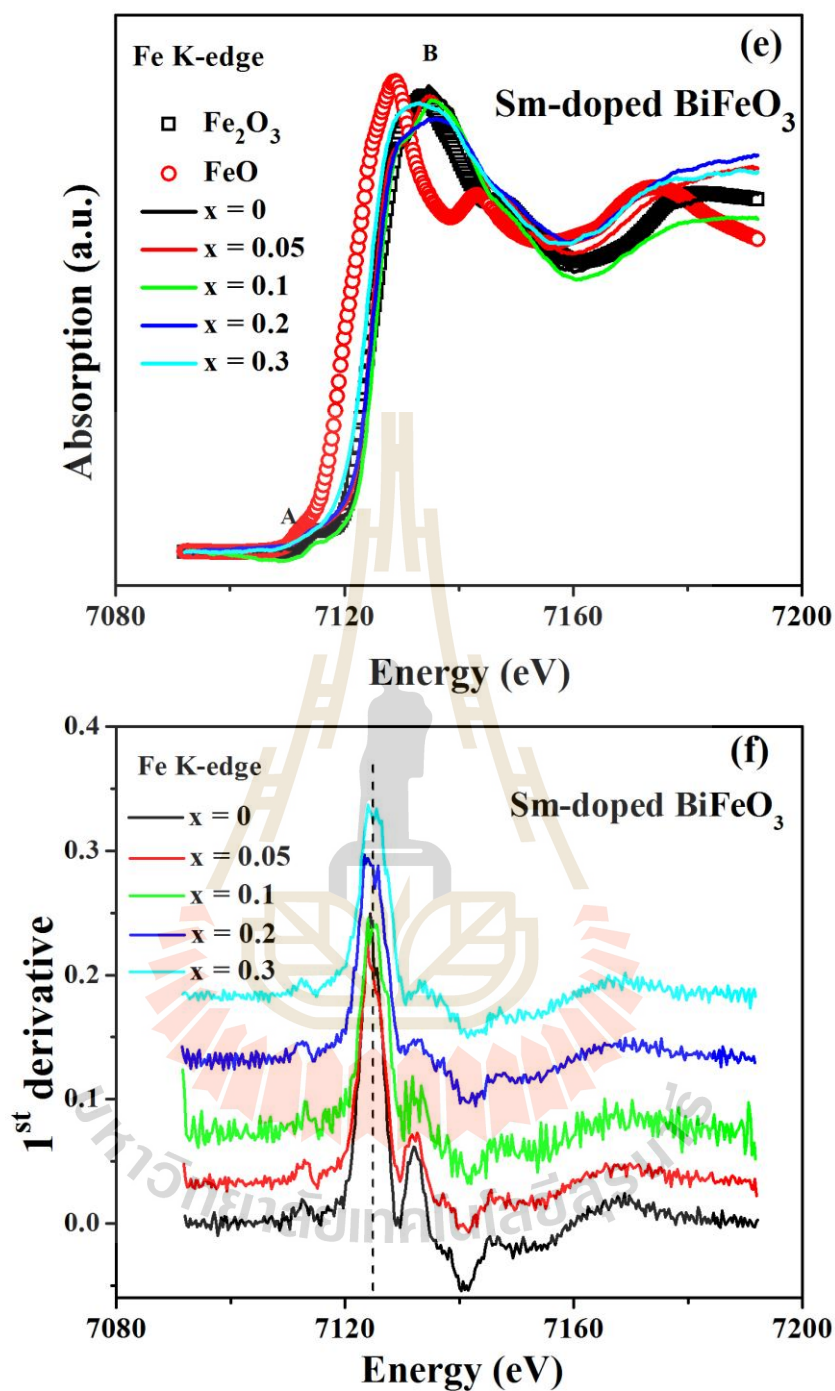


Figure 4.11 (e) Fe K-edge of XANES for Sm-doped BiFeO₃ (x = 0, 0.05, 0.1, 0.2, and 0.3) samples, Fe₂O₃ and Fe₃O₄ are reference materials for Fe²⁺ and Fe³⁺, the first derivative of Fe K-edge XANES spectrum in BiFeO₃ (f) (Continued).

4.1.4 Fourier transform infrared spectrometer (FTIR)

To study the metal bonds in the calcined powders a Fourier transform infrared (FTIR) spectrometer was used. The room temperature FTIR spectra of undoped BiFeO₃ and BiFeO₃ doped with different concentrations of doping ions (0.05, 0.1, 0.2, and 0.3) samples have been shown in Figure 4.12 in wavenumbers of 400–4000 cm⁻¹. The pure BiFeO₃ spectrum shows strong absorption peaks in wavenumbers at 432 and 531 cm⁻¹ which indicate the typical band characteristics of the overlapping of FeO₆ metal oxygen stretching and bending vibrations and BiO₆ octahedral structure (Kaur *et al.*, 2015). These two peaks are confirmed as the characteristics of FeO₆ bonds in the octahedral group in the perovskite structural units. The bands at around 811, 1045, and 1392 cm⁻¹ are due to the presence of traces of nitrate ion in the sample (Srivastav and S Gajbhiye, 2012; Wang *et al.*, 2013). The intense peak at 1392 cm⁻¹ corresponds to traces of carbonates C=O of coordinated oxalates which overlap with the intense nitrate band at around 1490 cm⁻¹. However, an absorption peak around 1632 cm⁻¹ associated with the stretching vibrations of free O–H group, which is attributable to the absorption of water molecules absorbed from the moisture at the surface when the sample was in contact with the environment. The broad low intensity band with the maximum around 3000–3400 cm⁻¹ has been assigned to the antisymmetric stretching of H₂O water from ambient moisture due to the contact of the sample with the environment.

The FTIR spectra for Ba-doped BiFeO₃ samples show two strong peaks around 443 and 530 cm⁻¹. The former was assigned to O–Fe–O bending and Fe–O stretching of the FeO₆ vibration group that is connected to the Bi ion, which confirms that the FeO₆ octahedral in the perovskite structure has been formed. The formation of

a perovskite structure can be confirmed by the presence of a metal–oxide structure in the compound (Lee *et al.*, 2005; Biasotto *et al.*, 2011). These band positions of Ba–doped BiFeO₃ with different concentrations of Ba ions are found to be in agreement with the characteristic infrared absorption bands of pure BiFeO₃. Furthermore, with the increase in Ba concentration, the peaks slightly shift towards the lower wavenumber which can be assigned to possible two reasons. Firstly, the decrease in particle size with increased Ba doping content results in more surface and grain boundaries (Reddy *et al.*, 2012). Secondly, the lattice strain relaxes with the presence of an orthorhombic crystal symmetry fraction in the samples (Kaur *et al.*, 2015), thus the results obtained are consistent with the quantitative crystallographic phase of the Rietveld analysis.

The FTIR spectra of calcined Bi_{1-x}La_xFeO₃ powders are represented in Figure 4.13(b). A comparative of the FTIR spectra of the parent BiFeO₃ and La–doped samples show that the broad band around 3000–3600 cm⁻¹ is due to water molecule vibrations flatten when La is increased. This flattening of the bands is the result of the effect of substituted ions that result in changes in the stretching and bending of the metal oxide bonds. As La doping concentration increases, it is found that the strong peaks at 432 and 811 cm⁻¹ become very weak and even disappear indicating the deformation of Fe–O stretching and bending vibrations and the removal of nitrates. Pure BiFeO₃ powder indicates a Fe–O absorption band close to 811 cm⁻¹ due to its highly crystalline BiFeO₃ phase. The presence of slightly shifted peaks towards higher wavenumbers in the FTIR spectra for Sm–doped BiFeO₃ samples shows the same trend as the parent sample.

The FTIR absorption spectra of pure and Sm-doped BiFeO₃ samples at room temperature are exhibited in Figure 4.12. It is clear that all the doped samples indicate slight differences in the spectra. It can be observed that the wide range of spectra (3000–3500 cm⁻¹) disappears with substituting the content of Sm doping, while other regions are similar to those observed in the FTIR spectra of the parent compound BiFeO₃. This wide range around 3000–3500 cm⁻¹ corresponds to the absorption of water and carbon dioxide from the environment. It can also be observed from the FTIR spectra of the Bi_{1-x}Ba_xFeO₃ system that an absorption band in the whole wave number range is similar to that observed in the Sm-doped BiFeO₃. These results are confirmed by the formation of a metal–oxygen band around at 400–600 cm⁻¹ in the perovskite structure. As shown in Figure 4.12(c), the FTIR spectra of Sm-doped samples which are found in the band position peaks of these samples do not change significantly with increases of Sm ions compared to the changes in the pure BiFeO₃ band.

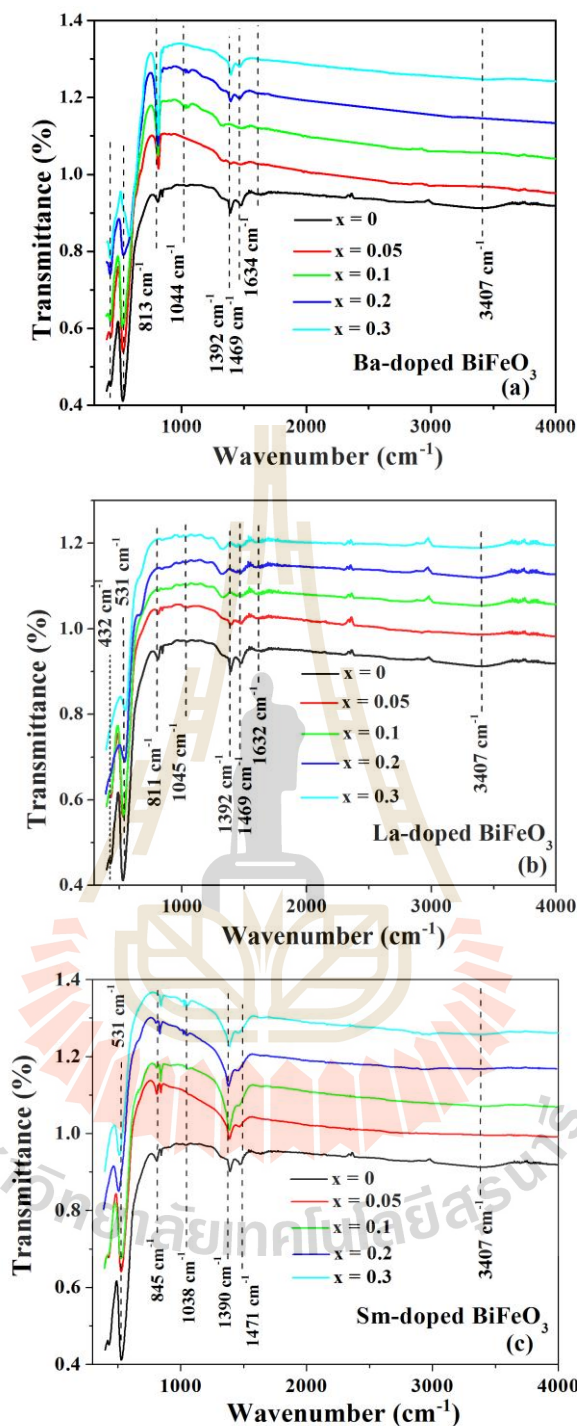


Figure 4.12 FTIR spectra for (a) $\text{Bi}_{1-x}\text{Ba}_x\text{FeO}_3$, (b), $\text{Bi}_{1-x}\text{La}_x\text{FeO}_3$ and (c) $\text{Bi}_{1-x}\text{Sm}_x\text{FeO}_3$ powders calcined at 600 °C for 3 h as a function of Ba, La, and Sm content with $x = 0.05, 0.1, 0.2,$ and 0.3 .

4.2 Optical properties (UV–Vis)

Generally, the optical absorption performance of semiconductors is relevant to the electronic structure features and their band gaps (Thakur *et al.*, 2014). The optical band gap is an important factor in understanding the optoelectric and photocatalytic properties of semiconductors. In optical absorption, the transition of charge carriers between different energy states occurs which results in an absorption edge. The optical properties of BiFeO₃ samples with different dopant ions and doping proportions were studied by measuring their UV–vis diffuse reflectance absorption spectra. The UV–Vis absorption spectra of all samples are shown in Figure 4.13. It is observed that the pure BiFeO₃ and doped samples can absorb a considerable amount of visible light tested in a range of 500 to 675 nm suggesting their potential application as photocatalytic performance under visible light irradiation (Gao *et al.*, 2014). Pure BiFeO₃ nanoparticles exhibit the absorption peaks at around 490–700 nm which shift towards a higher wavelength, for La–, Ba–, and Sm–substituted BiFeO₃ in the Bi site. Figure 4.13(a) shows the UV–Vis diffuse reflection spectrum of Bi_{1-x}Ba_xFeO₃ powders. There are three absorption edges of the undoped BiFeO₃ and Ba–doped BiFeO₃ samples. It can be observed from the figure that the two bands around 493 and 692 nm are the result of the crystal field transition and the other one is around 284 nm which is due to metal to metal transition (Gupta *et al.*, 2002). The absorption edges of Bi_{1-x}Ba_xFeO₃ with x = 0.05, 0.1, 0.2, and 0.3 are found to be 589, 601, 603, and 592 nm, respectively. According to the optical absorption results, the absorption edges of the Ba–doped BiFeO₃ powders are higher than that of the pure BiFeO₃ (~575 nm) sample and it slightly increases with increases in Ba the doping levels. It should be noted that in the case of La–doped in BiFeO₃, the absorption band

edges increase to 510–703 nm as compared to the absorption peaks of pure BiFeO₃. The absorption spectrum shows that the present samples can absorb visible light indicating their potential application as visible–light photocatalysts. As shown in Figure 4.13(b), the absorption edges of the Bi_{1-x}Ba_xFeO₃ samples are about 577.5, 577.6, 586.2, and 674.2 nm for x = 0.05, 0.1, 0.2, and 0.3 samples, respectively. For Sm–doped samples, we observed the absorption edges at around 591, 601, 658, and 666 nm for x = 0.05, 0.1, 0.2, and 0.3 samples, respectively. It can be seen that all of the absorption edges of the doped samples in BiFeO₃, increase with increases in dopant concentrations. The broadband in the UV spectra range of all samples can be observed (Figure 4.13) at 200 to 350 nm which can be attributed to the result of overlapping of electronic transitions, possibly due to oxygen vacancy and a minority channel dipole–allowed p–d charge transfer from 2p in oxygen to the Fe 3d orbital. The band centered at 1.8 eV is related to on–site d–d transitions due to Fe³⁺ ions in distorted octahedral coordination FeO₆ symmetry because of the crystal ligand field. This band is ascribed to the ${}^6A_{1g} \rightarrow {}^4T_{2g}$ excitation process and this excitation is a forbidden transition since it changes the total spin of Fe³⁺ from S = 5/2 to S = 3/2. Above 2 eV, the absorption spectra exhibit a weak band centered at 2.5 eV which can be assigned to a dipole–forbidden p–d charge transfer transition $t_{1g} \rightarrow t_{2g}$ in the FeO₆ octahedral. Two bands located at 3.2 and 4.5 eV are defined as dipole allowed p–d charge transfer (C–T) features in the octahedral center. Interestingly, a little shift in the d–d and C–T excitation bands were observed which clearly suggests that doping increases the internal chemical pressure as a result of changes in the unit cells (Arora and Kumar, 2015; Arora and Kumar, 2014).

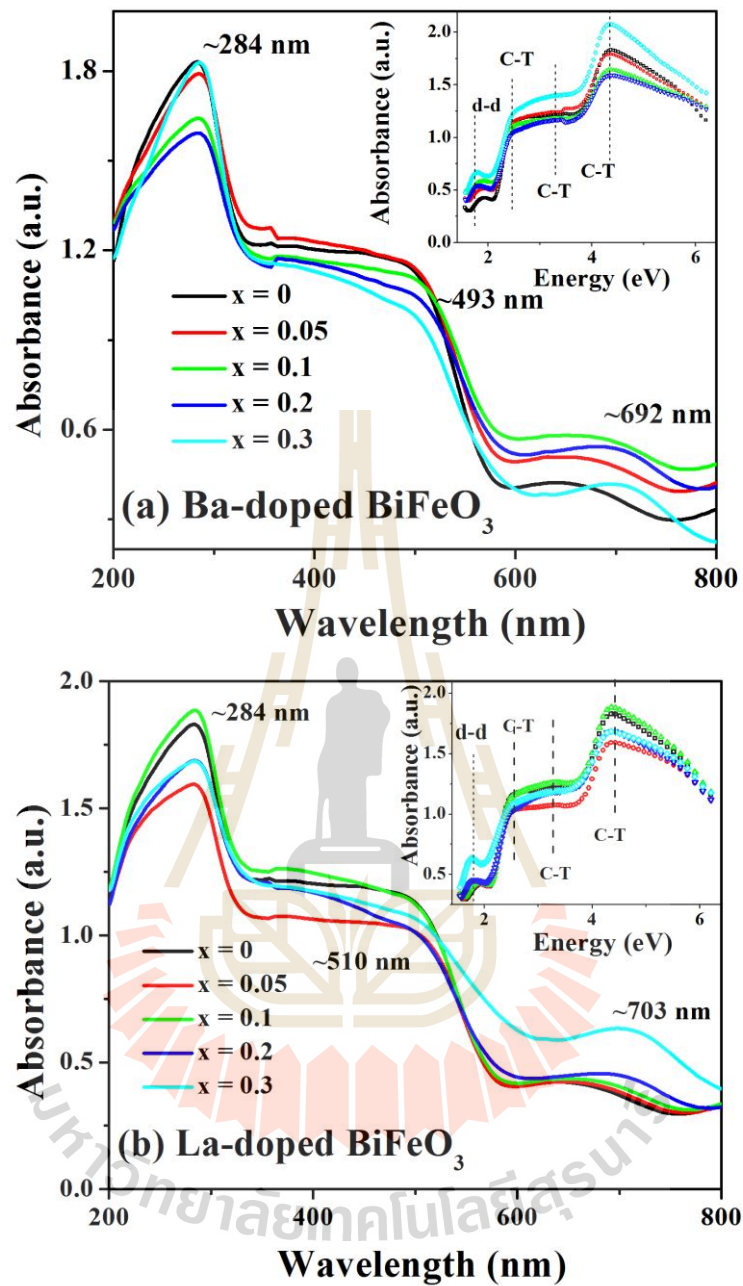


Figure 4.13 Room temperature optical absorbance spectra of undoped BiFeO_3 and doped BiFeO_3 nanoparticles; (a) Ba-, (b) La-, and (c) Sm-doped BiFeO_3 , respectively and (d) Schematic representation of the crystal-field effect lowering the symmetry from octahedral O_h to rhombohedral C_{3v} .

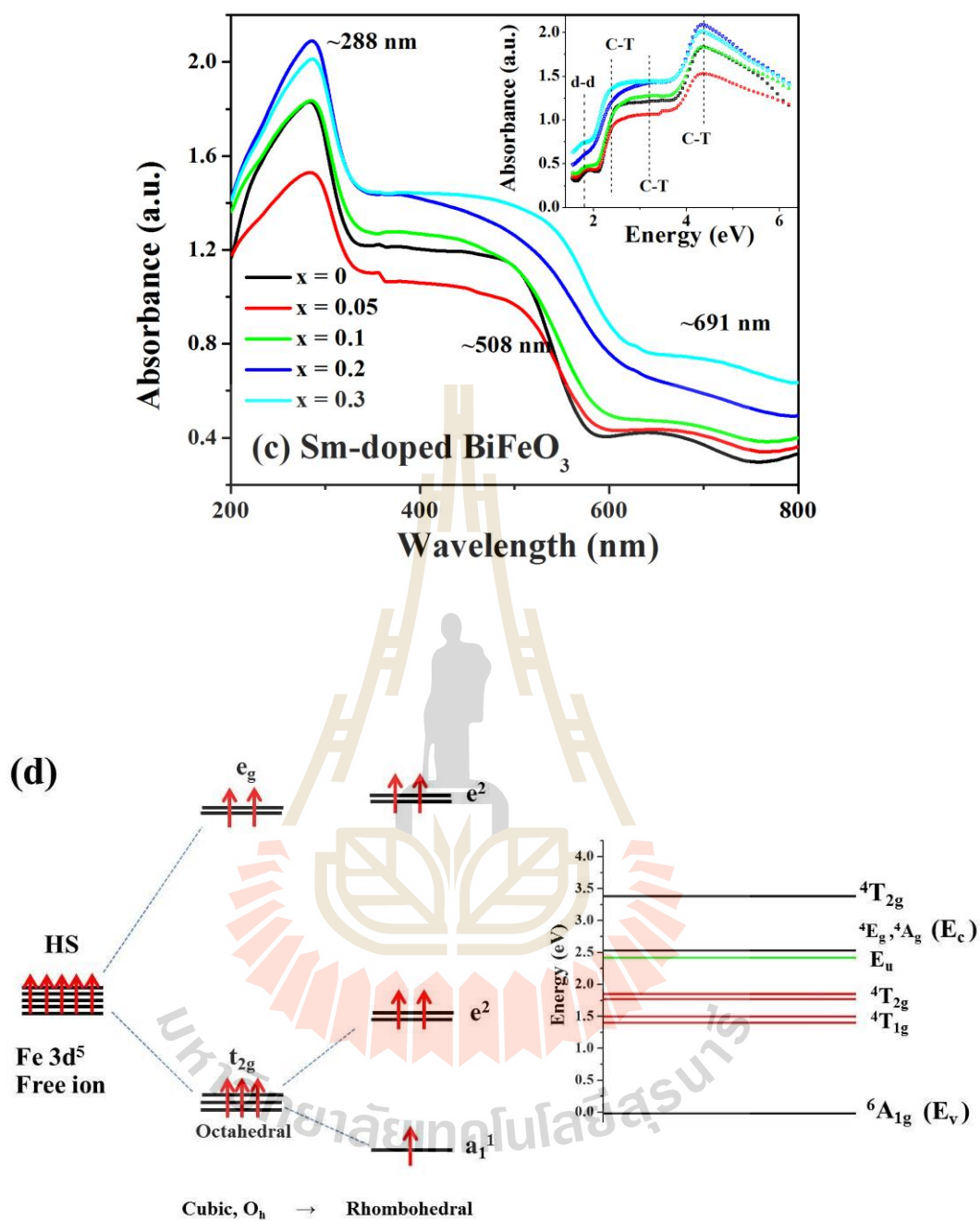


Figure 4.13 Room temperature optical absorbance spectra of undoped BiFeO_3 and doped BiFeO_3 nanoparticles. (a) Ba-, (b) La-, and (c) Sm-doped BiFeO_3 , respectively and (d) Schematic representation of the crystal-field effect lowering the symmetry from octahedral O_h to rhombohedral C_{3v} (Continued).

According to the theory of optical absorption, properties are related to their electronic structure and have an important role in determining optical band gaps. The optical band gap can be determined from the plot of the Kubelka–Munk function $(\alpha h\nu)^n$ vs. photon energy $A(h\nu - E_g)$ where α, h, ν, E_g and A are the absorption coefficient, the Planck constant, the light frequency, the band gap, and A constant, respectively (Muneeswaran *et al.*, 2015; Liu *et al.*, 2010). Thus, E_g values are calculated by the linear extrapolation portion of the plots to $(\alpha h\nu)^2 = 0$. The corresponding optical absorption edges in the Kubelka–Munk's plot for $\text{Bi}_{1-x}\text{A}_x\text{FeO}_3$ ($\text{A} = \text{La}, \text{Ba}, \text{Sm}$) samples with $x = 0, 0.05, 0.1, 0.2,$ and 0.3 and the band gap are determined by extrapolating the linear approach as illustrated in Figure 4.14. From Figure 4.14, it can be seen that the optical band gap of the parent BiFeO_3 compounds is estimated to be 2.12 eV which is quite comparable with current reports (Liu and Zuo, 2012). The optical band gap values obtained from the doped compounds are about 2.10–1.93, 2.09–2.03, and 2.05–1.91 eV for La-, Ba-, and Sm-doped BiFeO_3 , respectively. The optical band gap values for all rare earth substitutions in the BiFeO_3 nanoparticles were decreased gradually with increases in the doping content of the ions from $x = 0.0$ to 0.3 , which is in accordance with other reports (Arora and Kumar, 2015; Kumar *et al.*, 2010; Sakar *et al.*, 2015). The decreases in the optical band gaps of the substituted samples were found to be red shifted with the increase in doping concentration which may be attributed to increased internal chemical pressure (Arora and Kumar, 2014). The following effects will be discussed here to analyze the reason for the variations in band gap energy. Generally, the band gap is strongly dependent on the particle size and the existence of defect levels induction between the

conduction band and the valence band, especially when energy levels are close to the conduction band. Defects such as oxygen vacancy can reduce the band gap in BiFeO_3 , since these oxygen vacancies are reportedly lower than the adjacent Fe 3d energy levels, leading to the sub-band gap defect states as a kind of donor level. In BiFeO_3 , the formation of optical band gap structures is mainly comprised of hybridization between the Fe 3d and O 2p energy state levels. As dopant substitution increases, the concentration of oxygen vacancy is subsequently increased which could raise the defect-induced energy band gap, thus narrowing the distance between the conduction and the oxygen vacancy donor band which is shrinking as shown in Figure 4.14(d). Moreover, the change in the band gap could be attributed to the distortion in the FeO_6 octahedral and higher forced symmetry to decrease the band gap due to the doping of ions. The increase of the Fe–O–Fe angle (toward 180 degrees) is expected to enhance the bandwidth, especially of the occupied and unoccupied bands, thereby reducing the band gap. Another possible reason is that the effective interactions between the rare earth ions and the energy levels of BiFeO_3 can significantly modify its optical band gap. Hence, the variations in the band gap energy could be ascribed to the formation of new electronic states of rare earth ions located at the bottom of the conduction band. In the schematic diagram, the strong hybridization of O 2p, Bi 6p and rare earth 4f states located at the top of the valence band and the bottom of the conduction band are located by Fe 3d states. The presence of Re ions in the 4f shell have become closer to the lower bottom of the conduction band and hence the electron excitation in rare earth doped BiFeO_3 can be transferred from O 2p to Re 4f instead of the Fe 3d states, consequently decreasing the band gap energy, as illustrated in Figure 4.14(d).

Moreover, it can be seen that the band gap values of La^{3+} doped system are slightly larger than those of the Ba^{2+} and Sm^{3+} substituted systems.

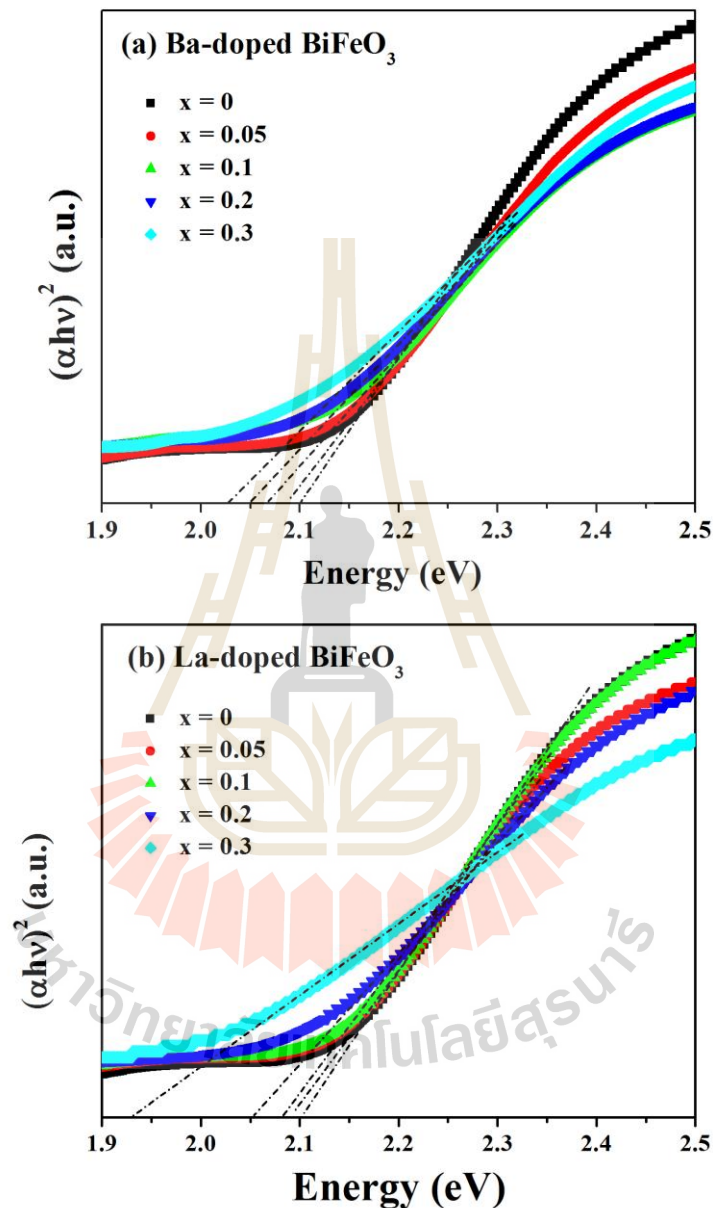


Figure 4.14 Plot of $(\alpha h\nu)^{1/2}$ as a function of photon energy ($h\nu$) for undoped BiFeO_3 nanorods prepared in air at $600\text{ }^\circ\text{C}$ for 3 h (a) Ba-doped BiFeO_3 , (b) La-doped BiFeO_3 , and (c) Sm-doped BiFeO_3 nanopowders, respectively and (d) the schematic diagram of the possible mechanism for electronic energy band.

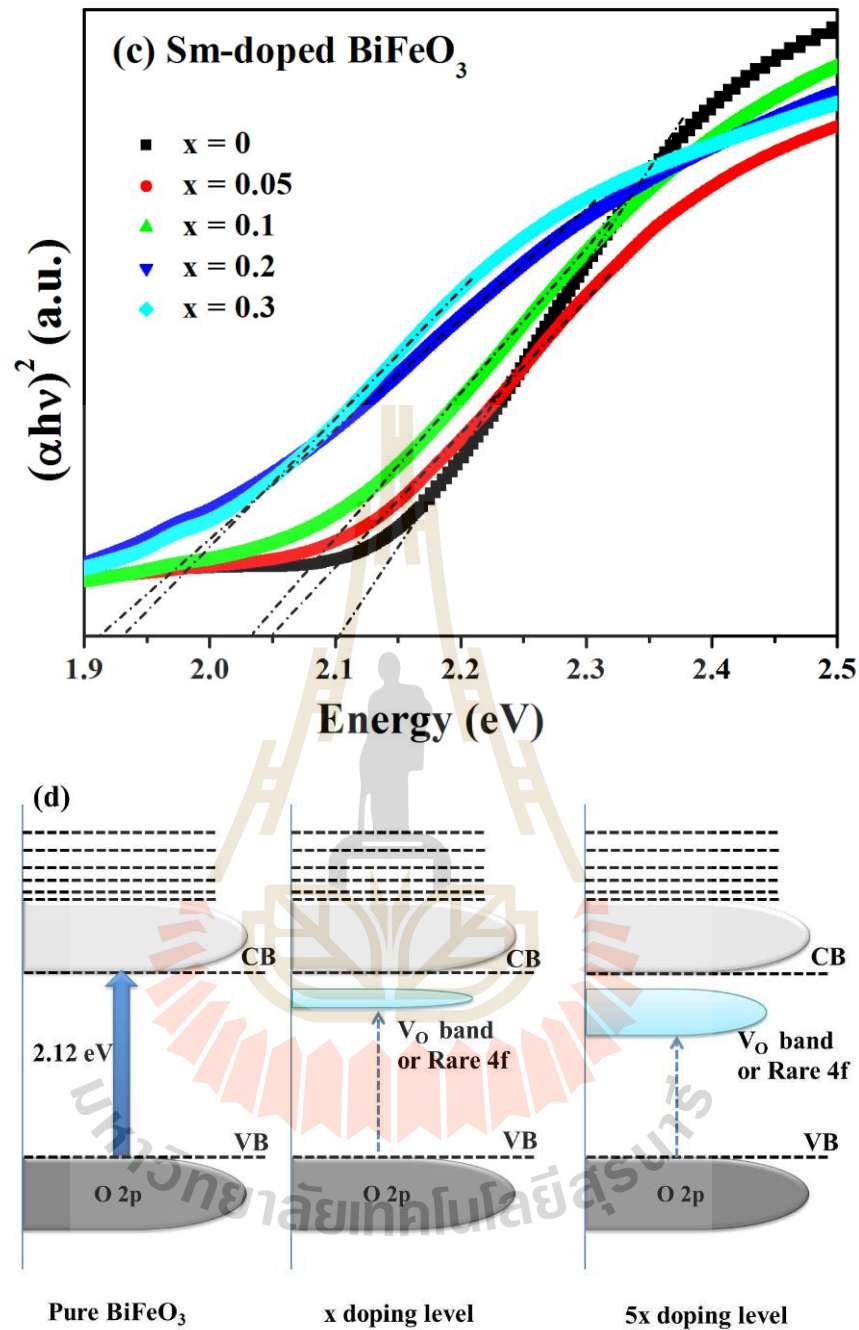


Figure 4.14 Plot of $(\alpha h\nu)^{1/2}$ as a function of photon energy ($h\nu$) for undoped BiFeO₃ nanorods prepared in air at 600 °C for 3 h (a) Ba-doped BiFeO₃, (b) La-doped BiFeO₃, and (c) Sm-doped BiFeO₃ nanopowders, respectively, and (d) the schematic diagram of the possible mechanism for electronic energy band (Continued).

Table 4.3 Summary of band gap energy (E_g) of undoped BiFeO₃ and Ba-, La-, and Sm-doped BiFeO₃ nanopowders calcined at 600 °C for 3h.

Doping level	E_g (eV)		
	Ba-doped BiFeO ₃	La-doped BiFeO ₃	Sm-doped BiFeO ₃
x = 0	2.12	2.12	2.12
x = 0.05	2.09	2.1	2.05
x = 0.1	2.07	2.09	2.03
x = 0.2	2.05	2.05	1.91
x = 0.3	2.03	1.93	1.93

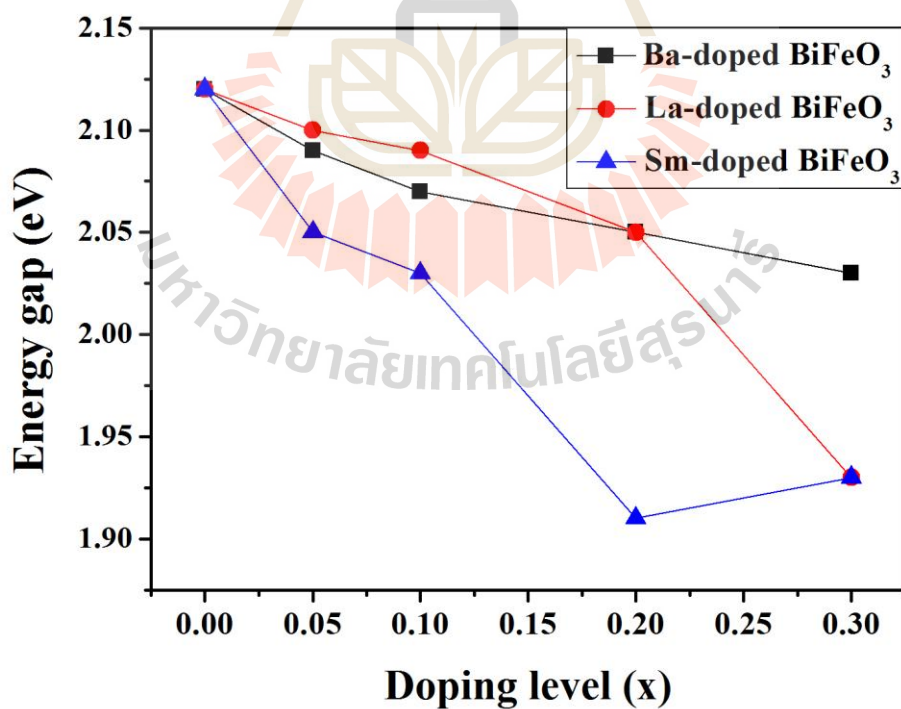


Figure 4.15 Band gap versus doping concentrations of undoped BiFeO₃ and Ba-, La-, and Sm-doped BiFeO₃ nanopowders calcined at 600 °C for 3 h.

4.3 Magnetic hysteresis (M–H) properties

4.3.1 Magnetic hysteresis (M–H) properties of the pure BiFeO₃ and Ba-doped BiFeO₃ nanopowders at room temperature

The magnetic measurements of calcined nanopowders for doped and undoped BiFeO₃ samples are characterized by using the vibrating sample magnetometer (VSM). The field dependence magnetization (M–H loop) properties of Re-doped BiFeO₃-based nanopowders are measured at room temperature with a maximum applied magnetic field of 10 T. In order to understand the effect of doped BiFeO₃-based samples on the magnetic ordering, the temperature dependent zero-field cooled (ZFC) and field cooled (FC) magnetization measurements are carried out in the temperature range 50–350 K under an applied field of 1000 Oe.

The hysteresis loop for pure BiFeO₃ samples reveal an almost straight line which indicates antiferromagnetic behaviour, that is, each Fe³⁺ spin is surrounded by six antiparallel spins on the nearest Fe neighbours. The pure BiFeO₃ nanopowder shows a saturation magnetization value of 0.06 emu/g at 10 kOe and a very small coercive field value of 38 Oe. The value of saturation magnetization for pure BiFeO₃ samples obtained in this work at 300 K is larger than for La doped BiFeO₃ as also reported by Chaudhuri and Mandal (Chaudhuri and Mandal, 2012). However, BiFeO₃ nanopowders show a narrow hysteresis loop with small remanent magnetization (M_r) of about 0.00014 emu/g. In this work, the crystal structure of BiFeO₃ is consistent with a G-type AFM ordering which in principle should render a null spontaneous magnetization. Further, the observation of a small residual magnetization in the antiferromagnetic systems can be ascribed to incomplete spin compensation between

two spin sublattices (Qian *et al.*, 2010). This gives rise to a measurable magnetic moment in the case of small antiferromagnetic phases.

Figure 4.16(a) exhibits the magnetic hysteresis loops of calcined $\text{Bi}_{1-x}\text{Ba}_x\text{FeO}_3$ nanopowders at 600 °C for 3 h at room temperature. It should be noted that undoped and Ba-doped BiFeO_3 samples are in an antiferromagnetic state and M–H loops show an almost linear dependence on the magnetic field. All of the doped compounds present a very slim hysteresis loop with nonzero remanent magnetization and a narrow coercive field which has similar magnetic behaviour to pure BiFeO_3 samples, indicating weak ferromagnetic behaviour at room temperature. The saturation magnetization values for doped compounds show a decrease after substituted Ba contents which are larger than that BiFeO_3 samples. The remanent magnetization values for $\text{Bi}_{1-x}\text{Ba}_x\text{FeO}_3$ (where $x = 0.05, 0.1, 0.2,$ and 0.3) are obtained by 1.83×10^{-3} , 1.99×10^{-4} , 7.30×10^{-5} , and 3.04×10^{-4} emu/g, respectively. Compared to normal weak ferromagnetic materials, the remanent magnetization is very small for Ba-doped BiFeO_3 nanopowders. A lower coercive field (H_c) for all doped samples reveal the possibility that the weak ferromagnetic order is basically an antiferromagnetic substrate with weak ferromagnetism which is because of the presence of antiferromagnetic impurities in $\text{Bi}_2\text{Fe}_4\text{O}_9$. According to the XRD results for all Ba-doped samples, the antiferromagnetic secondary phase in $\text{Bi}_2\text{Fe}_4\text{O}_9$ is clearly found, which can be attributed to the decrease of the remanent magnetization and the coercive field. Since the secondary phase corresponding to the high intensity peaks found in the XRD patterns of the Ba-doped BiFeO_3 samples do not have any magnetic order, this result means that the reduction magnetic properties may be due to the increase in intensity of the secondary phase. Another possible explanation for the

origin of spontaneous magnetization is that the charge defects promoted by substituting Ba^{2+} ions with BiFeO_3 might be obtained by the formation of Fe^{4+} or oxygen vacancies (Cheng *et al.*, 2015; Wang *et al.*, 2006). Cheng *et al.* reported that the Ba^{2+} substituted in BiFeO_3 ceramics can reduce the charge defects without varying the Fe valence state. Ba^{2+} substituted for Bi^{3+} in BiFeO_3 may suppress the charge defects and reduce the magnetism. The decrease of remanent magnetization confirms such a charge compensation principle.

Moreover, the enhancement of saturation magnetization values has been observed with the Ba^{2+} doping (Lotey *et al.*, 2013). The maximum magnetization of the undoped BiFeO_3 was found to be 0.06 emu/g and with the Ba-doped sample it was enhanced doubled as compared to the pure BiFeO_3 . The possible reasons for this may be attributed to the suppression spin spiral structure of pure BiFeO_3 being reduced to the particle size of 37.8 nm and the addition of divalent (Ba^{2+}) at trivalent (Bi^{3+}) sites in the structure. This creates oxygen vacancies which suppress spiral spin structures and hence result in the enhanced magnetization of the Ba^{2+} addition to the BiFeO_3 nanopowders.

4.3.2 Magnetic hysteresis (M–H) properties of La-doped nanopowders

Figure 4.17(b) shows the magnetization curves of $\text{Bi}_{1-x}\text{La}_x\text{FeO}_3$ (where $x = 0, 0.05, 0.1, 0.2,$ and 0.3) calcined at $600\text{ }^\circ\text{C}$ for 3 h measured at 298 K. At a low concentration $x = 0.05$, the La-doped BiFeO_3 reveals an increase in magnetization which is almost linear with increases in the magnetic field. When the concentration increases up to $x = 0.1$, the M–H curve exhibits a nonlinear initial magnetization curve and further increases in the La contents with $x = 0.2$ and 0.3 reveal a clearly weak ferromagnetic hysteresis loop. While open loops in the hysteresis loops for Bi_{1-}

$x\text{La}_x\text{FeO}_3$ ($0.1 < x \leq 0.3$) samples are observed, especially with the open loops in the $\text{Bi}_{0.8}\text{La}_{0.2}\text{FeO}_3$ and $\text{Bi}_{0.7}\text{La}_{0.3}\text{FeO}_3$ samples. The coercive field (H_c) of BiFeO_3 nanopowders is found to be around 36 Oe, as increases in the La doping contents result in a large enhancement in the coercive field to 89, 236, 388, and 2,387 Oe. This indicates an increase in the saturation magnetization (M_s) with increasing La doping concentration. The average particle size of these samples is in the range of 65–19 nm which is less than the spiral spin ordering of 62 nm. Thus, the primary cause for the presence of the weak ferromagnetism of the La-substituted BiFeO_3 nanoparticles can be attributed to the size effect of the prevention of the spiral spin ordering. Interestingly, the remanent magnetization of $\text{Bi}_{0.7}\text{La}_{0.3}\text{FeO}_3$ nanopowders is about 0.047 emu/g, which is about two orders higher than that of the parent BiFeO_3 compound. A detailed view of the low field region of La-doped BiFeO_3 is shown in Figure 4.16(b): the initial region of the M–H curve reveals a shoulder-like or nonlinear feature in these samples. Moreover, it is found that the hysteresis loop shifts towards a negative axis with increases in La concentrations. Both the shoulder-like features and the hysteresis loop shifts revealed in the low-field region indicate that there are two coupled magnetic phases, as suggested by a ferromagnetic component being embedded in an antiferromagnetic matrix at room temperature. These magnetic properties reveal an exchange interaction which promotes the components of ferromagnetism in La-doped BiFeO_3 nanoparticles, which arise from the competition between the antiferromagnetic and the ferromagnetic order. Thus, in the case of the La-doped samples, the gradual enhancement of their magnetization properties can be observed as a result of increases in La concentrations. The increase in magnetization with increases in the substitution may arise as a result of several factors. Firstly, the

average particle sizes decreases as shown in TEM images which induce the suppression of the cycloidal spin structures leading to the net magnetic moment. Thus, the large fraction of non-exact compensation spins from the surface is the cause of a high surface-to volume ratio in the nanoparticles. The periodic cycloid spin wavelength can be broken into small particles when their size is below 62 nm. This magnetization suppression in bulk BiFeO₃ occurs due to its spiral arrangement of magnetic spins having a wavelength of 62 nm (Park *et al.*, 2007; Suresh and Srinath, 2013). The TEM image for doped BiFeO₃ in this work reveals a decrease in particle size to around 19 nm which is lower than the long-length spiral spin structure of 62 nm. Hence, one of the important contributions for the enhancement of the magnetization of La-doped BiFeO₃ samples is the uncompensated spins from the surface which are induced by the size effect of the nanoparticles as has been reported (Huang *et al.*, 2013; Arora and Kumar, 2015; Suresh and Srinath, 2013). Secondly, the substitution of rare earth ions at the A-site could lead to modifications in the spiral spin structure from helical to linear results because of the change in Fe-oxygen bond angles associated with the observed distortion in the crystal structure (Yan *et al.*, 2010). This structural distortion induced by the La ions doping can be attributed to the substitutions of the larger ionic radii ions when there is mismatch between La³⁺ and Bi³⁺. Furthermore, some defects often exist in the lattices, such as lattice order, oxygen vacancies etc., which produce some ferromagnetic ordering and hence show its antiferromagnetic nature. However, the partial substitution Bi atoms with La ions with difference ionic radii can lead to a charge imbalance between adjacent antiparallel sublattice spins when the Fe ions are broken. The ferromagnetic coupling via oxygen rather than the antiferromagnetic order is preferable because that means

some of the latent magnetization locked within the BiFeO₃ lattices are released and there is an improvement of the net magnetic moment (Zhang *et al.*, 2009).

4.3.3 Magnetic hysteresis (M–H) properties of Sm–doped BiFeO₃ nanopowders

Investigations of the magnetic properties at room temperature confirm the existence of enhanced magnetization in the substituted samples. The magnetization hysteresis (M–H) loops of all Sm–doped and pristine BiFeO₃ samples measured at room temperature are shown in Figure 4.16(c). It can be seen that after Sm doping, the magnetization properties are significantly enhanced and that the characteristics of the hysteresis loops depend on the amount of doping concentrations. When Sm doped BiFeO₃ samples replace Bi ions, the samples $x = 0.05$ and 0.1 show weak ferromagnetic behaviour with a small amount of remanent magnetization (M_r) and a coercive field (H_c) of 0.0034, 0.0095 emu/g and 340, 723 Oe, respectively. Moreover, one can see that the orthorhombic $x = 0.2$ and $x = 0.3$ compounds exhibit a consistent of saturated ferromagnetic order with a maximum of M_s of 0.51 emu/g for the Bi_{0.7}Sm_{0.3}FeO₃ samples. The saturation magnetization values of Bi_{1-x}Sm_xFeO₃ samples have been found to be larger than that of pure bulk BiFeO₃ and La–doped samples. An increase of several times in the magnetization properties of the Bi_{1-x}Sm_xFeO₃ system have already been reported in the rare earth doped BiFeO₃ samples (Wu *et al.*, 2013; Suresh and Srinath, 2013). This observation is similar to that observed in the synthesized La–substituted BiFeO₃ nanoparticles. There are many possible explanations for the origin and remarkable improvement in magnetization which are similar to that ascribed to the La–doped samples: (i) by substituting Bi³⁺ atoms at A sites with Sm³⁺ atoms, a local ferromagnetic order can be expected to form

because of the destruction of the spiral spin structure. (ii) the higher magnetization is observed in the $x = 0.2$ and 0.3 samples due to the presence of the rhombohedral/orthorhombic phase boundaries of these samples. The bond length and bond angle of Fe–O bonds change significantly from one unit cell to another. Consequently, this change greatly enhances the magnetic properties of the system because the FeO_6 oxygen octahedral rotates which in turn increases spin canting (Yang *et al.*, 2012). (iii) in our case, the particle sizes for sintered pure and Sm-doped BiFeO_3 are decreased from 69 to 22 nm which is less than the cycloid spin structure with a period of 62 nm. The enhanced magnetic properties can be due to the decrease in particle size and the surface to volume ratio becomes higher and modifies the long range cycloidal spin structure of Sm doped BiFeO_3 compounds. (iv) compared to La-doped samples, the small total magnetic moment of the Sm^{3+} ions ($m = 1.5 \mu_B$, $\mu_B =$ Bohr magneton) causes no significant enhancement of the magnetic properties of the substituted compounds.

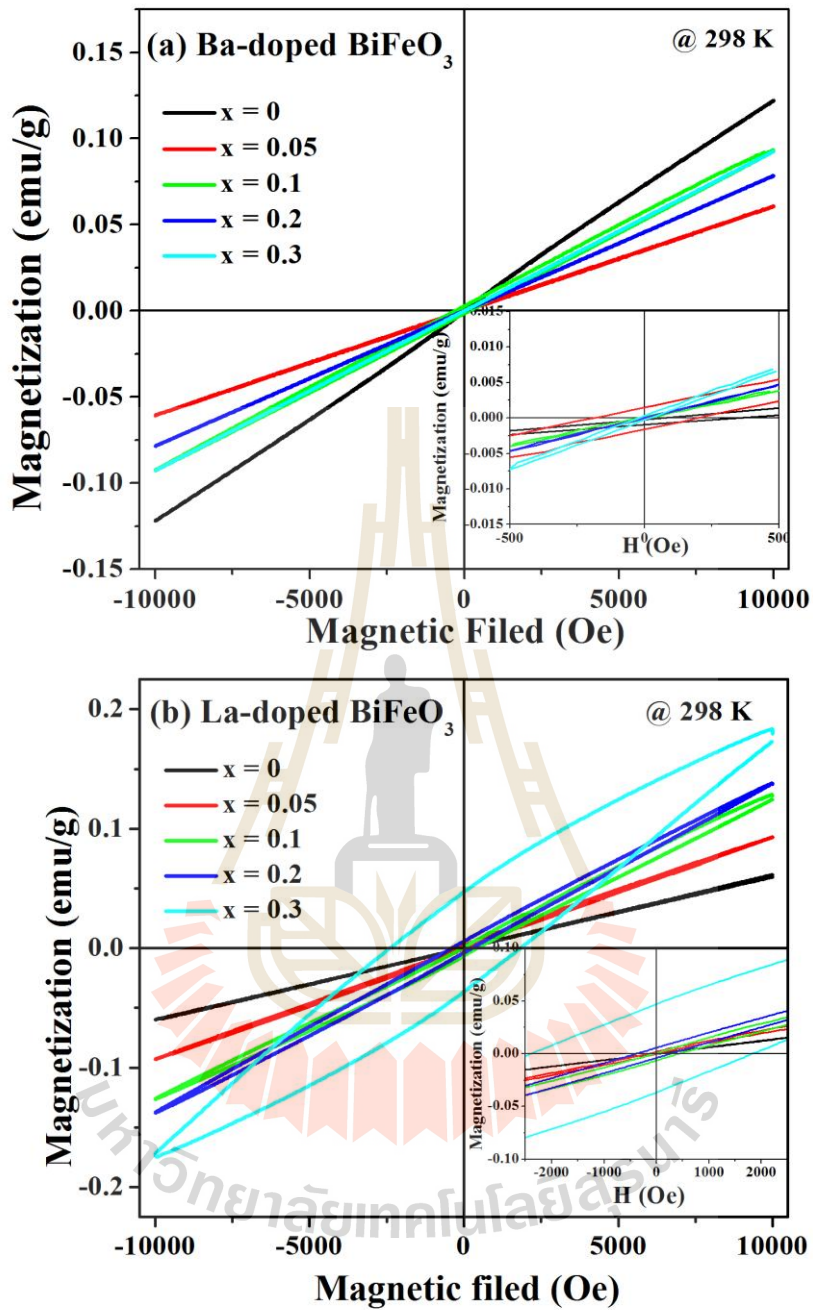


Figure 4.16 The magnetization magnetic measurement (M) versus applied magnetic field (H) were performed on undoped BiFeO₃, (a) Ba-doped, (b) La-doped, and (c) Sm-doped BiFeO₃ powders with different compositions obtained at 298 K from VSM measurements.

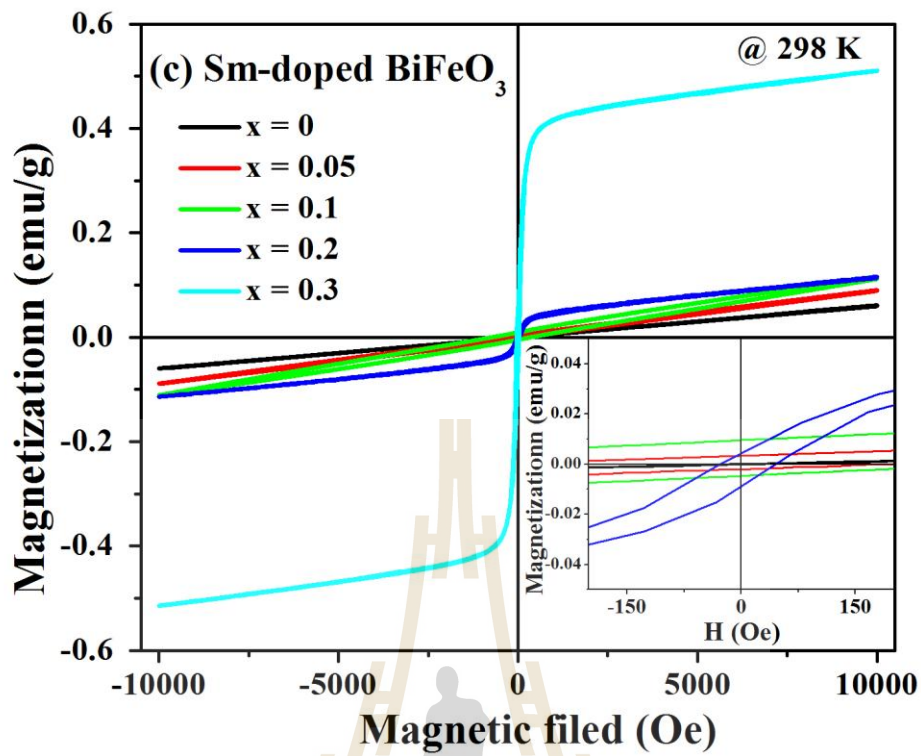


Figure 4.16 The magnetization magnetic measurement (M) versus applied magnetic field (H) were performed on undoped BiFeO_3 , (a) Ba-doped, (b) La-doped, and (c) Sm-doped BiFeO_3 powders with different compositions obtained at 298 K from VSM measurements (Continued).

Table 4.4 Summary of magnetization of Ba-, La-, and Sm-doped BiFeO₃ at room temperature.

Doping level	Ba-doped BiFeO ₃		La-doped BiFeO ₃		Sm-doped BiFeO ₃	
	M _r (emu/g)	H _c (Oe)	M _r (emu/g)	H _c (Oe)	M _r (emu/g)	H _c (Oe)
x = 0.0	2.20×10 ⁻⁴	36	2.20×10 ⁻⁴	36	2.20×10 ⁻⁴	36
x = 0.05	1.83×10 ⁻³	294	1.94×10 ⁻⁴	89	9.00×10 ⁻²	203
x = 0.1	1.99×10 ⁻⁴	25	3.60×10 ⁻³	236	1.12×10 ⁻¹	328
x = 0.2	7.30×10 ⁻⁵	6.8	5.50×10 ⁻³	388	1.15×10 ⁻¹	43
x = 0.3	3.04×10 ⁻⁴	17	4.70×10 ⁻²	2387	5.50×10 ⁻¹	31

4.3.4 Temperature dependence of magnetization for the pure BiFeO₃ and doped BiFeO₃ nanopowders

Figure 14.18(a) shows that as the temperature dependence measurements for the ZFC curve decrease from 350 to 130 K the magnetization also decreases. We can see that the FC measuring mode of the BiFeO₃ sample increases with decreasing the temperature. This result indicates that the BiFeO₃ is antiferromagnetic in nature. A slight upturn in the magnetization is observed below 130 to 50 K in the ZFC curve which could result from the ferromagnetic order in the BiFeO₃ nanopowders at this temperature range as reported by several articles (Peng-Ting *et al.*, 2014; Zhang *et al.*, 2010). In a low temperature range the magnetization increases (below 130 to 50 K), confirming that there is a magnetic phase transformation. Whereas the separation between the ZFC and FC curves is not observed in the measured temperature range, this means that the spin-glass transition can be observed above the 350 K temperature regions. Figure 4.18(b)–(e) reveals the

temperature dependence of magnetization of the $\text{Bi}_{1-x}\text{Ba}_x\text{FeO}_3$ samples. The effect of Ba doping concentration on the magnetic properties for $\text{Bi}_{1-x}\text{Ba}_x\text{FeO}_3$ samples is quite similar to that observed in the pure BiFeO_3 calcined powder and large distinct splitting between ZFC and FC curves can be seen for all Ba-doped samples. The ZFC and FC curves of two of the doped samples, $\text{Bi}_{0.95}\text{Ba}_{0.05}\text{FeO}_3$ and $\text{Bi}_{0.9}\text{Ba}_{0.1}\text{FeO}_3$ show that the magnetization increases as the temperature decreases to ~ 130 K. However, when the temperature decreases from 130 to 50 K, the ZFC curve shows a small increase in magnetization, which could result from the fractional ferromagnetic (FM) phase coexisting in the BFO sample (Yin *et al.*, 2009). In other words, the magnetic structure is accompanied by a so-called weak ferromagnetic Dzyaloshinskii–Moriya interaction (Fang *et al.*, 2010). In contrast, both the ZFC and FC magnetizations for the $\text{Bi}_{0.8}\text{Ba}_{0.2}\text{FeO}_3$ and $\text{Bi}_{0.7}\text{Ba}_{0.3}\text{FeO}_3$ samples continue to increase steadily with decreasing temperature. This behaviour of the magnetization curves demonstrates that these samples make a ferromagnetic contribution. However, a clear anomaly in the temperature dependence of magnetization curves for Ba-doped is observed in BiFeO_3 at about 250 K which is common for orthoferrites (Catalan and Scott, 2009) as seen in Figure 4.18. As already mentioned, the calcined sample contains the secondary phase $\text{Bi}_2\text{Fe}_4\text{O}_9$ in all the Ba-doped samples. This secondary phase is paramagnetic at room temperature which undergoes near $T_N = 264 \pm 3$ K (Tian *et al.*, 2009; Lazenka *et al.*, 2012) a transition from a paramagnetic to an antiferromagnetic state. Thus, the anomaly in the ZFC and FC curves of the doped samples may be due to the appearance of an impurity phase of $\text{Bi}_2\text{Fe}_4\text{O}_9$.

Figure 4.19(a)–(d) shows the temperature dependence of zero field cooled (ZFC) and field cooled (FC) La-doped BiFeO_3 nanopowders in the temperature range

50–350 K under applied field 1 kOe. Figures 4.18 show the ZFC and FC curves of $\text{Bi}_{1-x}\text{La}_x\text{FeO}_3$ nanopowders with $x = 0.05, 0.1, 0.2,$ and 0.3 were measured in field of 1 kOe. These FC plots show a decrease in magnetization with increasing temperatures up to 350 K in all La-doped samples, which indicate that these samples have typical ferromagnetic properties. The ZFC and FC curves are not in superposition which further confirms the presence of impurities. Surprisingly, a great dislocation between ZFC and FC curves and the hump in ZFC at about ~ 75 and 62 K at low temperatures and ~ 318 and 321 K at high temperatures can be clearly seen for $\text{Bi}_{0.9}\text{La}_{0.1}\text{FeO}_3$ and $\text{Bi}_{0.8}\text{La}_{0.2}\text{FeO}_3$ samples, respectively. A broad peak at low temperature is unique to the nanosize effect of BiFeO_3 (Park *et al.*, 2007), a spin glass nature (Suresh and Srinath, 2013) and an absence of polycrystalline are typical of BiFeO_3 samples (Singh *et al.*, 2008). The maximum peak corresponding to a blocking temperature takes place at T_b 75 and 62 K for the $\text{Bi}_{0.9}\text{La}_{0.1}\text{FeO}_3$ and $\text{Bi}_{0.8}\text{La}_{0.2}\text{FeO}_3$ samples, respectively. If the small hump displays a blocking state associated with the superparamagnetic relaxation processes of isolated magnetic nanosizes, one would predict a drastic dependence of T_b on particle size (Huang *et al.*, 2013). For $x = 0.05$ and 0.3 , ZFC curves indicate that the magnetization increases as the temperature increases, suggesting a typical AFM property. However, the FC curve for this sample reveals that the magnetization increases with decreasing temperature, which could result from the existence of a fractional ferromagnetic phase in this sample.

The temperature dependent magnetization curves from 50 to 350 K in the zero field cooling (ZFC) and field cooling (FC) measured a magnetic field of 1 kOe for the $\text{Bi}_{1-x}\text{Sm}_x\text{FeO}_3$ samples as shown in Figure 4.19. The ZFC and FC curves for $\text{Bi}_{0.95}\text{Sm}_{0.05}\text{FeO}_3$ sample was similar to those for BiFeO_3 as shown in Figure 4.20(a).

However, some different phenomena were observed concerning the temperature transition between AFM to FM in this sample which was around 175 K as compared to pure BiFeO₃. It was found that the transition temperature for the pure BiFeO₃ sample was near 130 K, suggesting that doping with Sm in BiFeO₃ samples can induce a transition in temperature. The particular ZFC curve of the Bi_{0.9}Sm_{0.1}FeO₃ sample is shown in Figure 4.20(b). The magnetization increases as the temperature increases indicating that this sample had weak ferromagnetic ordering. This result suggests that the spin cycloid structure can be destroyed by Sm doping and that the release of some latent magnetization locked within the cycloid spin structure and the samples becomes ferromagnetically ordered. Figures 4.19(c) and (d) reveal that the ZFC and FC curves of Bi_{0.8}Sm_{0.2}FeO₃ and Bi_{0.7}Sm_{0.3}FeO₃ samples are measured under 1 kOe, respectively. Interestingly, there is a great divergence between the ZFC–FC curves of the Bi_{0.8}Sm_{0.2}FeO₃ sample beginning at T ~350 K. In general, a splitting between ZFC–FC curves can be attributed to an inhomogeneous mixture of AFM and FM (Siwach *et al.*, 2008). An increase of magnetization as the temperature decreases confirms that the ferromagnetic (FM) phase coexists with the main antiferromagnetic type of (AFM). It can be clearly seen that both the ZFC and FC curves for Bi_{0.8}Sm_{0.2}FeO₃ and Bi_{0.7}Sm_{0.3}FeO₃ samples show a broad peak at ~55 and 125 K and that there is an increase in magnetization of ZFC and FC with decreasing temperature, and this shows the broad peak at low temperature is due to the magnetic blocking mechanism (Suresh and Srinath, 2013). The ZFC and the FC broad curves take place at higher temperatures for 30% Sm–doped samples which are associated with the rises in the blocking temperatures as the average particle size becomes larger.

The temperature dependence of the inverse magnetic susceptibility ($\chi^{-1}(T)$) curves and fitting curves in the temperature range of 50–350 K are revealed in the inset of the figure. The para/antiferromagnetic characteristics and the magnetic susceptibility can be explained by the Curie–Weiss law (Wang *et al.*, 2013; Yin *et al.*, 2009) quite well in a high temperature range (300–350 K).

$$\chi = \frac{C}{T - \theta} \quad (4.2)$$

Where χ is susceptibility, θ is the Curie–Weiss temperature and C defines the Curie constant. The Curie constant is given by

$$C = \frac{\mu_0 \mu_B^2}{3k_B} N g^2 s(s+1) \quad (4.3)$$

Where N is the number of magnetic ions per unit volume, g is the Lande g–factor, μ_B is the Bohr magneton, k_B is Boltzmann's constant, and s is 1/2 for unpaired electrons. So $\mu_{eff} = g\mu_B \sqrt{s(s+1)}$ with μ_{eff} is the effective magnetic moment. The paramagnetic Curie–Weiss temperature value obtained from the Curie–Weiss fit of the pure BiFeO₃ samples is -1810 K. The results of the Curie constant (C) and Curie–Weiss temperature (θ) for Sm–doped samples are obtained at -347 to 1.99 K and 1.97–1.6 emu.K/g.Oe respectively. As a result of Ba–doped BiFeO₃ samples, θ and C can be deduced from experiments at -145 to -1615 K and 2–5.7 emu.K/g.Oe respectively. In order to investigate further, we obtained θ and C values at -21.4 to 60.4 K and 1.5–8.15 emu.K/g.Oe for La–substituted in BiFeO₃ samples. The Curie–Weiss law fitting result provides a positive Curie temperature, which is probably due to the strong canted AFM ordering with a manifest FM component. The negative values of θ

indicate the antiferromagnetic characteristics of the calcined samples with weak FM and without FM components. The fitted parameter values of all samples are summarized in Table 4.5. In the theory, a Fe^{3+} ion at an octahedrally coordinated site suggests a High-spin (HS) configuration ($t_{2g}^3 e_g^2, \uparrow\uparrow\uparrow\uparrow; s = 5/2$) or Low-spin (LS) configuration ($t_{2g}^5 e_g^0, \uparrow\downarrow\uparrow\downarrow; s = 1/2$) (Templeton, Douglas). The calculated magnetic moments of High-spin Fe^{3+} and Low-spin Fe^{3+} are 5.92 and $1.73 \mu_B$ respectively. The fitting results we obtained from our experiments indicate that the value of the BiFeO_3 effective moment is about $\mu_{\text{eff}} \sim 6.62 \mu_B$ suggesting that Fe^{3+} must always be in a high spin configuration. As a result of the Curie constant we estimate the effective magnetic moment as $\mu_{\text{eff}} \sim 5.55, \sim 6.18, \sim 4.93,$ and $\sim 4.05 \mu_B$ for Ba-doped BiFeO_3 when $x = 0.05, 0.1, 0.2,$ and 0.3 samples, respectively. The fitting results show that all of the effective magnetic moment values for La-doped BiFeO_3 samples are about $\sim 7.85, \sim 5.32, \sim 3.39,$ and $\sim 8.13 \mu_B$ for $x = 0.05, 0.1, 0.2$ and 0.3 samples, respectively. Finally, for the Sm ions doped in BiFeO_3 , the effective magnetic moment is about $\sim 4.46, \sim 5.73, \sim 4.60,$ and $\sim 24.00 \mu_B$ with $x = 0.05, 0.1, 0.2,$ and 0.3 samples, respectively. The close values of the theoretical and the experimental effective magnetic moments indicate that all the magnetic ions are in the high spin configuration ($t_{2g}^3 e_g^2, \uparrow\uparrow\uparrow\uparrow; s = 5/2$). The effective magnetic moment μ_{eff} values obtained from the experiment for all doped samples are smaller than those for the theoretical values, and this suggests that there is competition between the antiferromagnetic and ferromagnetic interaction which are suppressed resulting from the magnetization values of the dopant samples which are much lower than their theoretical value.

Table 4.5 Effective magnetic moment (μ_{eff}), Curie–Weiss temperature (θ) obtained from Curie–Weiss law fitting results for doped BiFeO₃.

Doping level	Ba-doped BiFeO ₃		La-doped BiFeO ₃		Sm-doped BiFeO ₃	
	μ_{eff} (μ_B)	θ (K)	μ_{eff} (μ_B)	θ (K)	μ_{eff} (μ_B)	θ (K)
x = 0	6.6	-1810.7	6.6	-1810.7	6.6	-1810.7
x = 0.05	5.6	-197.0	7.8	46.3	4.5	-347.5
x = 0.1	6.2	-1466.0	5.3	-21.4	5.7	2.0
x = 0.2	4.9	-1615.7	3.4	60.3	4.6	26.3
x = 0.3	4.0	-144.9	8.1	24.4	24.00	-232.3

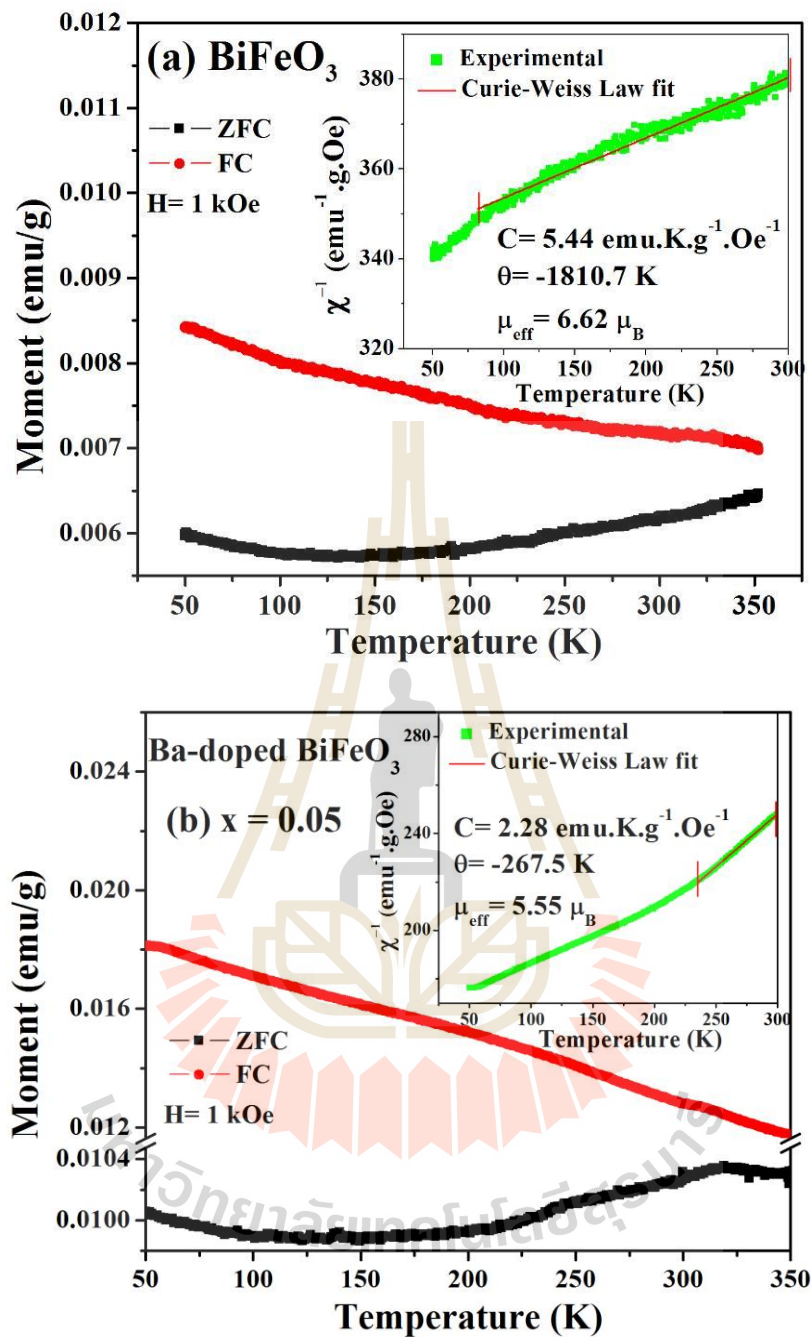


Figure 4.17 (a), (b), (c), (d), and (e) display the temperature–dependent magnetization (M–T) curves of pure BiFeO₃ and Ba–doped BiFeO₃ samples, respectively. Inset: fitting the data to the Curie–Weiss law between 150 and 300 K under 1 kOe as a function of temperature and fitting result using the Curie–Weiss law.

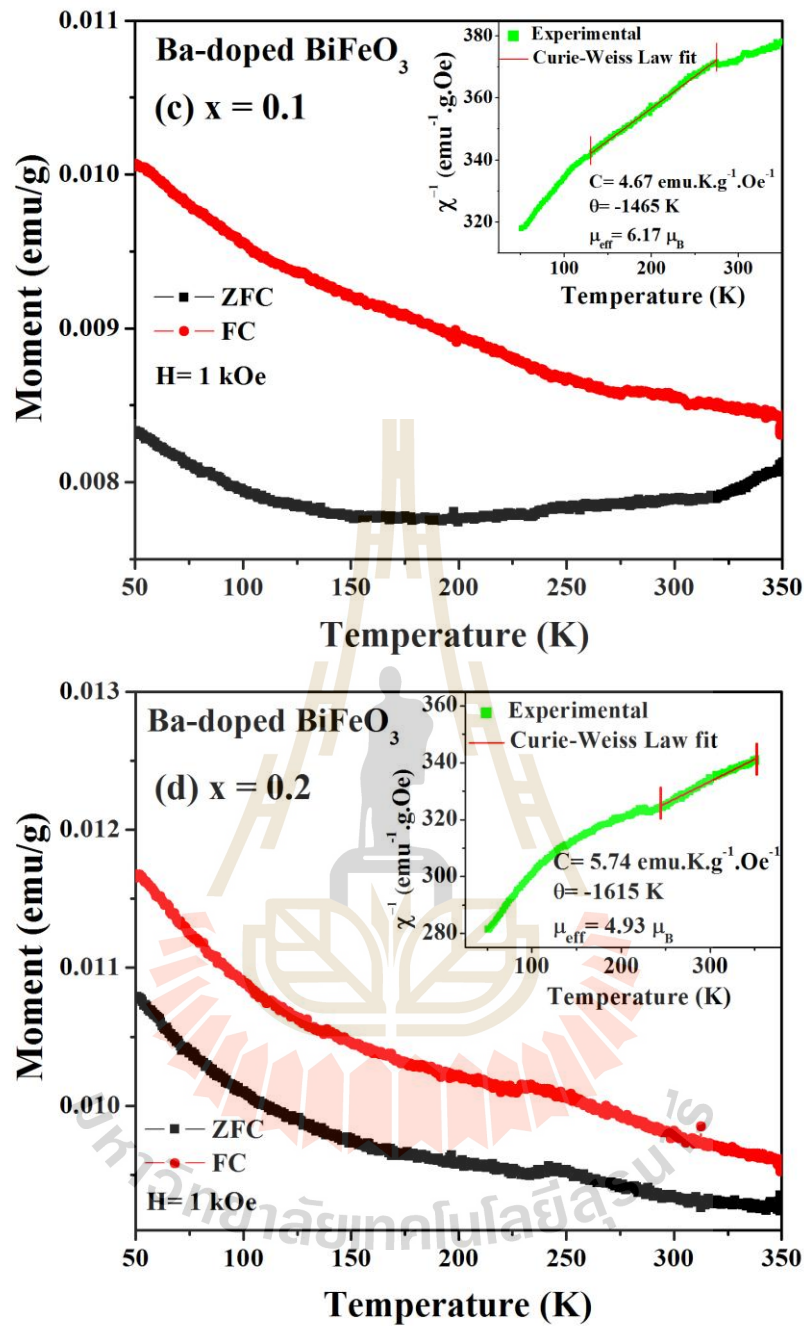


Figure 4.17 (a), (b), (c), (d), and (e) display the temperature–dependent magnetization (M–T) curves of pure BiFeO_3 and Ba–doped BiFeO_3 samples, respectively. Inset: fitting the data to the Curie–Weiss law between 150 and 300 K under 1 kOe as a function of temperature and fitting result using the Curie–Weiss law (Continued).

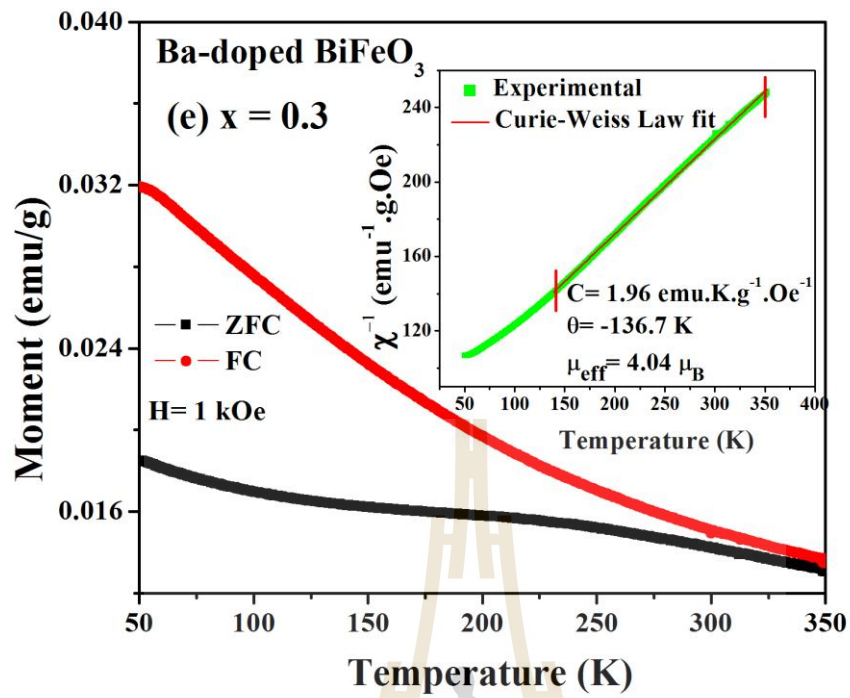


Figure 4.17 (a), (b), (c), (d), and (e) display the temperature-dependent magnetization (M–T) curves of pure BiFeO₃ and Ba-doped BiFeO₃ samples, respectively. Inset: the fitting the data to the Curie–Weiss law between 150 and 300 K under 1 kOe as a function of temperature and fitting result using the Curie–Weiss law (Continued).

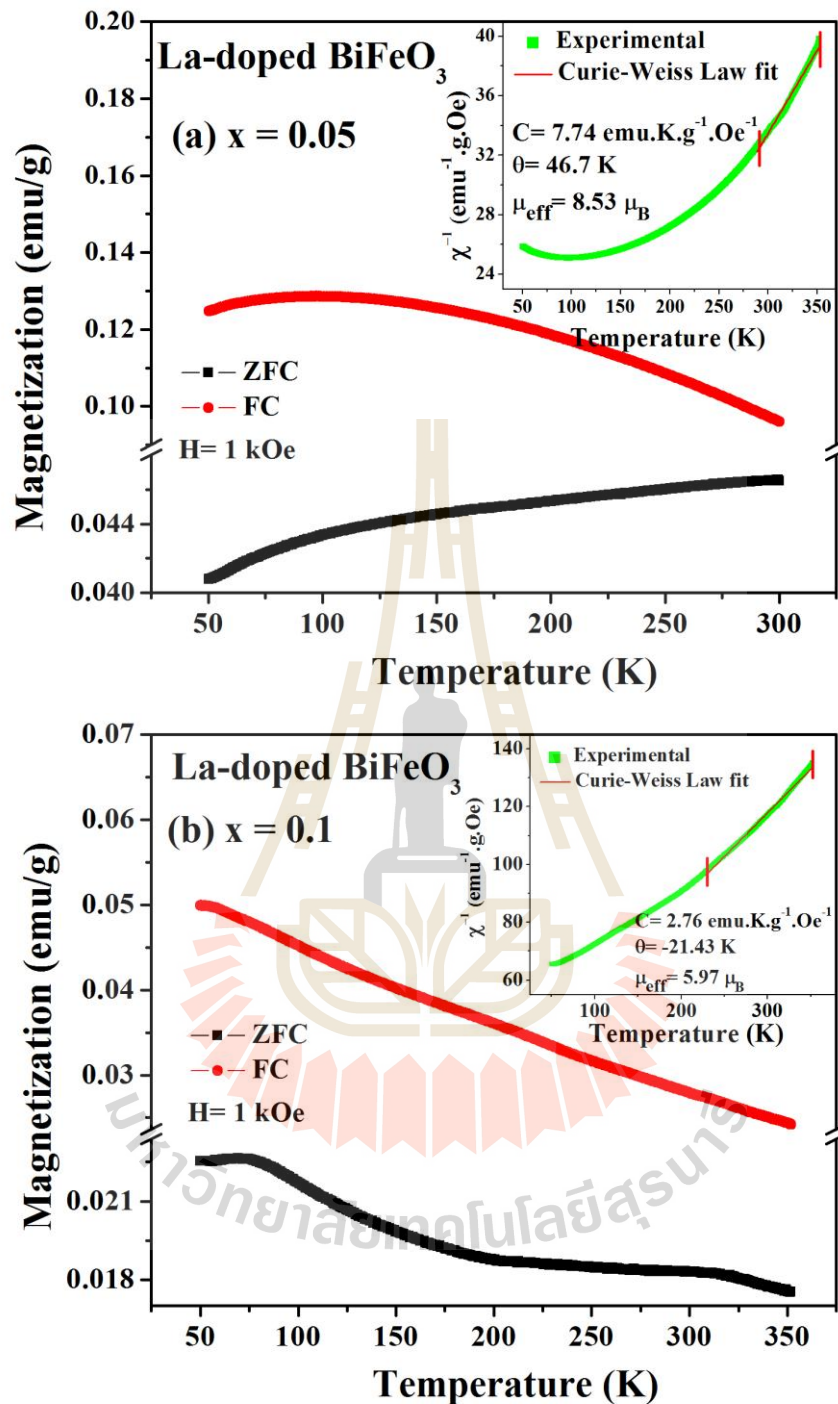


Figure 4.18 (a), (b), (c), and (d) display the temperature-dependent magnetization (M-T) curves of La-doped BiFeO₃ samples, respectively. Inset: fitting the data to the Curie-Weiss law between 150 and 300 K under 1 kOe as a function of temperature and fitting result using the Curie-Weiss law.

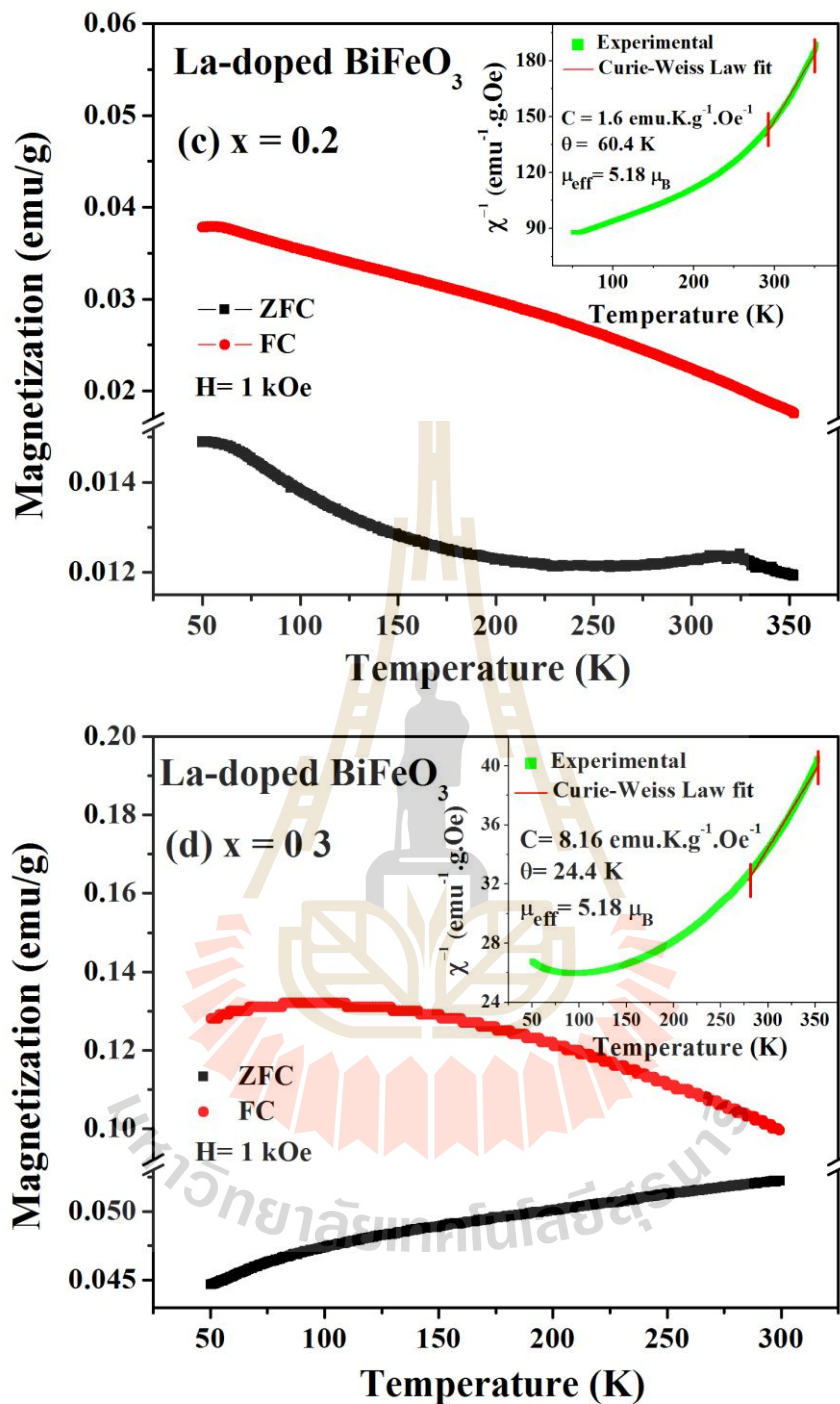


Figure 4.18 (a), (b), (c), and (d) display the temperature-dependent magnetization (M-T) curves of La-doped BiFeO_3 samples, respectively. Inset: fitting the data to the Curie-Weiss law between 150 and 300 K under 1 kOe as a function of temperature and fitting result using the Curie-Weiss law (Continued).

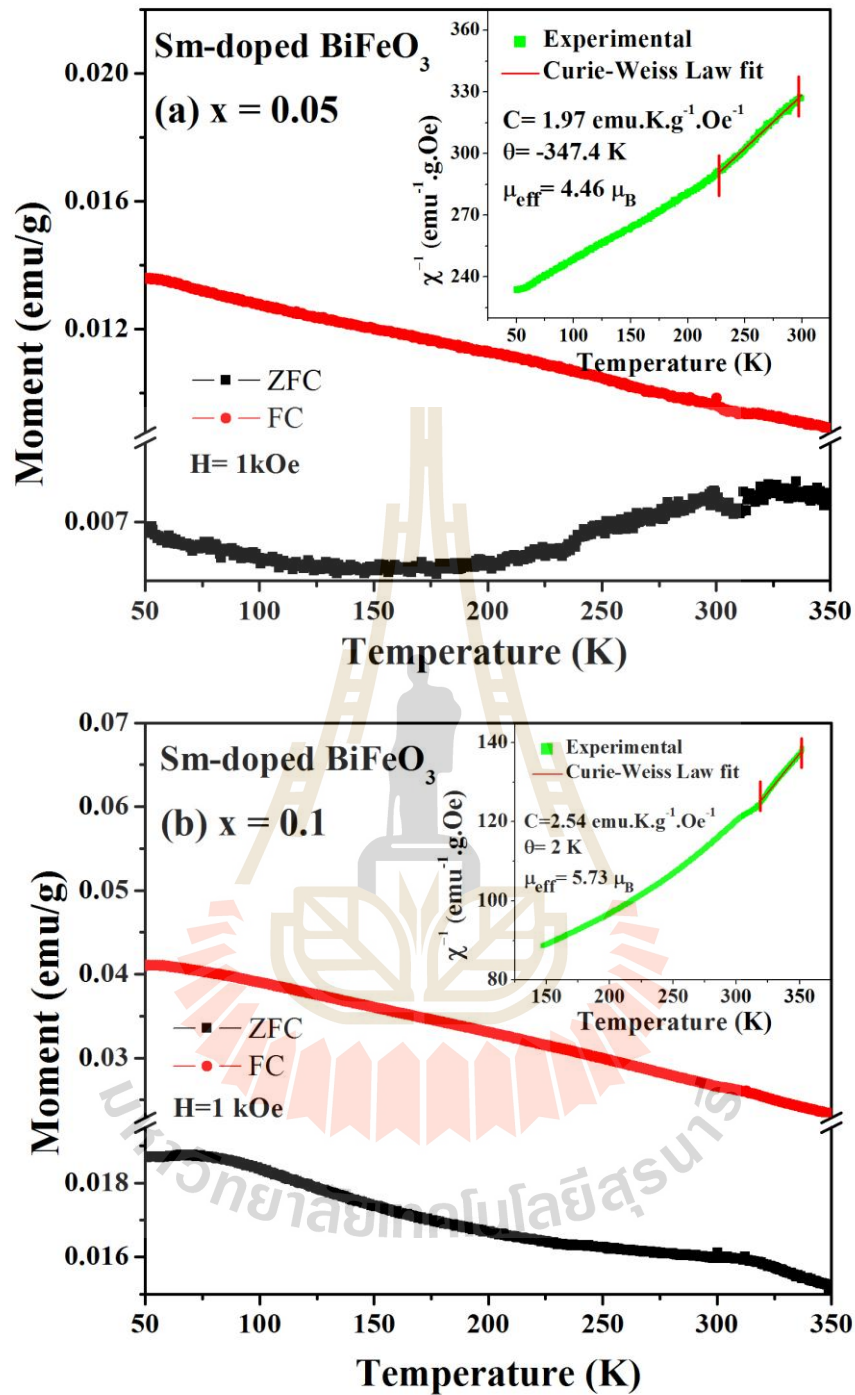


Figure 4.19 (a), (b), (c), and (d) display the temperature-dependent magnetization (M - T) curves of Sm-doped BiFeO₃ samples, respectively. Inset: fitting the data to the Curie-Weiss law between 150 and 300 K under 1 kOe as a function of temperature and fitting result using the Curie-Weiss law.

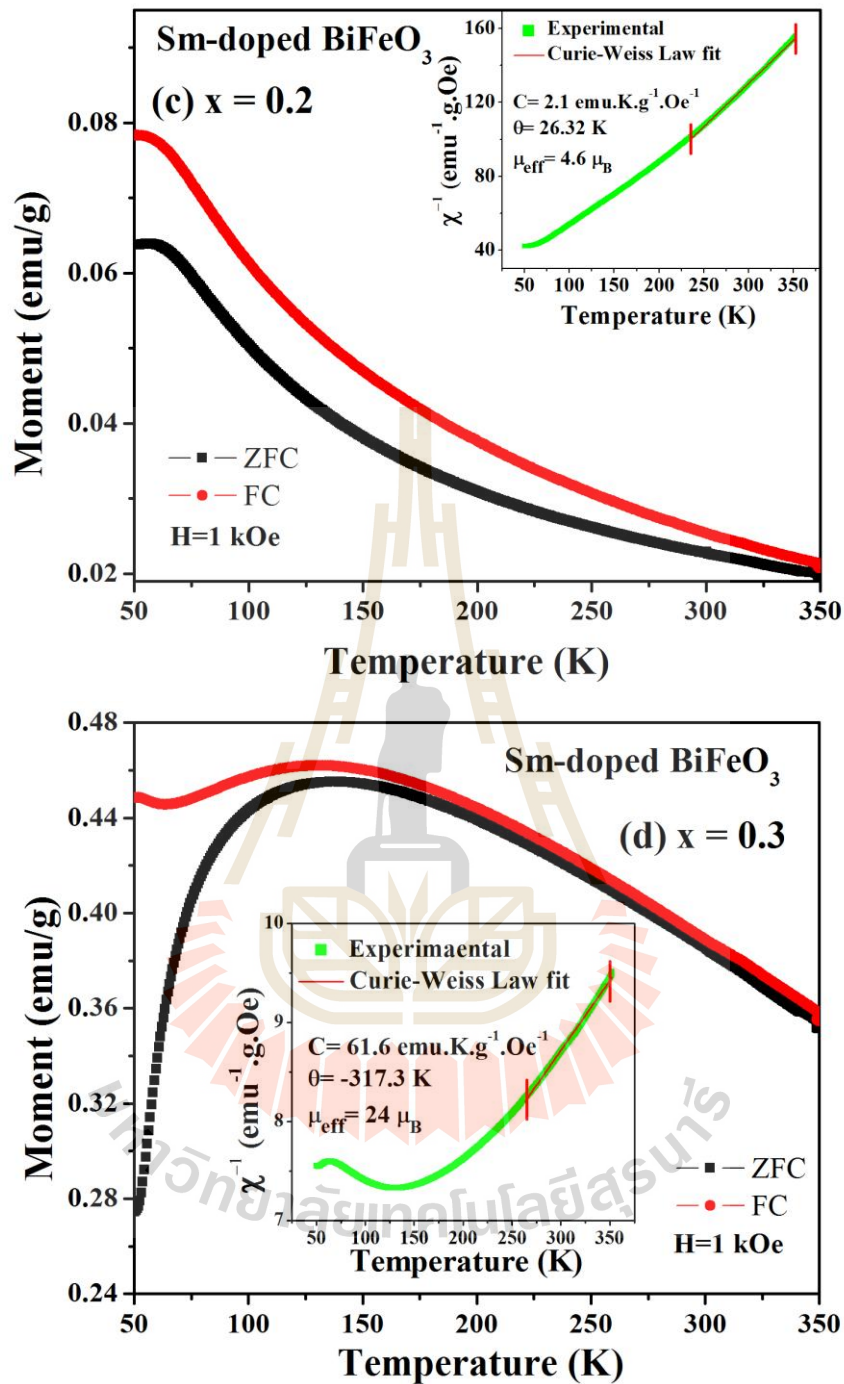


Figure 4.19 (a), (b), (c), and (d) display the temperature-dependent magnetization (M–T) curves of Sm-doped BiFeO₃ samples, respectively. Inset: fitting the data to the Curie–Weiss law between 150 and 300 K under 1 kOe as a function of temperature and fitting result using the Curie–Weiss law (Continued).

4.4 Ceramic characterization: crystal structure and morphologies

4.4.1 Crystal structure and phase formation

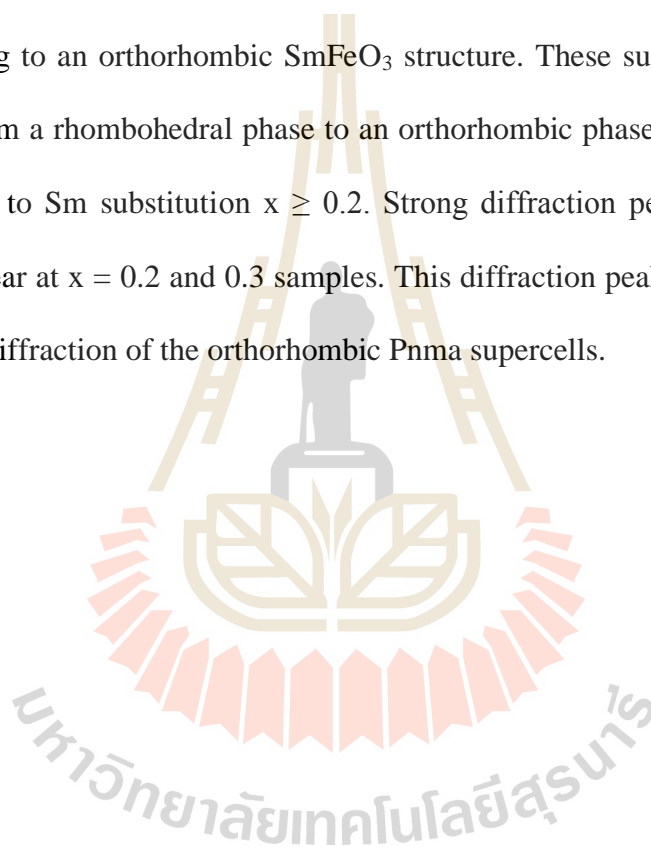
X-ray diffraction patterns of La-, Ba-, and Sm-doped BiFeO₃ bulk ceramics are exhibited in Figures 4.20–4.22. All the samples show XRD main peaks corresponding to the rhombohedral perovskite-like BiFeO₃ structure. Besides the formation of this pattern, some of samples represent small amounts of the impurity phases, i.e., Bi₂Fe₄O₉ phase (# mark) and Bi₂O₃ (* mark) for La- and Ba- doped BiFeO₃ systems. Sm-doped samples exhibit extra phase of SmFeO₃ as an impurity phase for high concentration of Sm doping (Bi_{0.8}Sm_{0.2}FeO₃ and Bi_{0.7}Sm_{0.3}FeO₃). The presence of Bi₂Fe₄O₉ and Bi₂O₃ as impurity phases in rare earth substituted bismuth ferrite samples have been reported by several authors (Rai *et al.*, 2011; Yang *et al.*, 2010). Figure 4.20 shows the XRD patterns of the Ba-doped BiFeO₃ system. All the diffraction peaks in the patterns correspond to BiFeO₃ phase in rhombohedrally distorted perovskite structure of R3c space group (JCPDS no.86–1518). Some amounts of Bi₂Fe₄O₉ and Bi₂O₃ were also detected in the impurity phases of the parent BiFeO₃ ceramics because of the volatilization of Bi₂O₃ during heat treatment. Figure 4.20(b) displays an enlarged view of XRD patterns in the vicinity of $2\theta \sim 32^\circ$ that has not resulted in structural transition of rhombohedral structure of pure BiFeO₃ because of double splitting of (104) and (110) diffraction peaks that do not merge into a single peak. This implies that there is no significant reduction in the lattice symmetry of the Bi_{1-x}Ba_xFeO₃ system. Similarly, some observations reported that no structural transitions are available for alkaline earth doped BiFeO₃ (Dhir *et al.*, 2014). However, the addition of Ba²⁺ ions in BiFeO₃ structure is confirmed by the shifting of diffraction peaks towards lower 2θ when compared to the parent BiFeO₃ sample. A

possible reason for this might be the fact that the ionic radius of Ba^{2+} (1.42\AA) is larger than that of Bi^{3+} ions (1.17\AA).

The diffraction peak positions for La-doped BiFeO_3 indicate slight changes in peaks as compared with pure BiFeO_3 . The main diffraction peaks in the XRD patterns for the La-doped BiFeO_3 samples were identified in a BiFeO_3 rhombohedral phase (R3c). The intensity of double split peaks near 32° ; (104) and (110) gradually weakens and the splits of these peaks thus decreasing them. In addition, the XRD peaks near around 39° ; (006) and (202) and 51° ; (116) and (122) also become broad and the peaks (006), (116), and (122) almost disappear when $x \leq 0.2$. It can be seen that all diffraction peaks slightly shift towards higher angles indicating a decrease in lattice parameters due to the addition of La atoms with slightly smaller ionic radius (1.22\AA) in Bi atoms (1.17\AA). The XRD pattern suggests the presence of bismuth ferrite secondary phase Bi_2O_3 (* marked) in La-doped sample with $x = 0.05$. Because of the kinetic formation, a composition of BiFeO_3 as a major phase along with other secondary phases was obtained during the synthesis process. It is noted that with increasing substitution of La in the samples $x = 0.1-0.3$ has been marked by an absence of the intensities of the impurity peaks. It is seen that doping with La eliminates the impurity phase, suggesting that the substitution of La^{3+} ions can spike the formation of impurity phases.

The XRD patterns of $\text{Bi}_{1-x}\text{Sm}_x\text{FeO}_3$ with $x = 0.05, 0.1, 0.2,$ and 0.3 ceramics are shown in Figure 4.22. The XRD patterns of Sm-doped samples show that all the main diffraction peaks can be indexed according to the rhombohedral phase of the BiFeO_3 structure. Some traces of secondary phases $\text{Bi}_2\text{Fe}_4\text{O}_9$ and Bi_2O_3 were not observed in the XRD patterns with $0.05 \leq x \leq 0.1$. The existence of the split peaks in

both samples confirms the distorted rhombohedral structure in these samples. The substitution of Sm^{3+} in BiFeO_3 does not lead to any structural transition up to 10% doping of Sm which can be possible with higher content as evidenced in the $x > 0.2$ doping in BiFeO_3 samples. The presence of the split peaks in the $\text{Bi}_{0.95}\text{Sm}_{0.05}\text{FeO}_3$ and $\text{Bi}_{0.9}\text{Sm}_{0.1}\text{FeO}_3$ samples confirms the distorted $R3c$ rhombohedral structure. For Sm-doped BiFeO_3 with $x \geq 0.2$, a new phase occurs whose peaks can be assigned corresponding to an orthorhombic SmFeO_3 structure. These suggest that a structural transition from a rhombohedral phase to an orthorhombic phase with the Pnma space group is due to Sm substitution $x \geq 0.2$. Strong diffraction peaks $\sim 25.4^\circ$ and $\sim 51^\circ$ begin to appear at $x = 0.2$ and 0.3 samples. This diffraction peak should come from a superlattice diffraction of the orthorhombic Pnma supercells.



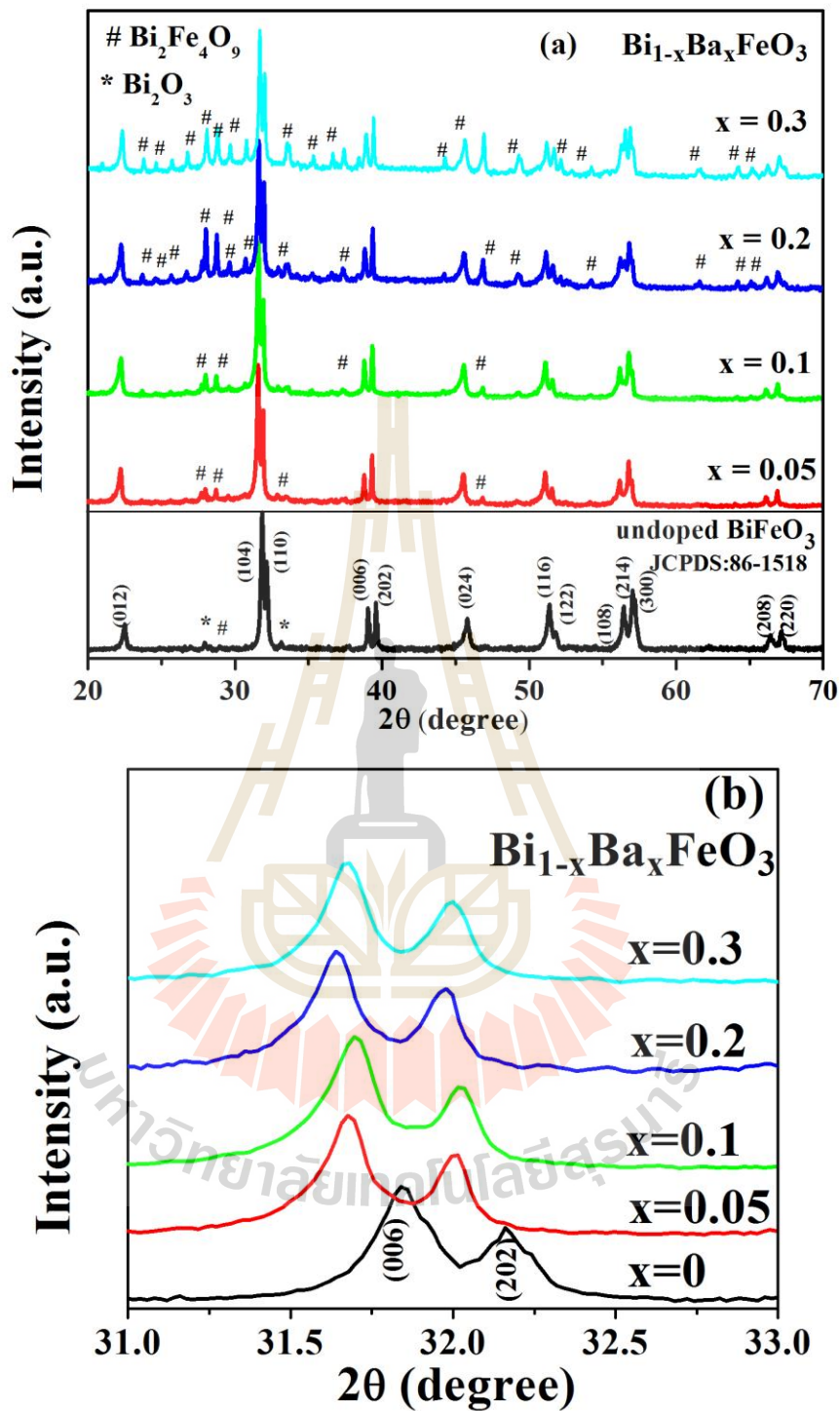


Figure 4.20 (a) X-ray diffraction patterns of $\text{Bi}_{1-x}\text{Ba}_x\text{FeO}_3$ with $x = 0, 0.05, 0.1, 0.2,$ and 0.3 ; (* and # indicate the secondary phase of Bi_2O_3 and $\text{Bi}_2\text{Fe}_4\text{O}_9$) and (b) an enlarged view of diffraction peaks at $2\theta \sim 32^\circ$.

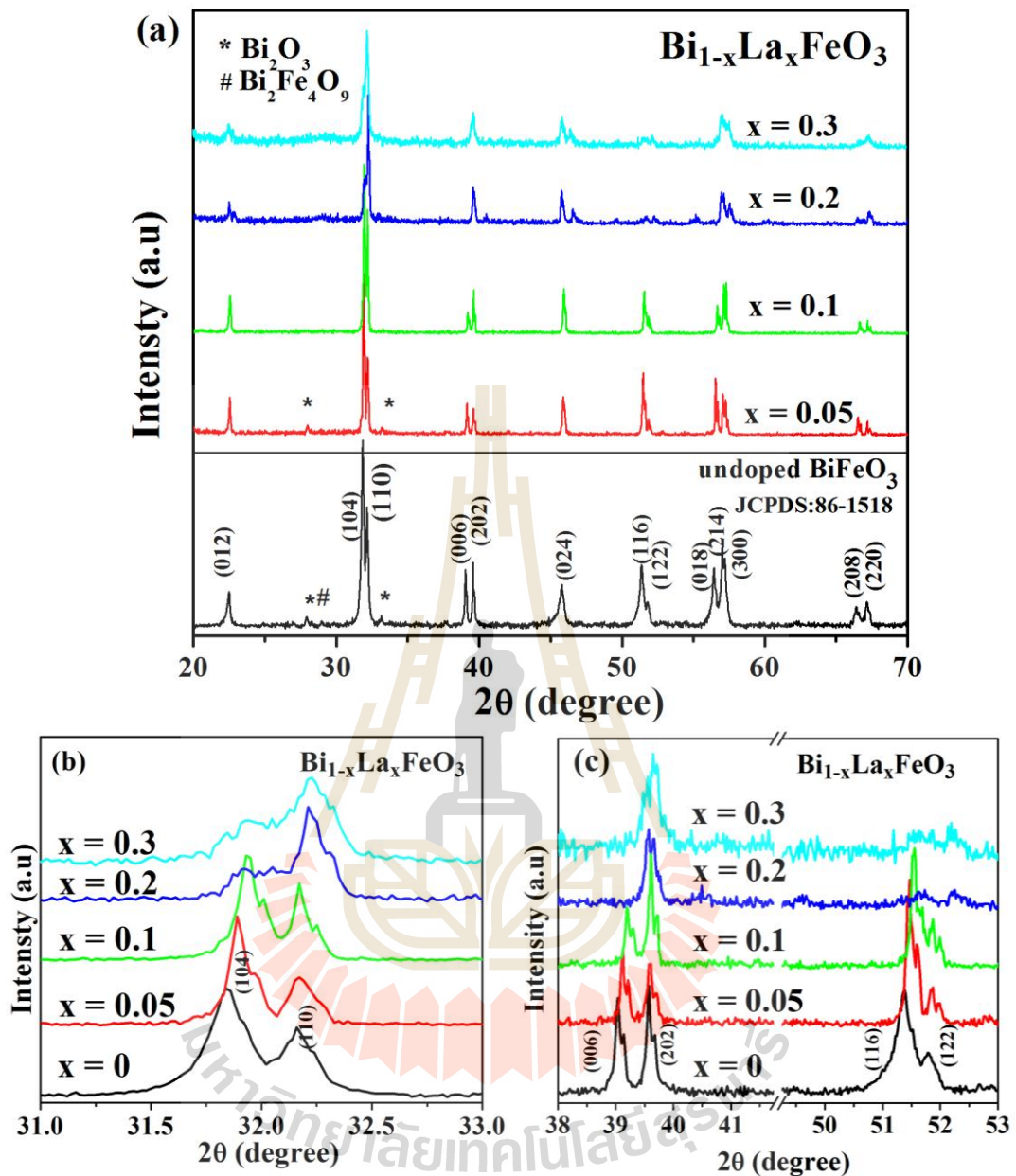


Figure 4.21 X-ray diffraction patterns of $\text{Bi}_{1-x}\text{La}_x\text{FeO}_3$ with $x = 0, 0.05, 0.1, 0.2,$ and 0.3 ; (* and # indicate the secondary phase of Bi_2O_3 and $\text{Bi}_2\text{Fe}_4\text{O}_9$), (b) an enlarged view of diffraction peaks at $2\theta \sim 32^\circ$, and (c) at $2\theta \sim 39^\circ$, and $2\theta \sim 51^\circ$.

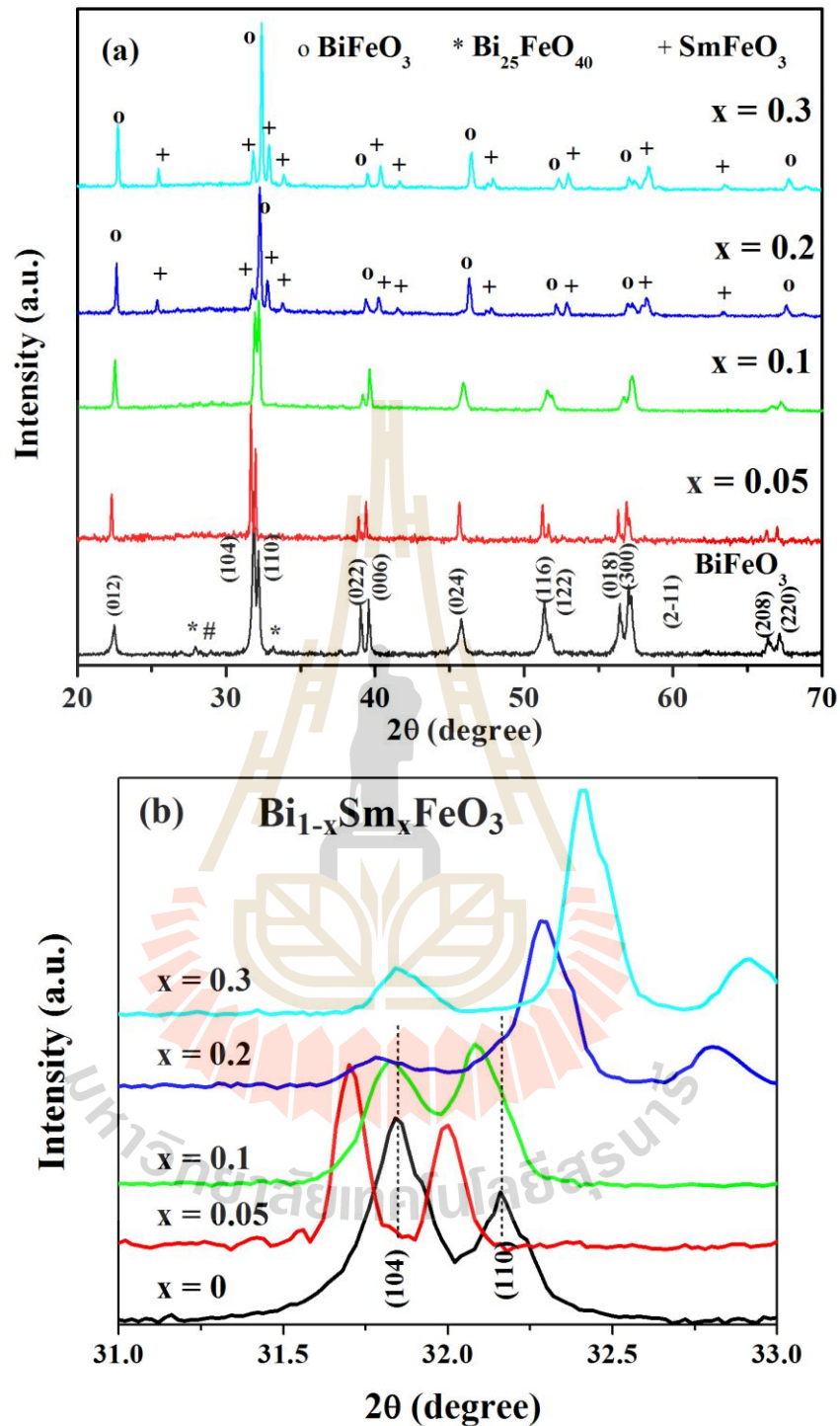


Figure 4.22 X-ray diffraction patterns of $\text{Bi}_{1-x}\text{Sm}_x\text{FeO}_3$ with $x = 0, 0.05, 0.1, 0.2,$ and 0.3 ; (* and # indicate the secondary phase of Bi_2O_3 and $\text{Bi}_2\text{Fe}_4\text{O}_9$) and (b) an enlarged view of diffraction peaks at $2\theta \sim 32^\circ$.

4.4.2 Surface morphology

A knowledge of surface microstructure in the materials is a powerful tool for the understanding of the electrical transport properties of the materials. The microstructure and surface morphology of BiFeO₃-based ceramics were investigated by using scanning electron microscopy (SEM). The microstructure and back scattering images of Bi_{1-x}A_xFeO₃ ceramics sintered at 800 °C for 3 h were revealed in Figure 4.23. It is clearly seen that the rare earth elements doped in BiFeO₃ have a significant effect on the microstructure of the parent BiFeO₃ ceramics; the microstructure changes with the Ba-, La-, and Sm-doped concentrations. In comparison, the microstructure of pure BiFeO₃ ceramics with the rare earth and alkaline earth doped BiFeO₃ ceramics, it is found that these elements have a significant effect on the microstructure of BiFeO₃ ceramics, for example porosity, grain size, and grain shape. There are a few properties which are absolutely independent of microstructure, thus the change in grain size may be the effects on the dielectric and electrical properties of doped-BiFeO₃ ceramics systems. The substitution of rare earth and alkaline elements in Bi-site is related to the evolution of the microstructure of BiFeO₃-based ceramics and these are divided into 3 different groups of samples preparation: Bi_{1-x}Ba_xFeO₃, Bi_{1-x}La_xFeO₃, and Bi_{1-x}Sm_xFeO₃ respectively.

The SEM micrographs of surface of Ba-doped BiFeO₃ ceramics are illustrated in Figure 4.23(b)–(e), showing the substitution of Ba has gradually changed the morphologies. The morphological analysis indicates uniformly distributed densely packed grain having fine grain boundaries. It can be also observed that the grain sizes decrease with decreases in Ba content and dense microstructures were obtained in all

samples. It can be seen that the undoped BiFeO_3 sample consists of relatively large grains with the average grain size of about $6.07 \pm 0.9 \mu\text{m}$. It is clear from Figure 4.23 that the average grain size slightly decreases with increasing Ba concentration. The average grain sizes of Ba-doped BiFeO_3 ceramics are 6.49 ± 0.9 , 5.02 ± 0.6 , 3.65 ± 0.4 and $3.28 \pm 0.4 \mu\text{m}$ for $x = 0.05$, 0.1 , 0.2 , and 0.3 , respectively. These SEM images show that microstructures are highly dense structures comprised of uniform grains of different sizes. A reduction of small geometry grains were still detected in the grain boundary or junction regions. With increases in Ba doping, most of the small geometrical grains become larger, the increases in the amount of these grains and these small grains tend to increase when the Ba doping level increases. The impurity phases were identified by XRD results in Ba-substituted BiFeO_3 , Bi_2O_3 and Fe-rich $\text{Bi}_2\text{Fe}_4\text{O}_9$, and were observed to increase the intensity of the diffraction peaks of these impurity phases with increases in Ba doping concentrations. From these results, it can be proposed that the small geometrical grain that in the surface microstructure of Ba-doped BiFeO_3 ceramics may be the impurity phases of Bi_2O_3 and Fe-rich $\text{Bi}_2\text{Fe}_4\text{O}_9$, as obtained from by their XRD data. As shown in Figure 4.23(b)–(e) (right), back scattered images of Ba-doped BiFeO_3 ceramics confirm the geometrical shapes, white regions, which represented the impurity phases in the ceramics.

Two distinct microstructure areas can be observed on the surface that differs in the grain shapes for doped- BiFeO_3 ceramics. The first one, with fine grain and large grain size and the other one, with a similar smaller geometrical grain size, and grain sizes from between 0.1 and $0.3 \mu\text{m}$. In this work, these results strongly imply that the average grain sizes observed in the rare earth elements substituted in BiFeO_3 systems have decreased. Therefore, doping can inhibit grain growth and result in a distribution

of small grain sizes in the samples, which is consistent with several reports (Makhdoom *et al.*, 2012). It has been suggested that the grain growth depends on the concentration of the oxygen vacancies and the diffusion rates of the ions. Because of the easy volatile nature of Bi ions, its evaporation generates large amounts of oxygen vacancies in the parent BiFeO₃, making it free for the ions to diffuse, which leads to a large grain size as compared to the rare earth doped BiFeO₃ ceramics. Another possible reason for the suppressed grain growth mechanism, is the grain boundary pinning, when the impurity or dopants are often concentrated at the interface (Sanjoom and Rujijanagul, 2013). These impurity phases may be formed at the grain boundary as a result of grain growth because the solutions which are concentrated at the interface have to be carried along. The diffusion efficiency of dopant elements such as Nb in BaTiO₃ are lower than the diffusion efficiency of the main matrix of the ceramics, hence the deceleration of the grain boundary mobility which is called the solute drag (Brzozowski *et al.*, 2002). In addition, a large amount of pores exist in some large grains on the fracture due to the rapid grain growth resulting from the formation of a liquid phase which occurs during the sintering process.

To confirm the prediction of grains and small grains sizes in the microstructure, as shown in Figure 4.23(right), backscattered electron images of Bi_{1-x}Ba_xFeO₃ system. Since there are multiphases in these ceramics, it is necessary to know the distribution of the multiphases observed in the microstructure of Bi_{1-x}Ba_xFeO₃ ceramics. Figure 4.23(right) reveals the backscattered electrons of pure BiFeO₃ ceramics, where the grey regions represent the matrix BiFeO₃ and the dark regions, where there are formations of small grains of the secondary phase Fe-rich, Bi₂Fe₄O₉. The lighter coloured granular, non-uniform grains are probably the Bi-rich,

Bi_2O_3 which can be identified from the XRD results. It can also be observed that two component phases which coexist in the morphology vary with the relative of addition of Ba ions.



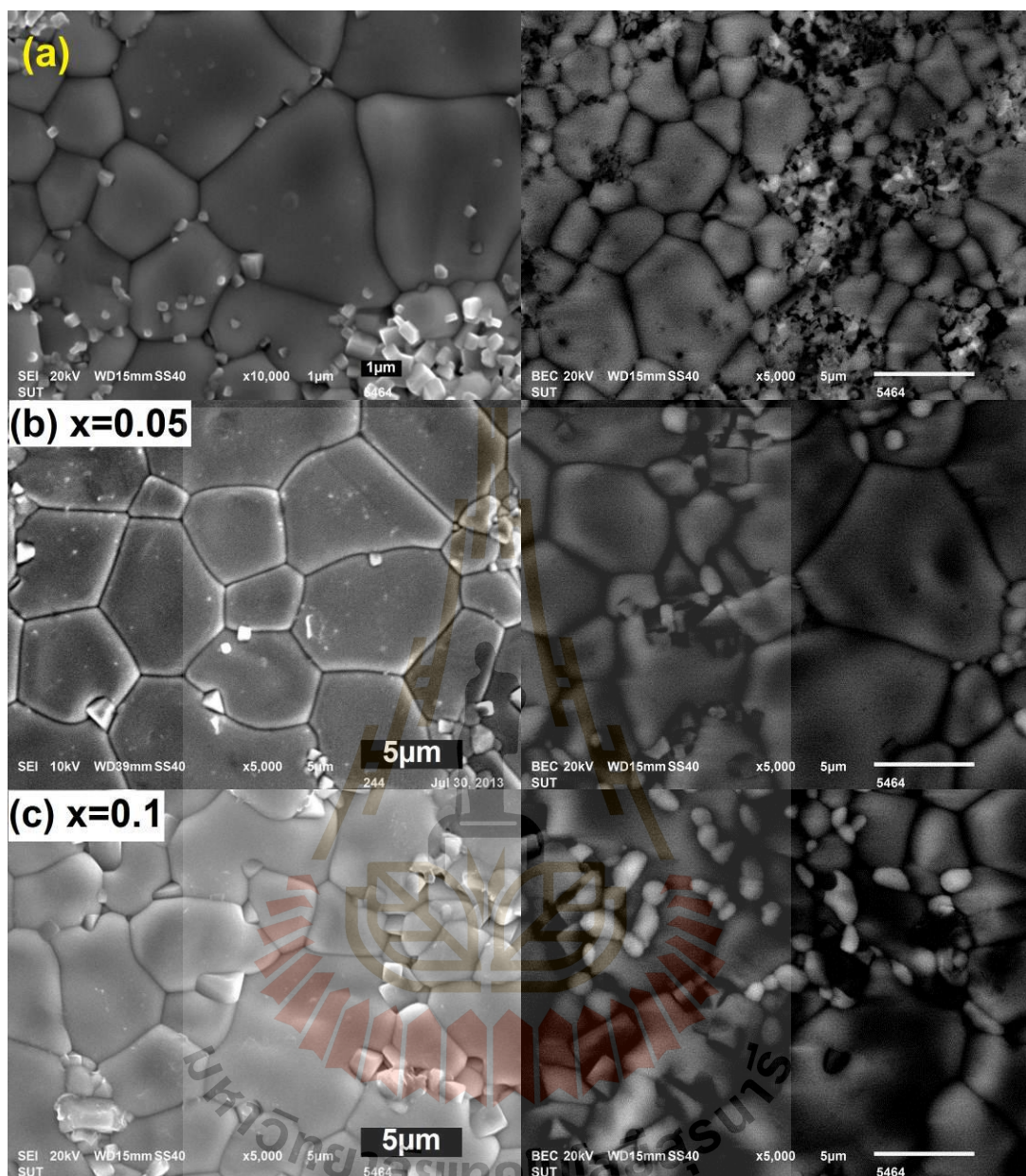


Figure 4.23 SEM micrographs for $\text{Bi}_{1-x}\text{Ba}_x\text{FeO}_3$ powders calcinated at $800\text{ }^\circ\text{C}$ for 3 h as a function of Ba content: (a) $x = 0$, (b) $x = 0.05$, (c) $x = 0.1$, (d) $x = 0.2$, and (e) $x = 0.30$.

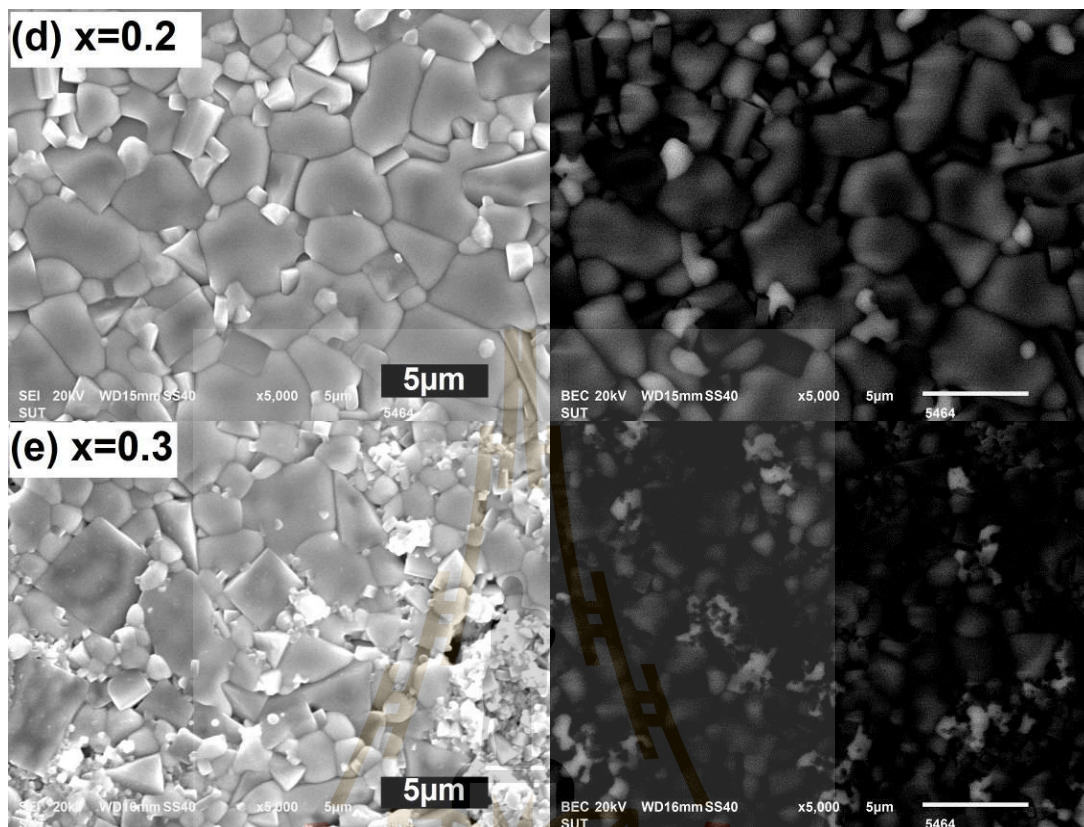


Figure 4.23 SEM micrographs for $\text{Bi}_{1-x}\text{Ba}_x\text{FeO}_3$ powders calcinated at 800°C for 3 h as a function of Ba content: (a) $x = 0$, (b) $x = 0.05$, (c) $x = 0.1$, (d) $x = 0.2$, and (e) $x = 0.30$ (Continued).

As shown in Figure 4.24(a)–(d), in the first group, the average grain size becomes larger than those of the ceramics with increases of La substituted up to 5% which is expected to be La substitution effect. It can be clearly seen that the average grain sizes of La-doped BiFeO₃ ceramics decrease with increases in the La contents. This result means that the La doping can suppress the grain growth in the ceramics which results in small grain sizes in the samples. This result is similar to that observed in the literature (Ianculescu *et al.*, 2011). From the SEM images, it is found that that grain size becomes lower with increases in La doping levels and the distribution of the grain size changes to a non-uniform nature. The average grain size is about 6.57±0.8, 5.47±0.9, 2.67±0.6, and 0.9±0.1 μm with the compositions x = 0.05, 0.1, 0.2, and 0.3 respectively. The decrease in the grain size of La-doped BiFeO₃ ceramics can be explained by the suppression of oxygen vacancies which results in the slow oxygen ions motion and lower diffusion grain growth rate (Deng *et al.*, 2015; Dai *et al.*, 2016). Since the highly volatile nature of Bi ions generates a large intensity of oxygen vacancies which make it easy to diffuse. As a result, the pure BiFeO₃ has a larger grain size than that of the La-doped samples. In general, rare earth elements can suppress grain growth in perovskite structure, which is probably attributable to their low diffusivity of grain growth (Sanjoom *et al.*, 2013). Thus, the observed decrease in the grain size of La substituted in BiFeO₃ may be suppressed by the occupation of certain probable evaporated Bi ions site by La ions at low doping levels. Most of them do not observe the pores in the surface morphology, except the Bi_{0.7}La_{0.3}FeO₃ ceramics, for which a small amount of pores can be seen on the surface. The density of the ceramics is observed to decrease systematically in small amounts with densities

of about (76 %) for the $x = 0.3$ sample. However, the appearance of some pores in the $\text{Bi}_{0.7}\text{La}_{0.3}\text{FeO}_3$ ceramics is less than that observed in the Sm-doped BiFeO_3 ceramics.

It is important to note that the grain growth has an effect on the evolution of the microstructure of La-doped BiFeO_3 ceramics which is also similar to that observed in the Ba doping. As revealed in Figure 4.24, the set of small grain sizes was observed in the microstructure with increases in La content up to 5% samples. Most of them exhibit a regular shape and are located at the corners of large regular grains with grain sizes in the range of about $0.5\text{--}0.8\ \mu\text{m}$. The grain sizes and small amounts of these small grain sizes are found to decrease when the La doping concentration increases. The microstructures of $\text{Bi}_{0.8}\text{La}_{0.2}\text{FeO}_3$ and $\text{Bi}_{0.7}\text{La}_{0.3}\text{FeO}_3$ ceramics reveal the disappearance of the small grain sizes. From the XRD results, it is observed that the impurity phases of Bi_2O_3 and $\text{Bi}_2\text{Fe}_4\text{O}_9$ are exhibited in the $\text{Bi}_{1-x}\text{La}_x\text{FeO}_3$ ($x = 0.05, 0.1$) ceramics which is revealed by the XRD results as previously shown in section 4.1.2. In addition, the XRD patterns show the disappearance of impurity phases in $\text{Bi}_{0.8}\text{La}_{0.2}\text{FeO}_3$ and $\text{Bi}_{0.7}\text{La}_{0.3}\text{FeO}_3$ ceramics. This variation in morphological behaviour is in good agreement with the XRD data, which means that the small grain sizes observed in the samples may be related to those secondary phases, as exhibited in the XRD results.

However, a dramatic microstructure is found to change for the samples with increased La contents up to $x = 0.05$. The inhibiting effect of the donor dopant on the grain growth process becomes evident, as it is found that the composition $x = 0.05$ has a slightly larger average grain size. Several approaches to grain growth prevention for the dopant levels above critical concentration in the perovskite BaTiO_3 were proposed to vary the features of the microstructure, including kinetic aspects (Daniel and

Härdtl, 1976), thermodynamic reasons (Drofenik, 1999), as well as grain boundary fracture phenomena (Desu and Payne, 1990). As can be seen in the SEM image of $\text{Bi}_{0.95}\text{La}_{0.05}\text{FeO}_3$ ceramics, the grain size is slightly larger and some small grain sizes were also observed. Therefore, in this case, we can conclude that the La composition at $x = 0.05$ is near the critical doping level for a grain growth inhibiting process.



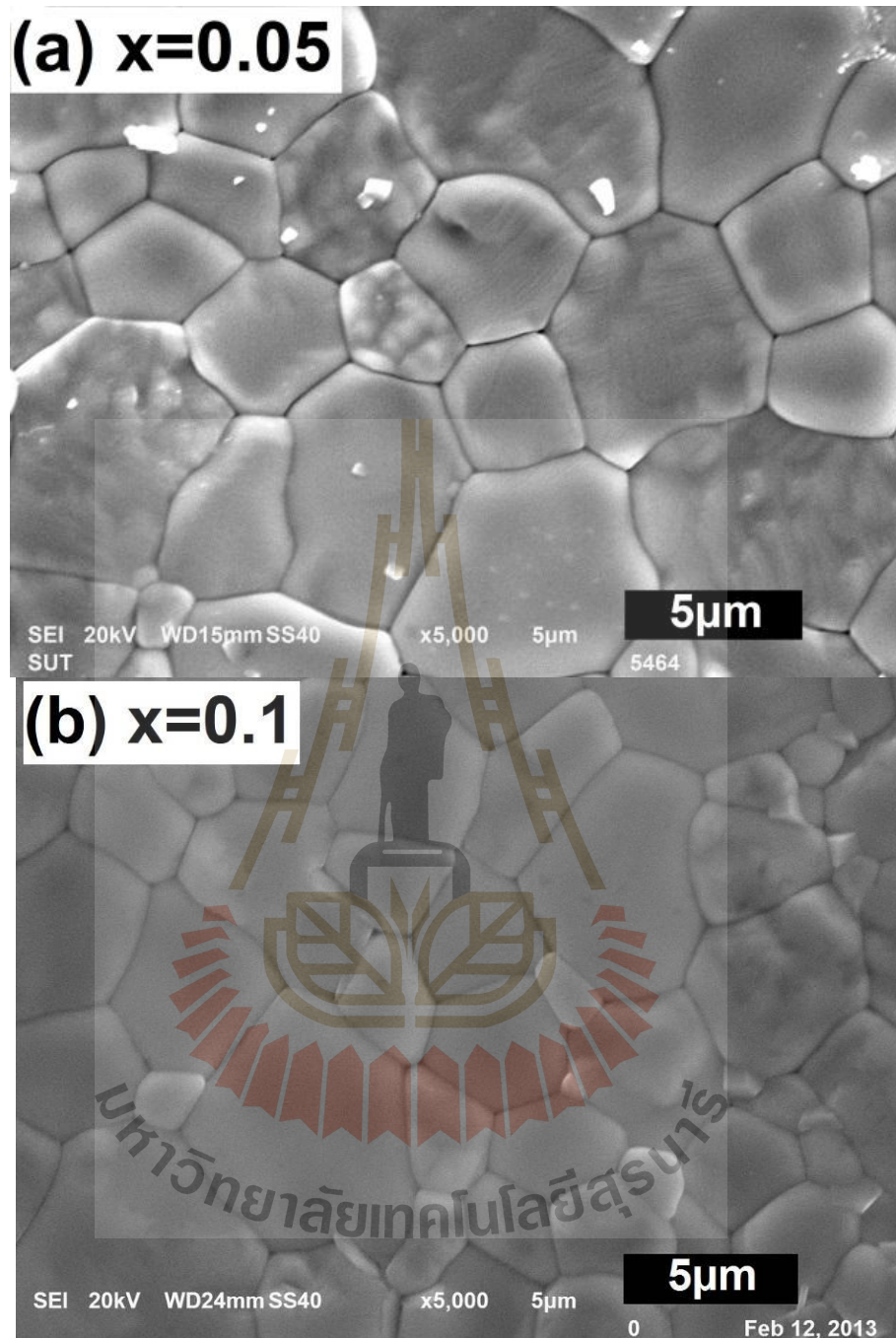


Figure 4.24 SEM micrographs for $\text{Bi}_{1-x}\text{La}_x\text{FeO}_3$ powders calcinated at 800 °C for 3 h as a function of La content: (a) $x = 0$, (b) $x = 0.05$, (c) $x = 0.1$, (d) $x = 0.2$, and (e) $x = 0.30$.

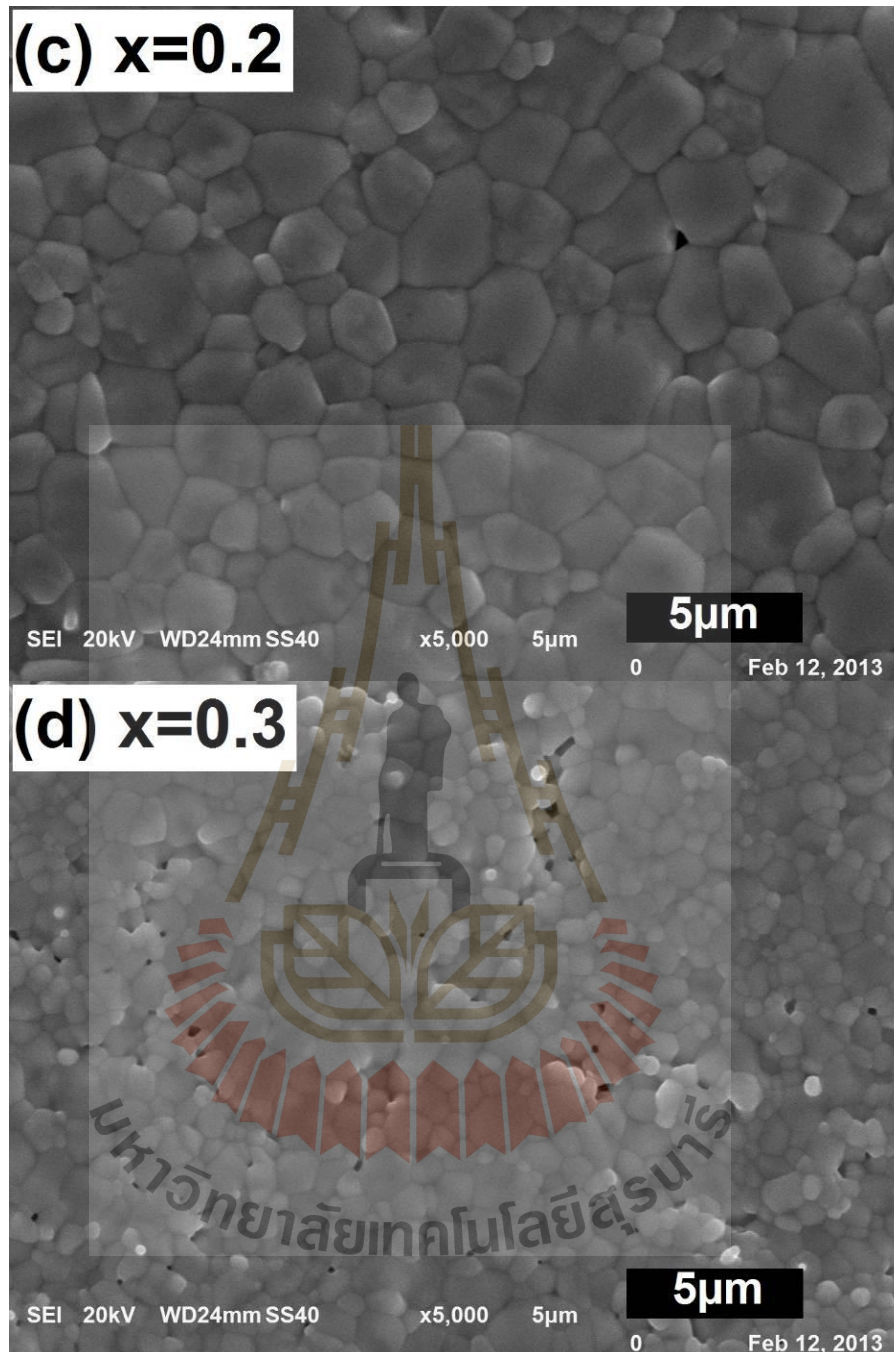


Figure 4.24 SEM micrographs for $\text{Bi}_{1-x}\text{La}_x\text{FeO}_3$ powders calcinated at 800 °C for 3 h as a function of La content: (a) $x = 0$, (b) $x = 0.05$, (c) $x = 0.1$, (d) $x = 0.2$, and (e) $x = 0.30$ (Continued).

The microstructure and surface morphologies of $\text{Bi}_{1-x}\text{Sm}_x\text{FeO}_3$ ($x = 0, 0.05, 0.1, 0.2, \text{ and } 0.3$) sintered at $800\text{ }^\circ\text{C}$ for 3 h ceramics are indicated by significant variations in microstructure, as shown in Figure 4.25(a)–(d). As can be seen in these SEM images, the grain size of pure BiFeO_3 has large grains in the range of about $6.07\text{ }\mu\text{m}$ which is non-uniform whereas the Sm doping samples exhibit lower grain sizes with increases in Sm doping of BiFeO_3 . The obtained average grain size are 4.09 ± 0.6 , 2.62 ± 0.5 , 1.54 ± 0.3 , and $0.71\pm 0.2\text{ }\mu\text{m}$ for $x = 0.05, 0.1, 0.2, \text{ and } 0.3$, respectively. According to the XRD patterns, phase purity for both the samples can be observed confirming the fine grain in the microstructure. It is very interesting to observe the agglomerated grains at the surface with present amount of porosity are clearly revealed in the micrographs of $\text{Bi}_{0.7}\text{Sm}_{0.3}\text{FeO}_3$ and $\text{Bi}_{0.8}\text{Sm}_{0.2}\text{FeO}_3$ samples. Moreover, can be clearly seen, the amount of pores observed in the surface morphologies of $\text{Bi}_{0.7}\text{Sm}_{0.3}\text{FeO}_3$ and $\text{Bi}_{0.8}\text{Sm}_{0.2}\text{FeO}_3$ bulk ceramics is larger than that observed in microstructure of $\text{Bi}_{1-x}\text{La}_x\text{FeO}_3$ ceramics. The porosity observed in the grain boundary region is noticeably higher compared with the undoped BiFeO_3 and low level of La-doped ($x = 0.05$ and 0.1) samples. This result means that these two samples have low density. However, it is not possible to observe the cluster of secondary phases in the back scattered images of those samples because they have a very small grain size that is beyond the limits of the scanning microscope. The amounts of pores observed in the microstructure and the decrease in the grain size for $\text{Bi}_{0.8}\text{Sm}_{0.2}\text{FeO}_3$ and $\text{Bi}_{0.7}\text{Sm}_{0.3}\text{FeO}_3$ samples can be explained by a diffusion mechanism. Moreover, clusters of smaller, randomly distributed grain sizes in the main BiFeO_3 phase were observed in the $\text{Bi}_{0.95}\text{Sm}_{0.05}\text{FeO}_3$ and $\text{Bi}_{0.9}\text{Sm}_{0.1}\text{FeO}_3$ samples. Thus, the ceramics density tended to decrease with increasing Sm content ($x \geq 0.2$). As presented in the

XRD patterns of Sm-doped BiFeO₃ samples, it can be suggested that the SmFeO₃ phase is indicated by the surface of the Bi_{0.95}Sm_{0.05}FeO₃ and Bi_{0.9}Sm_{0.1}FeO₃ samples as shown in Figure 4.25(a) and (b) (zone delimited by the circle). This observation of the phase formation corresponds to the SEM micrographs.

According to the SEM results, the main points concerning the mechanisms of phase formation and microstructural evolution can be summarized as follows. (i) The impurity phases of Bi₂Fe₄O₉ and Bi₂O₃ can be observed in the microstructure of high concentration of dopants, especially in all Ba-doped samples. (ii) The portion of porosity observed in the microstructure tends to increase with increasing content of dopants. (iii) With low addition of Ba and La contents, the grain size slightly increases and then decreases with a high addition of dopant content. It can be suggested that the grain growth depends on the diffusion rate of the ions (Beniwal *et al.*, 2016; Makhdoom *et al.*, 2012), melting point of dopant (Valant *et al.*, 2007) and the concentration of oxygen vacancies. The materials with low melting point such as aluminium (Al) have high atomic motion and will show high grain growth. While metal with a high melting point will have a small grain size during the growth process (Gupta, 2010). Therefore, doping of rare earth elements with higher melting temperature than the sintered temperature also has effects on the relationship between solid and liquid phases.

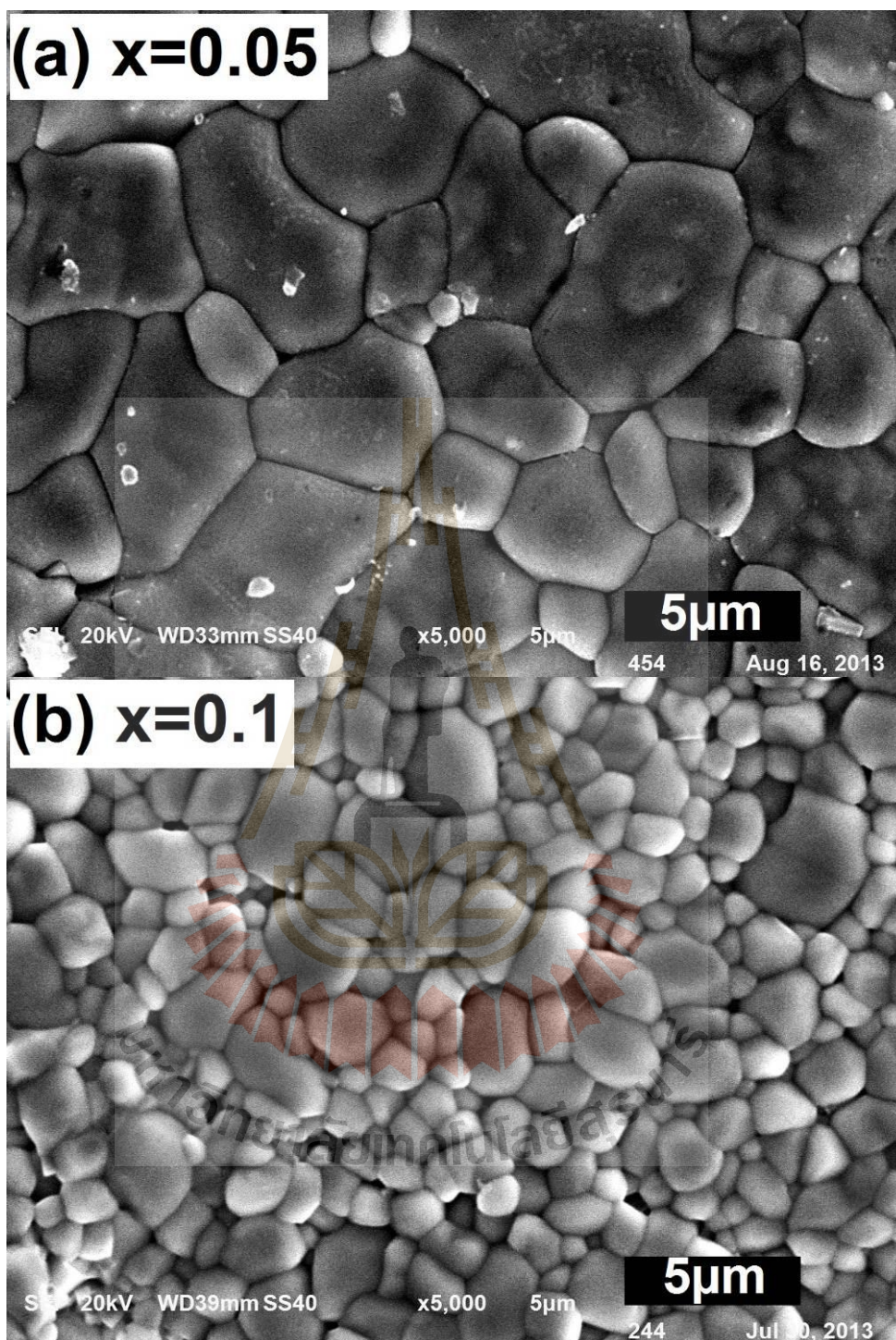


Figure 4.25 SEM micrographs for $\text{Bi}_{1-x}\text{Sm}_x\text{FeO}_3$ powders calcinated at 800 °C for 3 h as a function of Sm content: (a) $x = 0$, (b) $x = 0.05$, (c) $x = 0.1$, (d) $x = 0.2$, and (e) $x = 0.30$.

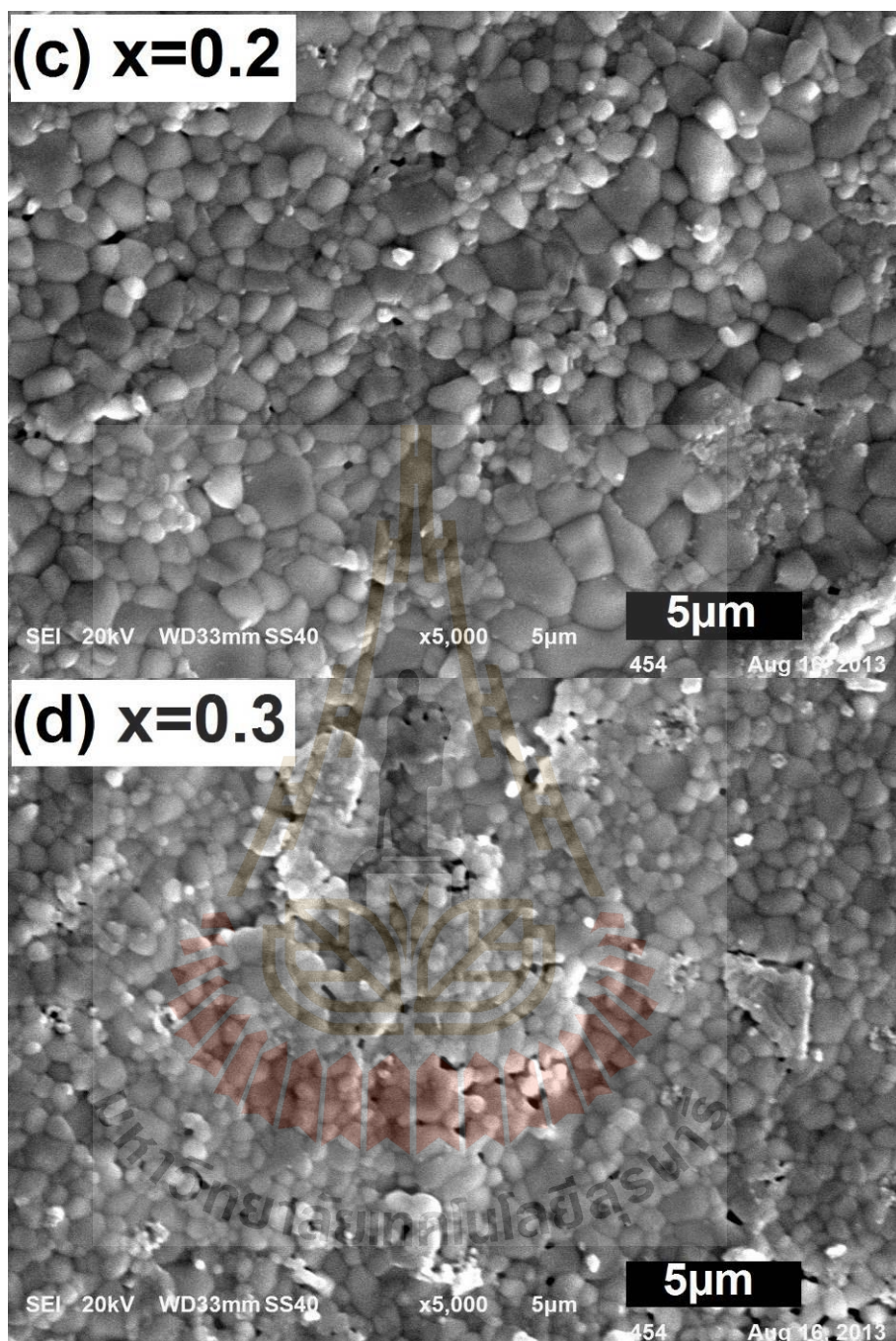


Figure 4.25 SEM micrographs for $\text{Bi}_{1-x}\text{Sm}_x\text{FeO}_3$ powders calcinated at 800 °C for 3 h as a function of Sm content: (a) $x = 0$, (b) $x = 0.05$, (c) $x = 0.1$, (d) $x = 0.2$, and (e) $x = 0.30$ (Continued).

Table 4.6 Relative densities and average grain size of undoped BiFeO₃ and Ba-, La-, and Sm-doped BiFeO₃ sintered at 800 °C for 3 h.

Doping level	Ba-doped BiFeO ₃		La-doped BiFeO ₃		Sm-doped BiFeO ₃	
	Relative densities	Grain size (μm)	Relative densities	Grain size (μm)	Relative densities	Grain size (μm)
x = 0	84.2	6.07±0.9	84.2	6.07±0.9	84.2	6.07±0.9
x = 0.05	91.0	6.49±0.9	93.1	6.57±0.8	104.2	4.09±0.6
x = 0.1	88.8	5.02±0.6	92.7	5.47±0.9	94.4	2.62±0.5
x = 0.2	89.2	3.65±0.4	90.1	2.67±0.6	96.9	1.54±0.3
x = 0.3	85.3	3.28±0.4	76.1	0.9±0.1	77.7	0.71±0.2

4.5 Frequency and temperature dependence on dielectric properties

4.5.1 Dielectric properties as a function of frequency for doped BiFeO₃ ceramics at room temperature

Figure 4.26 shows the variations in dielectric properties with frequency of sintered Bi_{1-x}Ba_xFeO₃ ceramics at room temperature. It is found that the dielectric constant slightly drops to a low value in a high frequency region ($> 10^5$ Hz). All of the samples exhibit dielectric relaxation behaviour which is the same as La-doped BiFeO₃ ceramics and which also agrees well with what was reported by (Mahbub *et al.*, 2015). In the case of doped BiFeO₃ samples, the dielectric constant decreases when substituted by Ba ions in all measured frequency ranges. The dielectric constant values as compared to pure BiFeO₃ increased from 10.4×10^3 to 25.3×10^3 with the addition of Ba ions to 5% and 10% whereas the dielectric constant is lower than that of BiFeO₃ for 20% and 30% of Ba doped in BiFeO₃ at frequency 100 Hz. However, in this work, the dielectric constant value of the Bi_{1-x}Ba_xFeO₃ system was larger than those reported for pure and Ba-doped BiFeO₃ ceramics (Cheng *et al.*, 2015; Mahbub *et al.*, 2015). Moreover, the loss tangent in all doped samples is found to have strong frequency dependence as shown in the Figure 4.26. In all doped conditions, at a low frequency region, the loss tangent has a high value which gradually decreases with increases in frequency up to 10^4 Hz and then increases with increasing frequency. There is no relaxation peak in the loss tangent spectra in the measured frequency range for all doped samples as shown in Figure 4.26. The exponential-like increase in loss tangents as frequency decreases to a lower-frequency region can be attributed to

the effect of DC conductivity. However, at a high-frequency range of 10^4 – 10^6 Hz, the dielectric constant and loss tangent also decrease with increases in Ba doping.

The dielectric properties for La-doped and undoped BiFeO₃ ceramics are investigated using an impedance analyser in parallel plate configuration. Figure 4.27 shows the dielectric constant and loss tangent of La-doped BiFeO₃ ceramics as a function of frequency at room temperature. It is clear that all of the samples reveal high dielectric constant values of about 10^3 – 10^4 Hz at low frequencies indicating that these ceramics can be categorized as giant dielectric materials, such as CaCu₃Ti₄O₁₂ (Zhang *et al.*, 2005). It is remarkable that the dielectric constant decreases with the substitution of La doping concentrations ($x = 0.05, 0.1, 0.2,$ and 0.3) in all measured frequency ranges. Compared to the parent BiFeO₃, at low frequency, the dielectric constant is higher than that of BiFeO₃ when it is doped with La ions. The decrease in dielectric constant values with increasing La-substituted corresponds to the slight reduction of the average grain sizes in the microstructure. It should be pointed out that the dielectric spectra for La-doped BiFeO₃ ceramics are similar in every way, i.e., their dielectric constants decrease with increases in frequency. These can be explained on the basis of the combined responses of the orientational relaxation of dipoles and the electrical conduction of the charge carriers (Sen *et al.*, 2012; Srivastava *et al.*, 2013). However, it is found that the presence of loss tangent peaks shows a shift to higher frequency regions with increases in La doping concentrations. It should also be noticed that the loss tangent value of all samples at the room temperature is around 0.2–0.8 at a measured frequency below 10^3 Hz. The loss tangent is due to the effect of the DC conduction found below the 10^3 Hz frequency regime. In fact the appropriate loss tangent values for the application in the capacitors must be lower than 0.05.

Therefore, the observations of high loss tangents in all samples are undesirable for the capacitor applications. As can be seen in the dielectric constant spectra, when the frequency level increases, there is a slight drop in the dielectric constant which also shifts forwards to lower frequencies with increase in the La contents. If the frequency greater, both the dielectric and the loss tangent should move out of the frequency region. This result may be attributed to the effect of the La substitution in BiFeO_3 ceramics on the dielectric properties.

Figure 4.28 shows the variation of dielectric properties with frequency at room temperature for $\text{Bi}_{1-x}\text{Sm}_x\text{FeO}_3$ ceramics. It can be seen that there are differences in the three curves in the dielectric constant: (i) decreases in the dielectric constant when the frequency is increased for pure BiFeO_3 (ii) two relaxation peaks at low-frequency relaxation (LFR) and high-frequency relaxation (HFR) are clearly observed in the 5% and 10% Sm doped BiFeO_3 and (iii) the dielectric dispersion as shown in the $\text{Bi}_{0.8}\text{Sm}_{0.2}\text{FeO}_3$ and $\text{Bi}_{0.7}\text{Sm}_{0.3}\text{FeO}_3$ samples. The presence of three groups in the dielectric spectra corresponds to the structural transitions that are observed in the XRD analysis. With regard to the first group, pure BiFeO_3 has been discussed in the above section. The second group with low concentrations of Sm doping show two thermally activated dielectric relaxations which can be observed in the dielectric curves. It should be noted that the apparent two sets of low and high-frequency dielectric relaxations in loss tangent peaks can be also observed. The dielectric loss (ϵ'') peaks are expected to be observed at the same frequency range for the samples in this group, that is, the dielectric loss peaks are located at 10^3 and 10^5 Hz (not shown here). The presence of low-frequency dielectric relaxation peaks may arise from a

large difference between impedances of the grains and grain boundaries which is a type of inhomogeneity resulting from the Maxwell–Wagner type relaxation.

In the last group, high concentrations of Sm are added, the dielectric constant curves show dispersion and maximum values in the low–frequency region which gradually decreases when the frequency increases. These samples show dielectric dispersion due to the Maxwell–Wagner type of interfacial polarization (Wagner, 1913). The reason is that the greater size and mass of dipoles can only obey at low frequency ranges whereas high frequencies do not have time to follow the increments in the applied electric field frequency and are relaxed down (Uniyal and Yadav, 2008). The dielectric constant values for this group are lower than those two groups of about 8.30×10^3 and 1.3×10^3 for $\text{Bi}_{0.8}\text{Sm}_{0.2}\text{FeO}_3$ and $\text{Bi}_{0.7}\text{Sm}_{0.3}\text{FeO}_3$ samples. It should be noted that, for this group, the presence of loss tangent peaks disappear and similarly there is no observed dielectric loss peaks. As seen in Figure 4.28, the ceramics with 30% Sm doping show the lowest dielectric constant value due to decreased average grain size and low charge defects concentration. For all doping levels, $\tan \delta$ has higher values in the lower frequency range and its value decreases with increasing frequency of the applied alternating field. However, at higher frequencies > 1 kHz, the dielectric constant and loss tangent peaks show weak dependence, along with a low value of $\tan \delta$ for $\text{Bi}_{0.7}\text{Sm}_{0.3}\text{FeO}_3$ of about 0.24–0.11. Higher values of $\tan \delta$ in the lower frequency range coincide with small increases in the conductivity of the ceramics.

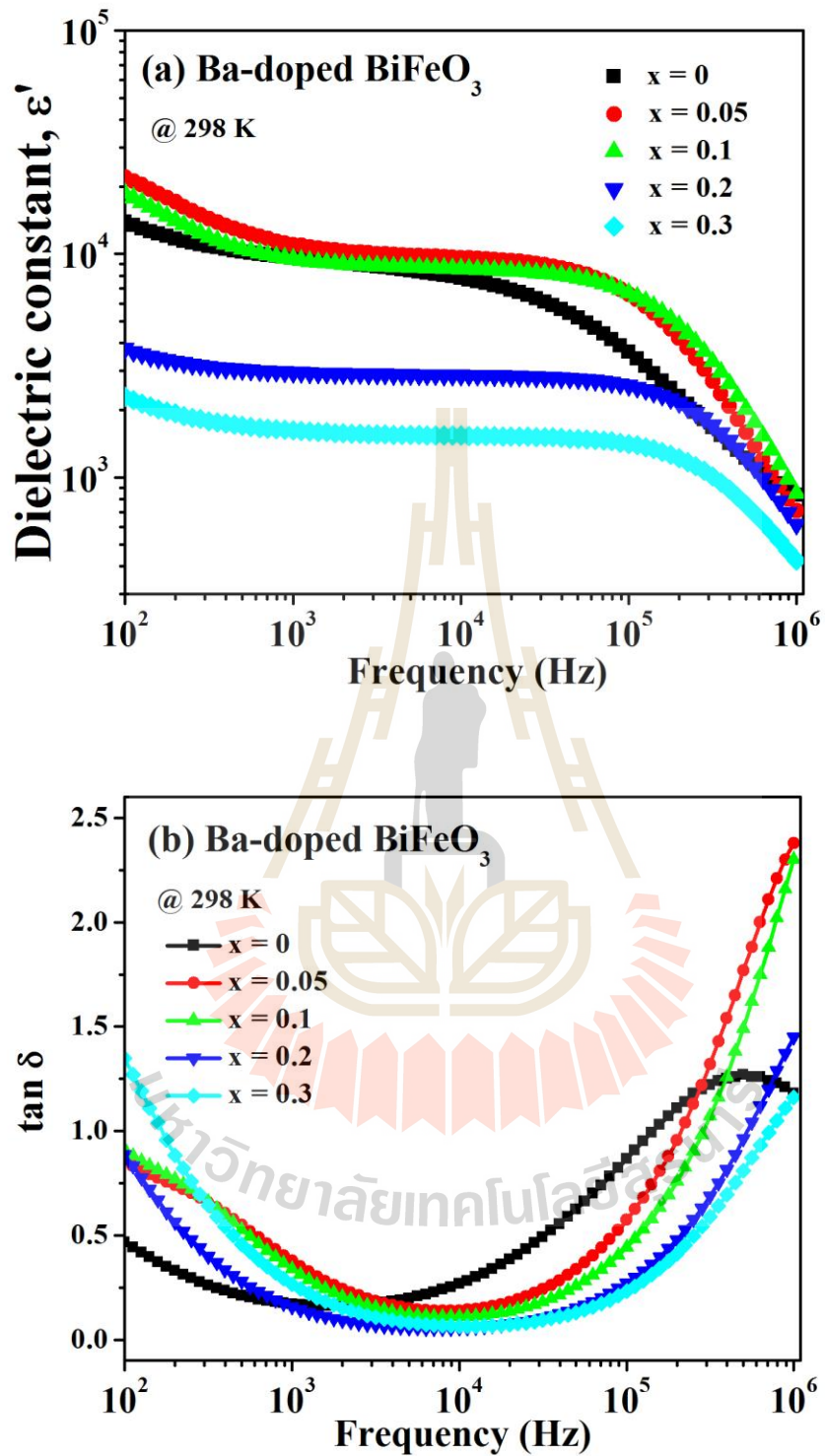


Figure 4.26 Frequency dependence of dielectric properties (dielectric constant (ϵ'), loss tangent ($\tan \delta$)) at room temperature for $\text{Bi}_{1-x}\text{Ba}_x\text{FeO}_3$ ceramics sintered at 800 °C for 3 h.

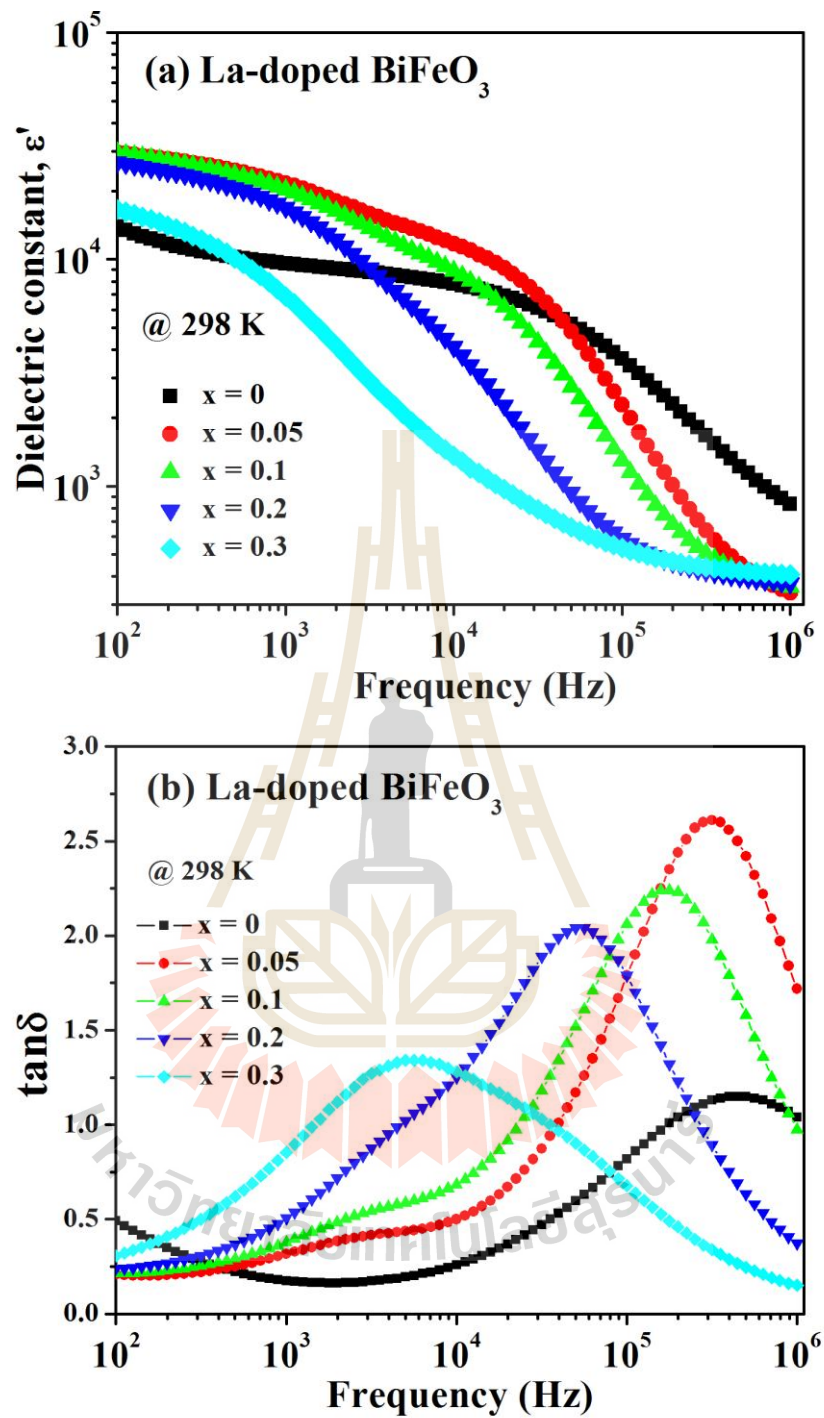


Figure 4.27 Frequency dependence of dielectric properties (dielectric constant (ϵ'), loss tangent ($\tan \delta$)) at room temperature for $\text{Bi}_{1-x}\text{La}_x\text{FeO}_3$ ceramics sintered at 800 °C for 3 h.

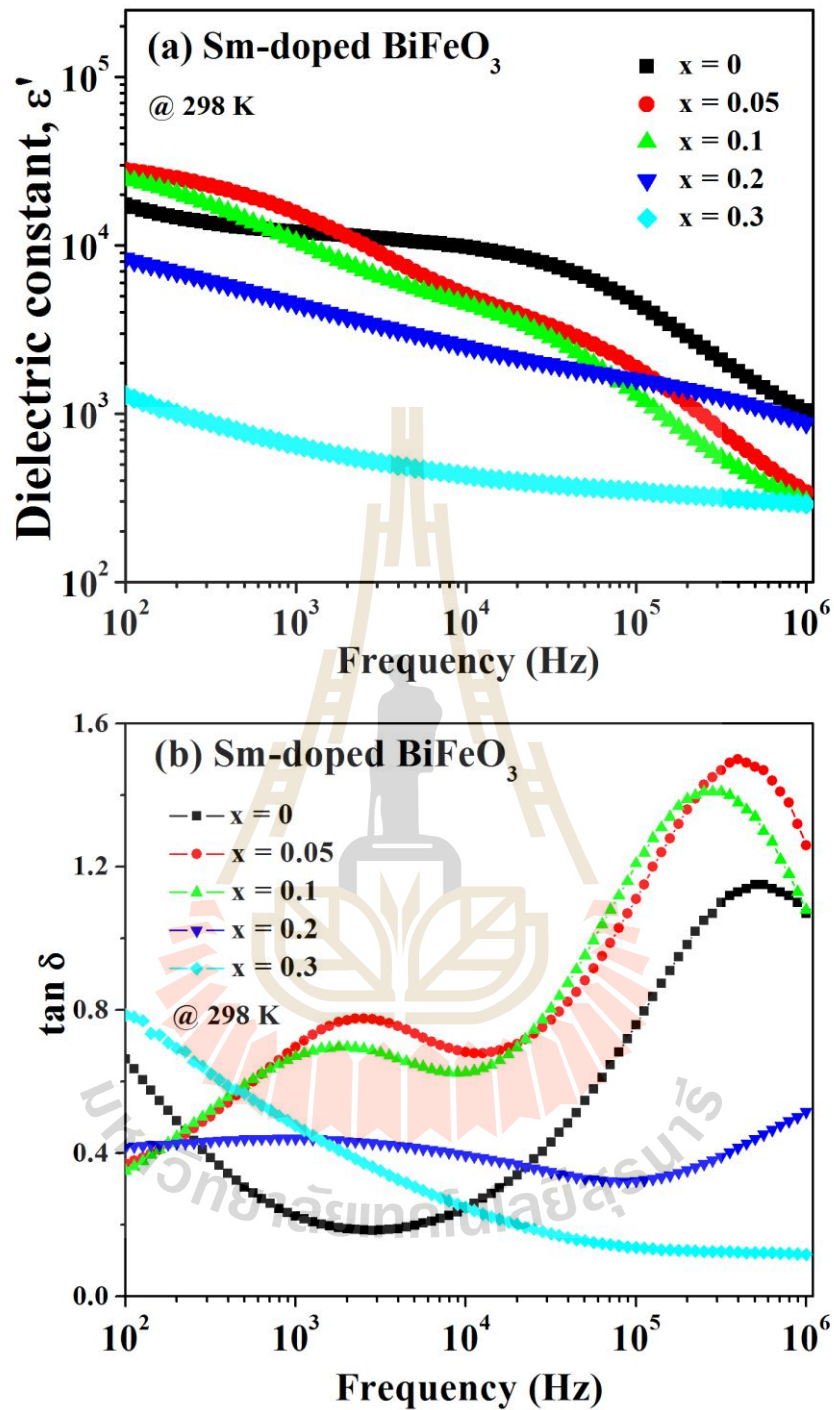


Figure 4.28 Frequency dependence of dielectric properties (dielectric constant (ϵ'), loss tangent ($\tan \delta$)) at room temperature for $\text{Bi}_{1-x}\text{Sm}_x\text{FeO}_3$ ceramics sintered at 800 °C for 3 h.

4.5.2 Dielectric properties as a function of frequency for doped BiFeO₃ ceramics at various temperatures

The real part of dielectric permittivity (ϵ'), loss tangent ($\tan \delta$) and dielectric loss (ϵ'') as a function of frequency at measured temperature range -50 to 200 °C for the parent BiFeO₃ ceramic sintered at 800 °C for 3 h are shown in Figure 4.29. A strong decrease in the frequency of the dielectric constant for all the measured temperatures ranges is characteristic of pure BiFeO₃ ceramics. The dielectric constant spectra show the highest value in the low-frequency range (below 10⁴ Hz) and high temperatures. It shows large dielectric curves which can be attributed to the Maxwell–Wagner polarization or interfacial space charge polarization (mostly located on the grain boundary) (Costa *et al.*, 2011; Wagner, 1913; Godara *et al.*, 2015). Since the large size and mass of dipoles can only relate to the low frequency region whereas in high frequencies regimes they are unable to change with the frequency of the applied electric field. The gradual drop in the dielectric constant value to a low value is observed in the high frequency region (10⁴–10⁶ Hz). At high frequencies of the applied electric field, these polarizations do not have sufficient time to rotate in the applied field direction and undergo relaxation. These dielectric spectra are similar to those reported by several researchers (Pandit *et al.*, 2011; Zhang *et al.*, 2013). At low frequency (100 Hz), the dielectric constant is 2.59×10⁴, at 200 °C, while at room temperature the dielectric constant decreases to 1.2×10⁴ in the same frequency region. This effect of the temperature dependence dielectric constant will be discussed in the next section. The frequency dependence of the loss tangent ($\tan \delta$) at various temperatures is shown in Figure 4.29(b). It can be seen that the gradual decrease in the dielectric constant is found to be associated with the appearance of loss tangent

($\tan \delta$) peaks and dielectric loss (ϵ''). The presence of the decreases continue in the dielectric constant as the frequency range increases which can attributed to relaxation dielectric behaviour. Interestingly, there is a gradual drop in dielectric constants and it is observed that the loss tangent and dielectric loss peaks are found to shift towards a higher frequency range as the temperature increases up to 200 °C.



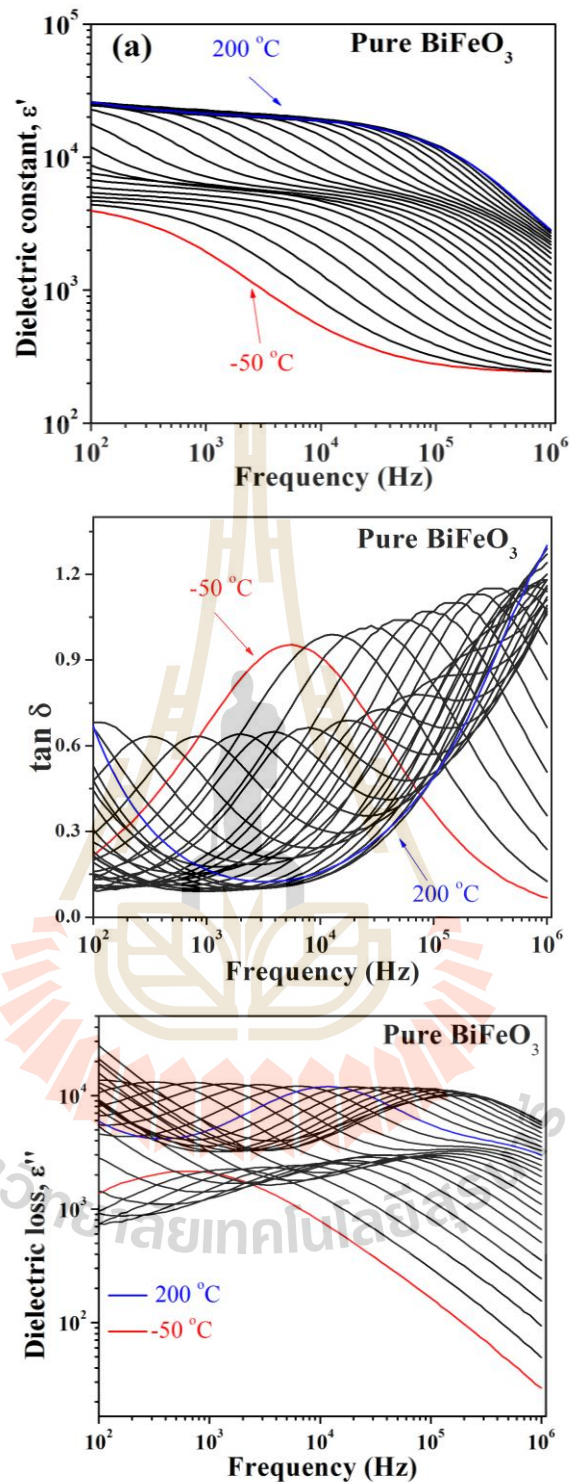


Figure 4.29 Frequency dependence of dielectric properties (dielectric constant (ϵ'), loss tangent ($\tan \delta$), and dielectric loss (ϵ'')) in the temperature range of -50 °C to 200 °C for BiFeO₃ ceramics sintered at 800 °C.

Figure 4.30 shows the dielectric constant, loss tangent and dielectric loss of $\text{Bi}_{1-x}\text{Ba}_x\text{FeO}_3$ ceramics is found when the dielectric properties are dependent on the frequency of all the samples which are very similar. At low temperatures (-50–30 °C), it is observed that the dielectric constant spectra decrease, as the frequency range increases which is related to the low-temperature dielectric relaxation (LTDR) in all samples. As the temperature increases, the dielectric constant is found to increase to low values for all samples which is similar to that observed in the La and Sm doped BiFeO_3 . This increase in the dielectric constant shift towards higher frequency with increasing temperature, which the thermally activated mechanism is also related to this observation. The gradual drop which is observed in the dielectric constant is found to be associated with the presence of the loss tangent ($\tan\delta$) peaks. It is noticeable that the drop corresponds to the $\tan\delta$ peaks which move towards a higher frequency with increasing temperature (in Figure 4.30(e)–(h)). If the temperature is sufficiently high, the $\tan\delta$ peaks move out of the measured temperature range indicating that the relaxation characteristic which suggests that it is a thermally activated mechanism.

Two thermally activated dielectric relaxations can be seen in the dielectric constant curve in the temperature range 40–100 °C for $\text{Bi}_{0.95}\text{Ba}_{0.05}\text{FeO}_3$ and $\text{Bi}_{0.9}\text{Ba}_{0.1}\text{FeO}_3$ ceramics (will be shown in the below). Interestingly, with regard to the 20% and 30% of Ba doped BiFeO_3 samples there can be found two sets of frequency dielectric relaxations which respond in the temperature range 40–70 °C. It should be noted that only a set of low-frequency relaxations in the loss tangent peaks can be observed at this temperature range. This observation implies that there are at least two sources of polarizations which contribute to the total dielectric response in these

samples. But the high-frequency relaxation peaks due to the low-frequency loss tangent peaks did not move out of the measured frequency range. The activation energy required for the relaxation behaviour should be investigated. Moreover, it is found that the dielectric constant decreases with dielectric relaxation can be referred to the middle-temperature dielectric relaxation (MTDR). A large value and rapid decrease of low frequency loss tangent at high temperature (110–200 °C) is observed which is attributed to the effect of DC conduction. The set of middle-temperature dielectric relaxation peaks can also be observed in the loss tangent spectra. The observed set of middle-temperature dielectric relaxation behaviour in all of the Ba-doped BiFeO₃ samples is similar to that observed in the literature, as reported by Hunpratub. Another interesting result which can be observed is that the values of the loss tangent ($\tan \delta$) at low frequencies are relatively high. The high value is due to the contribution of the DC conductivity on the dielectric relaxation type. The effect of the DC conduction will be explained in section 4.5.4 on the effect of DC conductivity on dielectric behavior.

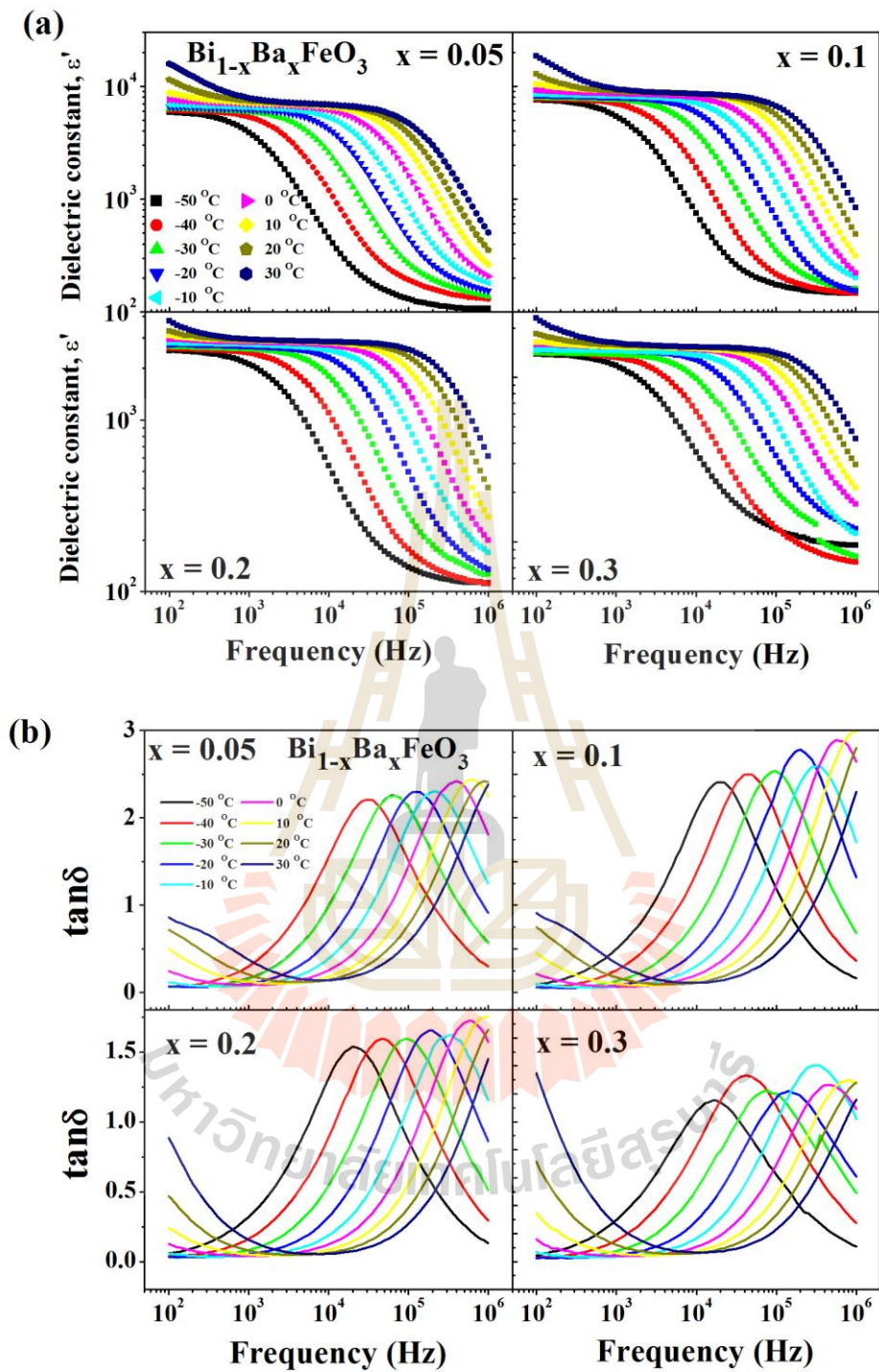
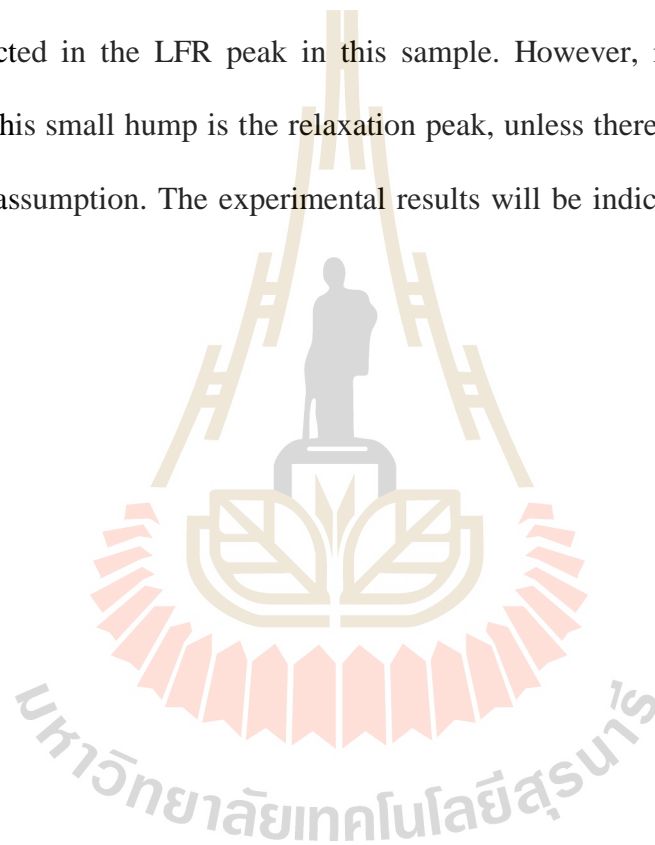


Figure 4.30 (a) Dielectric constant (ϵ') and (b) loss tangent ($\tan \delta$) in the temperature range -50 – 30 °C for the $\text{Bi}_{1-x}\text{Ba}_x\text{FeO}_3$ ceramics sintered at 800 °C .

Figures 4.31 exhibit the frequency dependence of the dielectric constant (ϵ') and loss tangent ($\tan \delta$) for the $\text{Bi}_{1-x}\text{La}_x\text{FeO}_3$ ceramics with different concentrations of La ions. It should be noted that the effect of La doping concentrations on the dielectric properties of $\text{Bi}_{1-x}\text{La}_x\text{FeO}_3$ ceramics is very similar to that observed in the parent BiFeO_3 ceramic. The dielectric constant shows the maximum values at the lower frequencies for high temperatures, but with increasing frequencies, the dielectric constant gradually drops to a low value. It can be observed that the dielectric constant decreases as the frequency increases and it becomes constant at high frequencies (-50 to -10 °C). This can be clearly seen in all samples. The dielectric constant for these samples is almost constant at high a temperature (≥ 170 °C) for the whole measured frequency range. In the high-temperature region, a plateau of high dielectric constant values can be observed at low-frequencies. The value of the dielectric constant increases as the temperature increases in all doped samples. It should be noted that the appearance of the loss tangent ($\tan \delta$) peaks can be related to the drop in dielectric constant values to a lower value for all La-doped samples. The gradual decreases in the dielectric constant and peaks of loss tangent ($\tan \delta$) to lower values can be found with shifts to higher frequencies with increasing temperature for all samples. Moreover, the dielectric constant drop and related loss of tangent peaks are found to move out of the measured frequencies region when the temperature is sufficiently high. Therefore, this dielectric relaxation behavior can be attributed to the thermally activated mechanism. These results for La-doped BiFeO_3 samples are similar to those discussed for the pure BiFeO_3 ceramic. The presence of low-relaxation and high-relaxation frequencies in this sample is associated with the appearance of loss tangent ($\tan \delta$) in the same frequency region. It is observed that

the exponential-like increases correspond to the increase in the loss tangent with decreasing frequency in the lower frequency region of the $\text{Bi}_{0.95}\text{La}_{0.05}\text{FeO}_3$, $\text{Bi}_{0.9}\text{La}_{0.1}\text{FeO}_3$, and $\text{Bi}_{0.8}\text{La}_{0.2}\text{FeO}_3$ samples which is due to the effect of DC conductivity (Pandit *et al.*, 2011). The DC conduction of the compound can be reduced by increasing the resistance. Although a small hump can be found in the low frequency region for the $\text{Bi}_{0.95}\text{La}_{0.05}\text{FeO}_3$, $\text{Bi}_{0.9}\text{La}_{0.1}\text{FeO}_3$ specimens, this small hump can be expected in the LFR peak in this sample. However, it is not advisable to believe that this small hump is the relaxation peak, unless there is strong evidence to support this assumption. The experimental results will be indicated and discussed in section 4.5.4.



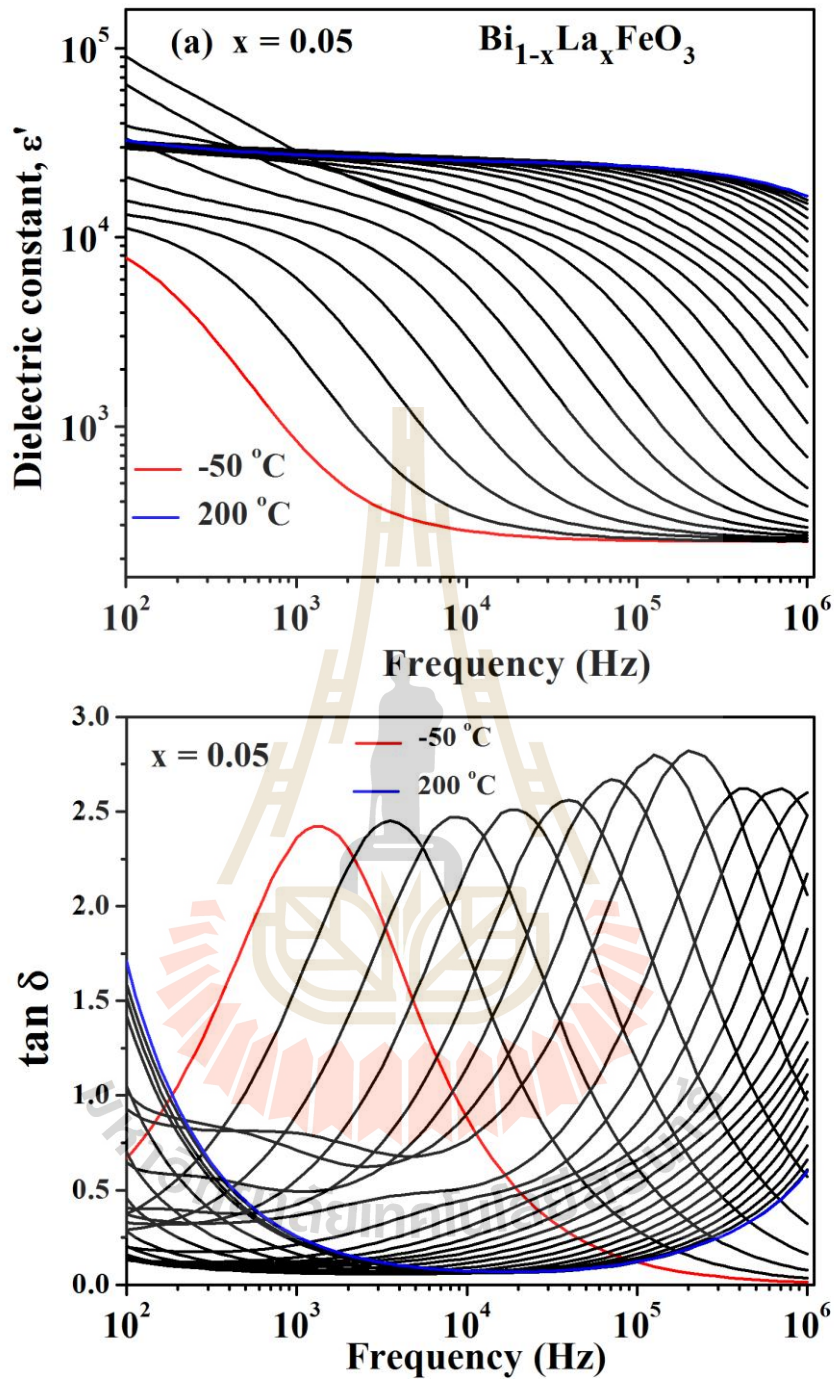


Figure 4.31 Frequency dependence of dielectric properties (dielectric constant (ϵ') and loss tangent ($\tan\delta$)) in the temperature range of -50 to 200 °C for $\text{Bi}_{1-x}\text{La}_x\text{FeO}_3$ ceramics.

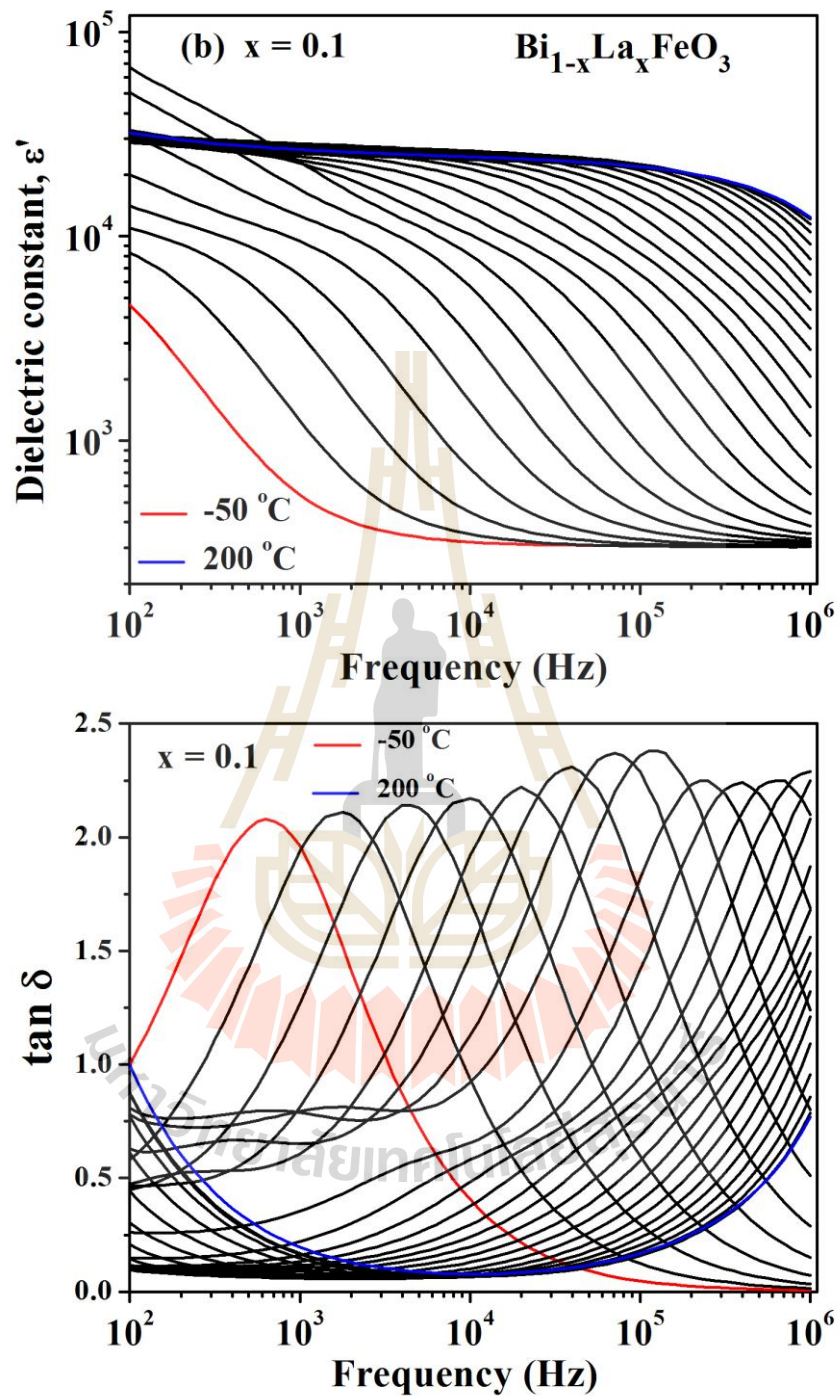


Figure 4.31 Frequency dependence of dielectric properties (dielectric constant (ϵ'), loss tangent ($\tan \delta$)) in the temperature range of -50 to 200 °C for $\text{Bi}_{1-x}\text{La}_x\text{FeO}_3$ ceramics (Continued).

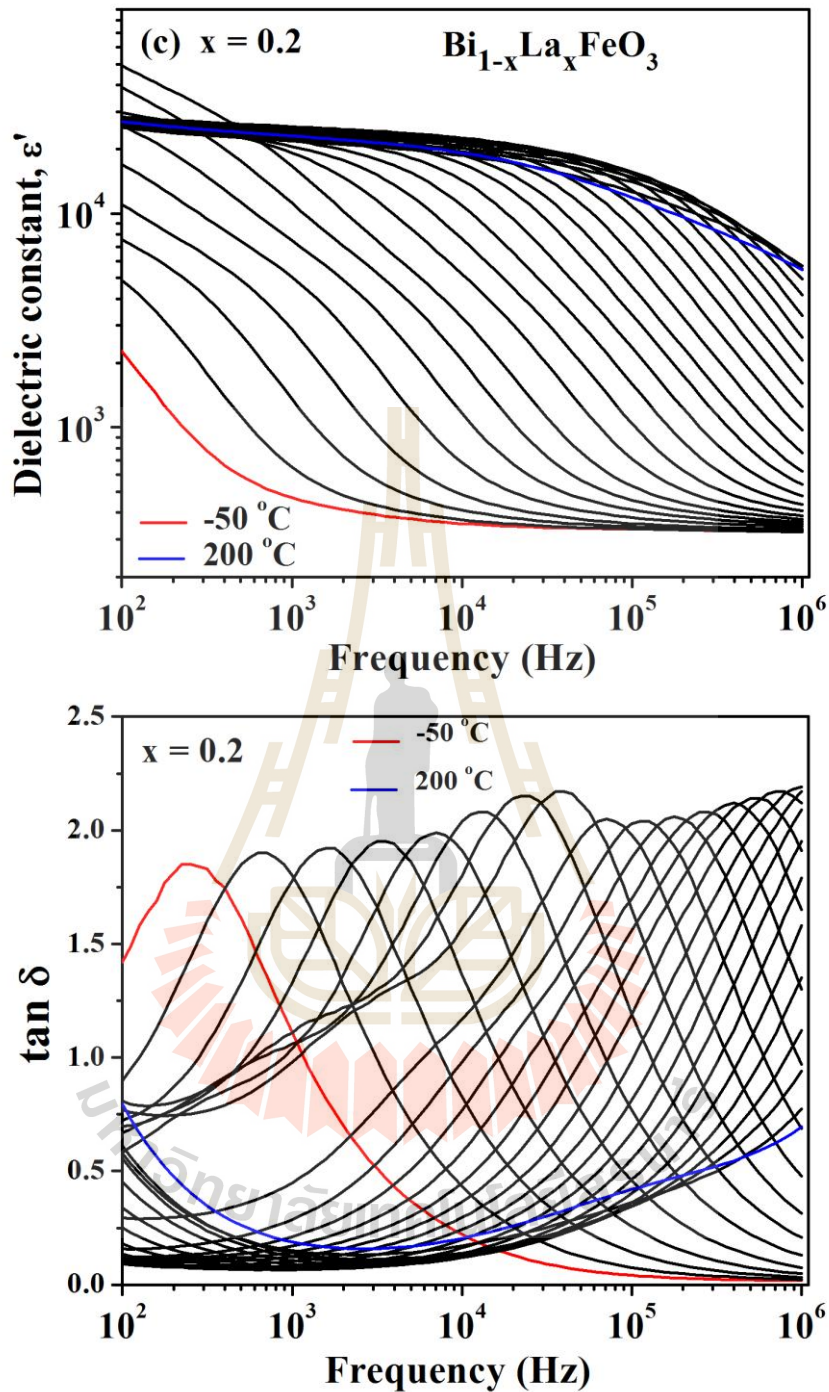


Figure 4.31 Frequency dependence of dielectric properties (dielectric constant (ϵ'), loss tangent ($\tan\delta$)) in the temperature range of -50 to $200\text{ }^\circ\text{C}$ for $\text{Bi}_{1-x}\text{La}_x\text{FeO}_3$ ceramics (Continued).

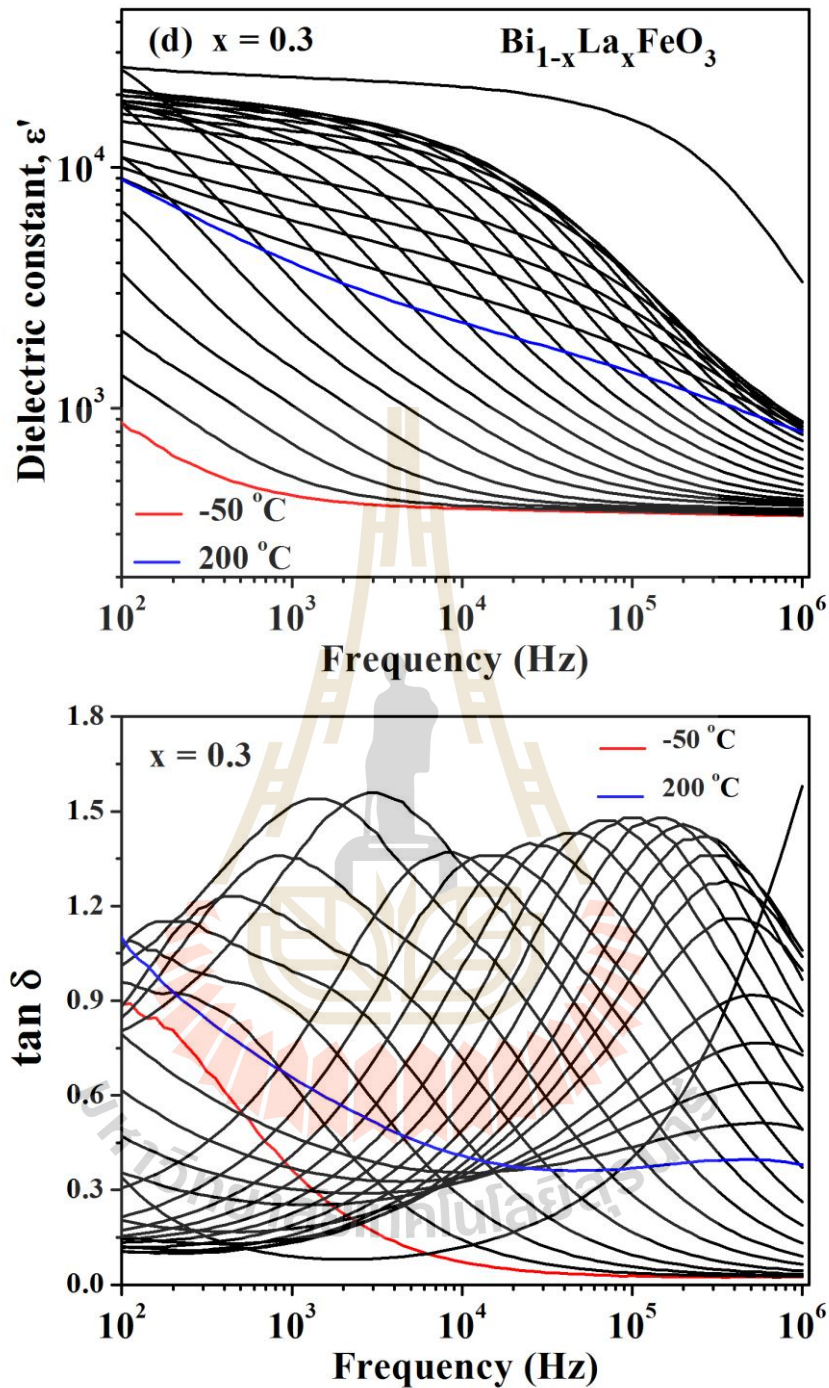


Figure 4.31 Frequency dependence of dielectric properties (dielectric constant (ϵ'), loss tangent ($\tan\delta$)) in the temperature range of -50 to $200\text{ }^\circ\text{C}$ for $\text{Bi}_{1-x}\text{La}_x\text{FeO}_3$ ceramics (Continued).

The dielectric properties of $\text{Bi}_{1-x}\text{Sm}_x\text{FeO}_3$ ceramics were investigated as a function of frequency at various temperatures in the frequency range 100–1 MHz. The dielectric properties for Sm-doped BiFeO_3 ceramics are similar to those observed for the dielectric properties of La doped samples. The large dielectric constant values in the low frequency region can be found in all samples. With regard to the $\text{Bi}_{0.95}\text{Sm}_{0.05}\text{FeO}_3$ samples, the dielectric constant strongly depends on the frequency range and it increases as the measured temperature increases. At low frequencies, this sample has a maximum dielectric constant value of 4.65×10^4 at a high temperature of 120 °C. The loss tangent spectra also show frequency dependence as revealed in Figure 4.32(a). At low temperatures, loss tangent peaks are observed and these loss tangent peaks shift to a higher frequency range as shown in the inset of Figure 4.32(a). The loss tangent peaks extended to the higher frequency range where the $\tan \delta$ peaks disappear when the temperature is sufficiently high (> 50 °C). Moreover, the change in the low-frequency loss tangent can be seen clearly in Figure 4.32(a) when there is a high temperature of 120 to 200 °C (indicated by a black arrow). At this temperature range, the low-frequency loss tangent is found to show exponential-like increases with increases in temperature. This observation demonstrates that the large low-frequency loss tangent is due to the effect of DC conductivity. While in the high-frequency range, exponential-like increases in the loss tangent forms a part of the HFR peaks. To confirm the HFR process, the dielectric loss peak can be found in the high-frequency and high-temperature ranges, i.e., 10^4 – 10^5 Hz and 180–200 °C, respectively. At the same time, the exponential-like increases in the dielectric loss in the low frequency regime are caused by the effect of the DC conductivity process in the high temperature range. In addition, two sets of gradual decreases in the dielectric

constant can be observed in both the low- and high-frequency range in the temperature range of 20–50 °C. These two sets of decreases in the dielectric constant indicate that there are two sets of thermally activated dielectric relaxation mechanisms in this sample. This result suggests that there are at least two sources of polarization which contribute to the dielectric response of this sample. Figure 4.32(b) shows the dielectric properties of the $\text{Bi}_{0.9}\text{Sm}_{0.1}\text{FeO}_3$ sample is very similar to those observed in the 5% of the Sm-doped samples. However, some different characteristics, which are prominent, can be observed in 10% of the Sm-doped concentrations. The two drop dielectric relaxation sets and related peaks of the loss tangent are found to extend higher than the temperature range of 0–60 °C. This observation of the extent of the temperature range of two sets of the dielectric relaxation processes may be attributed to the thermally activated mechanism. Moreover, the exponential-like increases in the dielectric loss are found to be in a larger temperature range than that of the 5% of Sm-doped samples, i.e., 150–200 °C.

In the case of high Sm doping concentrations of Sm 20%, the dielectric constant and loss tangent are weakly dependent on frequency. While, increasing the Sm content up to 30% reveals similar dielectric behaviors to 20% of Sm doping, that is weakly dependent on measuring frequencies. Neither of the high concentrations of Sm doping can be found in the two dielectric relaxation sets. With regard to the $\text{Bi}_{0.8}\text{Sm}_{0.2}\text{FeO}_3$ samples, the loss tangent peaks dominate in the low temperature range (-50–50 °C) firstly, then when the temperature increases the loss tangent peaks move out of the measurement range 1 MHz. Further, with increases in the temperature range (110–200 °C), the presence of the loss tangent peaks can be observed in the low frequency region. At this temperature, it is expected that the low-frequency relaxation

(LFR) will be displayed at a high-temperature. In general, the loss due to the relaxation process is prominent, the peak of dielectric loss is observed. It can be seen that there are loss tangent peaks in the low frequency range whereas there is no observed dielectric loss peaks in the same frequency range. Thus, the observation of low frequency loss tangent peaks at a high temperature is not suitable for the LFR. Finally, the dielectric response for the $\text{Bi}_{0.7}\text{Sm}_{0.3}\text{FeO}_3$ ceramic shows some of loss tangent peaks at low temperature.



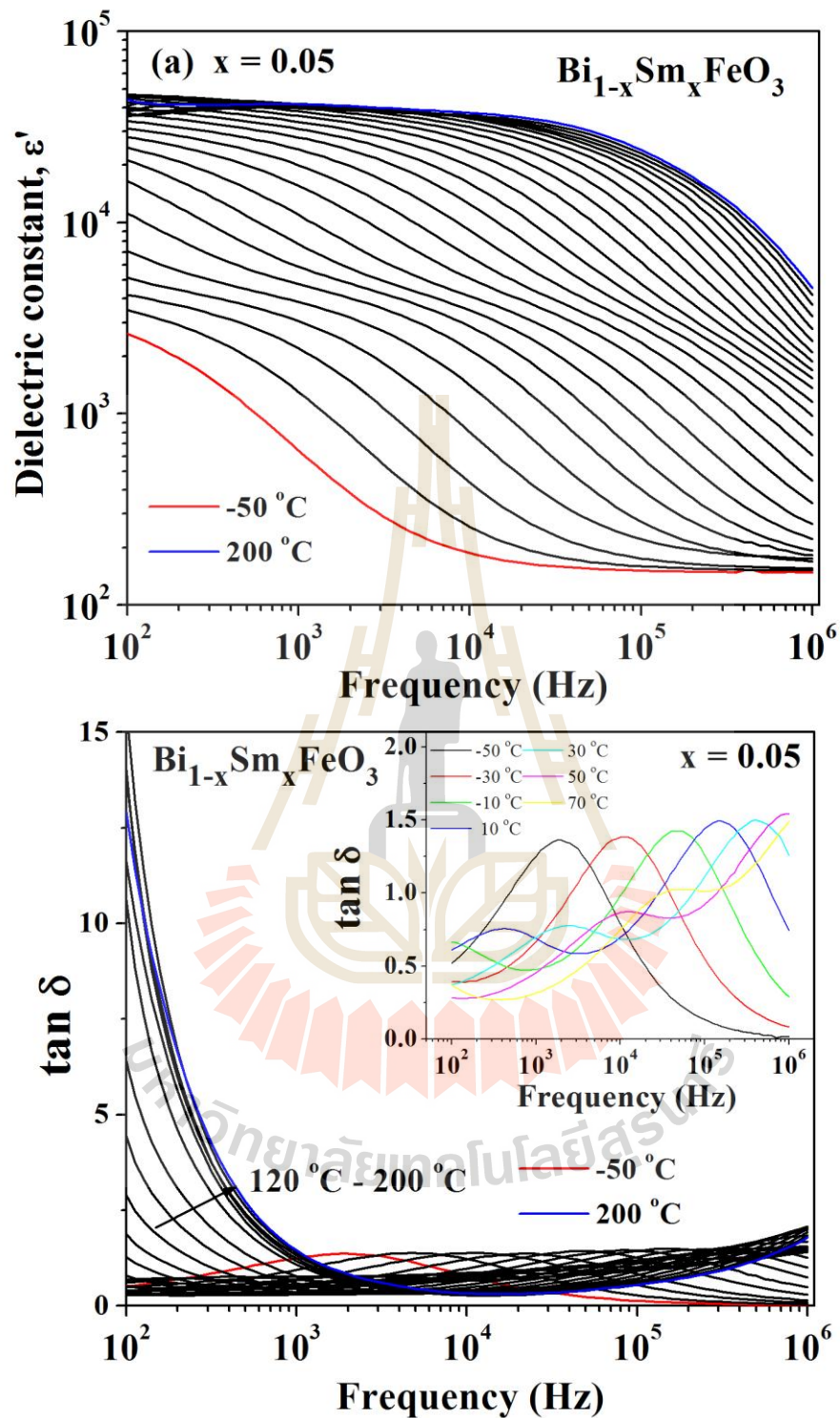


Figure 4.32 Frequency dependence of dielectric properties (dielectric constant (ϵ'), and loss tangent ($\tan\delta$)) at the temperature range of -50 to 200 °C for $\text{Bi}_{1-x}\text{Sm}_x\text{FeO}_3$ ceramics.

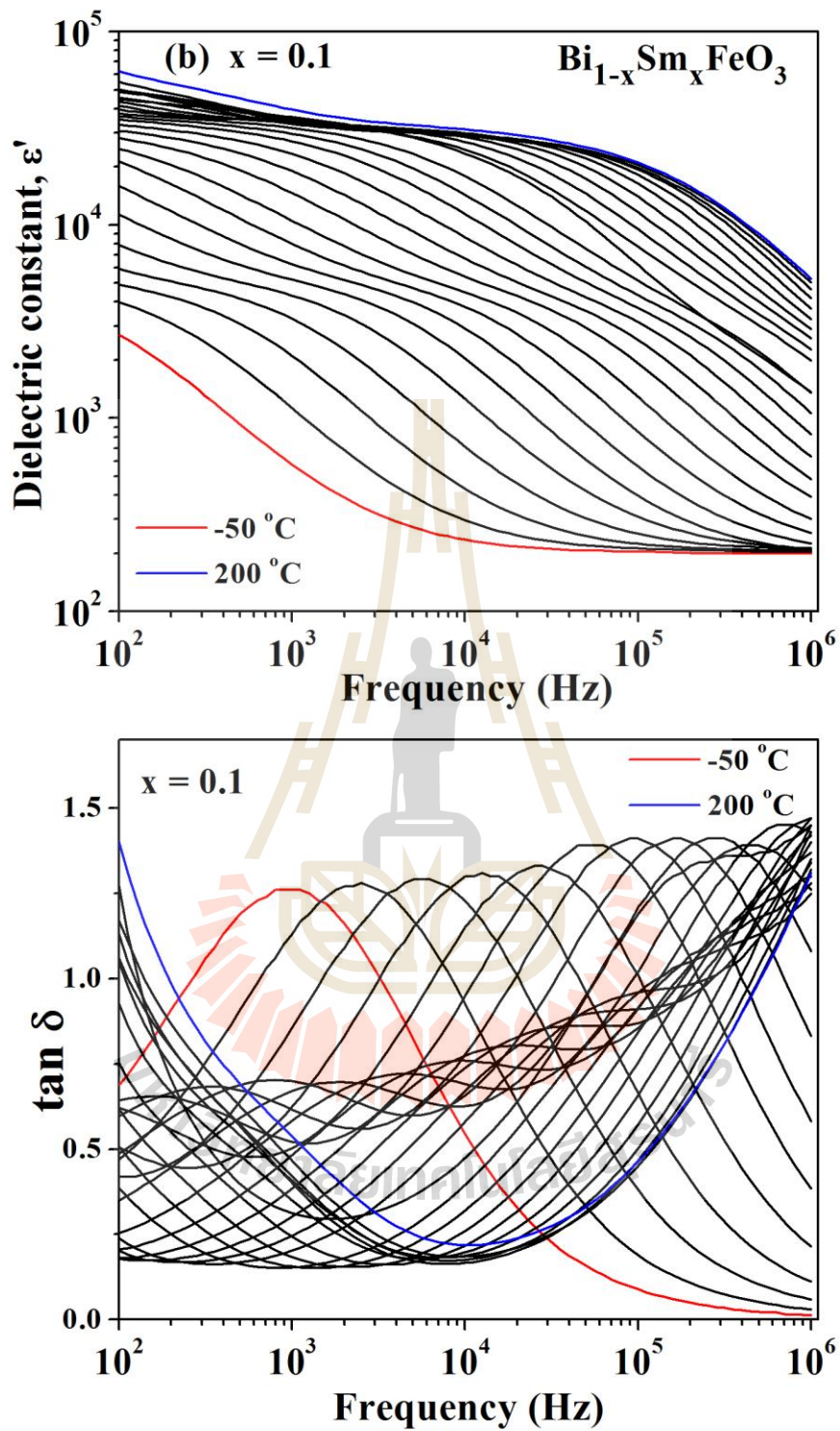


Figure 4.32 Frequency dependence of dielectric properties (dielectric constant (ϵ'), and loss tangent ($\tan \delta$)) at the temperature range of -50 to $200\text{ }^\circ\text{C}$ for $\text{Bi}_{1-x}\text{Sm}_x\text{FeO}_3$ ceramics (Continued).

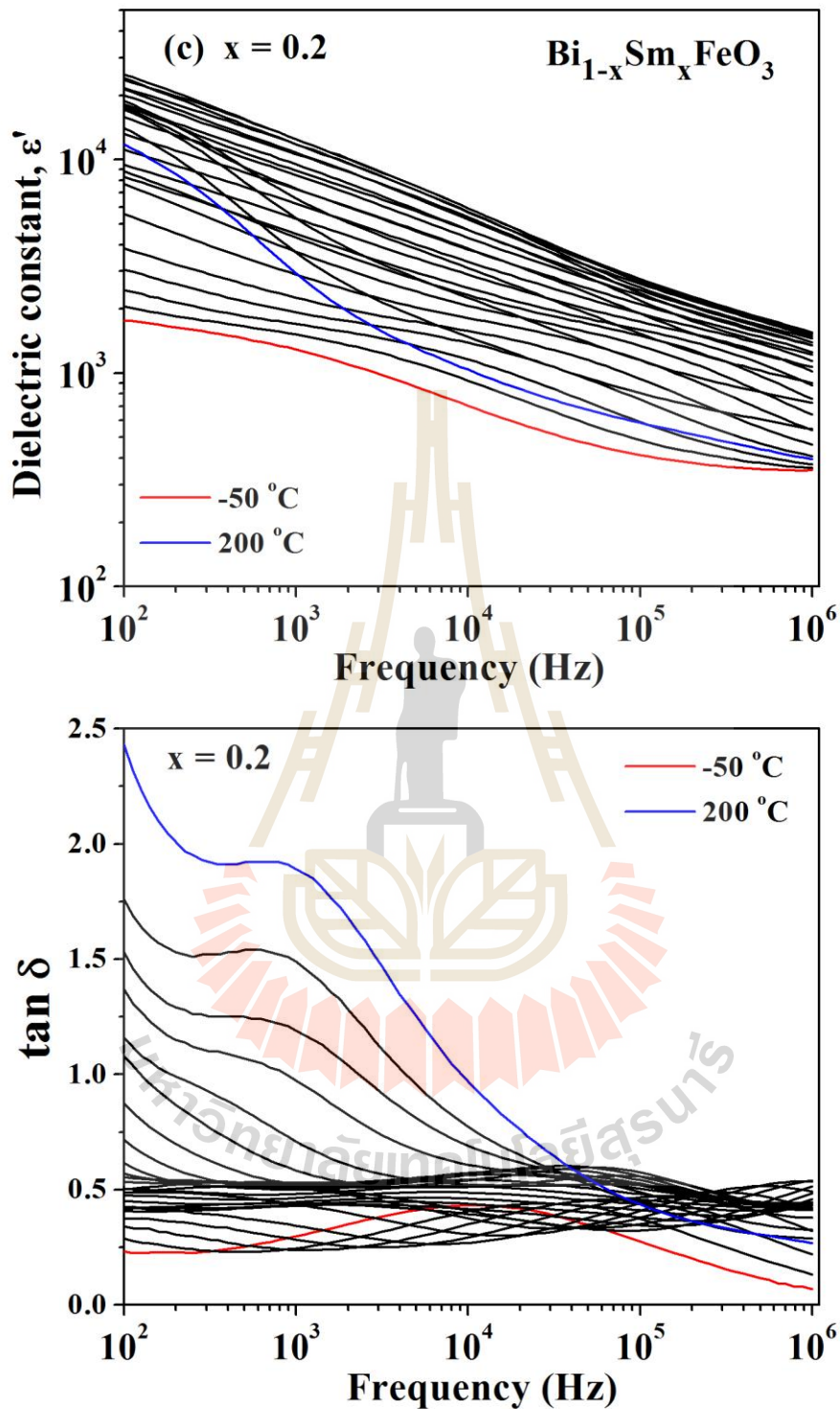


Figure 4.32 Frequency dependence of dielectric properties (dielectric constant (ϵ') and loss tangent ($\tan\delta$)) at the temperature range of -50 to 200 °C for $\text{Bi}_{1-x}\text{Sm}_x\text{FeO}_3$ ceramics (Continued).

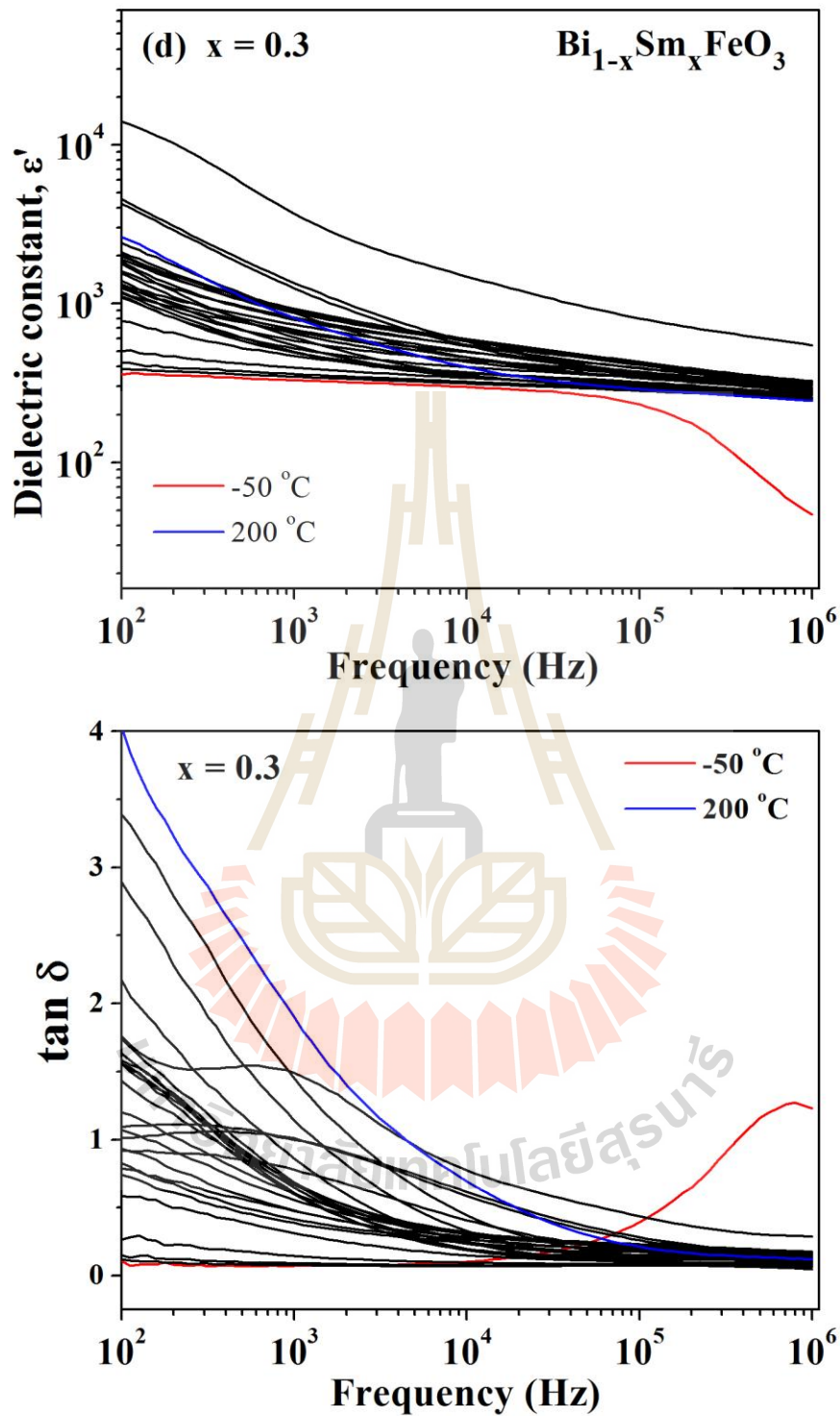


Figure 4.32 Frequency dependence of dielectric properties (dielectric constant (ϵ') and loss tangent ($\tan \delta$)) at the temperature range of -50 to $200\text{ }^\circ\text{C}$ for $\text{Bi}_{1-x}\text{Sm}_x\text{FeO}_3$ ceramics (Continued).

To understand the mechanism of the low-frequency relaxation (LFR) combined with the high-frequency relaxation (HFR), the parent BiFeO_3 , $\text{Bi}_{1-x}\text{Ba}_x\text{FeO}_3$ with $x = 0.05, 0.1, 0.2,$ and 0.3 samples (as shown in the Figures 4.33) reveal two sets of dielectric relaxation in the dielectric spectra in the low- and high-frequency region. By using the Cole-Cole model modified in terms of DC conductivity (Eq. (4.4)), the time relaxation (τ) is obtained from the fitted result at selected temperatures. According to the fitted result, it is observed that the τ values at various temperatures obey the Arrhenius equation (Eq. (4.8)), as illustrated in Figure 4.34. As demonstrated in Figure 4.34, E_a values of the LFR are shown in the ceramics for the parent BiFeO_3 , $\text{Bi}_{0.95}\text{Ba}_{0.05}\text{FeO}_3$, $\text{Bi}_{0.9}\text{Ba}_{0.1}\text{FeO}_3$, $\text{Bi}_{0.8}\text{Ba}_{0.2}\text{FeO}_3$, and $\text{Bi}_{0.7}\text{Ba}_{0.3}\text{FeO}_3$ can be calculated to be 0.64, 0.43, 0.56, 0.37, and 0.49 eV, respectively. These values are comparable to 0.21, 0.32, 0.27, 0.28, and 0.3 eV, which are the relaxation activation energy for the HFR of those samples. Generally, the value of relaxation activation energy of LFR is much larger than that of HFR. It should be noted that the close values of the relaxation activation energies between the LFR and HFR processes cannot completely account for the origins of LFR and HFR. However, it is possible that the LFR and HFR behaviors might correspond to the surface-layer and grain boundary effects. According to the microstructure analysis, it is found that the impurity phase of $\text{Bi}_2\text{Fe}_4\text{O}_9$ tends to accumulate on the top surface of the ceramics. Moreover, it is also often found at the grain boundaries, especially at the corners of the grains. As a result, it is possible that both relaxation behaviors might be explained as resulting from the same type of interface, namely, the interface between the insulating layer of the impurity phase at the grain boundary and the inner component of the semiconducting grains of the bulk BiFeO_3 .

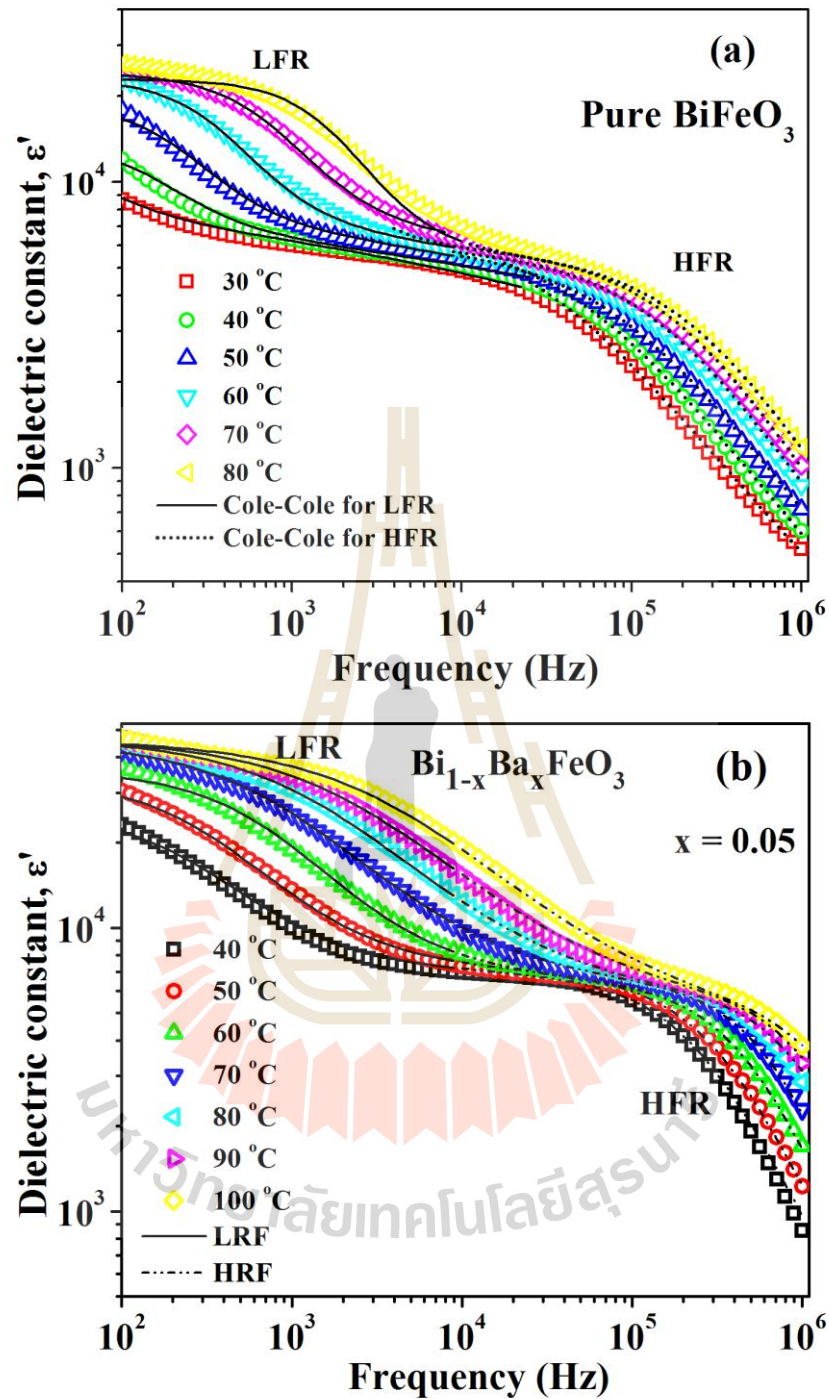


Figure 4.33 Low-frequency relaxation (LFR) and high-frequency relaxation (HFR) of (a) pure BiFeO_3 and (b)–(e) $\text{Bi}_{1-x}\text{Ba}_x\text{FeO}_3$ ceramics at various temperatures; the solid and dotted curves are the best fit to the Cole–Cole relaxation model for the LFR and HFR, respectively.

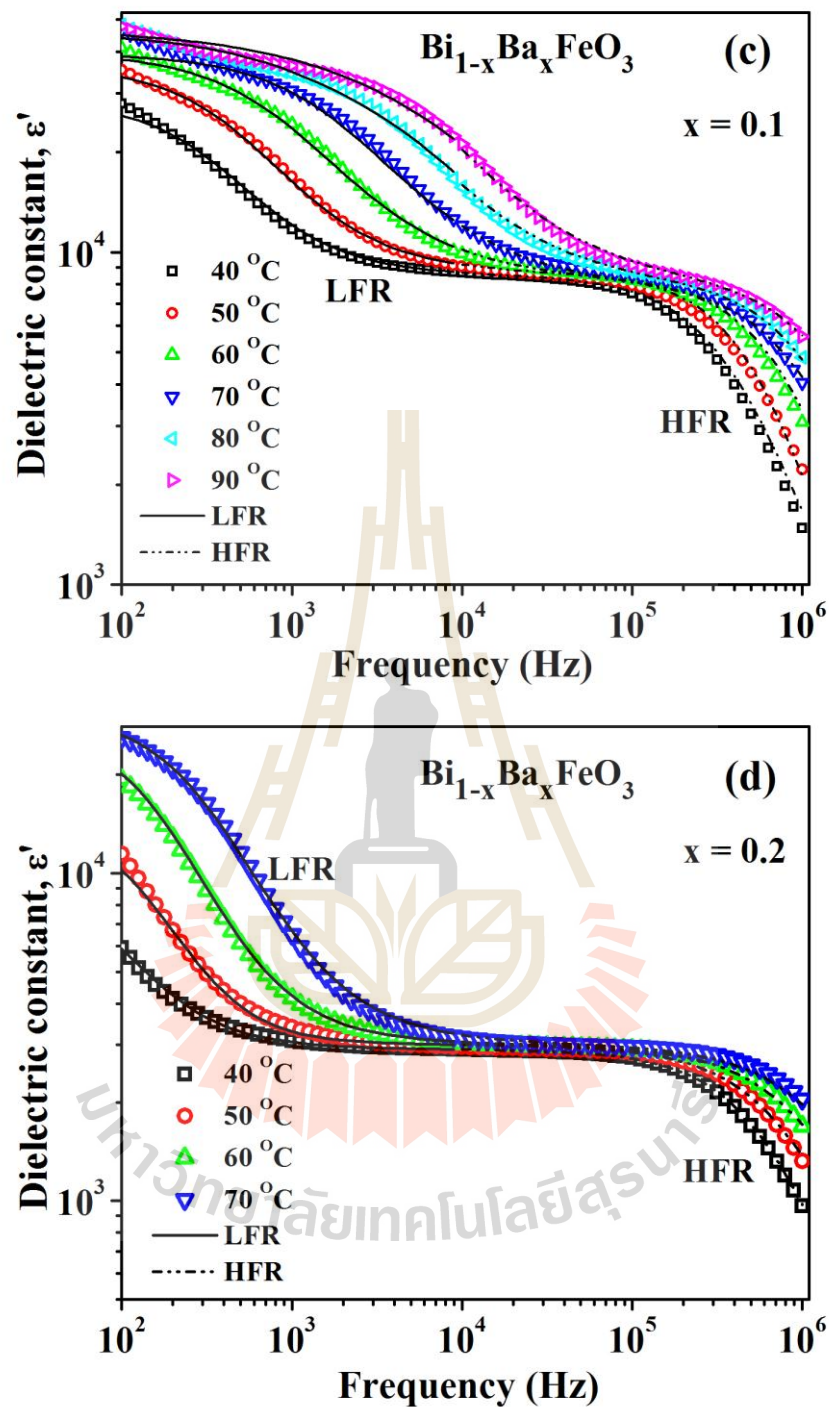


Figure 4.33 Low-frequency relaxation (LFR) and high-frequency relaxation (HFR) of (a) pure BiFeO_3 and (b)–(e) $\text{Bi}_{1-x}\text{Ba}_x\text{FeO}_3$ ceramics at various temperatures; the solid and dotted curves are the best fit to the Cole–Cole relaxation model for the LFR and HFR, respectively (Continued).

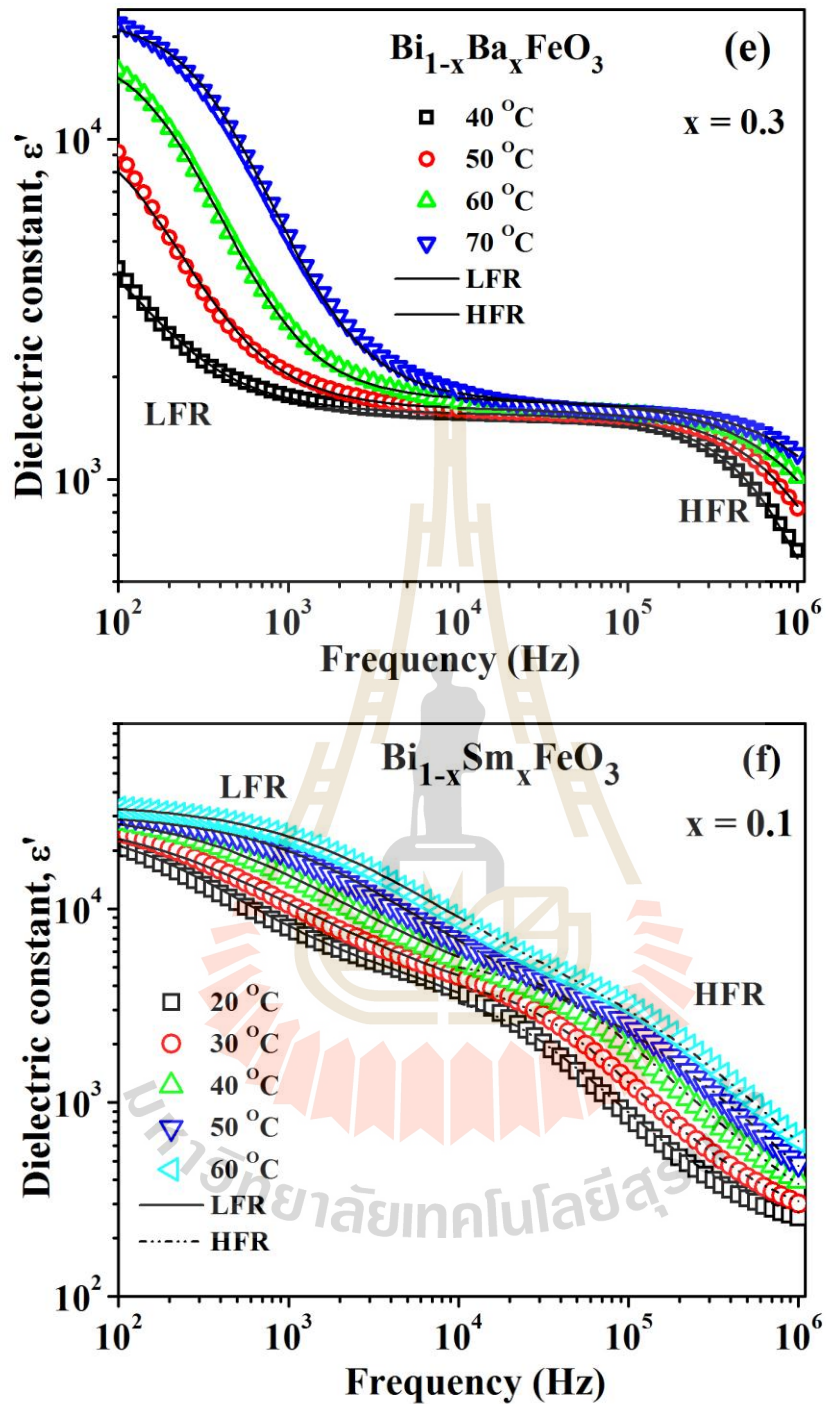
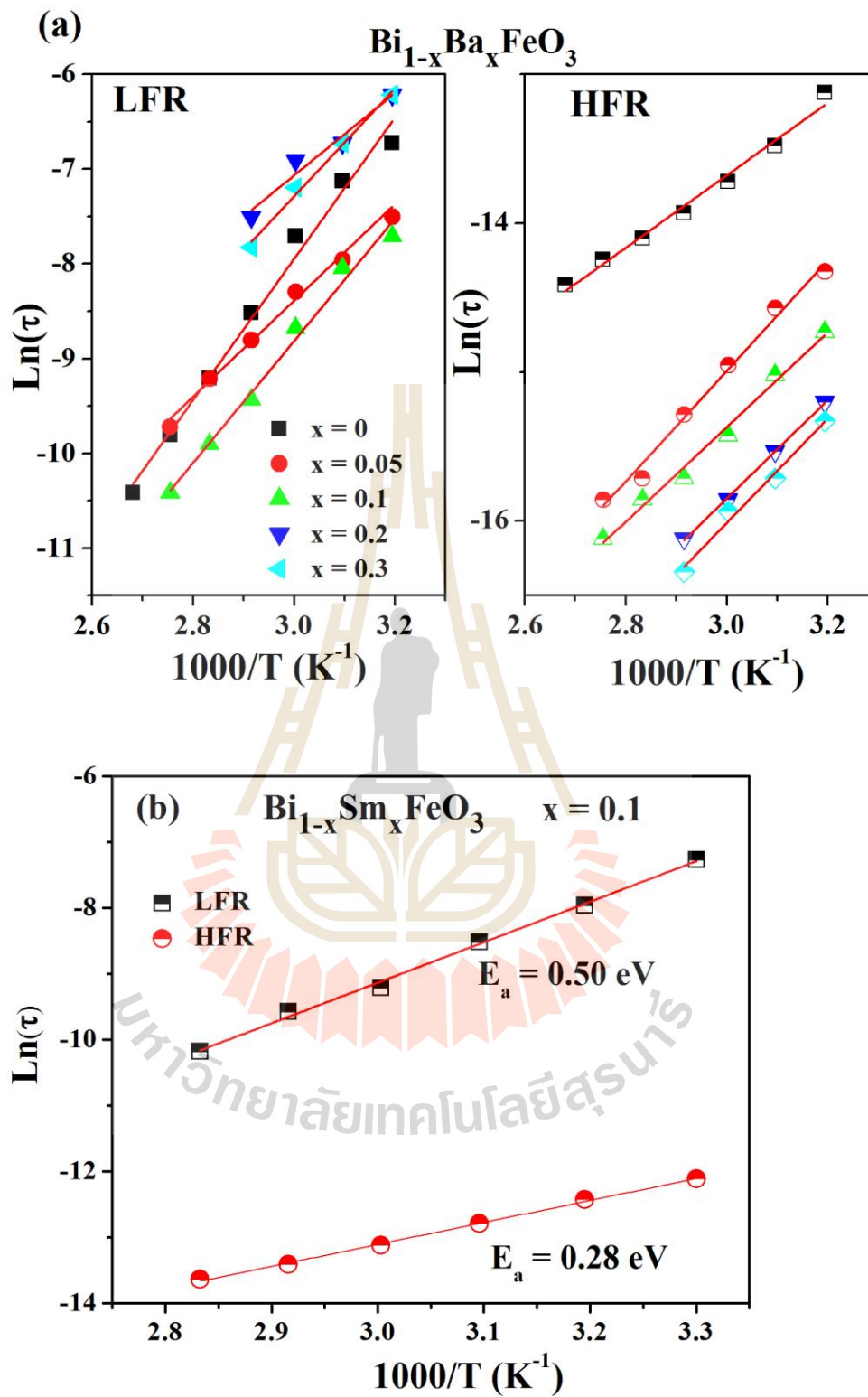


Figure 4.33 Low-frequency relaxation (LFR) and high-frequency relaxation (HFR) of (a) pure BiFeO_3 , (b)–(e) $\text{Bi}_{1-x}\text{Ba}_x\text{FeO}_3$, and (f) $\text{Bi}_{0.9}\text{Sm}_{0.1}\text{FeO}_3$ ceramics at various temperatures; the solid and dotted curves are the best fit to the Cole–Cole relaxation model for the LFR and HFR, respectively (Continued).



Figures 4.34 Arrhenius plots of the LFR and HFR of (a) the pure BiFeO_3 and Ba-doped BiFeO_3 ceramics and (b) $\text{Bi}_{0.9}\text{Sm}_{0.1}\text{FeO}_3$ ceramic.

4.5.3 The temperature dependence of dielectric properties of doped BiFeO₃ ceramics

Figures 4.35 exhibit the temperature dependent variations of the dielectric constant (ϵ') and loss tangent ($\tan \delta$) of pure and doped-BiFeO₃ ceramics at selected frequencies of 100–1 MHz. It can be observed for the pure BiFeO₃ ceramics that the dielectric constant increases with increasing temperature in all selected frequencies. This dielectric behaviour is caused by DC conductivity which is usually dependent on temperature. At low frequencies, the dielectric constant remains almost constant at higher temperatures. At any fixed temperature, for example, at 100 °C the dielectric constant decreases to lower values as the frequency increases. The dielectric constant curves gradually drop to low frequencies as the temperature falls below 30 °C. At low frequencies, it is found that the peaks of loss tangent (peaks (a)) correspond to a gradual drop in the dielectric constant spectra. When the frequency increases to more than 100 Hz, a gradual drop in is observed the dielectric constant at higher temperatures. Similar observations of loss tangent peaks can also be made at higher temperatures, which suggests that these dielectric behaviors are due to the dielectric relaxation behavior (Pandit *et al.*, 2011). Interestingly, in the loss tangent spectra, the second loss tangent peaks (peaks (b)) exhibit low temperatures with high frequencies up to 10⁵ Hz. However, the second gradual drop in dielectric relaxation cannot be observed at the related low temperature of loss tangent peaks. The second loss tangent peaks which are observed at low temperatures in the pure BiFeO₃ ceramics are not clear.

Under the conditions of Ba doping concentrations in BiFeO₃ ceramics, the temperature dependence of the dielectric constant and the loss tangent for the doped

samples are very similar to those observed for the BiFeO₃ samples. It is clear that all of samples reveal a dielectric constant which decreases at higher frequencies. The dielectric constant gradually rises at frequencies of 100 Hz and above temperatures at 0 °C. As frequency increases, a gradual increase can be seen in two temperature regions at both lower and higher temperatures. Interestingly, the gradual increase in the dielectric constant is observed at low temperatures (< 50 °C). The loss tangent peaks represented in the temperature ranges are related to the gradual increase of the dielectric constant spectra. It is found that the gradual increase of the dielectric constant and the associated loss tangent peaks move to higher temperatures when the frequency range increases. This result is similar to that observed and explained in the previous section.

The temperature dependence of the dielectric constant for La-doped BiFeO₃ ceramics is exhibited in Figures 4.36(f-i). The overall dielectric constant spectra of these La doped samples are similar in every way. The dielectric spectra at a low frequency of 100 Hz and 1 kHz are considered first i.e. a small hump in the dielectric constant can be seen at below room temperature and the loss tangent peaks are also present at the same temperature. As the selected frequency increases up to 1 MHz, a small hump in the dielectric constant spectra in the low temperature region disappears in all the La doped compositions. The dielectric constant is found to increase sharply with temperature due to thermally induced hopping conduction. At these frequency ranges, the loss tangent peaks can be observed and they shift to a higher temperature range, as already explained in the previous section. Generally, when the combined effects of temperature and frequency data are plotted, they show a sharp increase in the dielectric constant at low frequencies and high temperatures as a result of

electrode polarization (Kingery, 1960). According to Kingery's article, by contrast, the polarization effects at the electrodes may be assumed to be present at low temperatures in the case of La-doped BiFeO_3 ceramics. The investigation of the deep mechanism observed will be described by means of complex impedance spectroscopy in the next section.

Similar behavior can also be observed in Figures 4.36(j-k) for low concentrations ($x = 0.05$ and 0.1) of Sm ions doped in the Bi site. The dielectric constant of $\text{Bi}_{0.95}\text{Sm}_{0.05}\text{FeO}_3$ and $\text{Bi}_{0.9}\text{Sm}_{0.1}\text{FeO}_3$ samples increases significantly with increases in temperature. As Sm doping increases, the $\text{Bi}_{0.8}\text{Sm}_{0.2}\text{FeO}_3$ and $\text{Bi}_{0.7}\text{Sm}_{0.3}\text{FeO}_3$ samples show different characteristics for their dielectric properties. A broad peak in the dielectric constant can be observed in the temperature range 100–125 °C. In fact, the Neel transition temperature and Curie temperature of BiFeO_3 (> 200 °C) are out of our measurement temperature range which means these temperatures cannot be determined in this experiment.

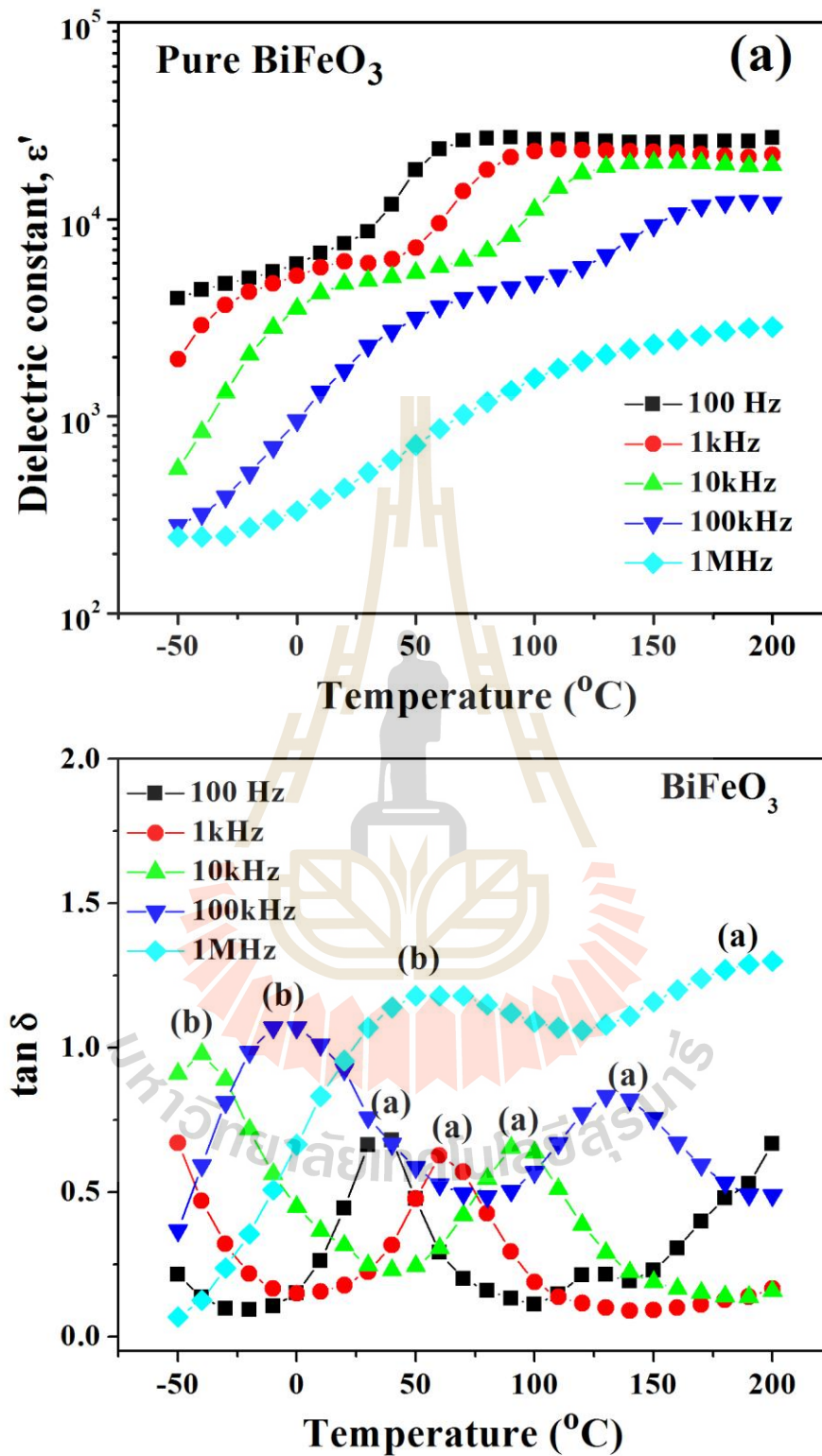


Figure 4.35 Temperature dependence of the dielectric constant (ϵ') and the loss tangent ($\tan \delta$) in the frequency range of 10^2 – 10^6 Hz for the pure BiFeO₃ ceramics.

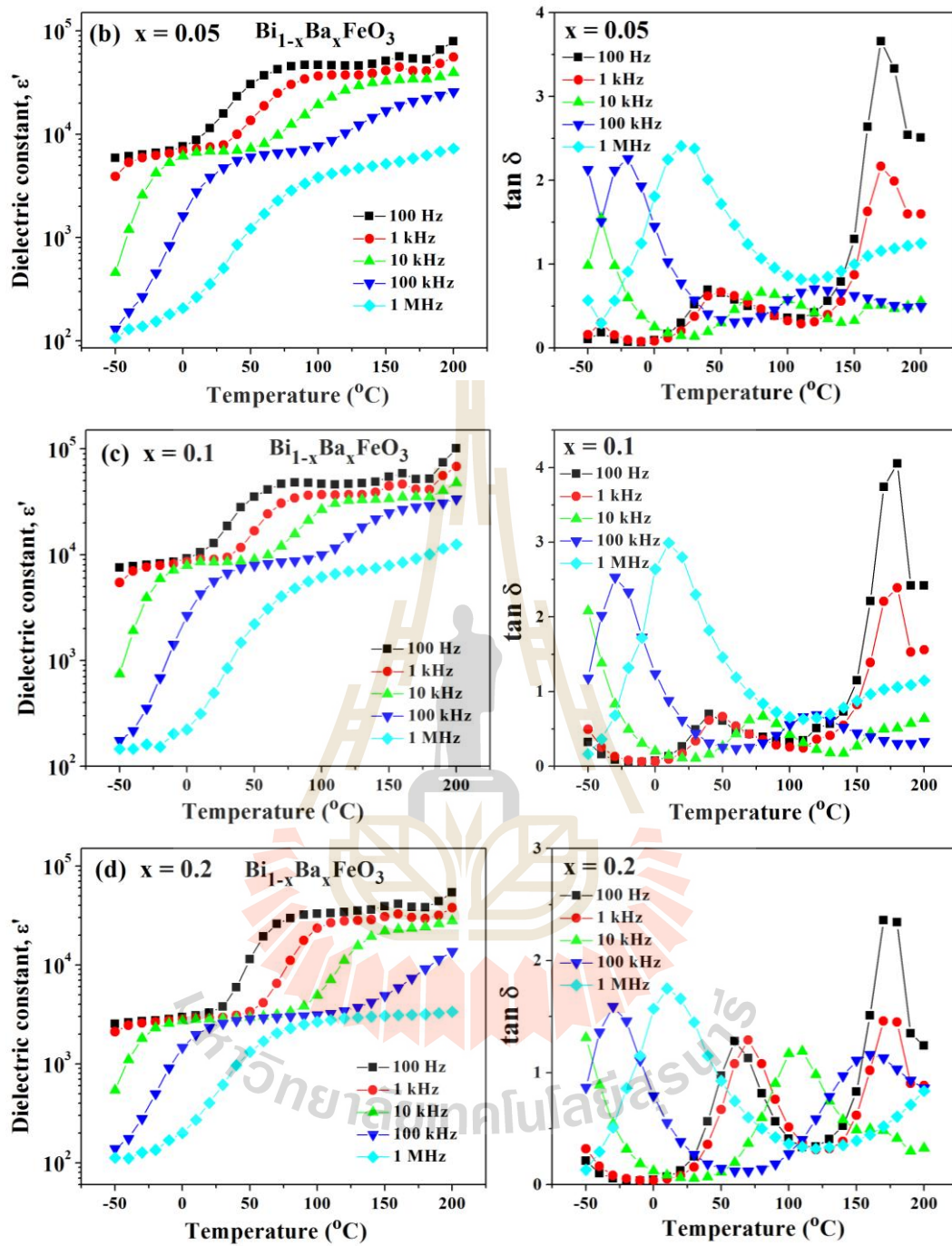


Figure 4.36 Temperature dependence of the dielectric constant (ϵ') and the loss tangent ($\tan \delta$) in the frequency range of 10^2 – 10^6 Hz for the doped BiFeO_3 ceramics.

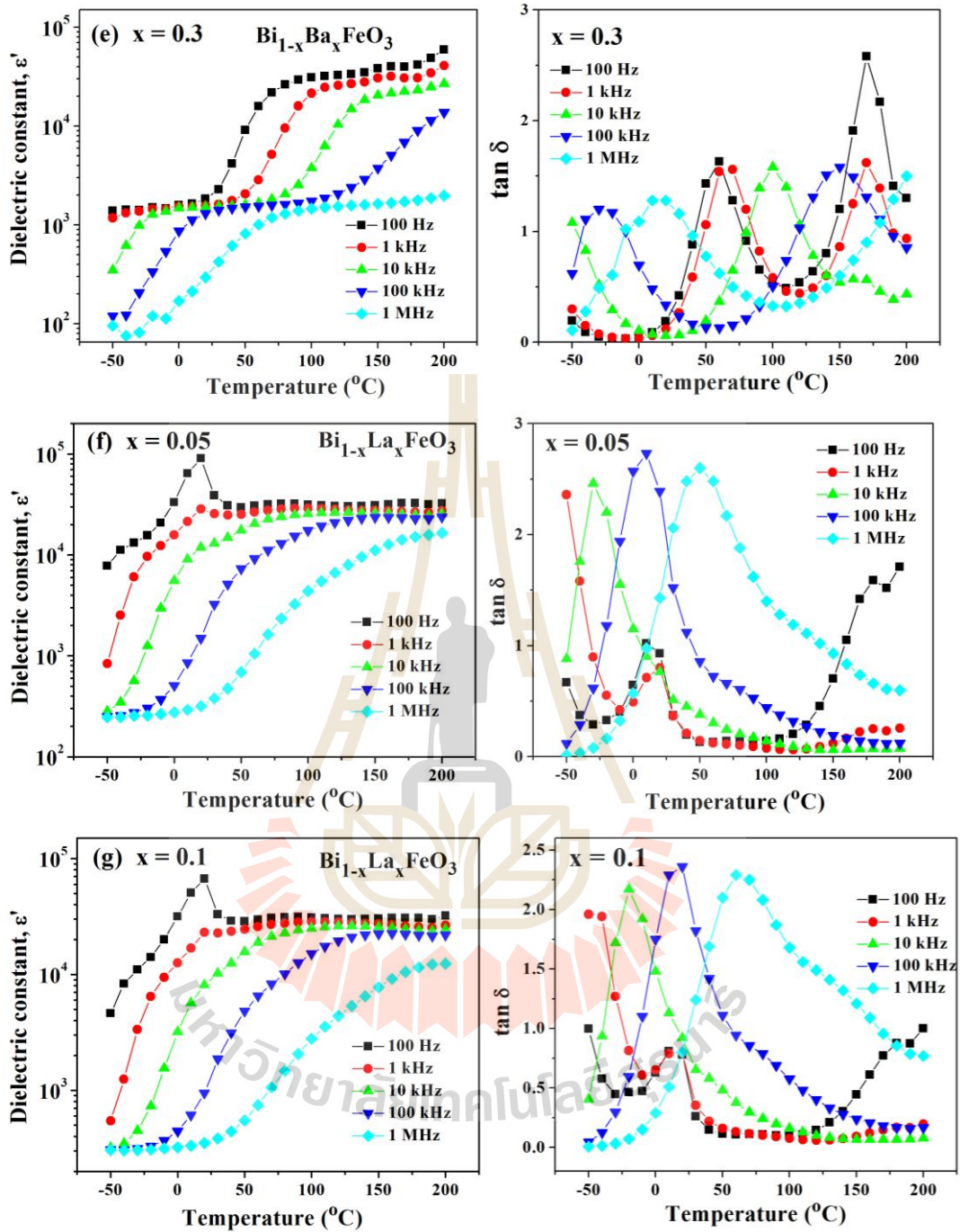


Figure 4.36 Temperature dependence of the dielectric constant (ϵ') and the loss tangent ($\tan \delta$) in the frequency range of 10^2 – 10^6 Hz for the doped-BiFeO₃ ceramics (Continued).

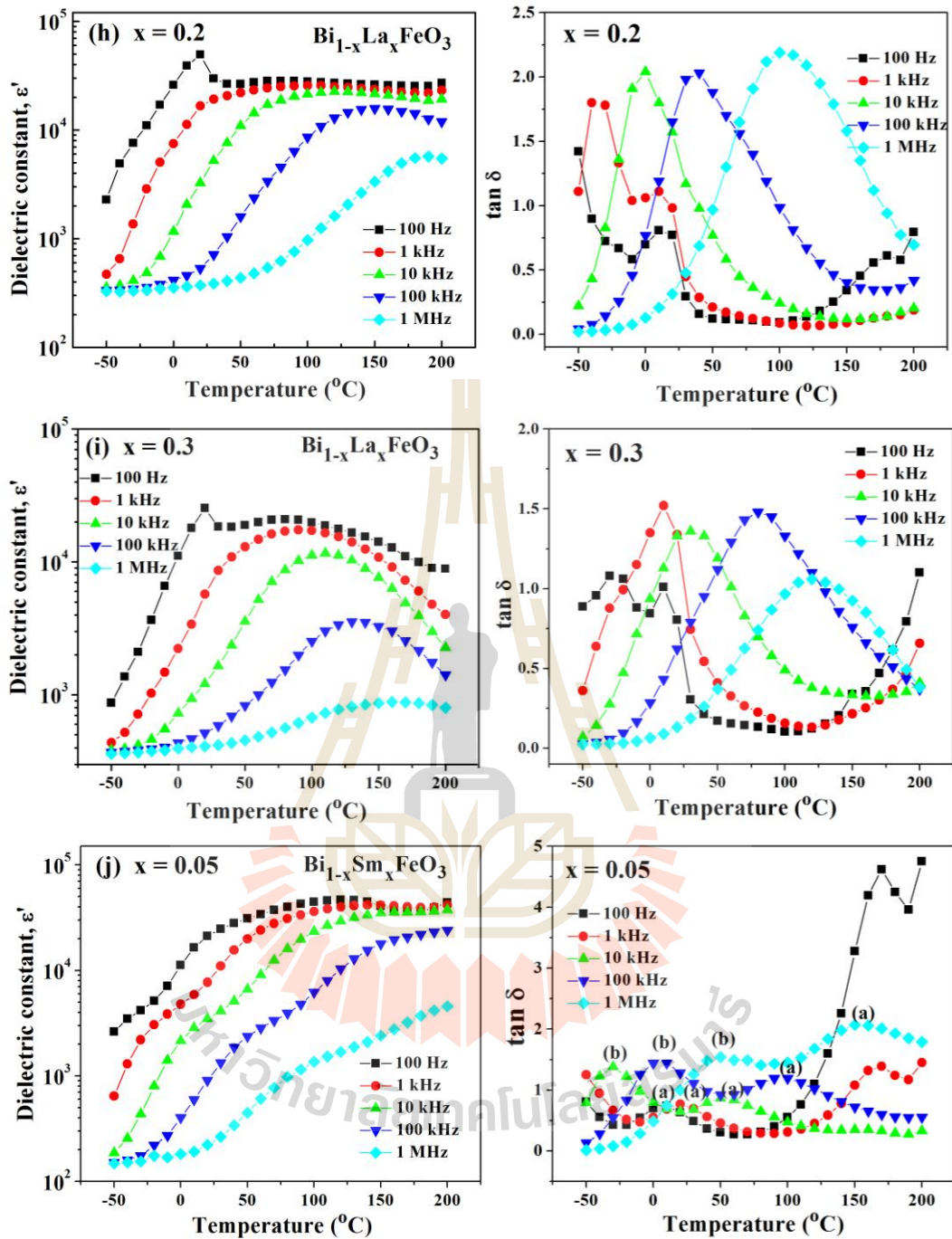


Figure 4.36 Temperature dependence of the dielectric constant (ϵ') and the loss tangent ($\tan \delta$) in the frequency range of 10^2 – 10^6 Hz for the doped-BiFeO₃ ceramics (Continued).

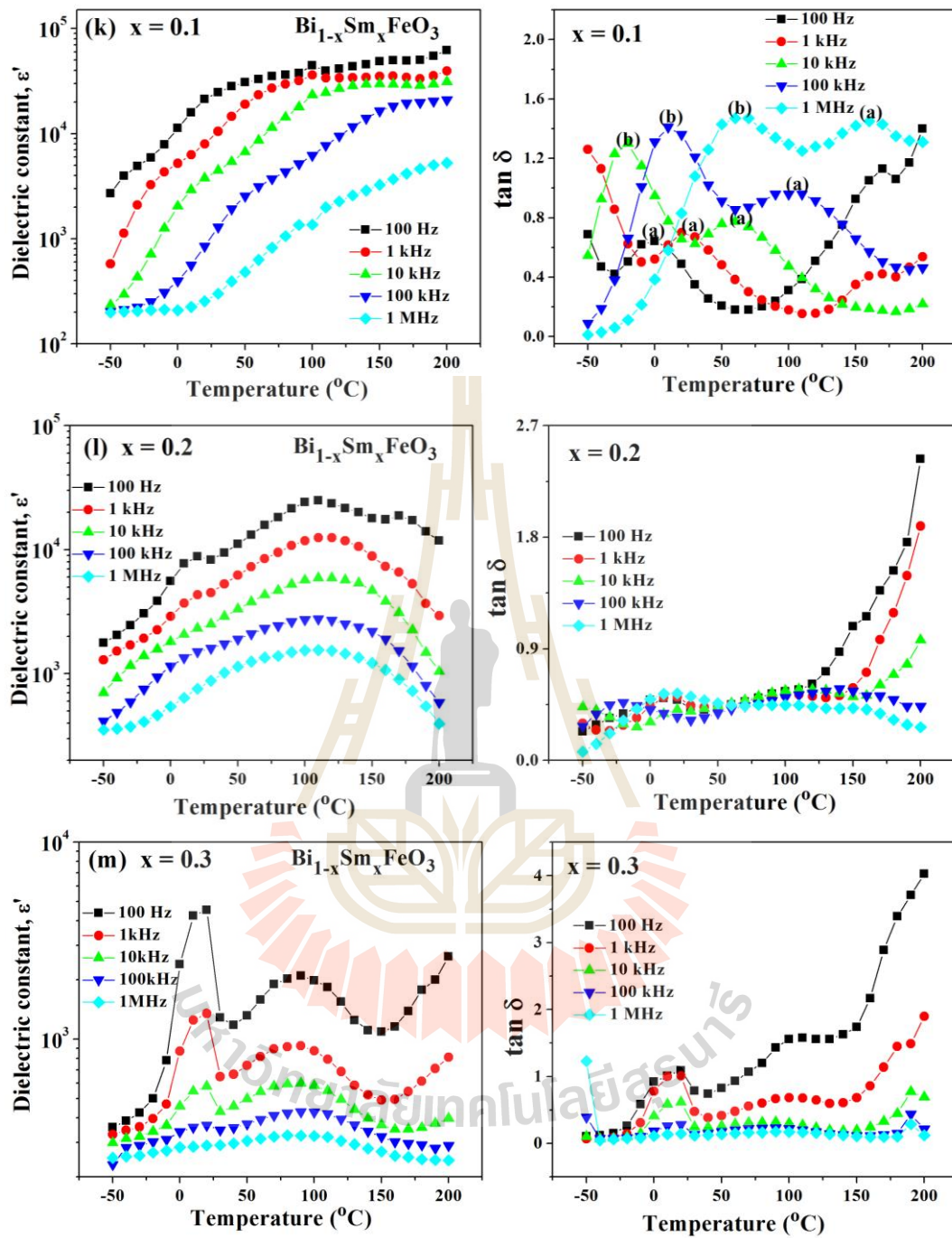


Figure 4.36 Temperature dependence of the dielectric constant (ϵ') and the loss tangent ($\tan \delta$) in the frequency range of 10^2 – 10^6 Hz for the doped- BiFeO_3 ceramics (Continued).

4.5.4 Effect of DC conductivity on dielectric behavior

Chapter II described the effects of DC conductivity on the dielectric properties of dielectric materials, where it was explained that DC conductivity can lead to the total dielectric loss of the samples. As in the previous sections, the results show the frequency dependence of the dielectric loss. The dielectric loss behavior of all the Ba-doped samples is very similar at high temperatures (> 150 °C). As in the low frequency regions, an exponential-like decrease is observed and they decrease exponentially to a low value at high-frequency and at high temperatures. If the frequency is sufficiently high, the loss due to the dielectric relaxation process is prominent and the dielectric loss peak can be clearly observed. The results show that DC conductivity has an effect on the total dielectric response of BiFeO₃-based ceramics. Therefore, the dielectric properties of BiFeO₃ and doped-BiFeO₃ ceramics may be explained by the Cole-Cole relaxation model modified in terms of DC conductivity (σ_{dc}), as

$$\varepsilon^* = \varepsilon' - j \left[\varepsilon'' + \frac{\sigma_{dc}}{\omega \varepsilon_0} \right] = \varepsilon'_\infty + \frac{\varepsilon'_s - \varepsilon'_\infty}{(1 + j\omega\tau)^\alpha} - j \frac{\sigma_{dc}}{\omega \varepsilon_0} \quad (4.4)$$

Where $\varepsilon^* = \varepsilon' - j\varepsilon''$, ε' is the real part of complex dielectric permittivity and ε'' is the imaginary part of permittivity, if $\alpha = 1$, the dielectric parameters can be presented as

$$\varepsilon' = \varepsilon'_\infty + \frac{\varepsilon'_s - \varepsilon'_\infty}{1 + j\omega\tau} \quad (4.5)$$

$$\varepsilon'' = \varepsilon'_s - \varepsilon'_\infty \left(\frac{\omega\tau}{(1 + \omega\tau)^2} \right) - \left(\frac{\sigma_{dc}}{\omega \varepsilon_0} \right) \quad (4.6)$$

The first term on the right-hand side of Eq. (4.6) represents a loss component due to the relaxation process while the second term shows the loss component due to DC conductivity. In the case of the Ba and Sm-doped BiFeO₃ samples, the peaks of the dielectric loss clearly appear at high-temperatures and at high frequencies. The peak of the dielectric loss cannot be observed in the high frequency range in the case of the Bi_{1-x}La_xFeO₃ ceramics. The loss due to the DC conductivity effect at frequencies below 10⁴ Hz can clearly be found for all of the doped samples. Therefore, the exponential decreases in the dielectric loss spectra can be assigned to the effects due to the DC conduction is dominant. Hence, the dielectric loss of the spectra according to the Eq. 4.7 is equal to

$$\varepsilon'' \approx \frac{\sigma_{dc}}{\varepsilon_0 \omega} \quad (4.7)$$

The experimental data of Ba-doped in BiFeO₃ with x = 0.05 and 0.3 samples (group I) show a similar result and it is observed that there is a small hump of the dielectric loss in the high frequency region. So the Eq. (4.4) can be used to fit the experimental data for the samples in this group. The fitted results of the experimental data are shown in Figure 4.37 with symbols for the experimental points and red lines are used above the equation to fit the experimental data. From the fitted results, it is clearly found that this relaxation model (Eq. (4.6)) can be used to give a good fit to the experimental data of the dielectric constant. In the high-frequency range rapid decreases in the dielectric constant and the relaxation peaks appear for the samples in group I. It should be noted that the low frequency range of the dielectric constants deviate from the spectra fitted according to the model. For group-II, with La-doped with x = 0.05, 0.1 and 0.3, the dielectric loss peak is observed and the dielectric

constant can be well fitted at a low–frequency range. Consequently, the dielectric response of Group–II can be fitted by the Eq. (4.4) when it is combined with the terms of DC conduction and the relaxation process. The fitted results of the experimental data are exhibited in Figure 4.38. Finally, Figures 4.39 show the frequency dependence of dielectric loss (ϵ'') in the high temperature range (150 to 180 °C) of Sm–doped BiFeO₃ with $x = 0.05$ and 0.1 ceramics. It should be noted that the dielectric loss plots of Sm–doped BiFeO₃ samples are similar to those observed in the La–doped samples. Therefore the plots of these samples can be fitted by using the Eq. (4.4).

The value of DC conductivity (σ_{dc}) is obtained from the fitted results showing decreases in frequency with increases in temperature. The plots of $\ln(\sigma_{dc})$ and $1000/T$ (K⁻¹) are presented as shown in Figures 4.40(a), (b), and (c). The conduction activation energy inside the grain can be calculated from the polaron theory, which can be expressed as

$$\sigma = \sigma_0 \exp\left(\frac{-E}{k_B T}\right) \quad (4.8)$$

where E is the conduction activation energy, σ_0 is the pre–exponential factor, k_B is the Bozmann constant and T is temperature (K). As a result, the DC conduction activation energies can be obtained from the above equation as shown in the paragraph below.

In the case of Group I, the DC conduction activation energy can be obtained by Eq. (4.8). The DC conductivity (σ_{dc}) is plotted as the function of $1000/T$ for Ba–doped samples in Figure 4.40(a). The calculated values of E_a are 0.29 eV and 0.77 eV

for $\text{Bi}_{1-x}\text{Ba}_x\text{FeO}_3$ (where $x = 0.05$ and 0.3) samples. The activation energy values obtained are 0.45 and 0.74 for Sm doping amounts of 5% and 10%. A surprising result is found in the E_a of Ba- and Sm-doped BiFeO_3 system. The result indicates that by increasing the E_a with increasing Ba and Sm doping concentrations up to a high concentration (10% for Sm and 30% for Ba). According to the experimental results, the highest value of σ_{dc} which results in the lowest dielectric constant values. Several reasons lead one to expect high conductivity for doped- BiFeO_3 . The temperature dependence of the conductivity for a semiconductor can be explained by the small polaron jumping mechanism. The activation energy for jumping is significantly related to the polaron binding energy and bandwidth. The additional amount of a higher Ba and Sm in Bi-site may result in the bending of the bonds angle or bonds length in the structure and location of the charge carriers with a decrease in bandwidth. Therefore, the decrease in the bandwidth and the increase in polaron binding energy results in an increase in activation energy (Lee and Manthiram, 2006). Moreover, at a higher dopant level, the localized defect associations most probably form at the expense of free oxygen vacancies, which are associated with the decrease in conductivity and increase in activation energy (Li *et al.*, 2001). As seen in Figure 4.40(b), the E_a values in the samples for $\text{Bi}_{1-x}\text{La}_x\text{FeO}_3$ (where $x = 0.05, 0.1,$ and 0.2) can be estimated as 0.47, 0.40, and 0.32 eV, respectively. The DC conduction activation energy decreases with the increases in La doping levels. The observations in all giant dielectric materials suggest an internal barrier layer capacitance (IBLC) effect based on the presence of Maxwell-Wagner polarization or interfacial polarization at grain boundaries (Kolte *et al.*, 2015). The accumulation of charge carriers at the insulating boundaries can produce the interfacial polarization under the

applied electric field. These accumulated charge carriers are referred to as the Maxwell–Wagner polarization. Therefore, with lower conduction activation energy, the promotion of polarization at the interfacial grains is easier. In addition, the decrease of E_a in doping levels might be due to a decrease in the defects in the charge bonds and vacancies as well as the creation of secondary phase levels within the band gap (Al-Douri *et al.*, 2011). It can also be observed that there is a small amount of secondary phases in the La-doped sample, so the decreases in the defects are only considered.



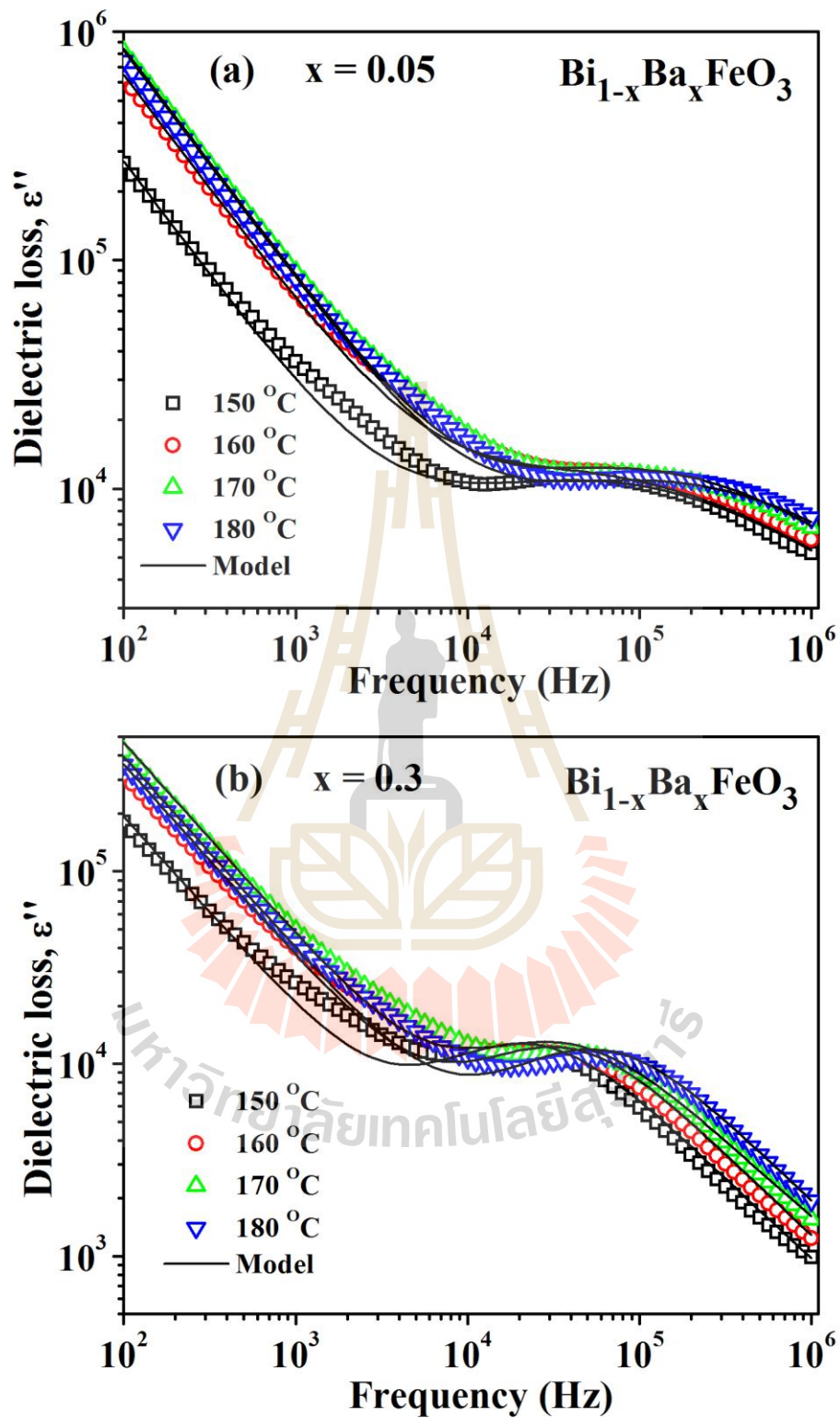


Figure 4.37 Dielectric loss and fitted results of $\text{Bi}_{1-x}\text{Ba}_x\text{FeO}_3$ sintered at 800 °C for 3 h for (a) $x = 0.05$ and (b) $x = 0.3$.

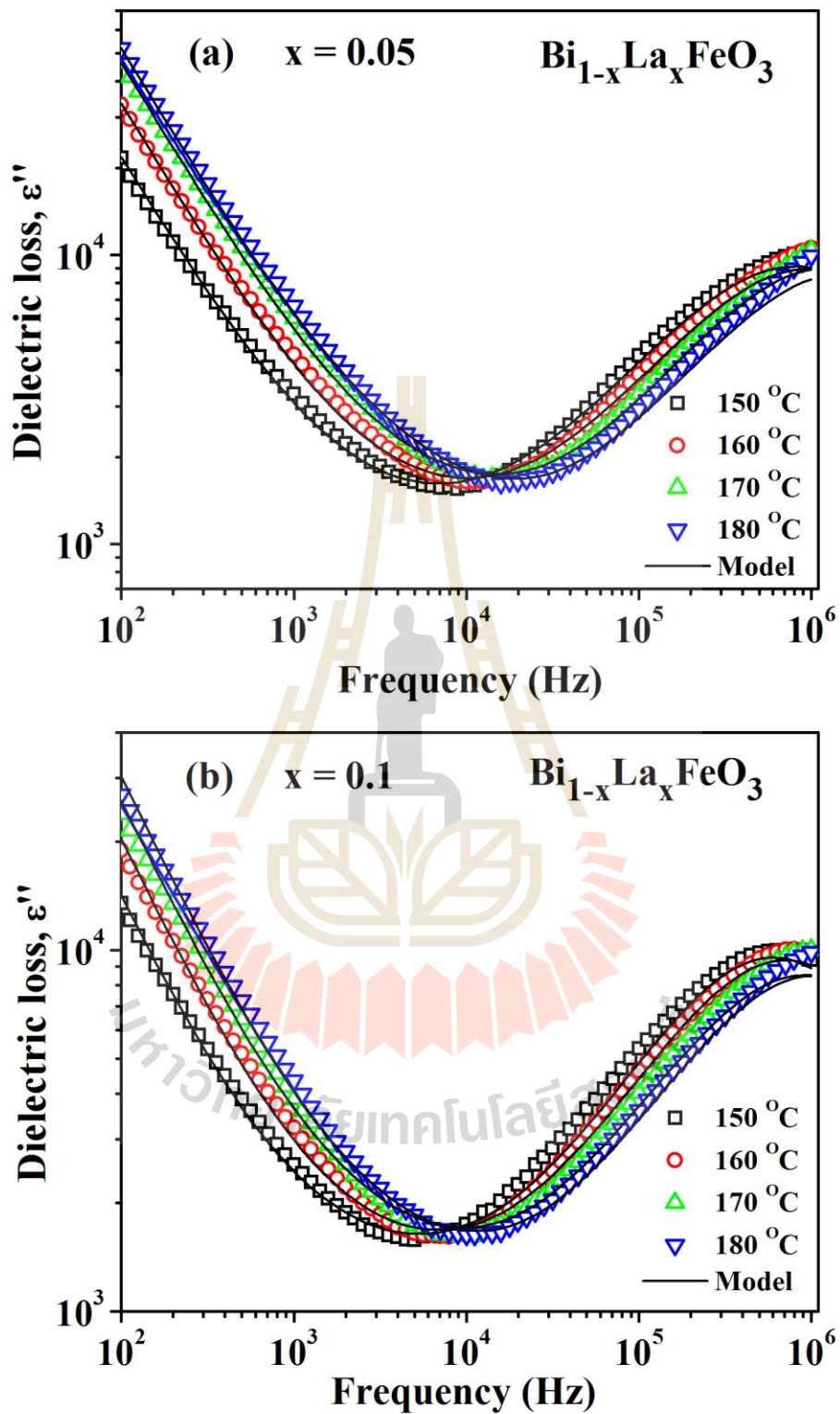


Figure 4.38 Dielectric loss and fitted results of $\text{Bi}_{1-x}\text{La}_x\text{FeO}_3$ sintered at 800 °C for 3 h for (a) $x = 0.05$, (b) $x = 0.1$, and (c) $x = 0.2$.

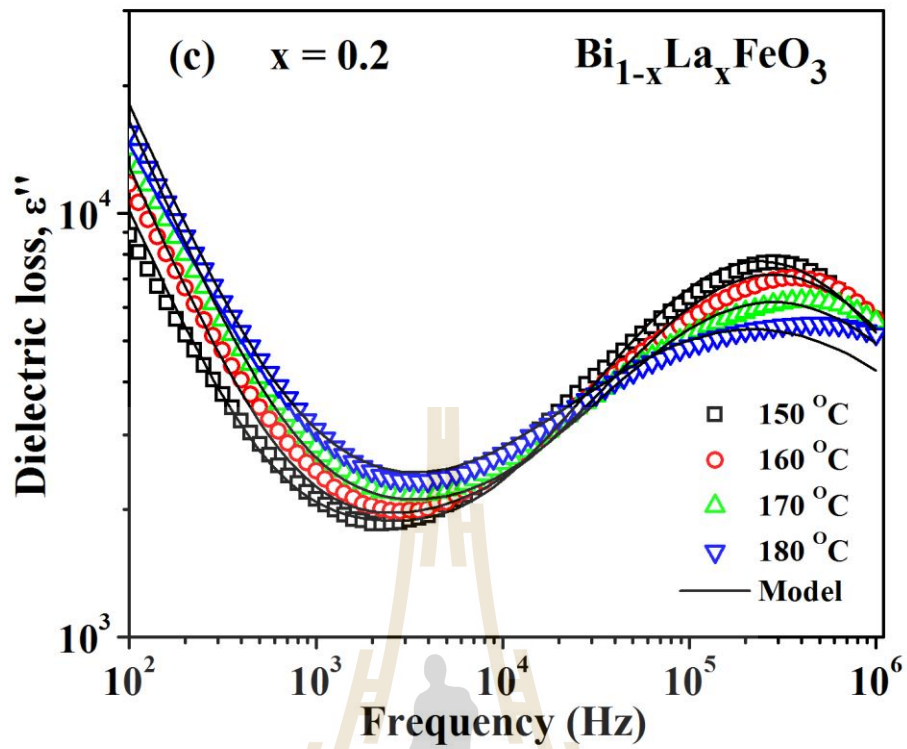


Figure 4.38 Dielectric loss and fitted results of $\text{Bi}_{1-x}\text{Ba}_x\text{FeO}_3$ sintered at 800 °C for 3 h for (a) $x = 0.05$, (b) $x = 0.1$, and (c) $x = 0.2$ (Continued).

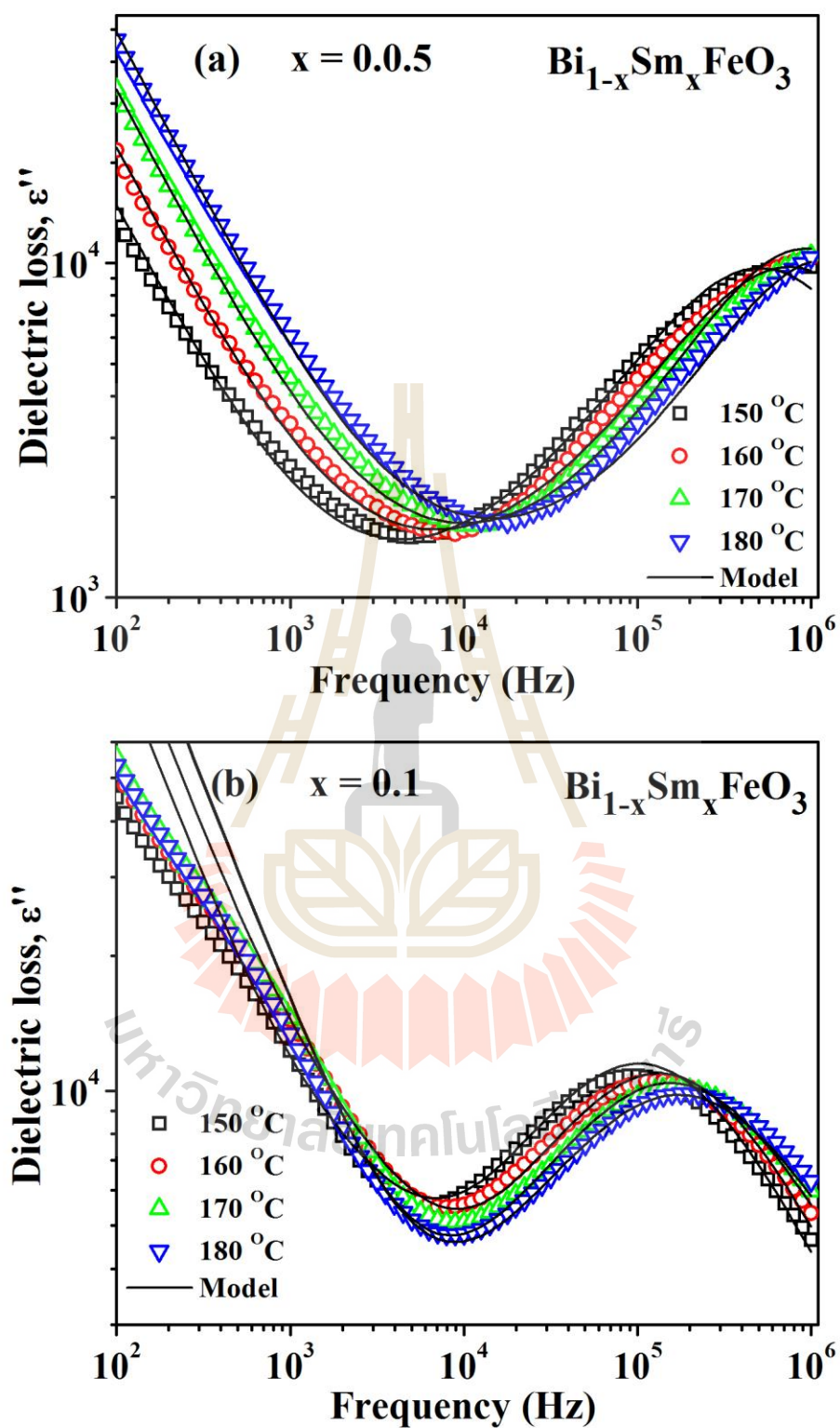


Figure 4.39 Dielectric loss and fitted results of $\text{Bi}_{1-x}\text{Sm}_x\text{FeO}_3$ sintered at 800 °C for 3 h for (a) $x = 0.05$ and (b) $x = 0.3$.

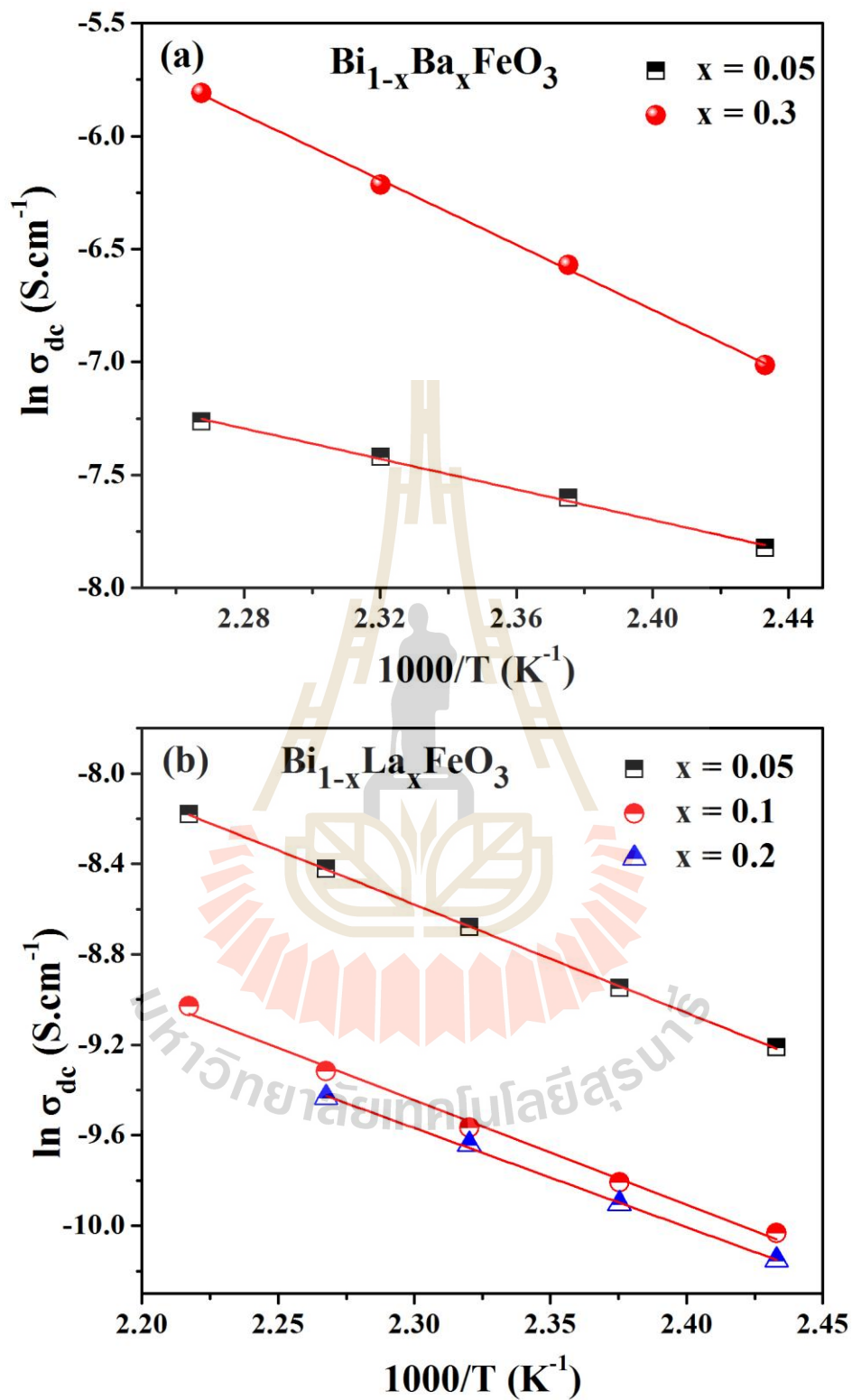


Figure 4.40 Temperature dependence of DC conductivity for (a) Ba-doped $BiFeO_3$, (b) La-doped $BiFeO_3$, and (c) Sm-doped $BiFeO_3$.

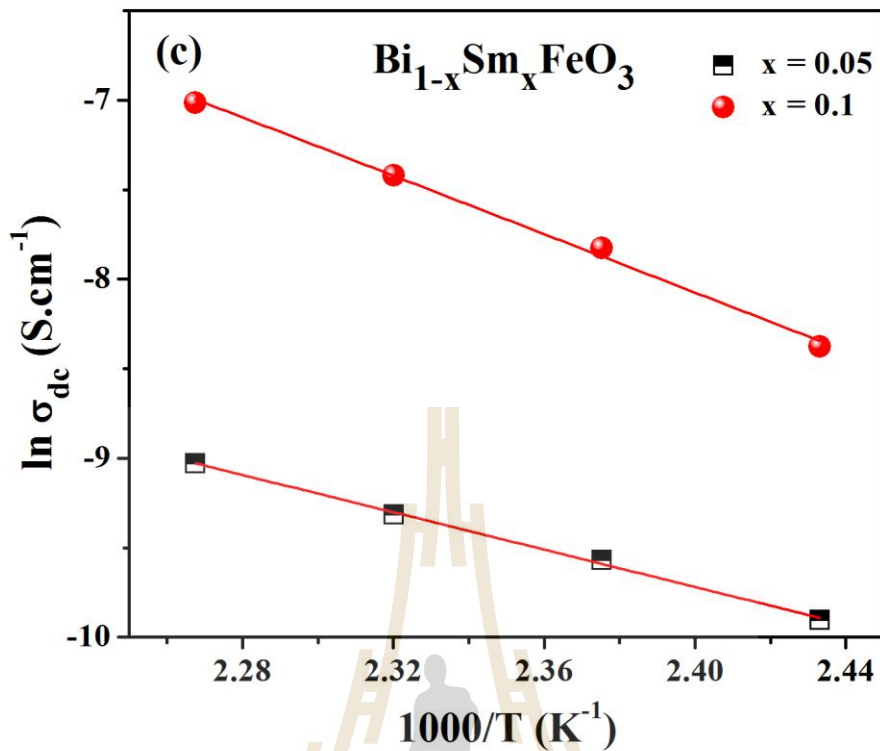


Figure 4.40 Temperature dependence of DC conductivity for (a) Ba-doped $BiFeO_3$, (b) La-doped $BiFeO_3$, and (c) Sm-doped $BiFeO_3$ (Continued).

4.5.5 Impedance spectroscopy

To understand the origin of the giant dielectric constant in the $BiFeO_3$ ceramics it has been suggested that giant dielectric properties may be attributed to the Maxwell-Wagner polarization or interfacial polarization at the grain boundaries. In fact, the interfacial polarization can be induced in heterogeneous materials, which are comprised of the semiconducting of grains and the insulation of their grain boundaries. It has also been suggested that the accumulated impurity phases can assume to the insulating properties of $BiFeO_3$ bulks and the grain bulk of $BiFeO_3$ act as semiconductors. The electrical behavior of the polycrystalline ceramics was further investigated in a wide range of frequency using a complex impedance spectroscopy

technique. This measurement enables us to separate the inhomogeneous dielectric response of the complex impedance. The polycrystalline ceramics usually exist of bulk (grain) and grain boundary components corresponding to real and imaginary parts of the complex impedance. The complex impedance of ceramics can be modeled as a parallel combination of resistance (R) and capacitance (C) equivalent circuit which can be mainly attributed to the dielectric response as described by using the Cole–Cole equation,

$$Z^* = Z' - iZ'' = \frac{1}{R_g^{-1} + (i\omega C_g)^\alpha} + \frac{1}{R_{gb}^{-1} + (i\omega C_{gb})^\beta} \quad (4.1)$$

where R_g , R_{gb} represent the resistance of grain and grain boundary; C_g , C_{gb} are the capacitance of grain and grain boundary; α , β are both constant values and $0 < \alpha, \beta \leq 1$. Figure 4.41 reveals the impedance spectra Z' and Z'' (called the Nyquist plot) of the pure BiFeO_3 and doped- BiFeO_3 ceramics at various temperatures. For the pure BiFeO_3 sample, the Z^* plots exhibited exponential-like increases at the lower temperatures (-50 to -10 °C), which indicate a non-Debye type of relaxation. As the temperature increases (≥ 10 °C), these plots display depressed semicircles indicating that the equivalent circuit must consist of a series of more than one parallel subcircuit in this temperature range but they cannot be seen. In the high frequency region for this temperature range, their tails are observed representing the electrode resistance. This observation in the high frequency range is similar to that observed for yttrium doped $\text{Li}_7\text{La}_3\text{Zr}_2\text{O}_{12}$ cubic lithium garnet and BiFeO_3 (Makhdoom *et al.*, 2013; Murugan *et al.*, 2011). The results show two different frequency regions for the complex impedance data of BiFeO_3 ceramics, of which one

is a high frequency region displaying the tail and the other is at a low frequency displaying a semicircular arc which indicates that the sample is electrically inhomogeneous. The impedance data corresponding to an ideal Debye-like response which can be analysed by using an equivalent circuit consisting of a parallel combination of R (resistance) and C (capacitance). As the temperature increases (above 100 °C), a single semicircle arc in the impedance spectra is formed and its tail is in a high frequency range which decreases with increasing temperature and this can be modelled as an equivalent electric circuit as shown in the inset of Figure 4.41(b). This implies that a single semicircular arc in complex impedance at a low frequency range of the pure BiFeO₃ sample can be identified as a grain boundary effect only and the effect of the electrodes seemed to be ignored. The non-zero intercept of the semicircular arc at a high frequency offers an estimation of the resistance of the grain bulk (R_b). In other words, as the temperature increases, the semicircular arc is associated to originate from the grain boundary and the non-zero intercept can be assigned to the resistance of the grain interior. The intercept of the semicircle is not significantly affected by the temperature increases indicating that resistance only slightly changes with temperature. From the fitted data, the resistances of the grain and grain boundaries can be obtained from the intercept of the curves with the real-axis of the impedance Z' axis. The grain and grain boundary resistances (R_b , R_{gb}) have been obtained from the fitted data as shown in Table 4.7. It can be seen from the table that the grain resistance (R_b) and the grain boundary resistance (R_{gb}) decrease with increases in temperature implying that the presence of a negative temperature coefficient of resistance (NTCR) behaviour which is in the nature of semiconductor materials. Indeed, these results were observed in the Nyquist plot of the pure BiFeO₃

samples which is similar to that observed for the NTCR behaviour in the frequency dependence of Z' and Z'' which confirms the existence of the NTCR behaviour in the BiFeO_3 ceramic.

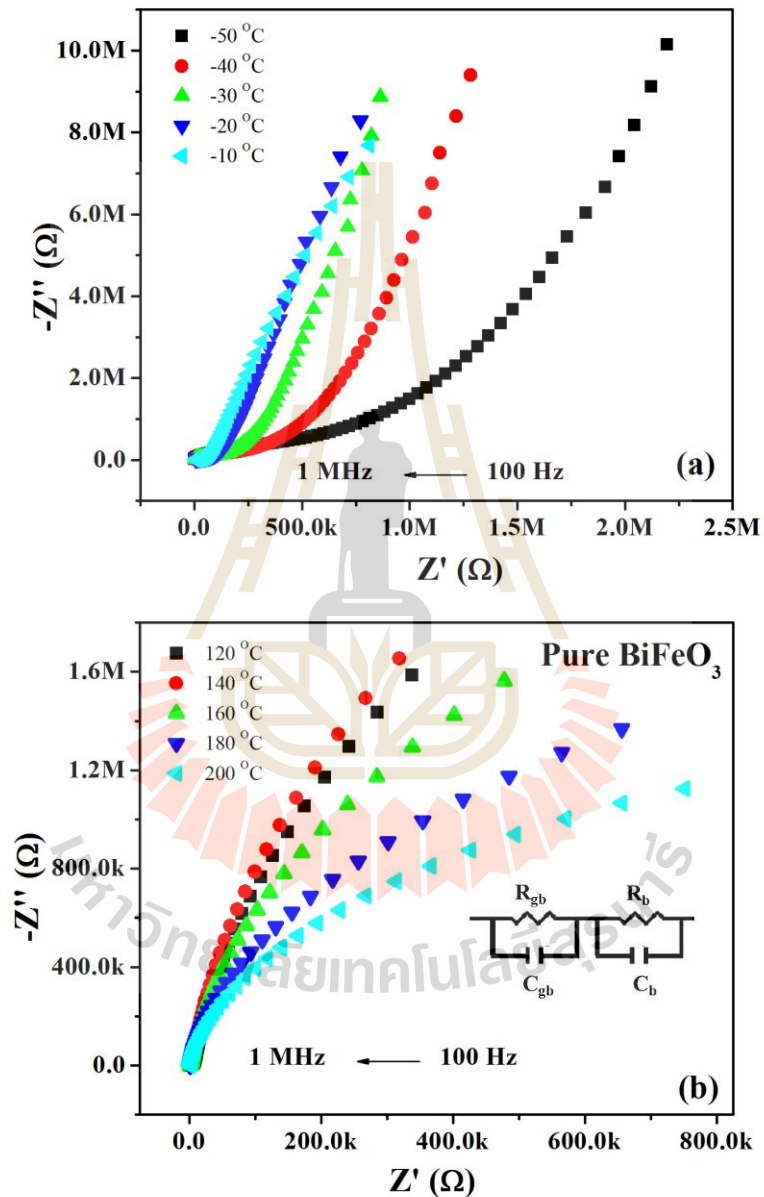


Figure 4.41 Complex impedance plane plot (Z' versus Z'') in the temperature range -50 to -10°C of the pure BiFeO_3 ceramic (a) and (b) the complex impedance plot in the temperature range 120 – 200°C .

The complex impedance spectra at selected temperatures for $\text{Bi}_{1-x}\text{Ba}_x\text{FeO}_3$ ceramics are shown in Figure 4.42. At temperatures above 50 °C, the complex impedance plots of all doped samples are comprised of two semicircular arcs with nonzero intercepts on a real axis in a high frequency range indicating that the sample is electrically inhomogeneous. It should be noted that the impedance plane clearly indicates the formation of small semicircular arcs in the low-frequency region and a large semicircular arc in the high-frequency region. With further increases in temperature (above 160 °C), the impedance spectra present a suppressed semicircular arc in a high-frequency region. At this temperature range, a single semicircular arc coexists with a low concentration of Ba doping (5% and 10%). At temperatures below 150 °C, the shape of the plot implies that there are at least two relaxation behaviours at different relaxation frequencies in the electrical process in these materials. The first arc at a high frequency is due to the contribution from the bulk grain properties and the appearance of the large one suggests a grain boundary contribution. Figure 4.42 indicates the complex impedance plots with fitted profiles using an electrical circuit model which corresponds to the Debye type model. The values of the fitted electrical parameters at different temperatures, which are deduced from the equivalent circuit model, are represented in Table 4.7. Decreases in resistance associated with the grain (R_g) and with increases in temperature imply that there is a thermally activated conduction mechanism. However, the grain boundaries resistance (R_{gb}) also shows a decrease in R_{gb} with increases in temperature. The decreases in both R_g and R_{gb} as the temperature increases are associated with the presence of a negative temperature coefficient of resistance (NTCR) in the materials.

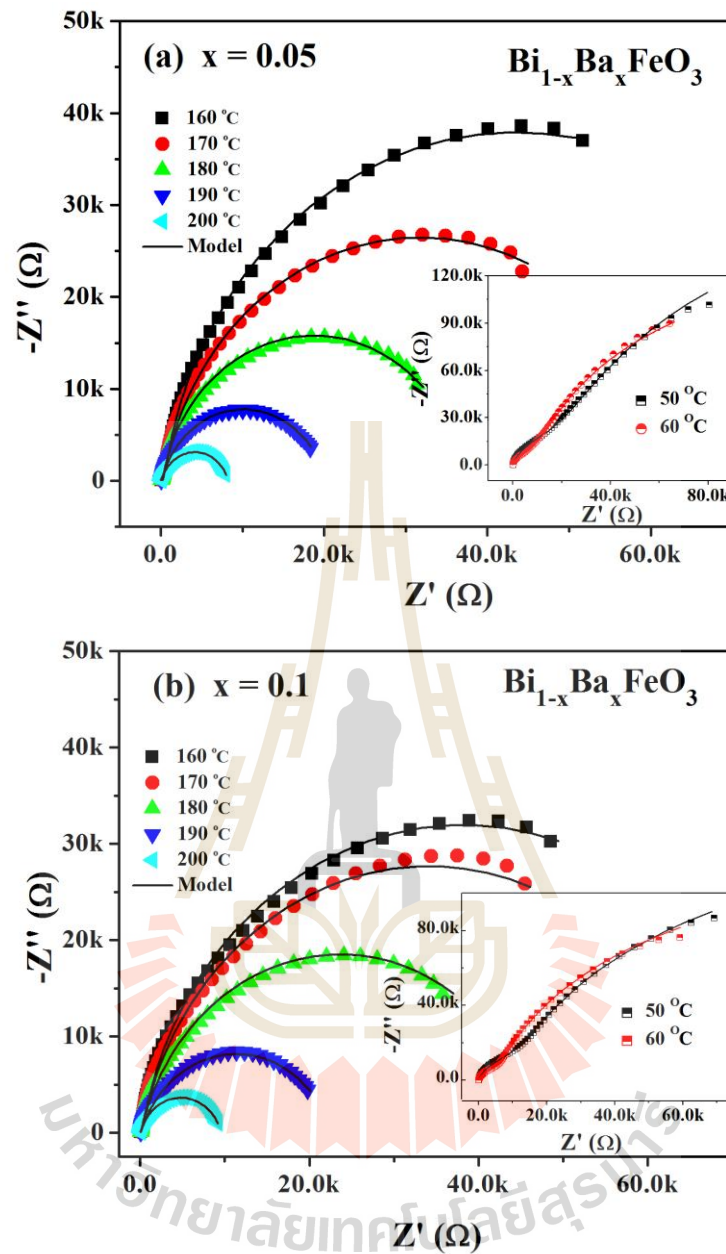


Figure 4.42 Complex impedance plane plot (Z' versus Z'') in the temperature range 120–200 °C of the pure BiFeO_3 and Ba-doped BiFeO_3 ceramics sintered at 800 °C for 3 h; inset is inset is complex impedance plot at 50 and 60 °C.

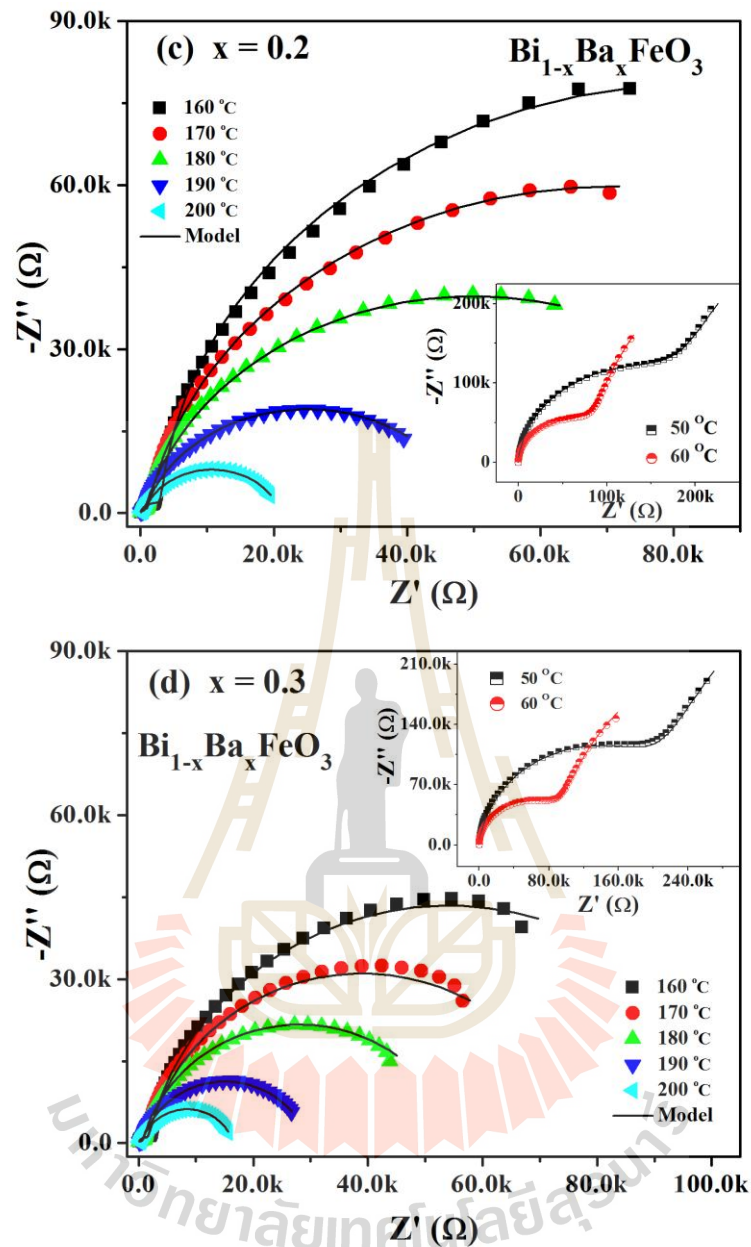
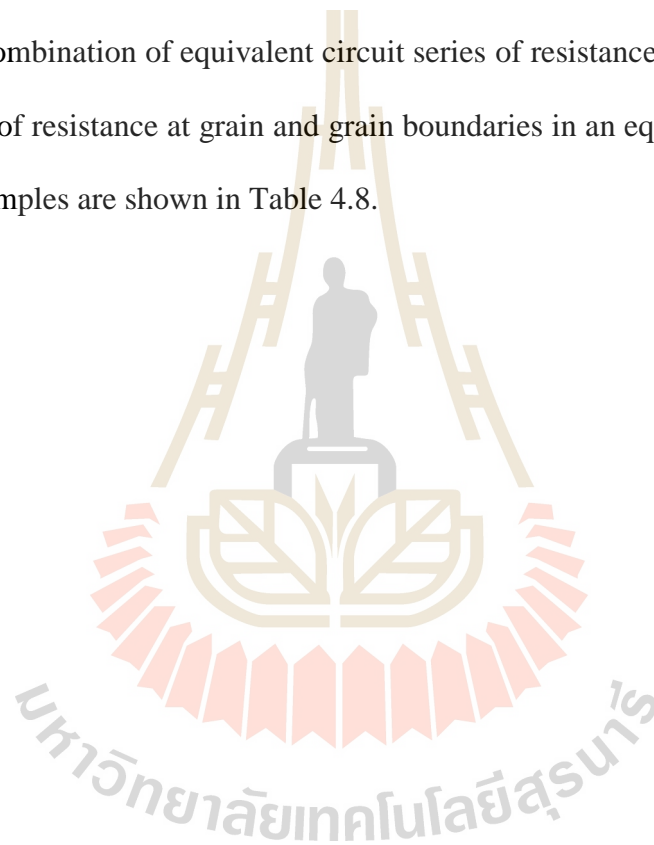


Figure 4.42 Complex impedance plane plots (Z' versus Z'') in the temperature range 120–200 °C of the pure BiFeO_3 and Ba-doped BiFeO_3 ceramics sintered at 800 °C for 3 h; the inset is complex impedance plots at 50 and 60 °C (Continued).

Figures 4.43 show the variations of the impedance spectra for La-modified BiFeO_3 samples at various x temperatures. A semicircular arc is observed at low temperatures (-50 to -10°C) of La-substituted materials, but with increases in

temperature this arc becomes a large semicircle. It should be noticed that the spike in the impedance spectra appears as a straight line with a slope of about 45° which can be modelled on the Warburg impedance. Therefore the complex impedance spectra can be represented by an equivalent combination circuit of resistors (R), capacitors (C), and Warburg type impedance elements (W). In a low temperature range, the equivalent circuit consists of a Warburg type circuit which was modified for impedance fitting as shown in the inset of Figure 4.43(b). The Warburg impedance is generally associated with the kinetic and diffusion process in a solid electrolyte (Dzik *et al.*, 2011). For this experiment the application of a Warburg type impedance made it possible to take into account the diffusion of ions on the electrode surface of the materials. It is also observed that the interception point on the Z' axis (real part) shifts towards the origin as the temperature increases which implies that there is a decrease in the bulk resistance (R_g). An equivalent circuit used for impedance plots was composed of R_g connected in a series with a parallel combination of C_{gb} and R_{gb} and a Warburg type impedance (W). The magnitudes of the grain resistance (R_g) and the grain boundary resistance (R_{gb}) at low temperatures are shown in Table 4.8. As the magnitude of the temperatures rises, the grain resistance (R_g) decreases, which indicate an increase in conductivity with increases in temperature. This result implies the existence of a negative temperature coefficient of resistance (NTCR) at low temperatures in this material. There is a tendency for a single semicircular arc to occur at temperatures up to 100°C for all La-doped in BiFeO_3 ceramics. It can be observed that the semicircles do not originate from zero on the x-axis (Z' axis). At a high temperature range, it was not possible to observe any part of Warburg type impedance in the Nyquist plots. The centers of the semicircular arcs are well below

the real axis which suggests that there is not any Debye type of relaxation in this material. It is also found that the non-zero intercept along Z' axis shows a small change. The intercept of the semicircular arcs on a real axis provide values for grain and grain boundary resistance. R_g and R_{gb} values decrease with increases in the temperature indicating a rise in the conductivity of the sample. It is found that semicircular arcs can be well described by the Cole–Cole equation, which provided a model of a combination of equivalent circuit series of resistance and capacitance. The fitted values of resistance at grain and grain boundaries in an equivalent circuit for all La-doped samples are shown in Table 4.8.



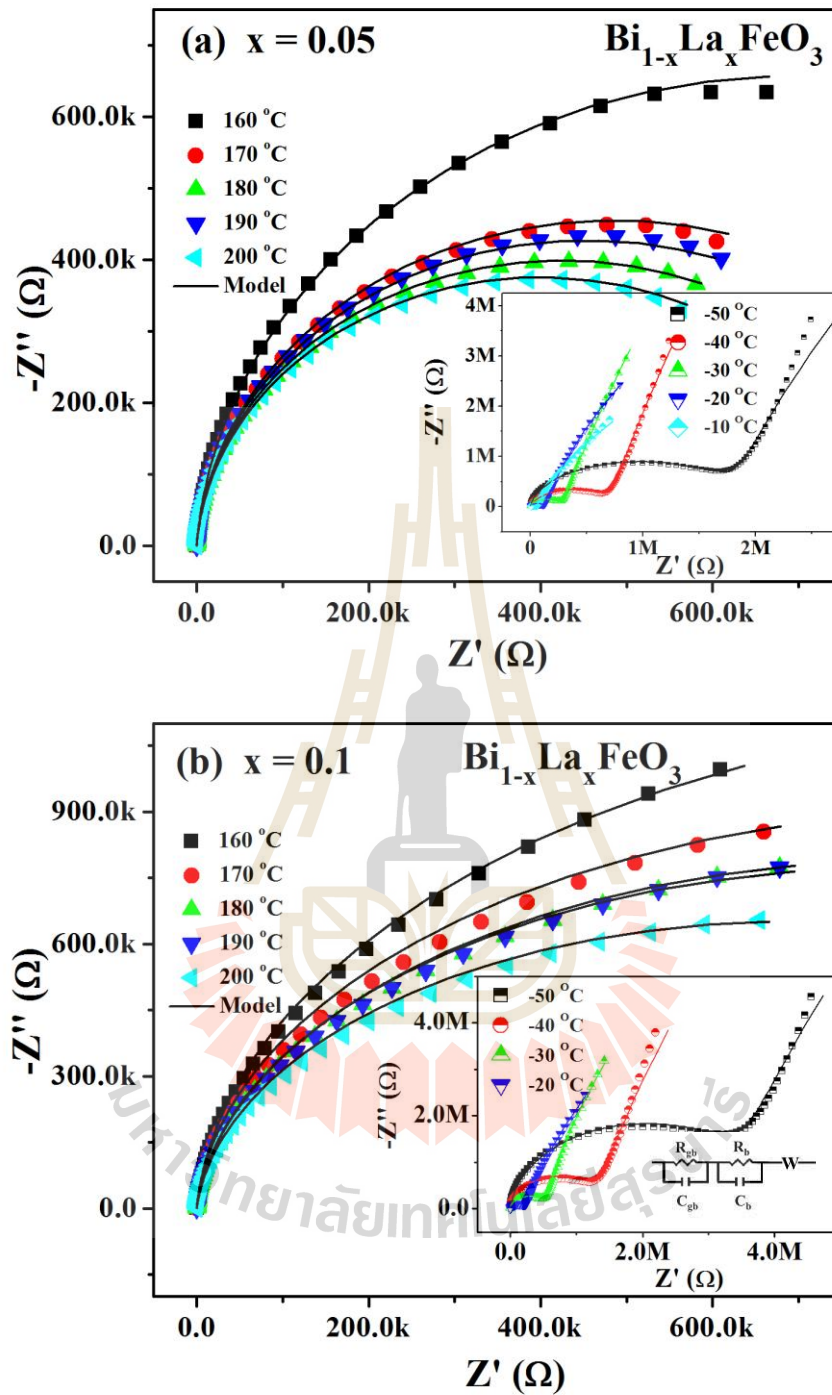


Figure 4.43 Complex impedance plane plots (Z' versus Z'') in the temperature range 120–200 °C of the pure BiFeO_3 and La-doped BiFeO_3 ceramics; the inset is the complex impedance plots in the temperature range -50 to -10 °C.

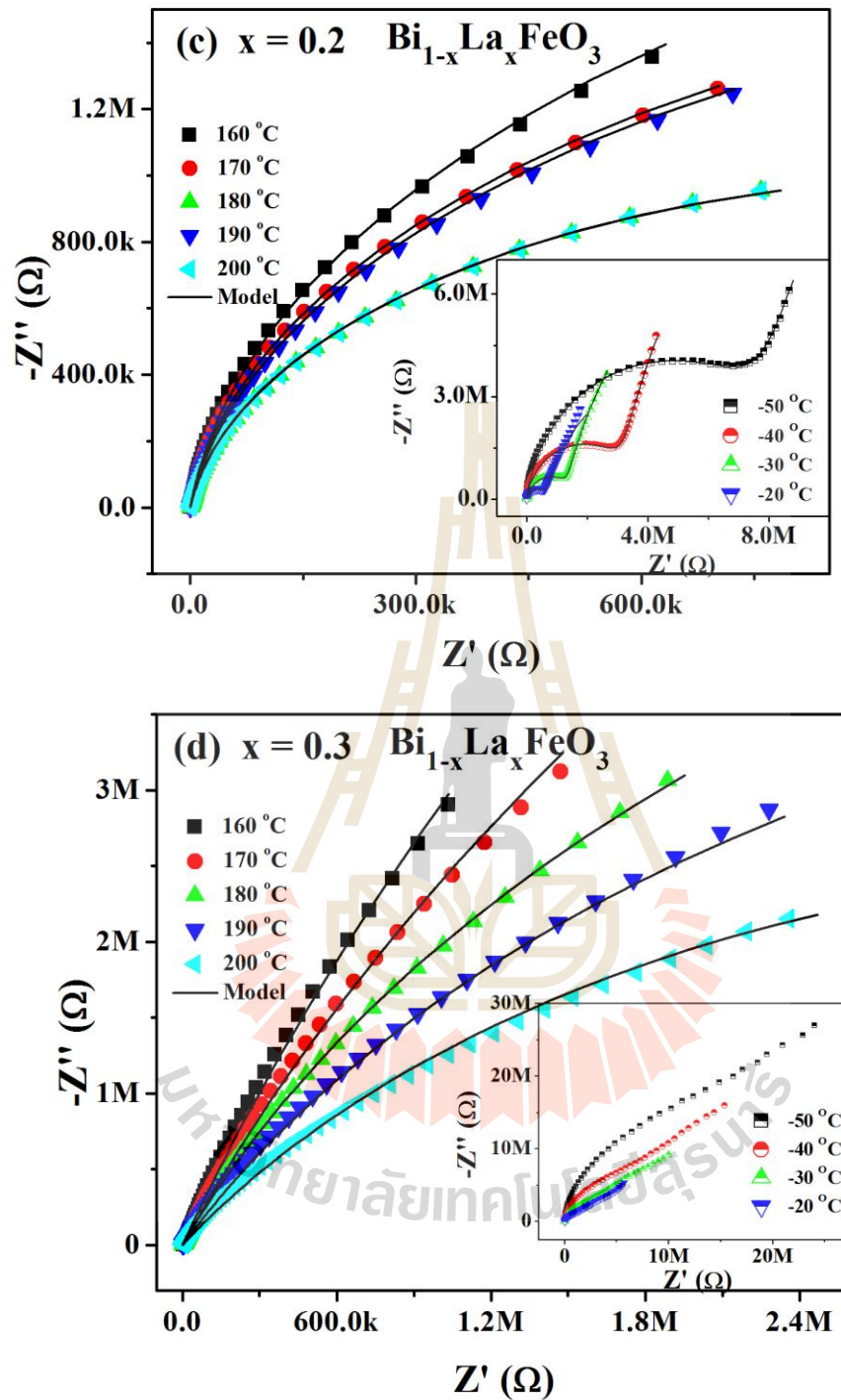


Figure 4.43 Complex impedance plane plots (Z' versus Z'') in the temperature range 120–200 °C of the pure BiFeO_3 and La-doped BiFeO_3 ceramics; the inset is the complex impedance plots in the temperature range -50 to -10 °C (Continued).

Figures 4.44 show the variations for the complex impedance plots, Z'' versus Z' (known as the Nyquist plot) for $\text{Bi}_{1-x}\text{Sm}_x\text{FeO}_3$ ceramics at different temperatures (150–200 °C). A semicircle is observed at temperatures from 150 to 200 °C for $\text{Bi}_{0.95}\text{Sm}_{0.05}\text{FeO}_3$ samples. The intercept of the semicircle along the x-axis provides the values of the bulk and grain boundary resistances which decrease with increasing temperatures indicating a rise in the conductivity of the ceramics. It is observed from the plots that at temperatures below 150 °C two semicircle arcs are dominant as revealed in the inset of Figure 4.44. The first of the very small semicircles in the high frequency region is due to the presence of bulk grain effects in the materials. The presence of the second semicircular arc in a low frequency range is mainly due to the grain boundary response. The small arc in the high-frequency range is observed which tends to be larger making it show the large arc in high-frequency region, which is because of the hug in the magnitudes of the resistance of the grains. With further increases in Sm ion doping, it can be observed that there are two semicircular arcs in the low temperature range as well. Above 150 °C, the shape of the plots is like a semicircular arc as the value of the Sm doped contents increases. The diameter of the semicircular-like shape decreases with increases in temperature has also been observed. However, the Nyquist plot of $\text{Bi}_{0.7}\text{Sm}_{0.3}\text{FeO}_3$ samples above 150 °C cannot fit the Cole–Cole relaxation plot well as shown in Figure 4.44(d). It is found that all the spectra of the Sm-doped samples show decreased semicircles with increases of temperature. The value of the bulk and grain boundary resistances (R_b , R_{gb}) were obtained from the intercept of the real part of the complex impedance (Z') as shown in Table 4.9. The grain boundary resistance (R_{gb}) decreases, which indicates an increase in conductivity. The decrease in R_{gb} with the increase in temperature indicates the

presence of a negative–temperature coefficient of resistance (NTCR) in the material as well, which is observed in semiconductors (Pattanayak *et al.*, 2013). These values indicate a decreasing trend with increases in temperature range as reported by (Lu and Qi, 2014). It has been observed that there is a decrease in the DC conductivity of both the grain and grain boundary increases in temperature.



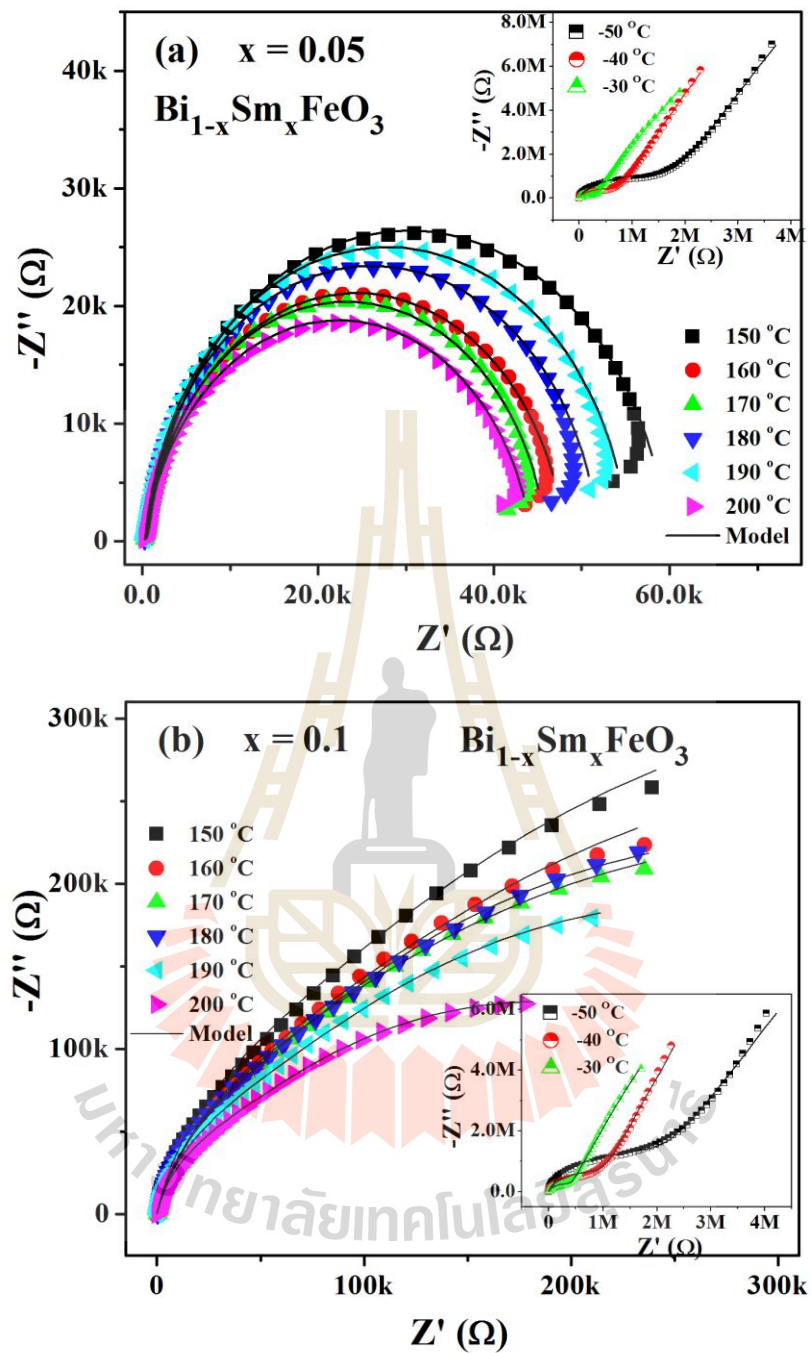


Figure 4.44 Complex impedance plane plots (Z' versus Z'') in the temperature range 120–200 °C of the pure BiFeO_3 and Sm-doped BiFeO_3 ceramics; the inset is the complex impedance plots in the temperature range -50 to -20 °C.

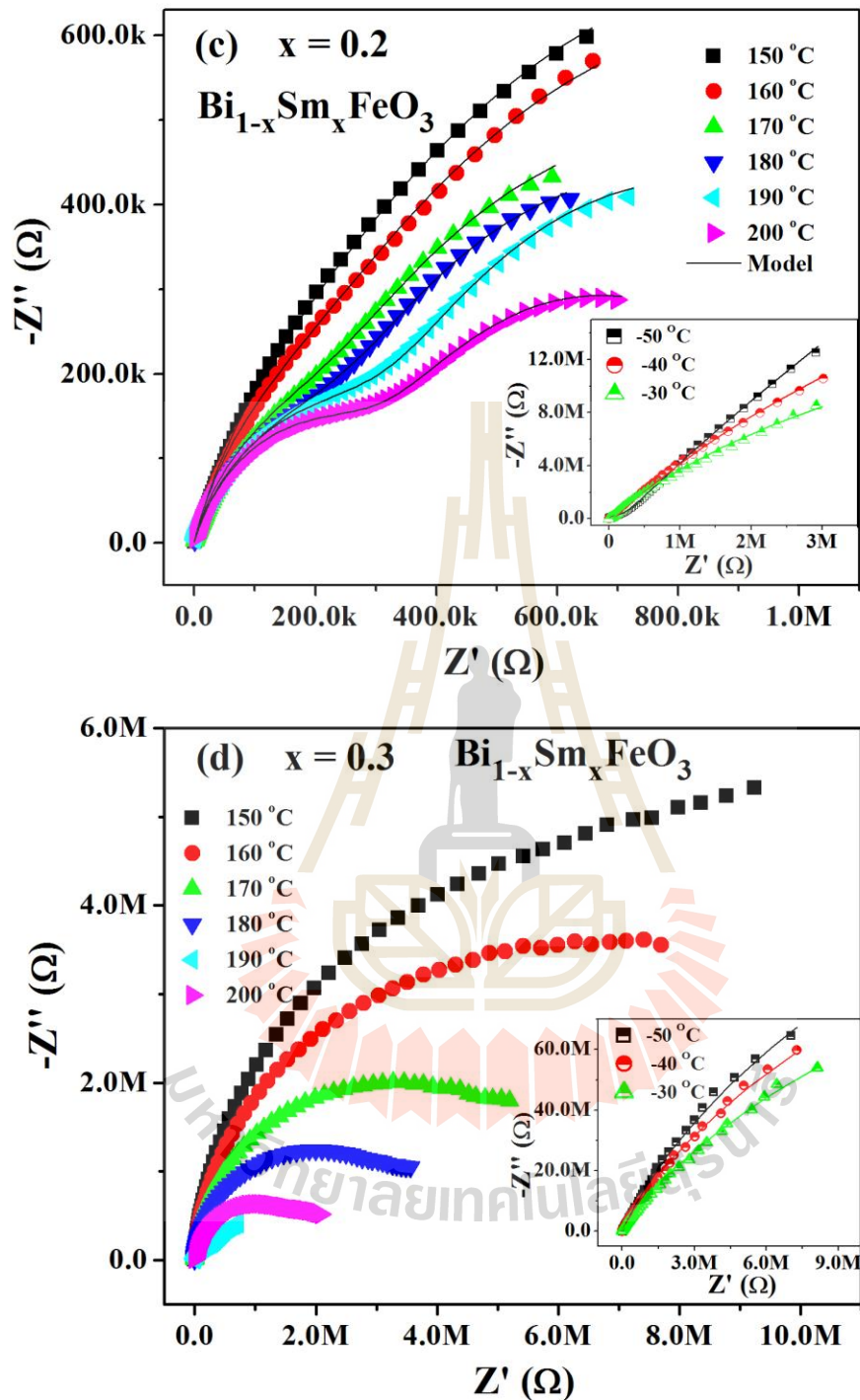


Figure 4.44 Complex impedance plane plots (Z' versus Z'') in the temperature range 120–200 °C of the pure BiFeO_3 and Sm-doped BiFeO_3 ceramics; the inset is the complex impedance plots in the temperature range -50 to -20 °C (Continued).

Table 4.7 Summarizing the fitting of parameters corresponding to equivalent circuits in the temperature range 50–170 °C and with different compositions of Ba–doped BiFeO₃ ceramics.

Temperature (°C)	Fitted result									
	Bi _{1-x} Ba _x FeO ₃									
	x = 0		x = 0.05		x = 0.1		x = 0.2		x = 0.3	
	R _g (kΩ)	R _{gb} (kΩ)	R _g (kΩ)	R _{gb} (kΩ)	R _g (kΩ)	R _{gb} (kΩ)	R _g (kΩ)	R _{gb} (kΩ)	R _g (kΩ)	R _{gb} (kΩ)
50	500	70000	19	380	11	270	190	850	21	75
70	200	45000	6.5	205	3	195	42	450	45	350
90	65	35000	2.5	135	0.8	125	13	280	13	200
110	25	20000	0.9	130	0.3	76	4.5	175	25	120
130	13	11000	0.3	630	0.1	45	1	100	4	72
150	6.8	7000		720		22.5	0.5	50	0.6	29
170	4.8						0.3			12

Table 4.8 Summarizing the fitting of parameters corresponding to equivalent circuits in the temperature range 50–140 °C and with different compositions of La-doped BiFeO₃ ceramics.

Temperature (°C)	Fitted result									
	Bi _{1-x} La _x FeO ₃									
	x = 0		x = 0.05		x = 0.1		x = 0.2		x = 0.3	
	R _g (kΩ)	R _{gb} (kΩ)	R _g (kΩ)	R _{gb} (kΩ)	R _g (kΩ)	R _{gb} (kΩ)	R _g (kΩ)	R _{gb} (kΩ)	R _g (kΩ)	R _{gb} (kΩ)
-50	3800		1750	57000	3400		7700		1300000	
-30	680		270	25000	500		1280		780000	
-10	130		55	11000	100		330		55000	
10	37		16	900	28		100		15000	
100	29	30000		15000		45000	2.1	32000		
120	20	15000		9500		15000	1.5	19000		
140	10	8500		3500		5300	1.0	9000		

Table 4.9 Summarizing the fitting of parameters corresponding to equivalent circuits in temperature range 50–170 °C and with different compositions of Sm-doped BiFeO₃ ceramics.

Temperature (°C)	Fitted result									
	Bi _{1-x} Sm _x FeO ₃									
	x = 0		x = 0.05		x = 0.1		x = 0.2		x = 0.3	
	R _g (kΩ)	R _{gb} (kΩ)	R _g (kΩ)	R _{gb} (kΩ)	R _g (kΩ)	R _{gb} (kΩ)	R _g (kΩ)	R _{gb} (kΩ)	R _g (kΩ)	R _{gb} (kΩ)
-50	3800		1600	485000	1850	480000	84	850000		
-30	680		300	115000	380	95000	50	60000		
-10	130		55	90000	90	11500	12	30000		
10	37		25	4000	30	8500	5			
100	29	30000	5	460	9	4500		6000		100
120	20	15000	1.5	300	7	1400		4000		55
140	10	8500	0.9	90	1	800		2800		36
160	5.8	6000	0.6	62		510		1600		20

These results can be described in terms of a thermal activated mechanism related to Arrhenius law $\alpha = \alpha_0 \exp(-E_a/k_B T)$. The fitting results for activation energy for both grain and grain boundaries are summarized in Table 4.10. It is found that La and Sm as a dopant decreases conduction activation energy for both grain and grain boundaries. Surprisingly, the value of E_a for both grain and grain boundaries is found to increase with an increase in Ba doping concentration. This result may be due to (i) the long range hopping process of space charges (Suresh and Srinath, 2013), (ii) the inhomogeneous microstructure in grains (Gong *et al.*, 2014). The enhancement of E_a at the grain boundary suggests increasing fractions of grain boundaries (Guo *et al.*, 2006). The E_a value at the grain and grain boundary is 0.42 and 0.3 eV respectively, which indicates that the first-ionization of oxygen vacancies is responsible for the p-type polaron hopping conduction. The values of activation energy for $\text{Bi}_{1-x}\text{La}_x\text{FeO}_3$ and $\text{Bi}_{1-x}\text{Sm}_x\text{FeO}_3$ systems are noticeably less than 0.7 eV and thereby the thermal excitation from the first-ionization of the oxygen vacancies is also governed. However, the E_a associated with grain has a value of 0.72 and 0.73 eV for $\text{Bi}_{0.8}\text{Ba}_{0.2}\text{FeO}_3$ and $\text{Bi}_{0.7}\text{Ba}_{0.3}\text{FeO}_3$ samples which should be attributed to the second-ionization of the oxygen vacancies. The complex reaction kinetics of BiFeO_3 is due to the highly volatile nature of Bi ions, which may create different types of defects in this compound. The Bi volatile may generate oxygen vacancies, which can be expressed as $V_o \leftrightarrow V_o^\bullet + e'$ and $V_o^\bullet \leftrightarrow V_o^{\bullet\bullet} + e'$. Therefore, the first-ionization and second-ionization of oxygen vacancies can be classified according to the values of activation energy of conduction. It should be noted that E_a at the grain boundary is revealed to be larger than the grain for La- and Sm-doped BiFeO_3 samples confirming that the grains are more conductive than the grain boundaries, as is clearly

evident from the equivalent circuit fitting. Another possible reason for the low value of E_a in grains as compared to that of the grain boundaries might result from a more ordered structure in the grains, as seen in the microstructure images (Makhdoom *et al.*, 2013).

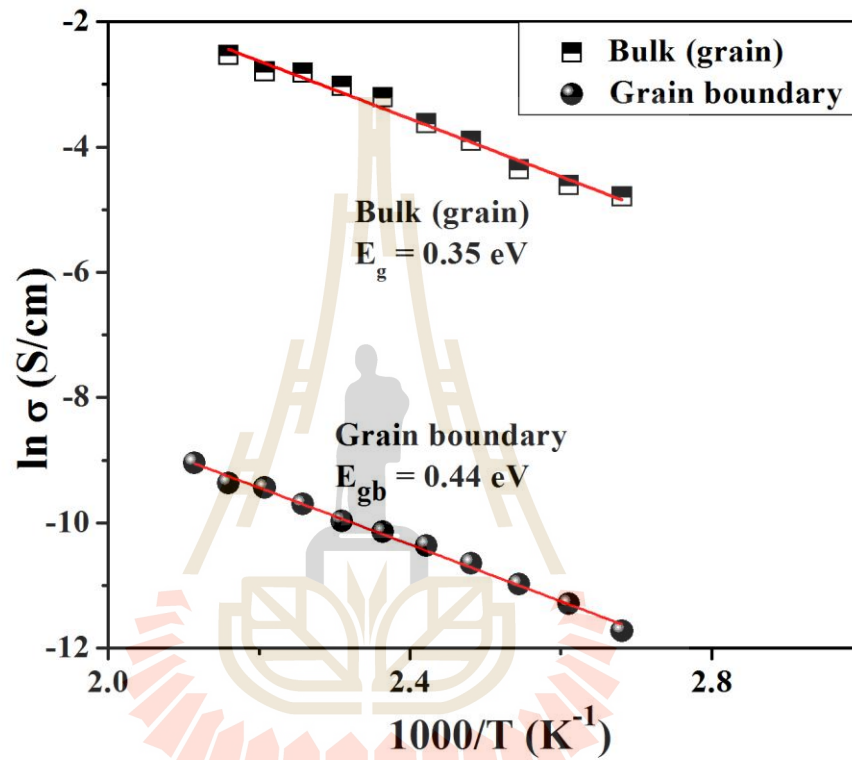


Figure 4.45 Temperature dependence of grain and grain boundary conductivity for the pure BiFeO₃ sample.

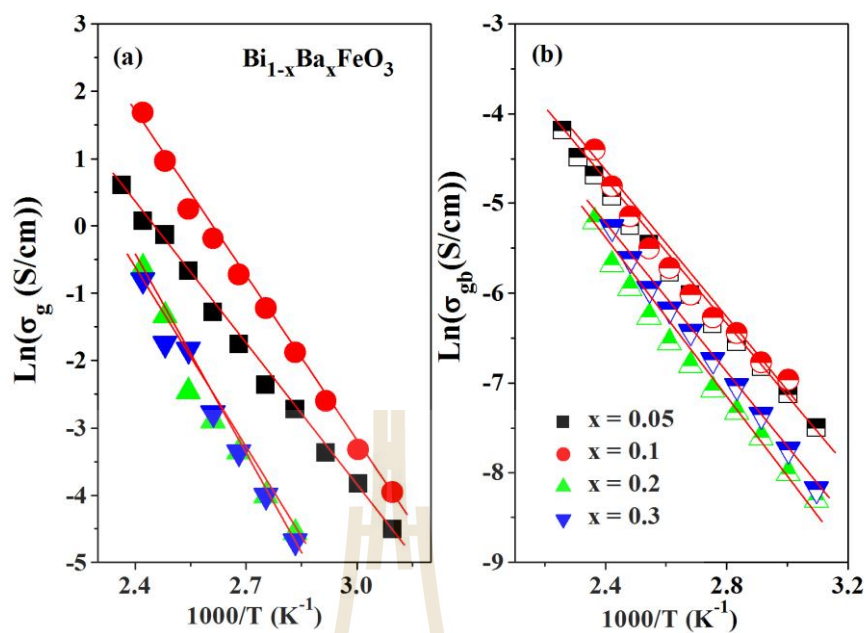


Figure 4.46 Temperature dependence of grain (a) and (b) grain boundary conductivity for the Ba-doped BiFeO₃ samples.

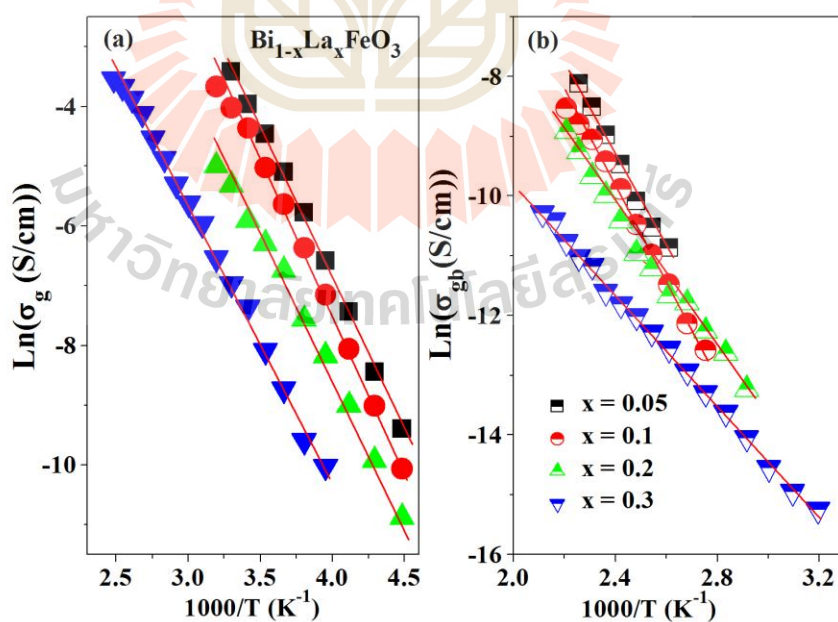


Figure 4.47 Temperature dependence of grain (a) and (b) grain boundary conductivity for the La-doped BiFeO₃ samples.

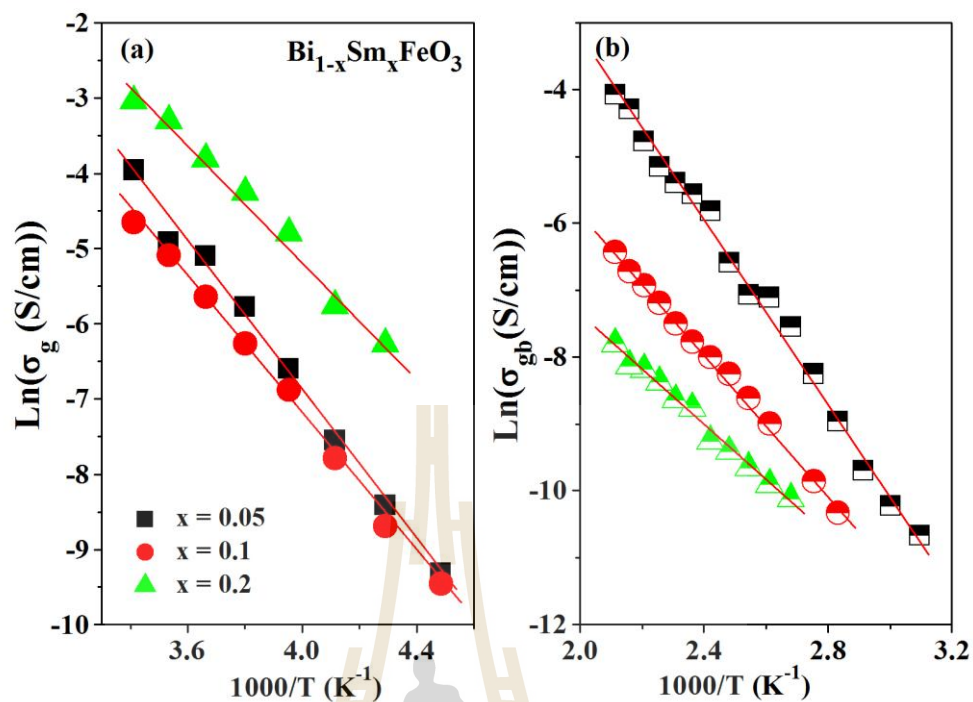


Figure 4.48 Temperature dependence of grain (a) and (b) grain boundary conductivity for the Sm-doped BiFeO₃ samples.

Table 4.10 Activation energy of conductivity at grain and grain boundary for pure BiFeO₃ and doped BiFeO₃ ceramics.

Sample	Ba-doped BiFeO ₃		La-doped BiFeO ₃		Sm-doped BiFeO ₃	
	E_g (eV)	E_{gb} (eV)	E_g (eV)	E_{gb} (eV)	E_g (eV)	E_{gb} (eV)
x = 0	0.44	0.35	0.44	0.35	0.44	0.35
x = 0.05	0.60	0.33	0.44	0.70	0.43	0.59
x = 0.1	0.70	0.34	0.44	0.67	0.40	0.46
x = 0.2	0.75	0.35	0.40	0.51	0.33	0.35
x = 0.3	0.76	0.36	0.39	0.40	-	-

4.6 Effect of DC bias voltage on dielectric response

The capacitance of a ceramic capacitor changes according to the external applied voltage. When a DC voltage is applied, this property is described as DC bias behavior. Frequency dependence of the dielectric constant (ϵ') and loss tangent ($\tan\delta$) measured under 0–20 V DC bias for the $\text{Bi}_{1-x}\text{A}_x\text{FeO}_3$ sintered samples are exhibited in Figures 4.49–4.52. As shown in Figure 4.49, the pure BiFeO_3 ceramic without an applied DC bias has a high dielectric constant of 1.59×10^4 at 100 Hz. This figure shows that the dielectric constant and loss tangent gradually decrease with increasing frequency, whereas it slightly increases with increases in applied DC bias voltage. These slight increases in the dielectric constant with increases in DC bias are observed from 100 to 10^4 Hz, indicating a low-frequency dielectric relaxation. It should be noted that ϵ' above 10^4 Hz becomes reduced by an applied DC bias. The observed decrease in the dielectric constant in the high-frequency region may be attributed to the transition from a grain dielectric response to a grain boundary dielectric response. However, the dielectric constant in the higher frequency range ($> 10^5$ Hz) is independent of the applied DC bias.

It is found that with regard to the dielectric constant and the loss tangent of Ba-doped BiFeO_3 ceramics, the overall spectra are similar to that observed for the pure BiFeO_3 sample as revealed in Figure 4.50. The step drop of the dielectric constant can be observed in the high-frequency range which leads to the loss tangent peak not being visible because its peak shifts out of the measured frequency range. This spectrum is found prominently in low frequency regions ($< 10^3$ Hz). It should be noted that the dielectric constant as well as the loss tangent of all Ba-doped BiFeO_3

ceramics increases with increases in DC bias but there is no significant change at frequencies above 10^4 Hz.

In the case of the La substituted in Bi site, the dielectric properties are different from those observed for pure BiFeO₃ and Ba-doped samples. The dielectric constant of La-doped BiFeO₃ under 0–20 V DC bias decreases as an applied DC bias voltage increases, as shown in Figure 4.51. This result is similar to that observed in the BiFeO₃ thin film (Liu *et al.*, 2008), where it was found that the capacitance significantly decreases with increases in forward bias voltage in the low frequency range. If there are further increases in frequency and applied DC bias voltage, the magnitude of the dielectric constant becomes independent of the applied DC bias voltage and frequency. It is surprising to observe such losses in these ceramics. The magnitude of the loss tangent is directly proportional to the applied DC bias level for all La-doped samples, which increases with increasing DC bias in the low frequency region. Furthermore, the dielectric behavior has a Debye-relaxation characteristic while the loss tangent shows a relaxation peak for all La-doped ceramics.

Frequency dependence of the dielectric constant and loss tangent measured under 0–20 V of Sm-doped BiFeO₃ samples are exhibited in Figure 4.52. The dielectric behavior of Sm-doped BiFeO₃ ceramics is similar to that observed in the La-doped samples. It is found that the dielectric constant gradually decreases as the DC bias voltage increases, while the loss tangent increases in the low frequency range, except for the highest concentrations in the Sm-doped (Bi_{0.7}Sm_{0.3}FeO₃) samples. The different behavior of the dielectric response to these ceramics is due to the fact there is less change in the dielectric constant and loss tangent in the whole frequency range. Similarly, the appearance of relaxation peaks in the loss tangent

spectra is observed, except for the $\text{Bi}_{0.7}\text{Sm}_{0.3}\text{FeO}_3$ samples. We observed relaxation peaks in the loss tangent curves in the high frequency range and a hump in the low frequency range. This indicates that there are different contributions of polarization in these samples.

The drop in the dielectric constant with increasing DC bias is related to the decrease in the capacitance of the grain boundary. The capacitance of the grain boundaries for CCTO decreases with increasing DC bias as has been previously reported (Liu *et al.*, 2007). These results imply that as the applied DC voltage increases, the accumulated charge carriers are more easily able to overcome the barrier at the grain boundaries, indicating that these charges become free charges. Therefore, the intensity of space charge polarization in this area decreases as the applied DC bias increases, while the conductivity of the material increases due to the increases in the free charge. Moreover, the variations in the dielectric responses is attributed to the direction of the spontaneous polarization in the domain wall (Waugh, 2010). This suggests that, if an external DC voltage is applied, the spontaneous polarization is tied to the direction of the electric field and a free reversal of spontaneous polarization becomes much more difficult. As a result, the obtained capacitance becomes lower compared to the capacitance before the bias was applied.

However, it is found that the dielectric constant and the loss tangent of all samples are independent of applied DC bias in the high–frequency range. The DC bias voltage study shows that the bias is an independent term in the high frequency region which is related to the grain contribution (Prakash *et al.*, 2011). In addition, it has also been reported that the increases in the dielectric constant of $\text{CaCu}_3\text{Ti}_4\text{O}_{12}$ capacitors in a low frequency range could be associated with an electrode contact

problem (Guo *et al.*, 2006). While a larger dielectric constant enhancement can be observed as the DC bias is increased which means that there are free charge carriers in the single layer of $\text{CaCu}_3\text{Ti}_4\text{O}_{12}$ films (Fang *et al.*, 2006).



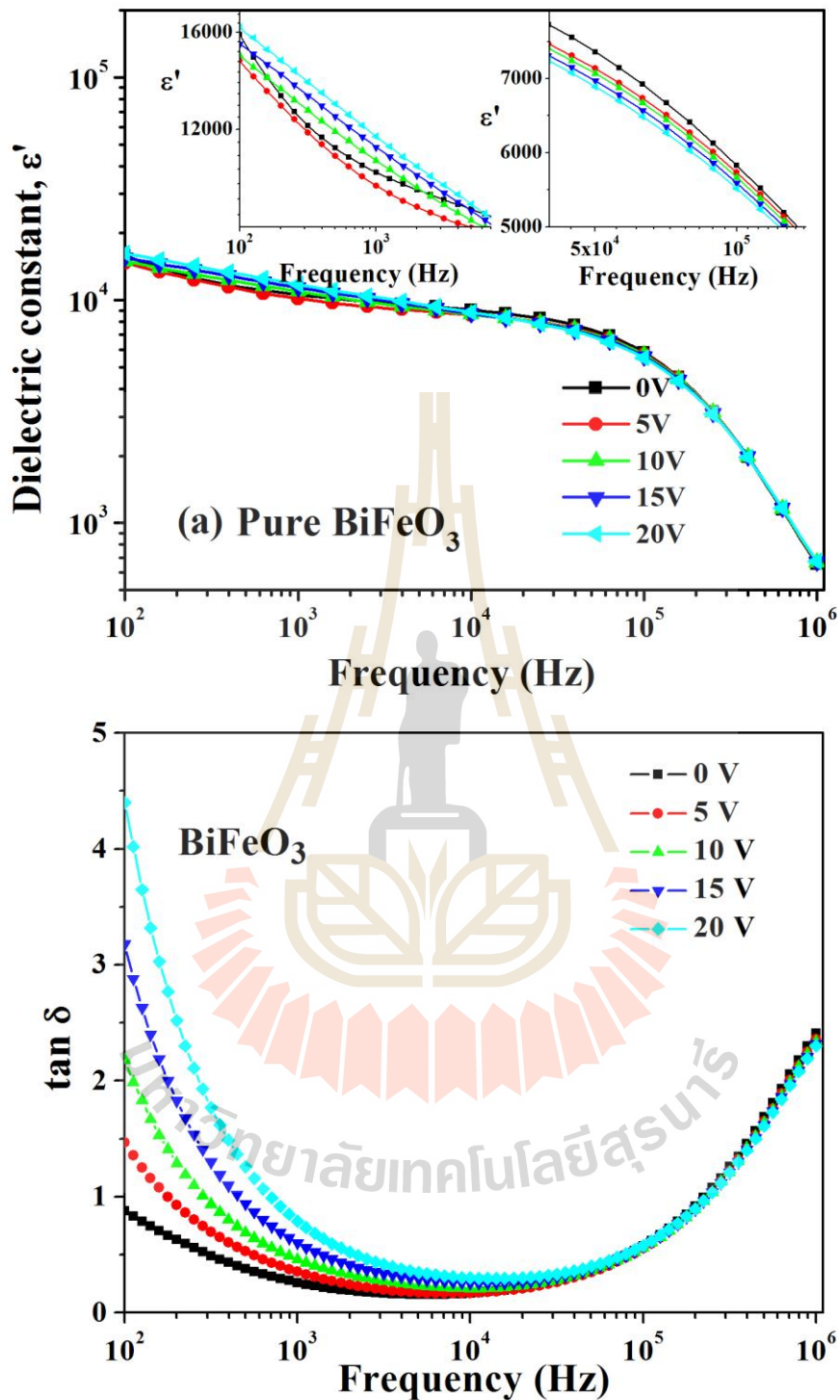


Figure 4.49 The dielectric constant (ϵ') and loss tangent ($\tan \delta$) for the pure BiFeO_3 ceramics sintered at 800°C for 3 h under various applied voltages with DC bias as a function of frequency at room temperature.

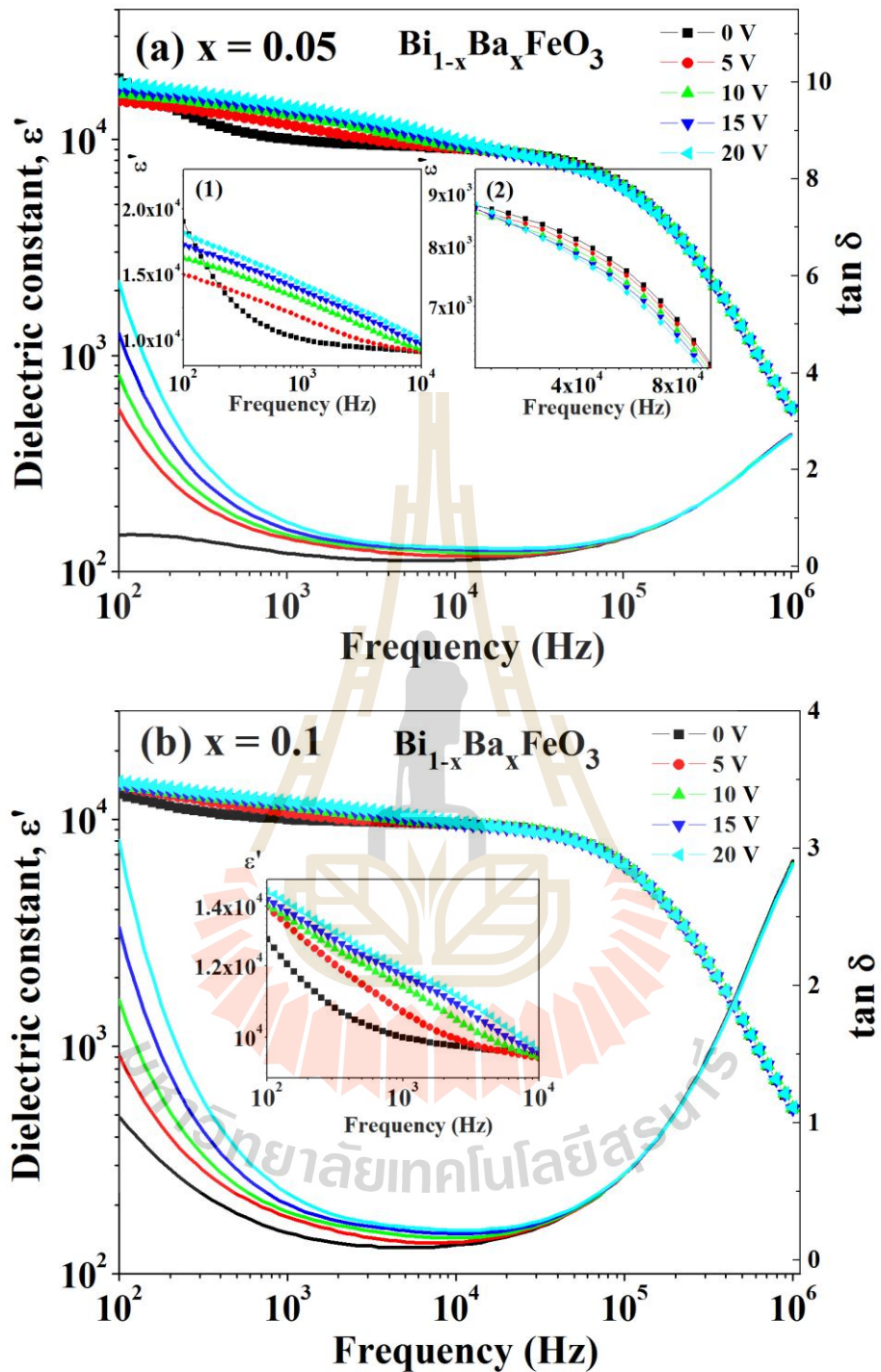


Figure 4.50 The dielectric constant (ϵ') and loss tangent ($\tan \delta$) at for Ba-doped BiFeO_3 ceramics sintered at 800°C for 3 h under various applied voltages with DC bias as a function of frequency at room temperature.

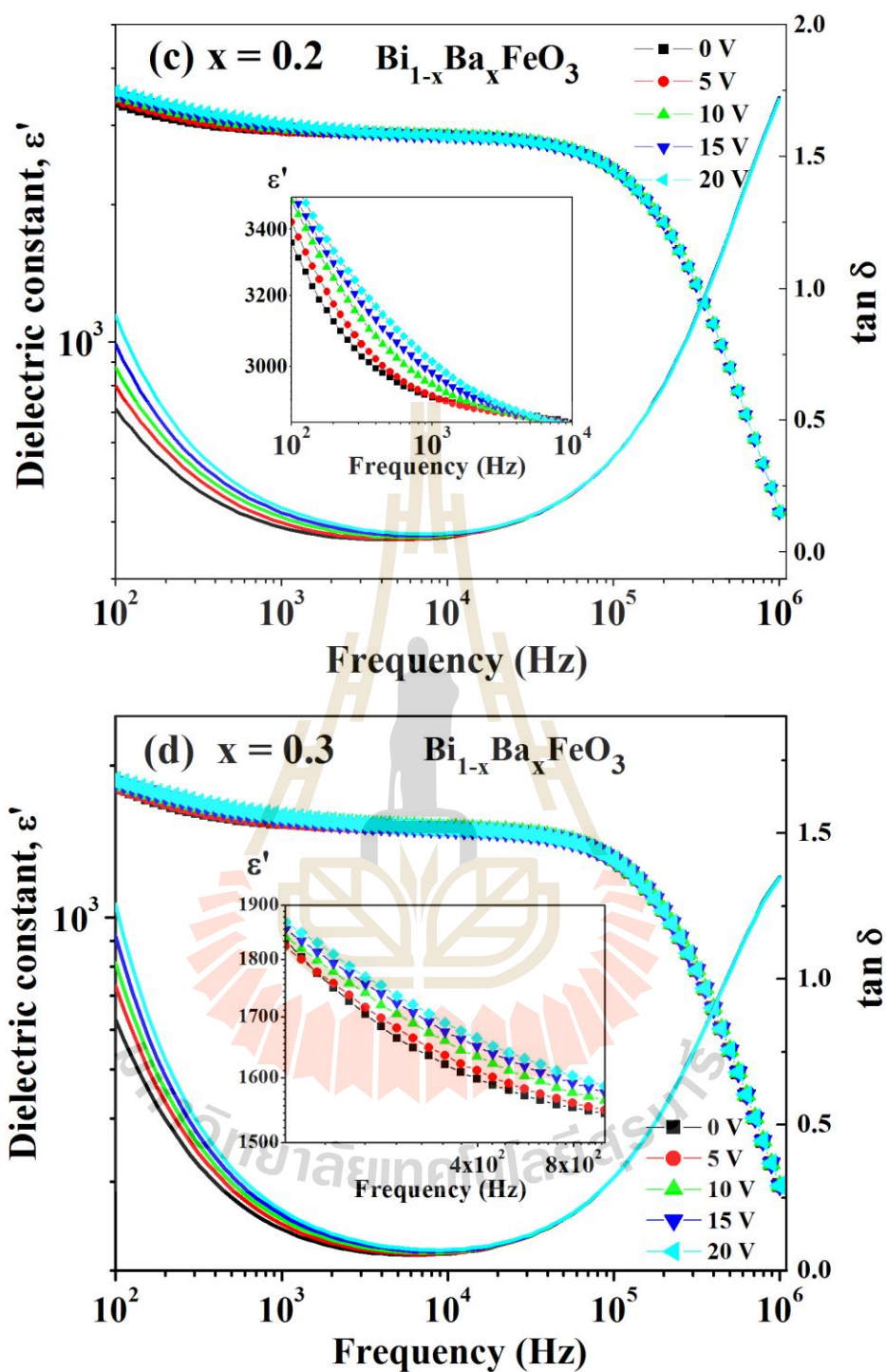


Figure 4.50 The dielectric constant (ϵ') and loss tangent ($\tan\delta$) for Ba-doped BiFeO_3 ceramics sintered at 800°C for 3 h under various applied voltages with DC bias as a function of frequency at room temperature (Continued).

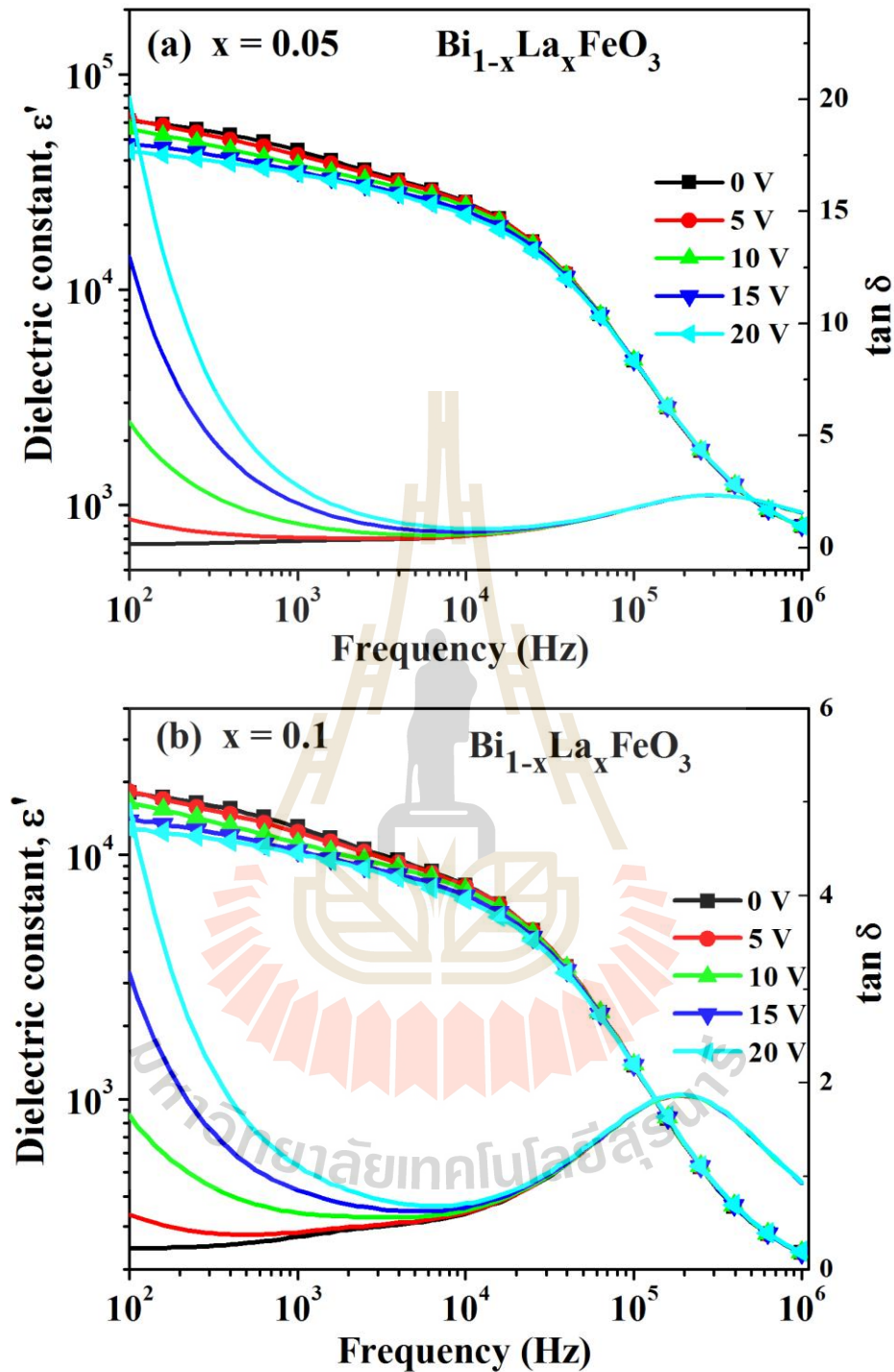


Figure 4.51 The dielectric constant (ϵ') and loss tangent ($\tan \delta$) for La-doped BiFeO_3 samples sintered at 800°C for 3 h under various applied voltages with DC bias as a function of frequency at room temperature.

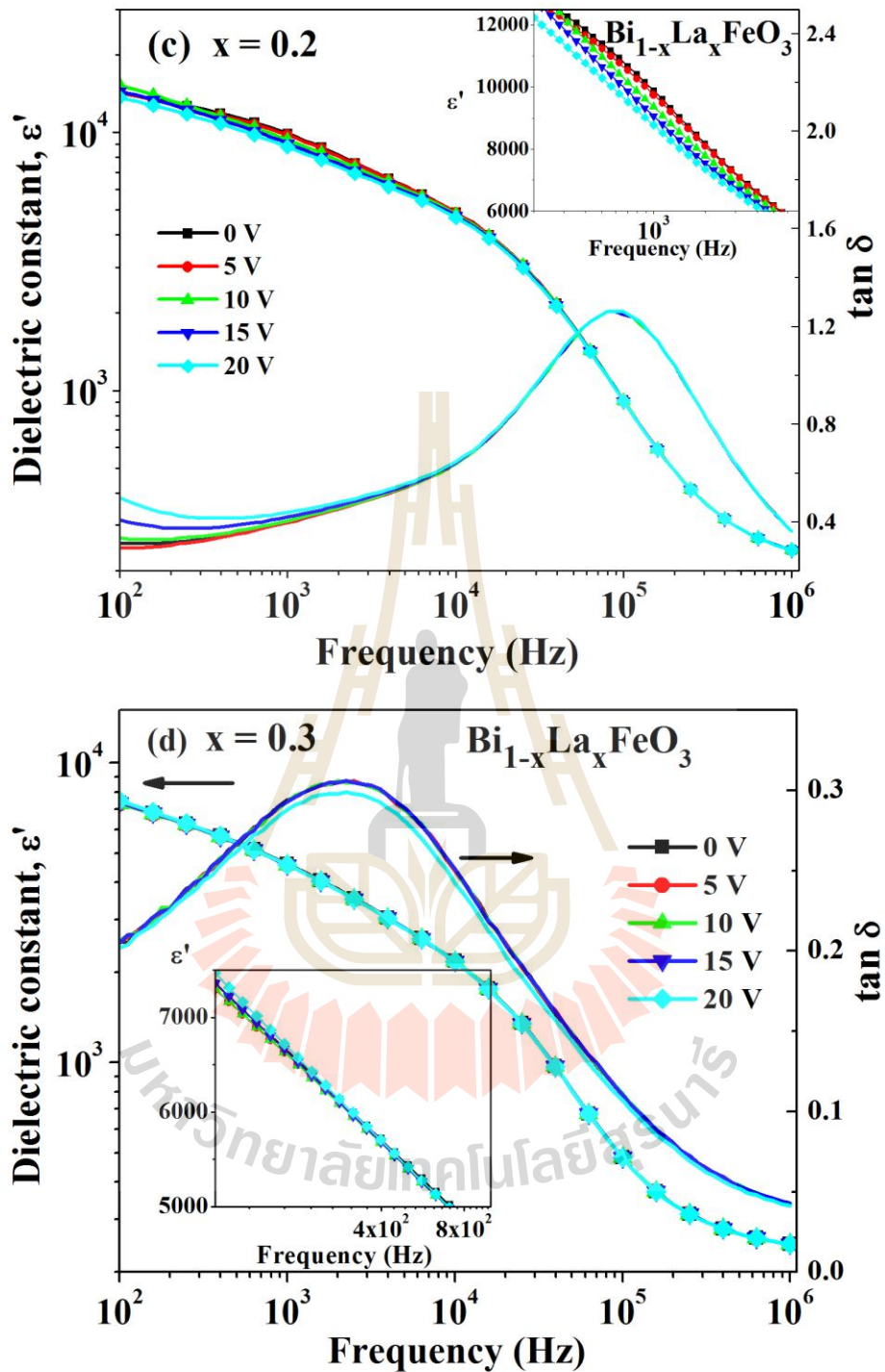


Figure 4.51 The dielectric constant (ϵ') and loss tangent ($\tan \delta$) for La-doped BiFeO_3 samples sintered at 800°C for 3 h under various applied voltages with DC bias as a function of frequency at room temperature (Continued).

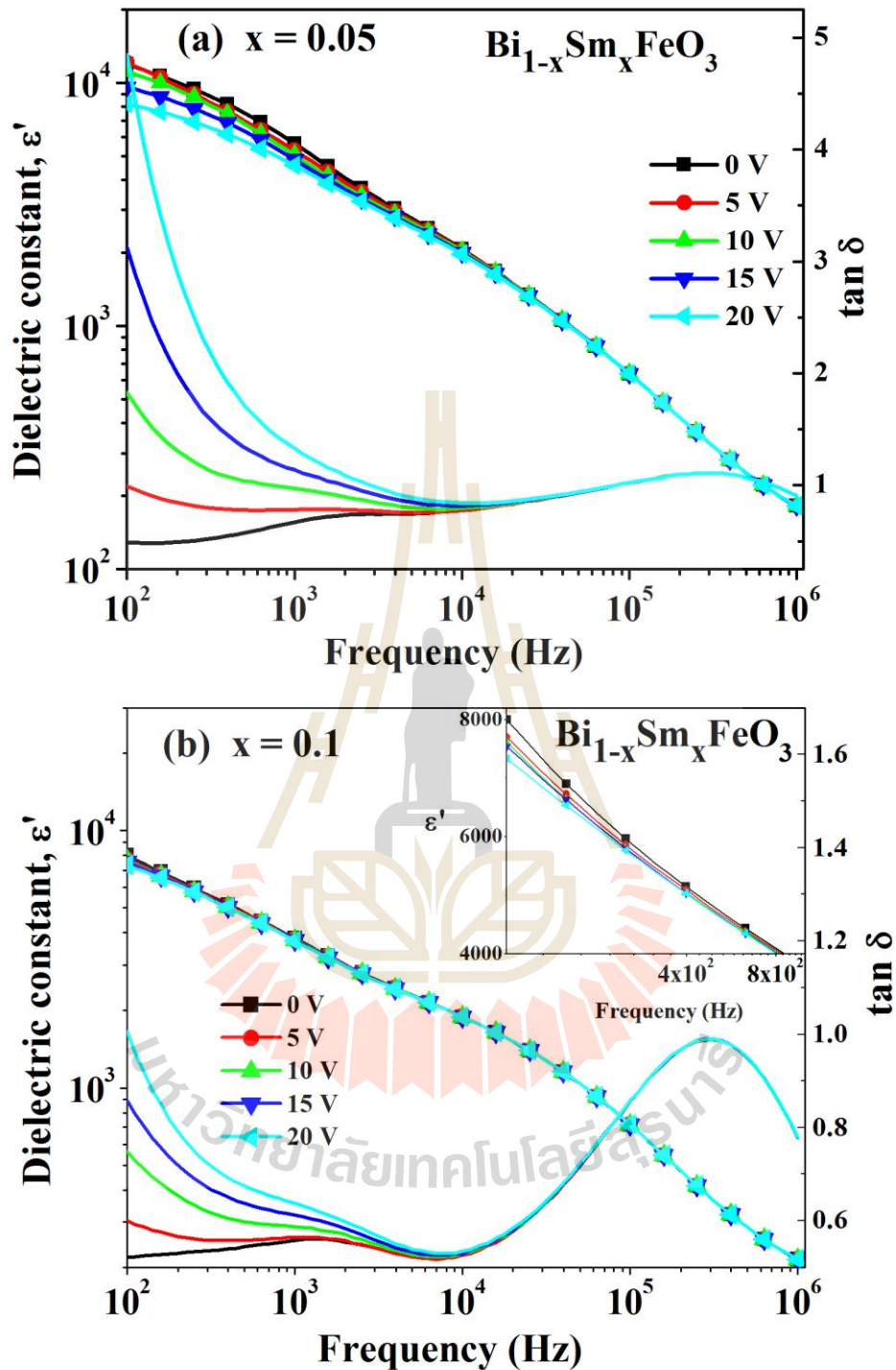


Figure 4.52 The dielectric constant (ϵ') and loss tangent ($\tan \delta$) for Sm-doped BiFeO_3 samples sintered at 800°C for 3 h under various applied voltages with DC bias as a function of frequency at room temperature.

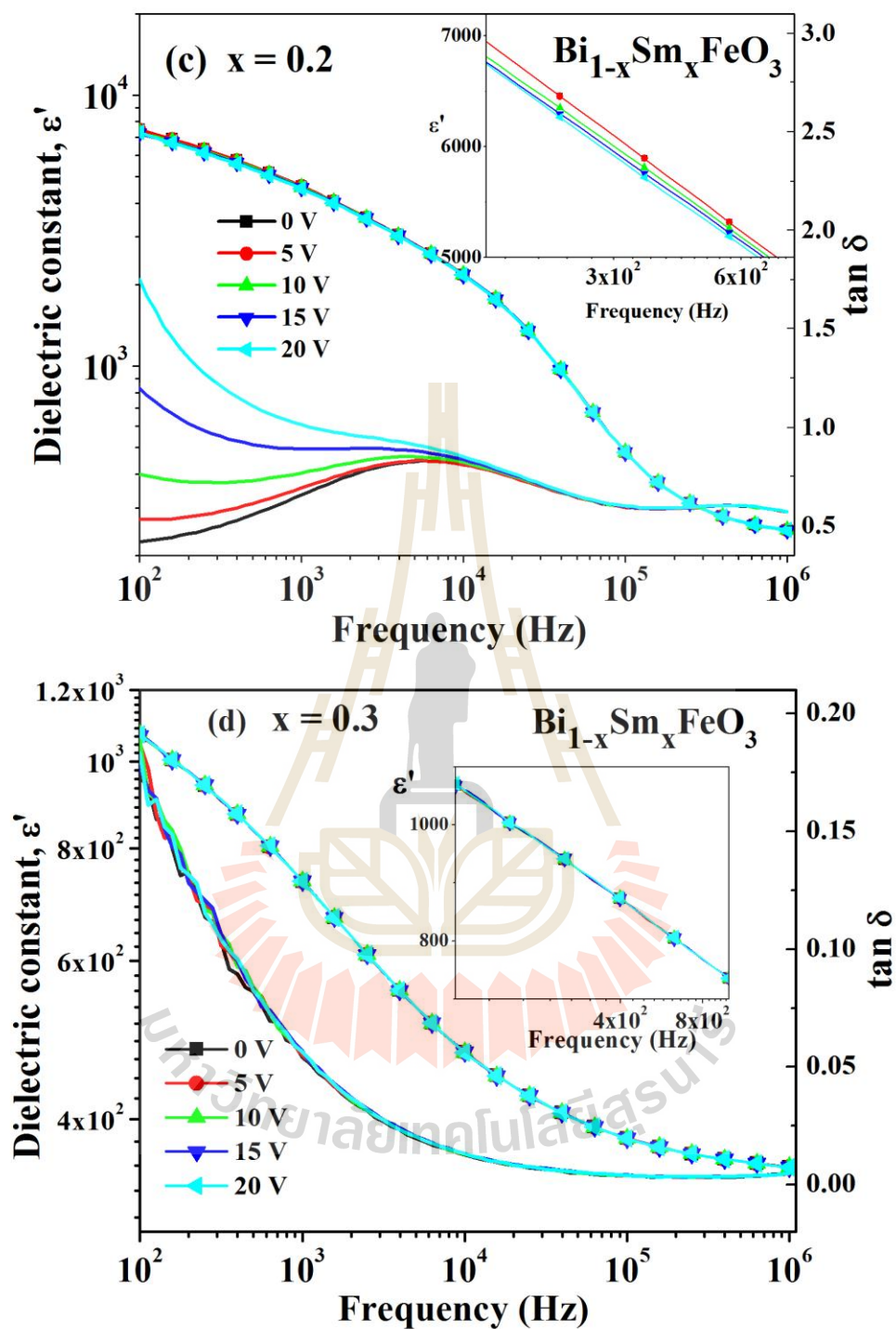


Figure 4.52 The dielectric constant (ϵ') and loss tangent ($\tan \delta$) for Sm-doped BiFeO_3 samples sintered at 800°C for 3 h under various applied voltages with DC bias as a function of frequency at room temperature (Continued).

The grain boundary based dielectric properties behaviors have been studied by impedance spectroscopy. Figure 4.53 reveals typical real (Z') and imaginary (Z'') components of the impedance plots (Z^*) for undoped and Ba-, La-, and Sm-doped BiFeO_3 ceramics as a function of frequency and DC bias. Impedance plots of the pure BiFeO_3 samples contain only one semicircular arc with a nonzero intercept on the real axis (Z') at a high-frequency under 0–20 V DC bias. The semicircular arcs do not originate from the origin as shown in the inset of Figure 4.53 because the nonzero intercepts are found at the origin. The observed semicircular arcs are understood to originate from the grain boundary, whereas the high-frequency intercepts with the Z' -axis are associated with the grain response as indicated by the impedance plots. Therefore, the diameter of semicirculars and intercepts at low- and high-frequency can be considered as caused by the grain boundary and grain resistance, respectively. With increasing DC bias, the diameters of the semicircular arcs for the pure BiFeO_3 ceramics is significantly decreased, but the high-frequency intercept is bias independent. The Z^* plots for the doped BiFeO_3 ceramics appear as one semicircle with its tail with a non-zero intercept on the Z' axis in the high-frequency region. This observed tail indicates a high-frequency component of the large semicircle. Furthermore, it is seen from the impedance plots of the $\text{Bi}_{1-x}\text{La}_x\text{FeO}_3$ ceramics that the tail becomes a small semicircular arc and increases in diameter with increasing DC bias voltage. In the Z^* plots we found that the semicircular arc can be analyzed by using an equivalent circuit of series combinations of two parallel RC elements. Thus, the resistance (R) and capacitance (C) values of the grain and grain boundary in the polycrystalline ceramics can be obtained. From fitting the impedance plots for La-, Sm- and Ba-doped BiFeO_3 , all of the samples represent a clear decrease in the grain

boundary resistance (R_{gb}) with increasing DC bias and reveal a decrease in DC conductivity. Whereas the grain resistance of all La-doped samples remains constant at high-frequency. This independent frequency is due to the release of the space charges accumulated at the interface between the grain and grain boundary. The calculated values of the DC conductivity for undoped and doped samples display a remarkable increase in grain boundary conductivity with an increase in DC bias voltage as shown in Figure 4.54. It is clear from the figure that the DC conductivity shows a non-linear current-voltage behavior (I-V). This dependence of the grain boundary conductivity on DC bias indicates the non-Ohmic electrical properties of the grain boundary. In general, in crystalline materials, grain boundaries often have significant influence on the flow of an electric current. The non-linear electrical response of the grain boundary indicates that the potential barrier formation at the grain boundary is identical to the double (or back-to-back) Schottky barriers. The double Schottky barrier is ascribed to the interface between the two grains and the boundary region. Furthermore, the Schottky diode-like electrical at the grain boundary gives a potential energy barrier of high resistance which pins the motion of the free charge carriers. Several reports suggest that the barriers are generated due to p-n type diodes with acceptor-like interface trap states at the interfaces between the two adjacent n-type grains and p-type grain boundary region. When a bias voltage is applied, one of the space charge contributions is decreased, and this situation could cause strong variations within the depletion layer and lead to a suppression of the potential barrier height with a higher biased condition. Such a situation results in an increase of the total depletion of region. As the width of the depletion region has increased this may explain the decrease in the capacitance at the grain boundary. If we

consider the capacitance dependence of the DC bias is consistent with expectation of a thermionic emission from the Shottky barrier model, the electric conduction may be related to the electric field and temperature. Therefore, the potential barrier height can be estimated from the relative difference between the current density and the electric field ($J-E$) characteristics.

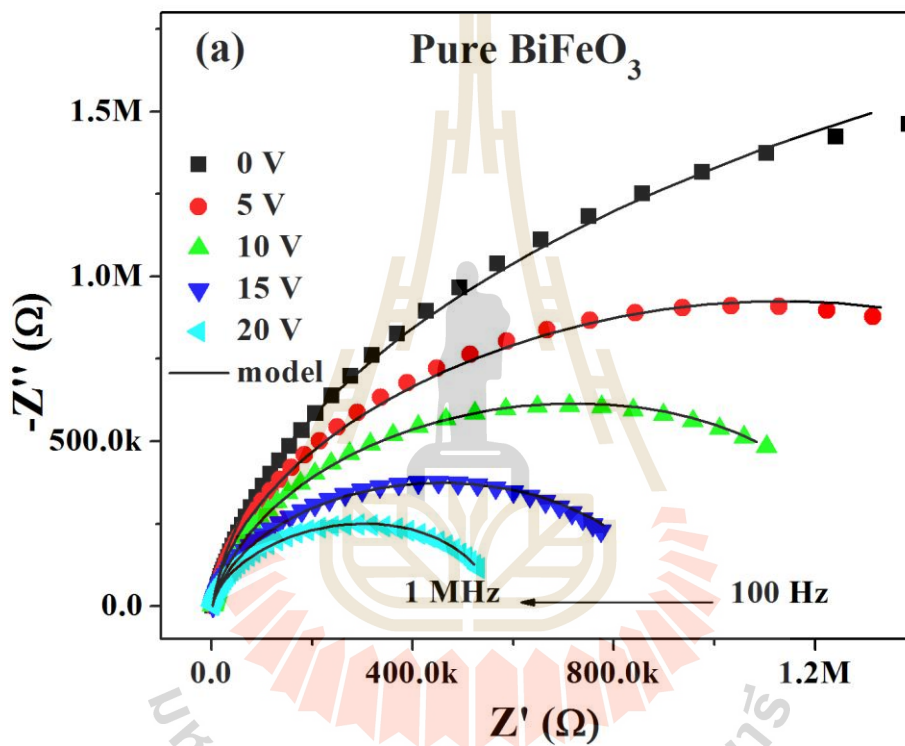


Figure 4.53 Complex impedance spectra of the undoped BiFeO_3 ceramics sintered at 800°C for 3 h as a function of DC bias voltages.

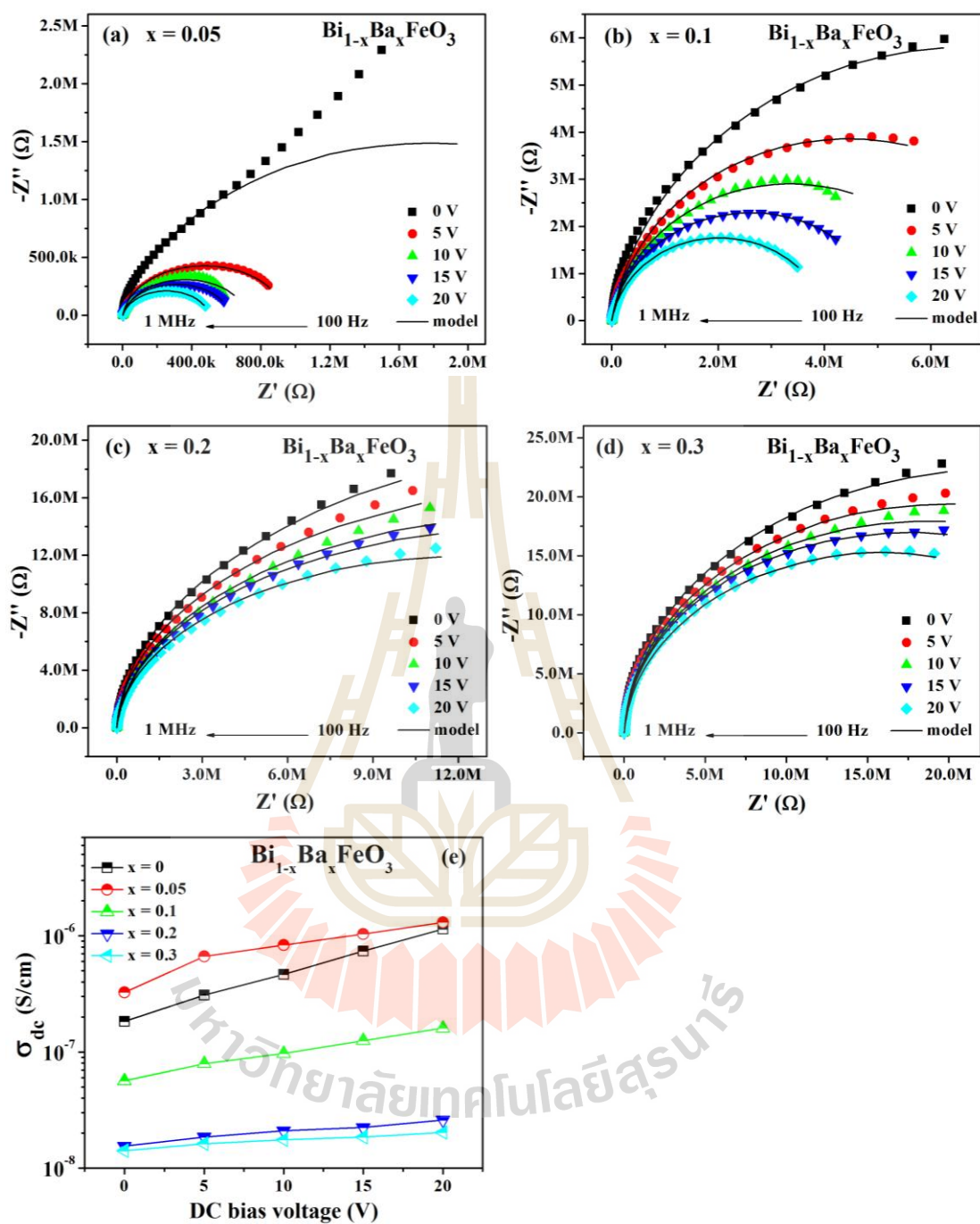


Figure 4.54 Complex impedance spectra of the Ba-doped BiFeO₃ ceramics sintered at 800 °C for 3 h as a function of DC bias voltages (a)–(d) and (e) variations in conductivity with applied DC bias voltage of Ba-doped BiFeO₃.

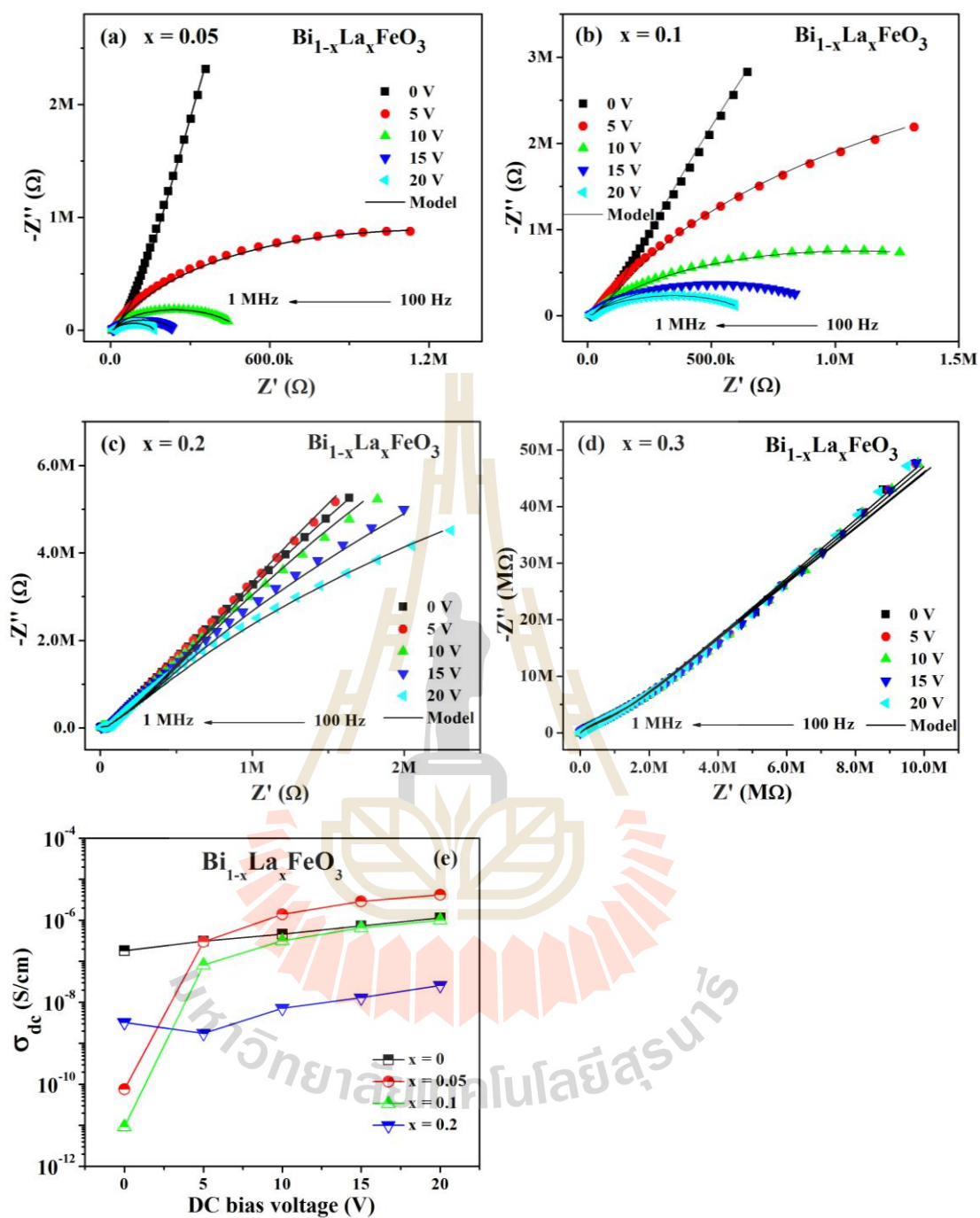


Figure 4.55 Complex impedance spectra of the La-doped BiFeO₃ ceramics sintered at 800 °C for 3 h as a function of DC bias voltages (a)–(d) and (e) variations in conductivity with applied DC bias voltage of La-doped BiFeO₃.

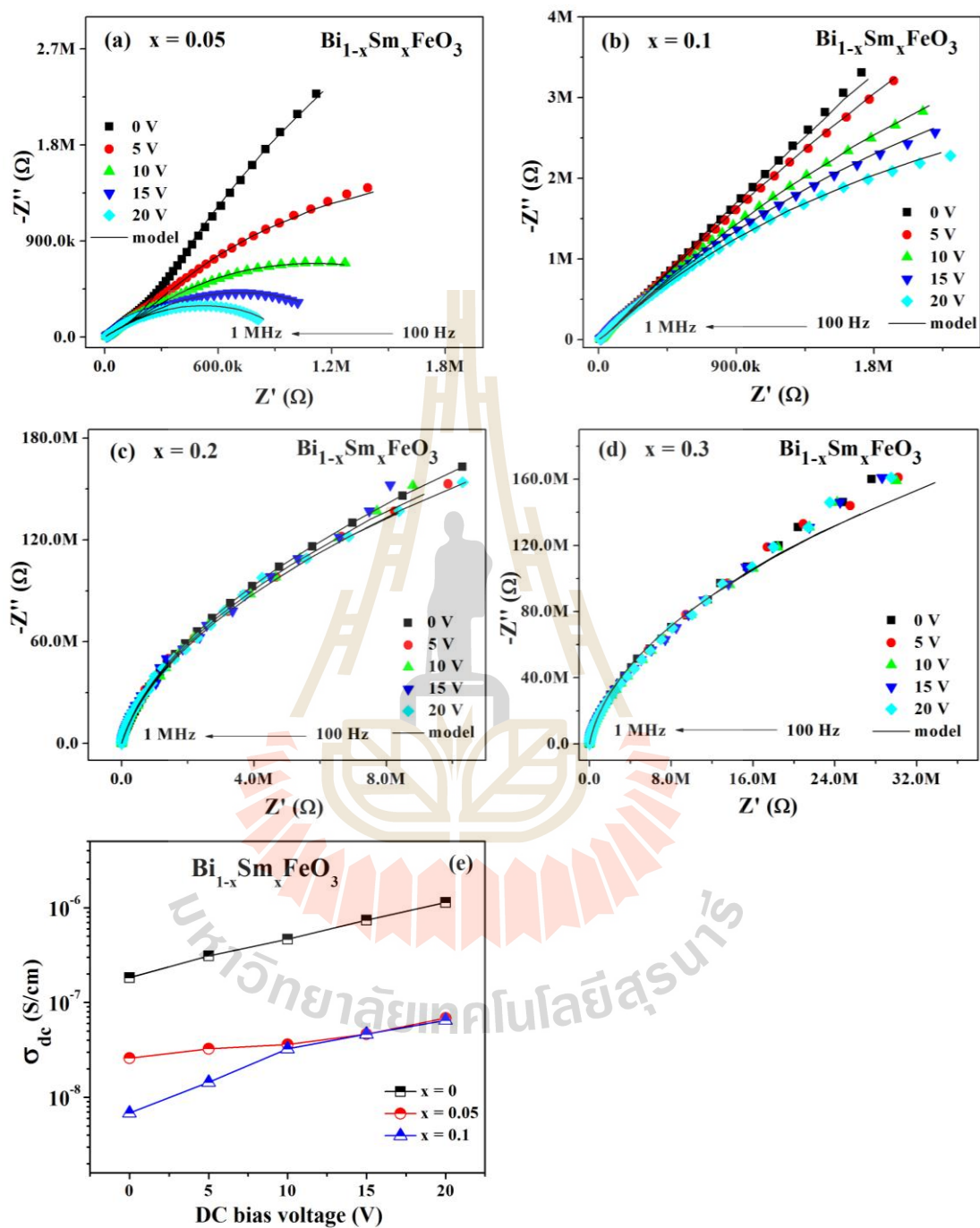


Figure 4.56 Complex impedance spectra of the Sm-doped BiFeO₃ ceramics sintered at 800 °C for 3 h as a function of DC bias voltages (a)–(d) and (e) variations in conductivity with applied DC bias voltage of Sm-doped BiFeO₃.

4.7 Current–voltage characteristic

In addition to the dielectric properties, we also investigated the current–voltage characteristics of BiFeO₃–based samples in order to study the physical nature of electrical transport in the grain boundary region. To investigate the origin of the leakage of current of the pure BiFeO₃ and La– and Ba–doped samples, these samples were investigated out at room temperature in the electric field range of 7 kV/cm. The current density (J) as a function of the applied electric field (E) at room temperature for the pure BiFeO₃ and doped ceramics are shown in Figure 4.57. As can be clearly seen in Figure 4.57, the BiFeO₃ and doped samples can display non–Ohmic behaviours. From the J – E curves shown in figure, we can see that the leakage current density increases with increases in the electric field under all conditions. It is observed that the leakage current value of pure BiFeO₃ ceramic is obtained 2.69 at electric field 1 kV/cm². The leakage current of Bi_{1-x}Ba_xFeO₃ with $x = 0.05, 0.1, 0.2,$ and 0.3 samples is about 3.04, 1.21, 0.05, and 0.016 mA/cm², respectively. For the Ba–doped samples with $x = 0.3$, the leakage current density is found to be 1.6×10^{-2} mA/cm² in the electric field 1 kV/cm, which is two orders of magnitude lower than that of the pure BiFeO₃ ceramics. The leakage current density shows the lowest value with $x = 0.3$, which is in accordance with the lowest loss tangent for these ceramics as discussed above. It was that a small content of Ba substitution gradually increases the leakage current density whereas a high concentration of Ba ($x \geq 10\%$) ions reduces the leakage current up to two orders of magnitude as compared to the parent BiFeO₃ ceramics. The effects of La doping greatly reduce the leakage current density for La doping. For the La–doped samples with $x = 0.3$, the leakage current density is found to be 4×10^{-2} mA/cm² at 1 kV/cm. As La doping increases from 5% to 20% in BiFeO₃,

the leakage current is 3.3, 2 and 0.47 mA/cm² in the electric field of 500 V/cm. With increases in concentration of La up to 0.3 the leakage current greatly decreases, which is about one order lower than that of pure BiFeO₃ at electric field 1 kV/cm². Figure 4.57(b) displays the leakage current density in the applied electric field for undoped and Sm-doped BiFeO₃ ceramics at room temperature. The leakage current curves of all samples clearly show non-linear behaviour. The leakage current density in the electric field of 1 kV/cm is 1.85, 2.36, and 2.15 mA/cm² for Bi_{1-x}Sm_xFeO₃ (x = 0.05, 0.1, and 0.2) samples, respectively. In Figure 4.57(c), it is found that the current density increases with increases in doping levels from 0.05 to 0.2 in a high electric field.

The leakage current is found to decrease with La and Ba doping. It is well known that the charge defects such as the presence of Fe²⁺, V_{Bi}²⁺, and V_O²⁺ are believed to be the main cause of the high leakage of current density in BiFeO₃ ceramics and their thin film. The Bi_{0.7}La_{0.3}FeO₃ and Bi_{0.7}Ba_{0.3}FeO₃ ceramics have the lowest leakage current density, which is possibly associated with the following reason. Firstly, the La- and Ba-doped decreases the size of the grains which leads to an increase in the density of the grain boundaries, which in turn gives rise directly to increases in resistivity in La- and Ba-doped BiFeO₃ samples. We can give a preliminary explanation for this result in terms of changes in the microstructure, i.e., the relatively larger lattice distortion, larger grain size and surface morphology of the ceramics, as exhibited by the XRD data and the SEM features. The other possible reason is due to the suppression of oxygen vacancies by La and Ba substitutions, which has been reported by several previous research studies.

The breakdown field (E_b) is usually taken as the electric field applied when the current flowing through the material is 1 mA/cm^2 . For Ba-doped BiFeO_3 samples, at first the E_b values decrease with substitutions of Ba up to 0.05 ($E_b \sim 630 \text{ V/cm}$). The E_b value increases with further increases of Ba doping which are found to be 928, 2937, and 3933 V/cm for $x = 0.1, 0.2,$ and 0.3 , especially when there are 30% decreases in the leakage current density of Ba in BiFeO_3 samples which is 5.3 times of magnitude compared to the pure sample. The E_b values are 336, 360, 690, and 2981 V/cm , for La = 0.05, 0.1, 0.2, and 0.3, while the breakdown field of the pure BiFeO_3 is about 742 V/cm . It can be observed that the E_b initially decreases and later increases, which is in conflict with the variations in grain size with increases in La concentration. This result means that the substitution of La ions enhances the electric field of BiFeO_3 ceramics by 4 times as compared to the undoped BiFeO_3 samples. Moreover, the E_b is found to be 705, 610, and 648 V/cm for Sm-doped BiFeO_3 ceramics with $x = 0.05, 0.1,$ and 0.2 . The effect on the leakage of the current density of Ba doping in the BiFeO_3 samples slightly decreases its leakage of the current density as compared to pure BiFeO_3 . The variations in the behaviour of the breakdown field with the content of Ba, La, and Sm samples can be explained by the variations in the average grain size. This means that the increases in the mean grain size results in decreases in the number of grain boundaries, which causes the decrease of E_b .

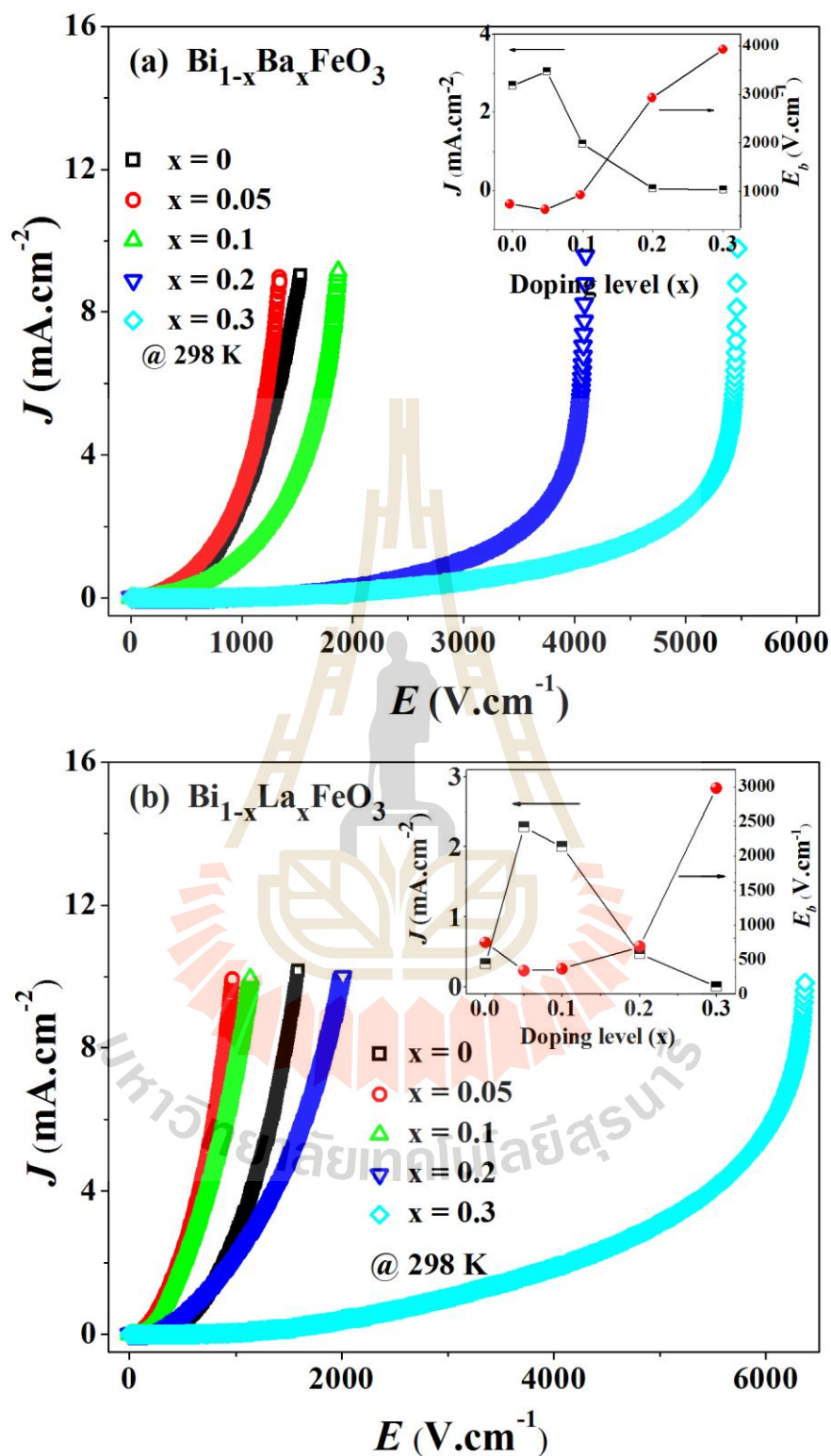


Figure 4.57 (a)–(c) Current–voltage curves of doped BiFeO_3 samples at room temperature and (inset) current leakage and breakdown field as a function of doping content for the BiFeO_3 ceramics.

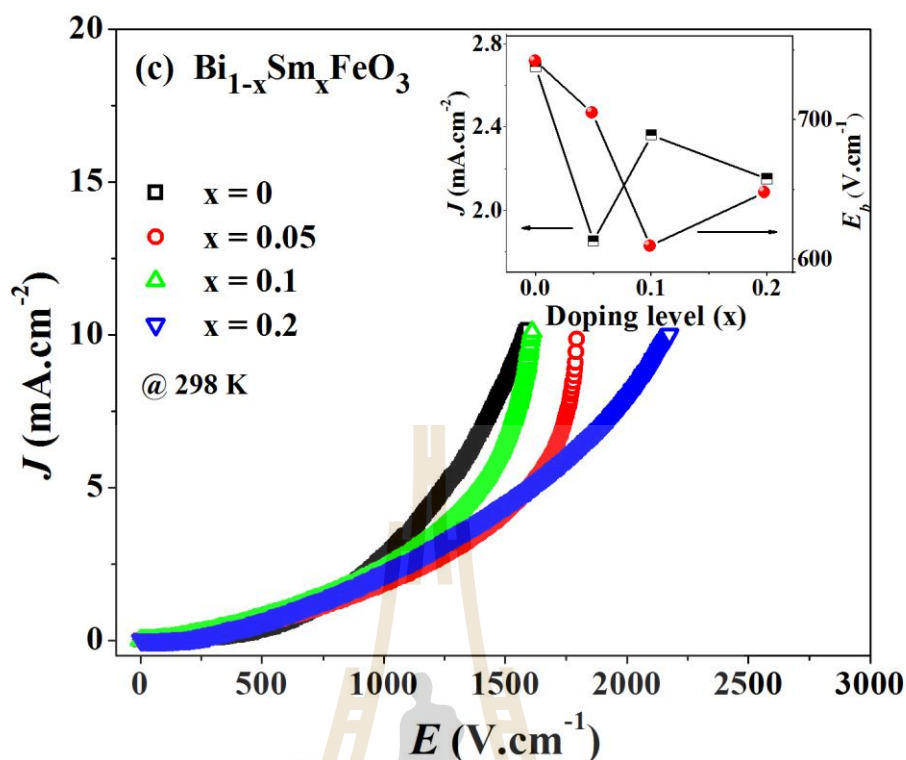


Figure 4.57 (a)–(c) Current–voltage curves of doped BiFeO_3 samples at room temperature and (inset) current leakage and breakdown field as a function of doping content for the BiFeO_3 ceramics (Continued).

A logarithmic plot of the current density as a function of the electric field is a useful tool to understand the electrical conduction mechanism. As is well known, the power law current density (J) and electric field (E) relationship ($J \propto V^\alpha$) is a characteristic of space–charge–limited conduction (SCLC) and we plot $\log(J)$ versus $\log(E)$ in Figure 4.58 for the BiFeO_3 samples. The nonlinear coefficient (α) was determined from the slope of the log–log scale over the range 1–10 mA/cm². The slope value (α) for a specific region of these curves provides information about the conduction mechanism involved in that area. Furthermore, value of α suggests directly the capacity of the current transport of the varistors. The nonlinear coefficient

from the plot describes the type of conduction, i.e., Ohmic conduction; slope ~ 1 , space charge-limited conduction (SCLC); slope ~ 2 and for the other slopes larger than 2. The nonlinear coefficient of pure BiFeO_3 is obtained as 2.31 indicating the SCLC is dominant for the undoped BiFeO_3 samples. According to the plot of $\log(J)$ versus $\log(E)$ each curve can be divided into 2 to 3 regions in different electric field ranges. Regarding the Ba-doped BiFeO_3 ceramics, the values of α for the low electric field region I are 2.42, 2.6, 3.67 and 3.71 for $x = 0, 0.05, 0.1, 0.2,$ and 0.3 , respectively. Whereas the nonlinear coefficient (α) for the pure BiFeO_3 samples exhibit a gradually larger slope value ($\alpha = 2.31$). With increases in the electric field, all of the Ba-substituted ceramics show the α values = 3.92, 4.43, 8.15, and 8.24 in the high field region II. Finally, the slope values increase from 37.1 to 65 in the highest electric field region III for $\text{Bi}_{0.8}\text{Ba}_{0.2}\text{FeO}_3$ and $\text{Bi}_{0.7}\text{Ba}_{0.3}\text{FeO}_3$ samples, respectively. It is clearly seen that the nonlinear coefficient values for the third and second regions are larger than that of the region I for all Ba-doped samples. These regions of conduction are enhanced by Ba additions, and their values are higher than those reported for Ba additions prepared by the conventional solid state reaction method. In the case of Ba-doped samples, SCLC conduction occurs in region I and the slope value increases in region II and region III which is quite different from that of SCLC theory which is responsible for such a high value slope.

It is found that the α value of La-doped samples with 5% of La is equal to 2.27 of the whole electric field range and room temperature which is in good agreement with the SCLC mechanism. The $\text{Bi}_{0.9}\text{La}_{0.1}\text{FeO}_3$ ceramics show the Ohmic conduction ($\alpha \sim 1.94$) in the testing of the whole electric field range. The slope is found to be between 1 and 2 for this sample, suggesting the co-existence of Ohmic as

well as SCLC behaviour. However, the plots of $\text{Bi}_{0.8}\text{La}_{0.2}\text{FeO}_3$ and $\text{Bi}_{0.7}\text{La}_{0.3}\text{FeO}_3$ ceramics indicate two or three different regions according to their slope values. The α value of $\text{Bi}_{0.8}\text{La}_{0.2}\text{FeO}_3$ ceramics changes from 2.02 to 2.67 with increases in the electric field which can be attributed to the SCLC mechanism in these samples. On the other hand, with regard to the $\text{Bi}_{0.7}\text{La}_{0.3}\text{FeO}_3$ ceramics, the SCLC mechanism appears in the low electric field region I. Moreover, the slope values increase from 3.94 to 11.26 in region II to region III, suggesting that a mechanism other than that of the SCLC is responsible for such a high value of these samples. In a high electric field, the value of α becomes larger than 3.94 and 11.26, deviating greatly from the Ohmic and SCLC behavior. With increases in the electric fields (region III) the mechanisms should be related to either the Poole–Frenkel conduction mechanism or the Schottky emission mechanism. The plots of $\log(J)$ as a function of $\log(E)$ for the Sm-doped BiFeO_3 samples are shown in Figure 4.59(c). With increases in the electric field, the slope value of the $\text{Bi}_{0.95}\text{Sm}_{0.05}\text{FeO}_3$ and $\text{Bi}_{0.9}\text{Sm}_{0.1}\text{FeO}_3$ samples reveal three different slopes. The slope values are found to be 1.84, 3.11, and 7.78 for $\text{Bi}_{0.95}\text{Sm}_{0.05}\text{FeO}_3$ ceramics and 1.81, 3.03, and 6.12 for $\text{Bi}_{0.9}\text{Sm}_{0.1}\text{FeO}_3$ ceramics in regions I, II, and III, respectively. The slope value for $\text{Bi}_{0.8}\text{Sm}_{0.2}\text{FeO}_3$, changes from 1.77 to 2.36 which implies that Ohmic conduction occurs in region I and that the conduction mechanism changes from an Ohmic to a SCLC mechanism in region II. In the high electric field, the value of α becomes larger with values of 3.31, 7.78, and 3.03, 6.12 for the $\text{Bi}_{0.95}\text{Sm}_{0.05}\text{FeO}_3$ and $\text{Bi}_{0.9}\text{Sm}_{0.1}\text{FeO}_3$ samples which deviates greatly from the Ohmic and SCLC behavior whose conduction mechanisms may be due to the combination of Poole–Frenkel and Schottky emissions. The specific applications depend on the range of the values of the nonlinear coefficient (α). In ceramic

varistors and with applications for low voltage, the value is in the range of 1.2–13 (Marques *et al.*, 2007) and for high voltage applications, it tends to be the range 65–900 (Ramírez *et al.*, 2006). Therefore, the results obtained from the BiFeO₃ samples suggest the applicability of the varistors in the low voltage range at room temperature.

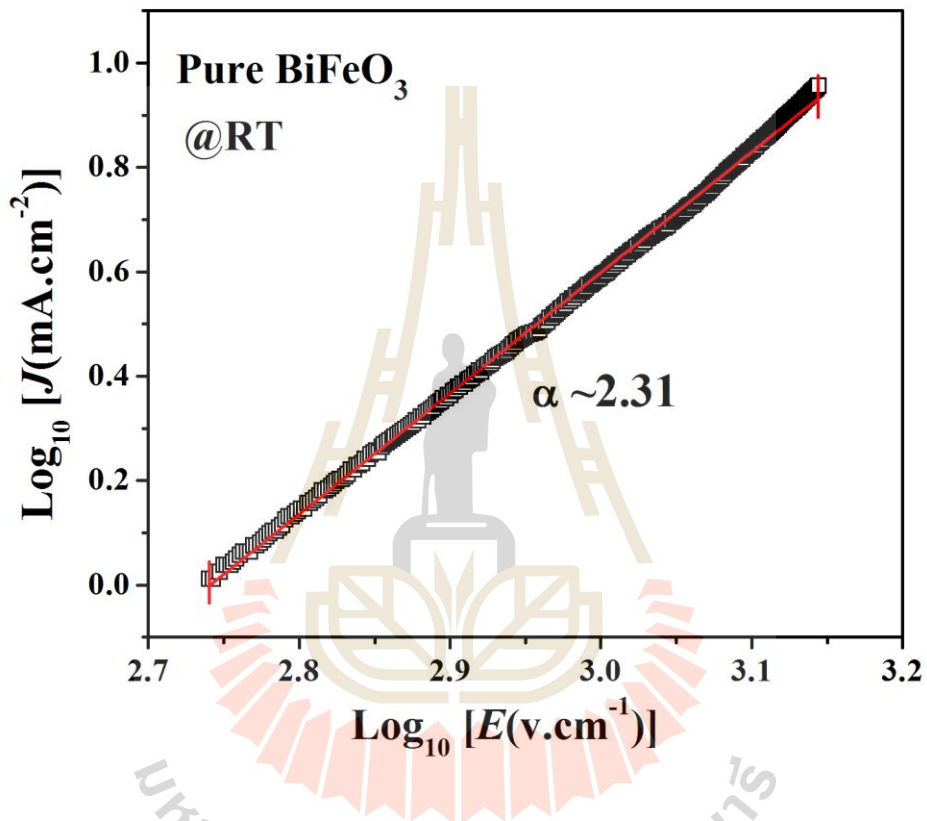


Figure 4.58 Logarithmic plots of dependence of J as a function of E measured at room temperature for BiFeO₃ ceramics sintered at 800 °C for 3 h.

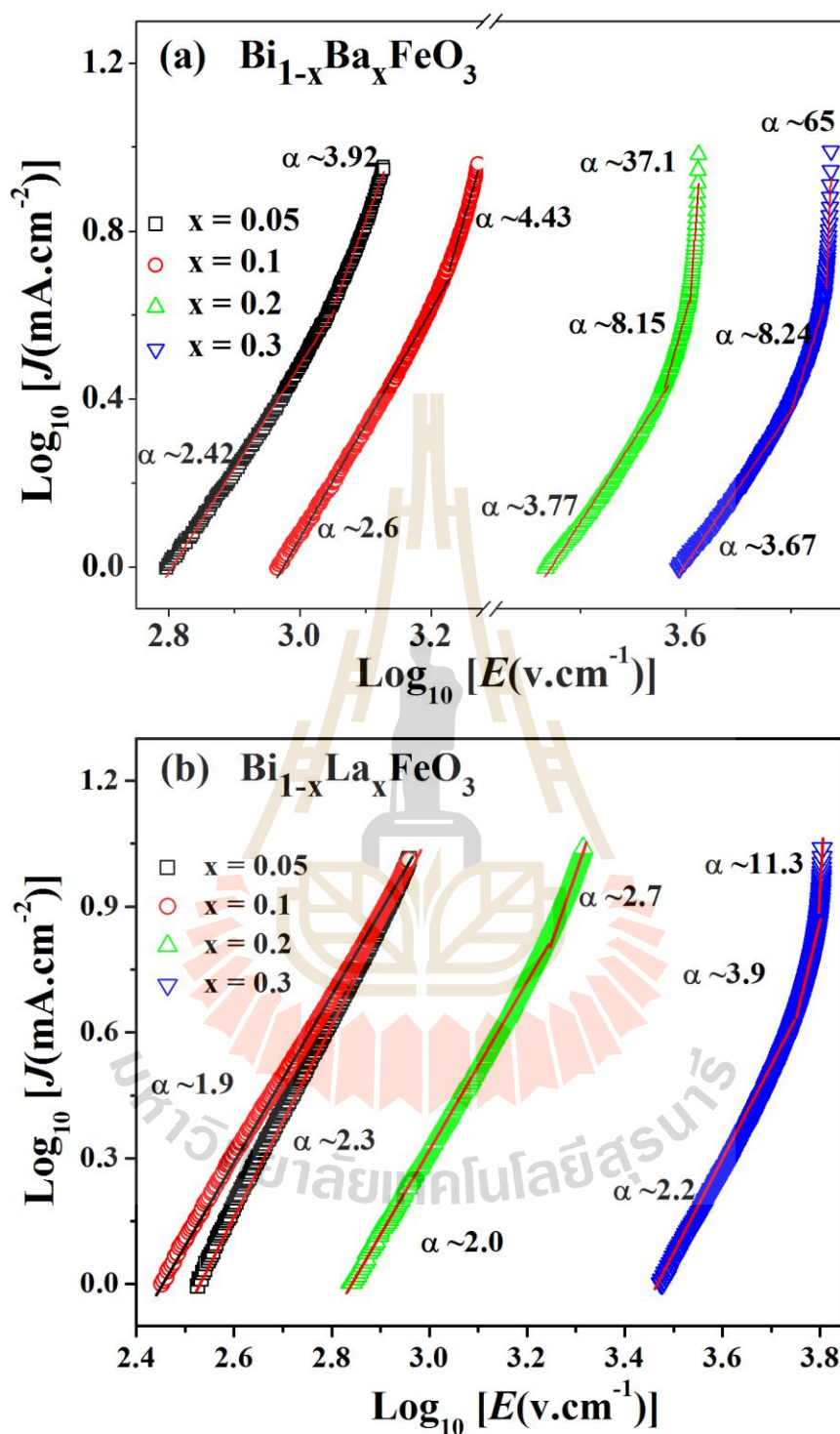


Figure 4.59 Logarithmic plots of dependence of J as a function of E measured at room temperature for (a) $\text{Bi}_{1-x}\text{Ba}_x\text{FeO}_3$, (b) $\text{Bi}_{1-x}\text{La}_x\text{FeO}_3$, and (c) $\text{Bi}_{1-x}\text{Sm}_x\text{FeO}_3$ ceramics sintered at $800\text{ }^\circ\text{C}$ for 3 h.

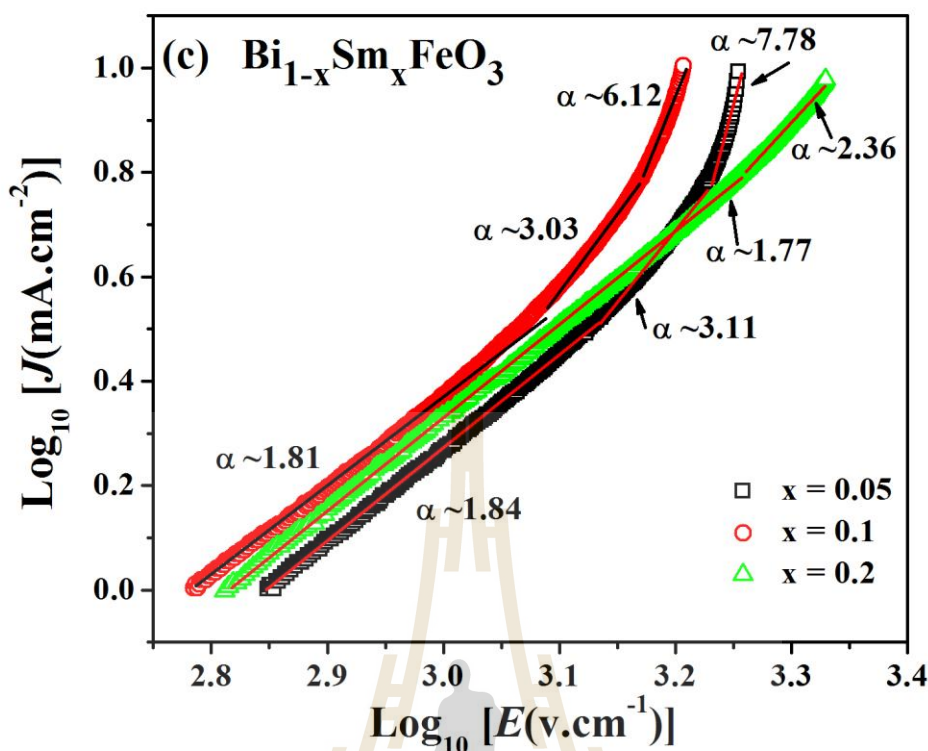


Figure 4.59 Logarithmic plots of dependence of J as a function of E measured at room temperature for (a) $\text{Bi}_{1-x}\text{Ba}_x\text{FeO}_3$, (b) $\text{Bi}_{1-x}\text{La}_x\text{FeO}_3$ and (c) $\text{Bi}_{1-x}\text{Sm}_x\text{FeO}_3$ ceramics sintered at 800°C for 3 h (Continued).

To understand the effect of doping ions on the electrical responses of the grain boundaries of BiFeO_3 -based ceramics, the nonlinear J - E properties were investigated at different temperatures. Figure 4.60 illustrates the J - E behaviours at various temperatures of BiFeO_3 and $\text{Bi}_{1-x}\text{Ba}_x\text{FeO}_3$ ceramics when the breakdown field decreases with increasing temperature and nonlinear behaviour tends to show linear Ohmic characteristics as temperature increases. This result indicates the effects of temperature of the Schottky barrier on the grain boundaries. The nonlinear J - E curves in this temperature range (298–393K) of $\text{Bi}_{1-x}\text{Ba}_x\text{FeO}_3$ when $x = 0.05, 0.1, 0.2,$ and 0.3 are similar to those observed for the pure BiFeO_3 samples. It can be seen that E_b

linear decreases with increasing temperatures for all samples. As shown in Figures 4.61 and Figure 4.62, the nonlinear J - E plots of the La- and Sm-doped BiFeO₃ ceramics show overall nonlinear curves which are similar to those observed for the pure BiFeO₃ ceramics.

According to the relationship of the current-voltage varistor, the fitted log-log scale results indicate that the nonlinear coefficients of the samples decrease the slope value to ~ 1 as temperature increases. This result implies that the conduction mechanism changes from non-Ohmic to linear Ohmic behavior. Because of the evidence of the grain and grain boundary characteristics, it seems possible to use the Schottky barrier to explain the effect of the grain boundary on these samples. Considering the potential barriers in the BiFeO₃-based systems to be of the Schottky type, conduction in the pre-breakdown region should be related to the thermionic emission of the Schottky type and associated with the electric field and temperature. Therefore, the variations in current density (J) with the electric field (E) and the temperature (T) can be given by Eq. (2.94) as described in chapter II. Nonlinear current density as a function of the electric field curves at various temperatures in the La- and Sm-doped samples are similar to those observed for the Ba-doped samples. The breakdown field decreases with increasing temperature, and the non-Ohmic characteristics tend to show linear Ohmic behavior which are very similar to those observed for the La- and Sm-doped BiFeO₃ ceramics.

By applying the Schottky type conduction model, the plots of $\ln J$ versus $E^{1/2}$ for the pure BiFeO₃ and Ba-, La-, and Sm-doped BiFeO₃ ceramics can be used to calculate the potential barrier height (ϕ_b). The current density versus the electric field was measured at different temperatures, and a good linear relationship between $\ln J$

and $E^{1/2}$ was observed, which indicates that in these field regions electrical conduction contributes to the thermal emissions over a potential barrier Schottky at the grain boundaries Using Eq. (2.94), J_0 we can obtained various temperatures from the plots of $\ln J - E^{1/2}$ by linearly fitting the data as the curves are extrapolated to $E = 0$. Inset figure shows the fitting of $\ln J_0$ versus $1000/T$ curves from which a good linear behavior can also be obtained, which indicates that the variations in the pre-exponential terms in Eq. (2.94) are very small and negligible. Thus we can calculate the potential barrier height from the slope of the plots. As revealed in Figure 4.63(a), the ϕ_B values were approximately 0.321, 0.332, 0.43, and 0.54 for $\text{Bi}_{1-x}\text{Ba}_x\text{FeO}_3$ with $x = 0.05, 0.1, 0.2,$ and 0.3 respectively. The values of ϕ_B for the Ba-doped BiFeO_3 samples were slightly enhanced by substituting with Ba^{2+} ions. The values for the $\text{Bi}_{1-x}\text{La}_x\text{FeO}_3$ ($x = 0, 0.05, 0.1, 0.2,$ and 0.3) ceramics are found to be 0.53, 0.24, 0.194, 0.188, and 0.062 eV, respectively. As revealed in Figure 4.63(c), the values of ϕ_B can be calculated from the slopes and are 0.26, 0.23, and 0.09 for the $\text{Bi}_{0.95}\text{Sm}_{0.05}\text{FeO}_3$, $\text{Bi}_{0.9}\text{Sm}_{0.1}\text{FeO}_3$, and $\text{Bi}_{0.8}\text{Sm}_{0.2}\text{FeO}_3$ samples, respectively. The results represent an increasing concentration of La^{3+} and Sm^{3+} doping ions which makes the potential barrier height decrease as compared to the pure BiFeO_3 ceramics. These results are similar to those observed in the $\text{CaCu}_3\text{Ti}_{4-x}\text{La}_x\text{O}_{12}$ ceramics.

Without the applied DC bias voltage, the Schottky barrier height at the grain boundary of the compound can be expressed as

$$\phi_B = \frac{qN_s^2}{8\epsilon_0\epsilon N_d} \quad (4.2)$$

where q is the electronic charge, N_s is the acceptor concentration, ϵ' is the relative permittivity of materials, and N_d is the charge carrier concentration in the semiconducting grain. From the results obtained from the above equation, it is possible that the reduction of ϕ_B observed in the La-doped BiFeO₃ ceramics is primarily caused by changes either in increases in N_d or a huge decrease in N_s . In general, an increase in N_d can cause a decrease in resistance at the grain boundary (R_g) (Thongbai *et al.*, 2014). With impedance spectroscopy of the La-doped BiFeO₃ system, it was found that there was a small dependence on the resistance of the grain bulk (R_g) for these samples. To investigate the electrical properties of the grain and grain boundary materials we used impedance spectroscopy. It was observed that the R_g values of these La-doped samples were larger than those of the Bi_{0.95}La_{0.05}FeO₃ samples. This result suggests that N_d does not increase with replacement of La³⁺ ions. It should be noted that the decreases in the dielectric constant as the La doping levels increase might be due to their lower potential barrier value. It is possible that the potential barrier height of this system is not sufficient to completely trap the electrons at surface acceptor states as in the grain boundary regions lead to most of them being able to move across the grain boundaries. Therefore, when the intensity of the interfacial polarization decreases, it leads to a decrease in the dielectric constant. Interestingly, the potential barrier height increases with increases in the Ba doping content of the BiFeO₃ ceramics. Khassaf reported that the height of the potential barrier increases with Gd substitutions in the BiFeO₃ thin film (Khassaf *et al.*, 2012). They explain the results in terms of assuming an ionic compensation by the holes, introduced by the presence of Bi vacancies, and by the electrons introduced via Gd doping. Gd substitutions can compensate for the p-type conduction, so the Fermi

level moves towards the middle of the forbidden band resulting in an increase in the potential barrier height of holes.

Table 4.11 The current–voltage characteristics of various Ba–, La–, and Sm–doped BiFeO₃ samples.

sample	E_b (V/cm ²)	Leakage current	α	ϕ_B (eV)
Pure BiFeO ₃	742	2.69	2.31	0.53
Bi_{1-x}Ba_xFeO₃				
x = 0.05	629	3.04	2.42	0.32
x = 0.1	928	1.21	2.6	0.33
x = 0.2	2937	0.05	3.67	0.43
x = 0.3	3933	0.016	3.71	0.54
Bi_{1-x}La_xFeO₃				
x = 0.05	336	3.3	2.27	0.24
x = 0.1	360	2	1.94	0.194
x = 0.2	690	0.47	2.02	0.188
x = 0.3	2981	-	2.21	0.062
Bi_{1-x}Sm_xFeO₃				
x = 0.05	705	1.85	1.84	0.26
x = 0.1	610	2.36	1.81	0.34
x = 0.2	648	2.15	1.77	0.35
x = 0.3	-	-	-	-

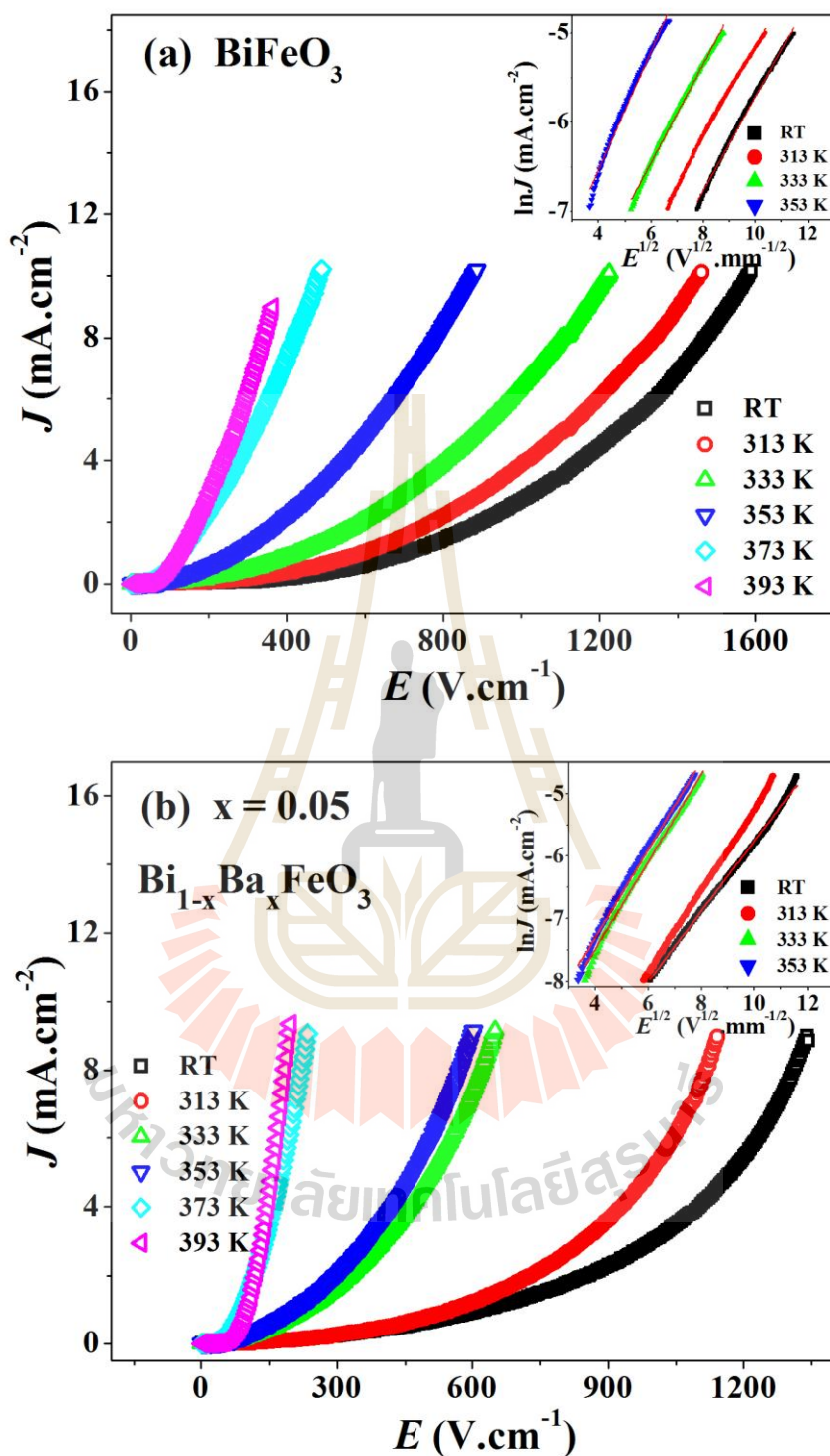


Figure 4.60 Nonlinear characteristics (J - E curves) of the pure BiFeO₃ (a) and (b)-(e) Ba-doped BiFeO₃ ceramics at various temperatures and (inset) plots of $\ln J$ versus $E^{1/2}$.

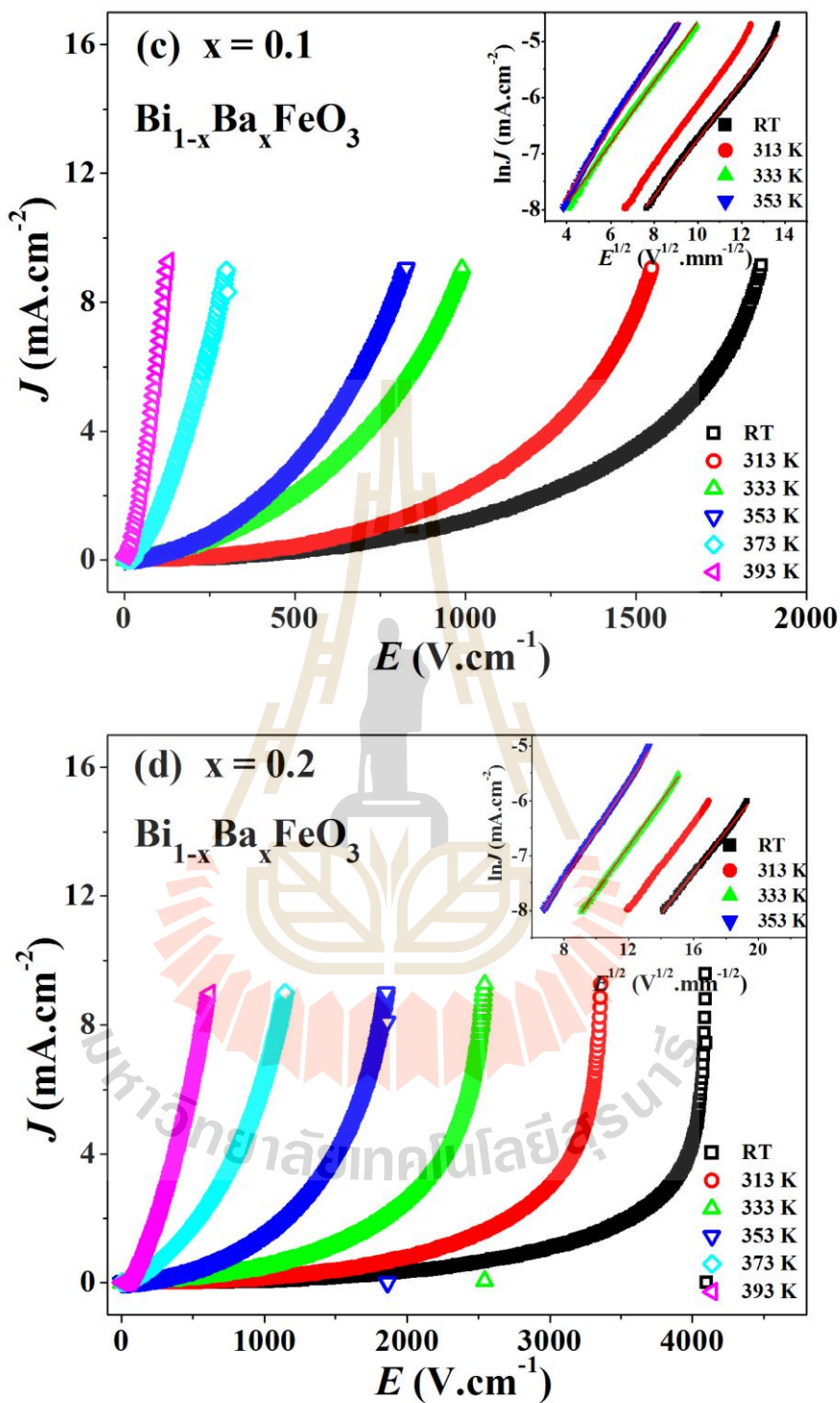


Figure 4.60 Nonlinear characteristics (J - E curves) of the pure BiFeO_3 (a) and (b)–(e) Ba-doped BiFeO_3 ceramics at various temperatures and (inset) plots of $\ln J$ versus $E^{1/2}$ (Continued).

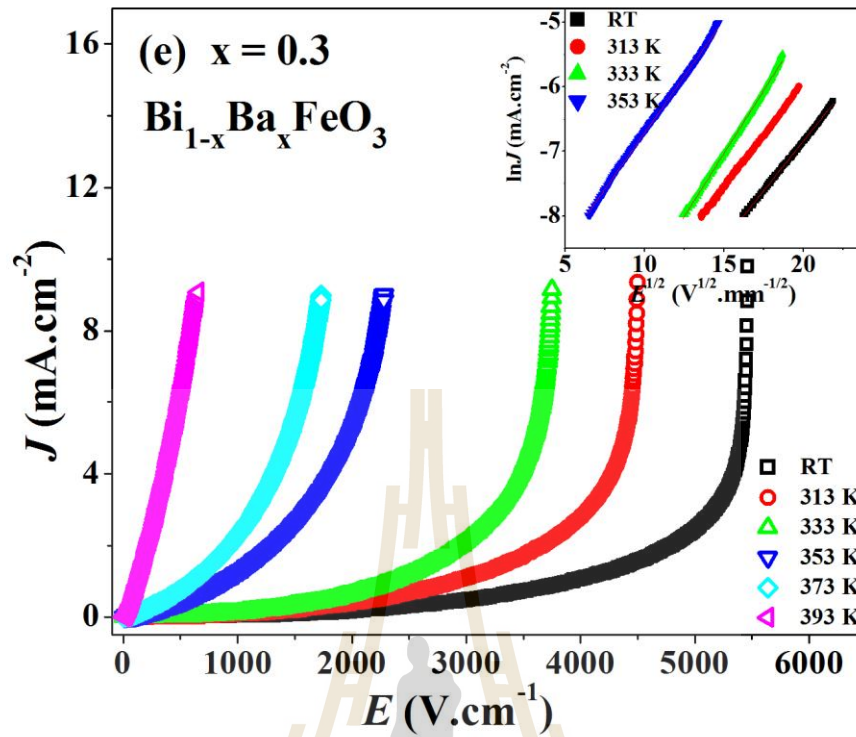


Figure 4.60 Nonlinear characteristics (J – E curves) of the pure BiFeO_3 (a) and (b)–(e) Ba–doped BiFeO_3 ceramics at various temperatures and (inset) plots of $\ln J$ versus $E^{1/2}$ (Continued).

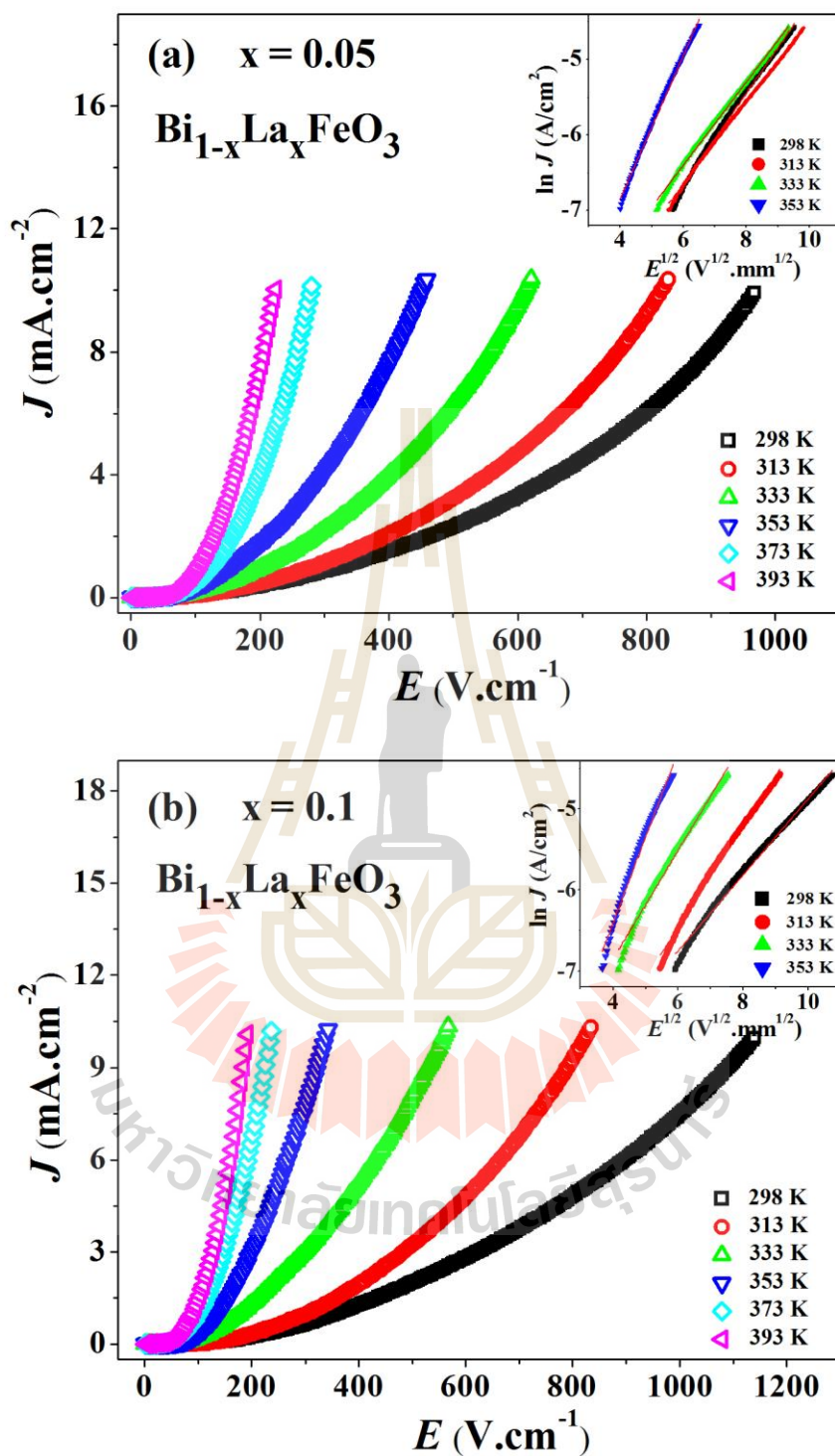


Figure 4.61 Nonlinear characteristics (J - E curves) of the pure BiFeO₃ (a) and (b)-(e) La-doped BiFeO₃ ceramics at various temperatures and (inset) plots of $\ln J$ versus $E^{1/2}$.

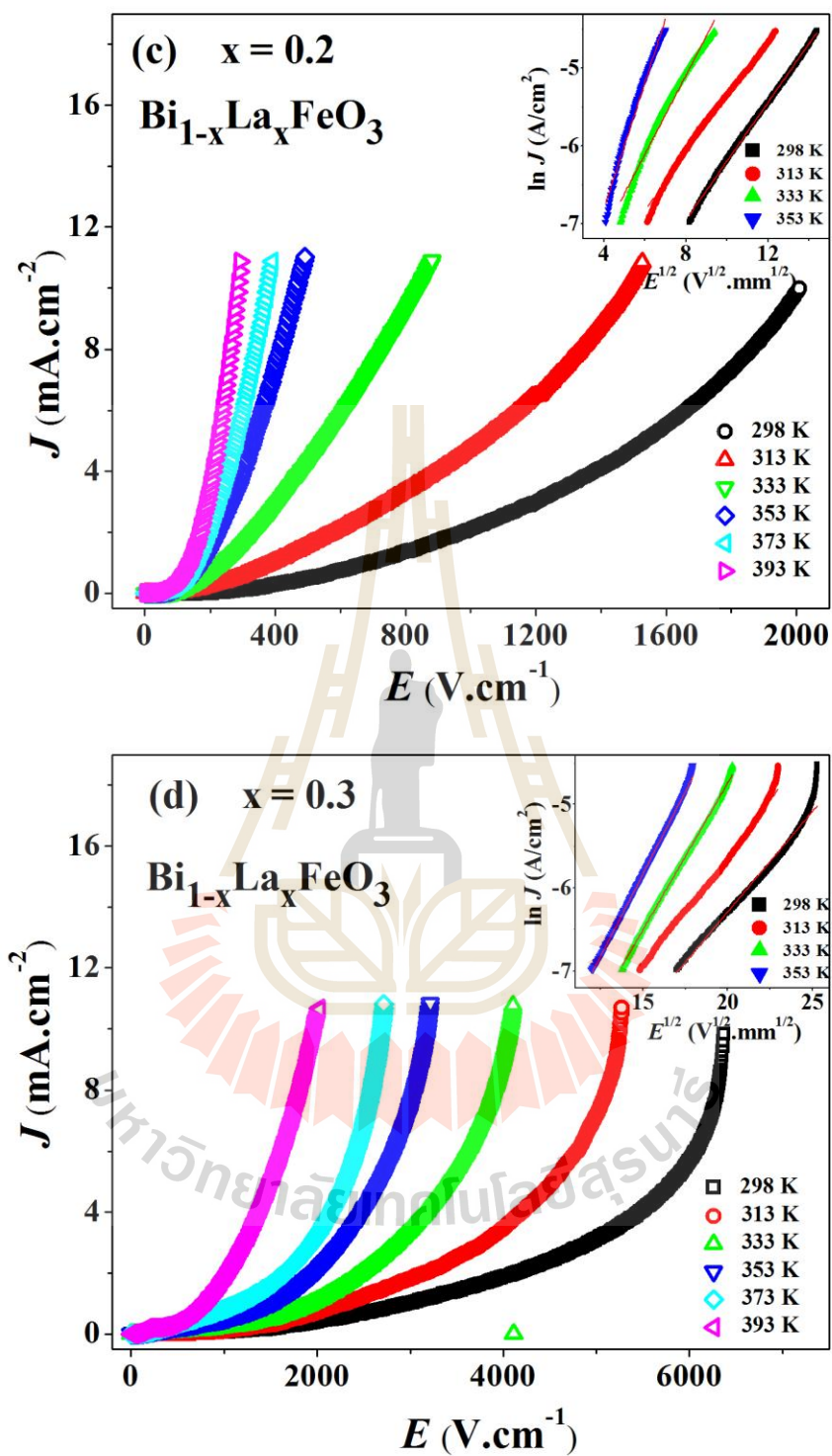


Figure 4.61 Nonlinear characteristics (J - E curves) of the pure BiFeO_3 (a) and (b)-(e) La-doped BiFeO_3 ceramics at various temperatures and (inset) plots of $\ln J$ versus $E^{1/2}$ (Continued).

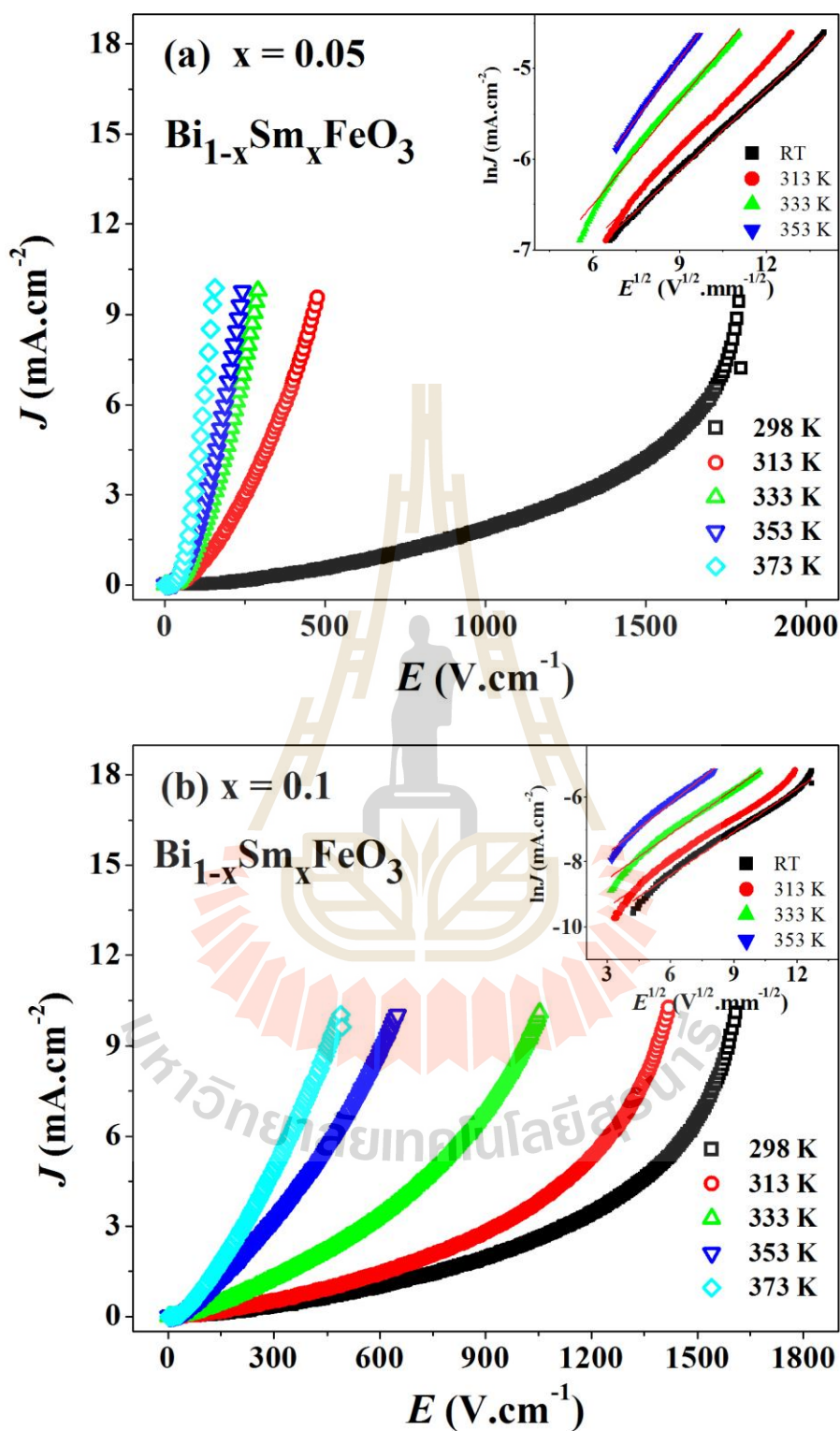


Figure 4.62 Nonlinear characteristics (J - E curves) of the Sm-doped BiFeO₃ ceramics at various temperatures; (a) $x = 0.05$, (b) $x = 0.1$, and (c) $x = 0.2$ and (inset) plots of $\ln J$ versus $E^{1/2}$.

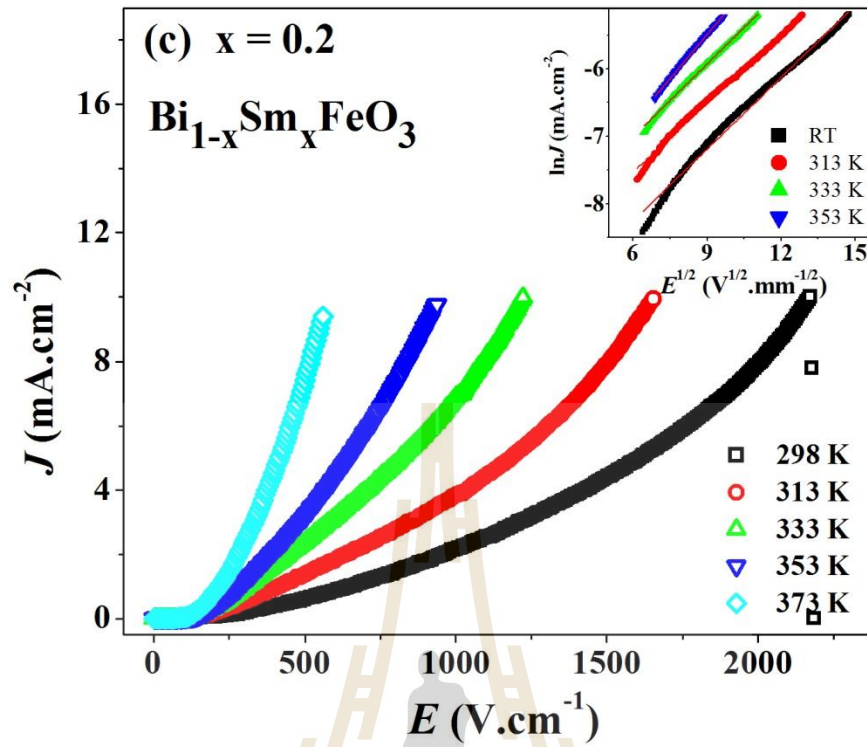


Figure 4.62 Nonlinear characteristics (J - E curves) of the Sm-doped BiFeO_3 ceramics at various temperatures; (a) $x = 0.05$, (b) $x = 0.1$, and (c) $x = 0.2$ and (inset) plots of $\ln J$ versus $E^{1/2}$ (Continued).

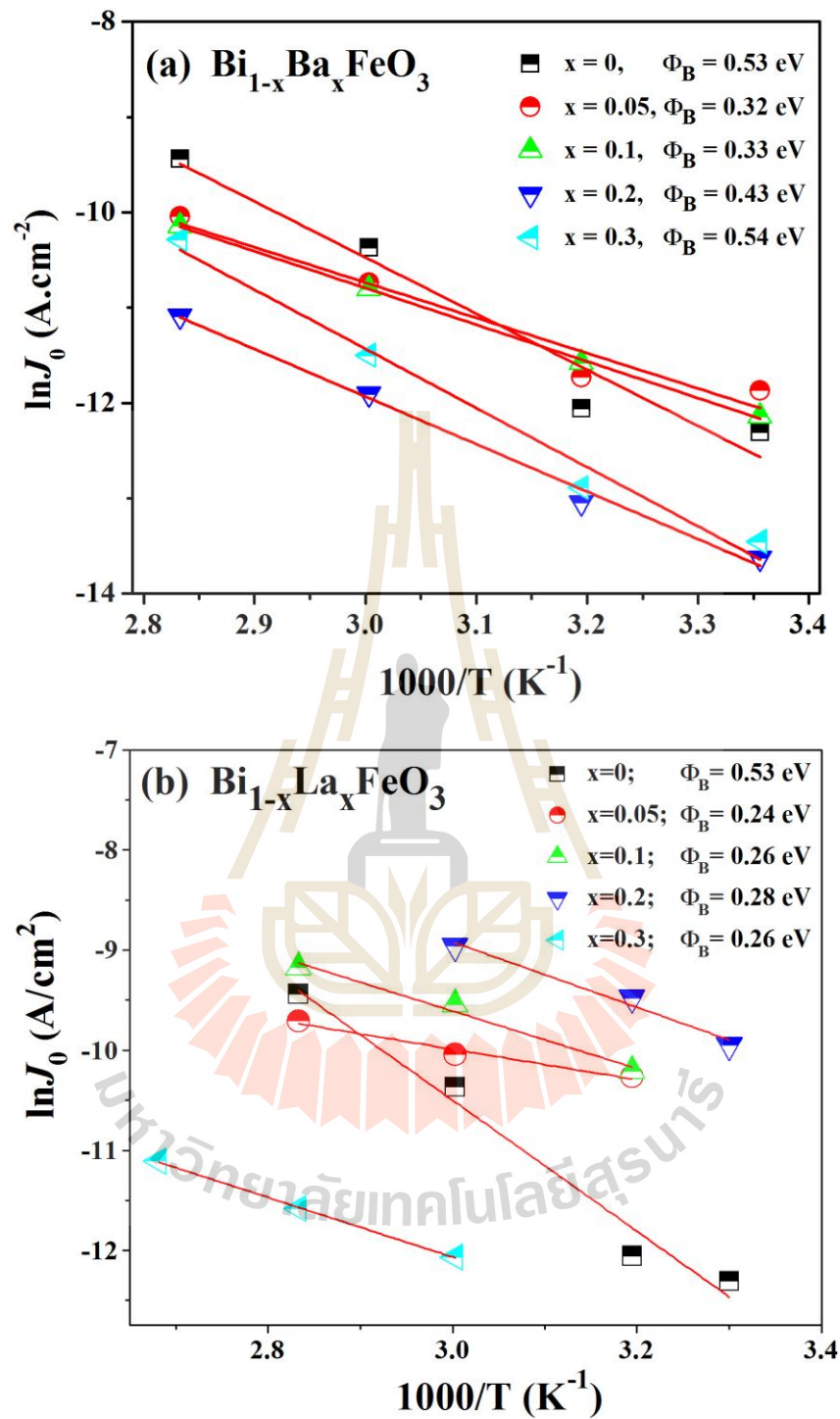


Figure 4.63 Plots of $\ln J_0$ vs $1/T$ for pure BiFeO_3 and (a) Ba– (b) La–, and (c) Sm–doped BiFeO_3 samples and the estimated potential barrier height, ϕ_B .

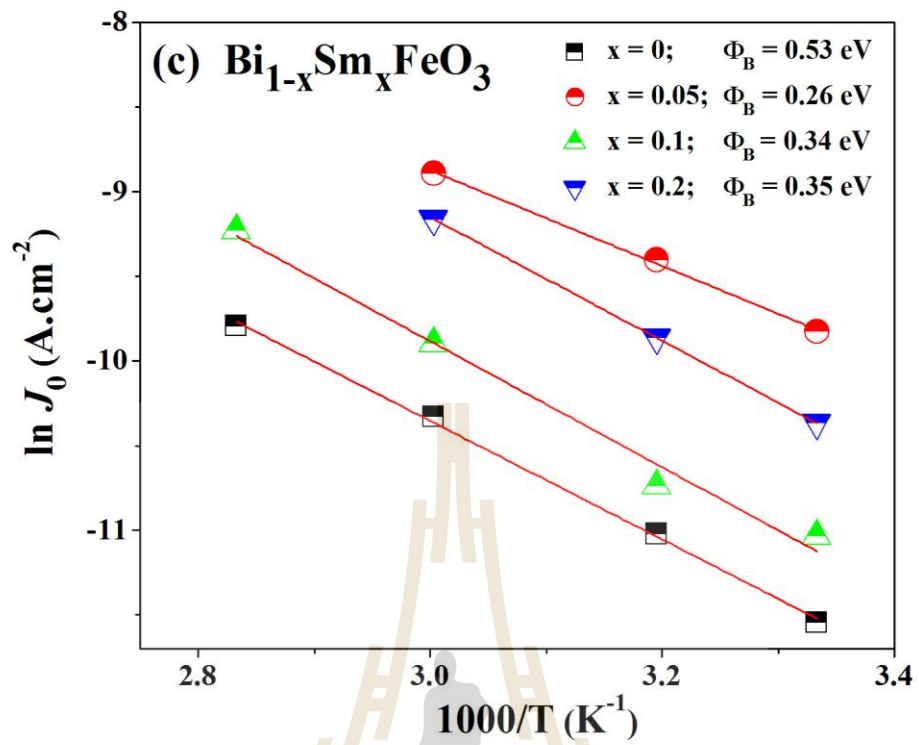


Figure 4.63 Plots of $\ln J_0$ vs $1/T$ for pure BiFeO_3 and (a) Ba-, (b) La-, and (c) Sm-doped BiFeO_3 samples and the estimated potential barrier height, ϕ_B (Continued).

CHAPTER V

CONCLUSIONS

In this thesis, pure BiFeO_3 and $\text{Bi}_{1-x}\text{A}_x\text{FeO}_3$ ($\text{A} = \text{Ba}, \text{La}, \text{and Sm}$) powders have been successfully prepared by using a co-precipitation method. The concentration values of the doping elements are $x = 0, 0.05, 0.1, 0.2,$ and 0.3 in each composition system. The surface morphology, structure formation and local structure of the prepared powder were characterized by XRD, TEM, SEM, FTIT, and XAS techniques. The optical properties were investigated by UV-vis, while the magnetic properties were determined by VSM. The dielectric properties of the BiFeO_3 -based ceramic samples were studied using a Hewlett Packard 4194A impedance gain phase analyzer associated with the dc bias voltage. The current-voltage behavior has also been studied using a high-voltage measurement unit (Keithley Model 247, Estado St Pasadena, CA). The conclusions of these studies can be summarized as follows:

5.1 The structure and surface morphology characterization

The XRD results exhibit the formation of the rhombohedral crystal phase BiFeO_3 with $R3c$ space group accompanied by some impurity phases such as Bi_2O_3 and $\text{Bi}_2\text{Fe}_4\text{O}_9$. The XRD patterns indicate that the Ba doping does not give rise to a structural transition, while the rare earth (La and Sm) concentrations increase

up to 30%, showing that a structural transition from a rhombohedral to an orthorhombic phase has occurred. The La substitution can suppress the impurity phase of the composition at about $x = 0.05$, while the Sm addition indicates that a suppression of the impurity phase occurs at $x = 0.1$. The average particle size of undoped BiFeO_3 nanoparticles was observed to be about 67 nm. The average particle size of the doped samples is found to decrease with the addition of Ba, La, and Sm ions. The microstructure of doped BiFeO_3 ceramics shows that dopant concentration has a significant influence on grain growth. Increases in Ba, La, and Sm doping levels caused a decrease in the average grain size of the ceramics. La and Sm doped in BiFeO_3 exhibited smaller grain sizes than reported in any rare earth doped materials which suppresses the grain growth. Rare earth ions are known to suppress oxygen vacancy concentrations in perovskite, which is attributed to their lower oxygen ion motion and lower grain growth rate. Although further Ba doping oxygen vacancies are generated with charge neutralization which can help to minimize Bi volatilization and reduce the oxygen vacancy concentration. Consequently, lower oxygen ion motion results in lower grain growth rate. From the XANES results, it was clearly observed that the features of XANES spectra were in good agreement with the Fe_2O_3 standard, indicating that oxidation state of Fe ion in BiFeO_3 structure is 3+. In addition we also confirmed that the oxidation state of Fe ion in Ba-, La-, and Sm-doped BiFeO_3 structure is 3+. FTIR spectra were used to study the bond interaction in the BiFeO_3 -based compound. The strong absorption peaks near 400 to 540 cm^{-1} are assigned to Fe-O stretching and bending vibrations, being characteristics of the octahedral FeO_6 group in the perovskite structure.

5.2 Optical properties

UV–vis spectroscopy shows that the strong absorption of UV and visible light in the wavenumber range of 200–800 nm. It was observed that the pure BiFeO₃ and doped samples absorbed considerable amounts of visible light in the range of 500 to 675 nm suggesting their potential application for photocatalytic performance under visible light irradiation. Pure BiFeO₃ nanoparticles exhibit absorption peaks at around 490–700 nm which shift towards higher wavelengths for La, Ba, and Sm–substituted in BiFeO₃ samples. The absorption edges of Ba–doped BiFeO₃ powders are seen to be higher than that of pure BiFeO₃ (~575 nm) samples and slightly increase with increases in Ba doping concentrations. It should be noted that in the case of La–doped BiFeO₃, the absorption band edges increase to 510–703 nm as compared to the absorption peaks of pure BiFeO₃. For Sm–doped samples, we observed that the absorption edges were around 591, 601, 658, and 666 nm for $x = 0.05, 0.1, 0.2,$ and 0.3 samples, respectively. All of the doped BiFeO₃ samples showed that the absorption edges increased with increasing doping concentrations. It was observed that the band centered at 1.8 eV was related to on–site d–d transitions and a weak band centered at 2.5 eV was assigned to dipole–forbidden p–d charge transfer transitions. Two bands located at 3.2 and 4.5 eV are defined as dipole allowed p–d charge transfer (C–T) features in the octahedral center. The band gap of pure BiFeO₃ powder was found to be 2.12 eV as determined from the absorption coefficient spectra. The obtained optical band gap values of the doped compounds are about 2.10–1.93 eV, 2.09–2.03 eV, and 2.05–1.91 eV for La, Ba, and Sm–doped samples, respectively. The decrease in the optical band gaps of the substituted samples were found to be red shifted with the increase in doping concentrations which may be

attributed to increased internal chemical pressure. As the dopant substitutions is increased, the concentration of oxygen vacancy is ulteriorly increased which can give rise to the defect-induced energy band gap, thus narrowing the distance between the conduction band and the oxygen vacancy donor band which shrinks.

5.3 Magnetic properties

The field dependence magnetization (M–H loop) properties of doped–BiFeO₃ nanopowders are measured at room temperature with a maximum applied magnetic field of 10000 Oe. In order to understand the effect of doped BiFeO₃ on the magnetic ordering, the temperature dependent zero–field cooled (ZFC) and field cooled (FC) magnetization measurements are carried out within temperature ranges 50–350 K under an applied field of 1000 Oe. The nanocrystalline sample of undoped BiFeO₃ exhibits antiferromagnetic behavior at room temperature. The fitting of the Curie–Weiss law for BiFeO₃ samples shows the negative value of θ , indicating an antiferromagnetic exchange interaction between unpaired ions in the samples. All of Ba–doped compounds display a very slim hysteresis loop with nonzero remnant magnetization and a narrow coercive field which has similar magnetic behaviors to the pure BiFeO₃ samples, implying antiferromagnetic behavior at room temperature. A lower coercive field (H_c) for all doped samples reveals the possibility that the weak ferromagnetic order is basically an antiferromagnetic substrate with weak ferromagnetism which is because of the presence of antiferromagnetic impurities in Bi₂Fe₄O₉. The maximum magnetization of the undoped BiFeO₃ was found to be 0.06 emu/g and with the Ba–doped sample it is enhanced twice as compared to the pure

BiFeO₃. With the fitting of the Curie–Weiss law, we obtain θ negative values for our samples, indicating antiferromagnetic interactions among the magnetic ions. The nanocrystalline BiFeO₃ doped samples with La and Sm reveal increasing x values, and the ferromagnetic interaction is dominant. The fitting of the Curie–Weiss law to some of the La–doped BiFeO₃ and Sm–doped BiFeO₃ samples shows the positive value of θ . When the Curie–Weiss law is fitted to the results which provide positive Curie temperatures, this is probably due to the strongly canted AFM ordering with a manifest FM component. It was found that all magnetic ions in all doped–BiFeO₃ samples are in the high spin configuration ($t_{2g}^3 e_g^2, \uparrow\uparrow\uparrow\uparrow; s = 5/2$).

5.4 Dielectric properties

In conclusion, the high dielectric constant of $\sim 1.04 \times 10^4$ was observed in pure BiFeO₃ ceramics at a frequency of 1 kHz. A strong decrease in the frequency of the dielectric constant in whole temperatures range is the characteristic of pure BiFeO₃ ceramics. The dielectric constant spectra show the highest values at a low–frequency range (below 10^4 Hz) and high temperatures. They reveal large dielectric curves attributed to the Maxwell–Wagner polarization or interfacial space charge polarization (mostly located at the grain boundary). It was found that the dielectric constant increased with increasing grain size. As the temperature increases, the dielectric constant is found to increase to higher values. Interestingly, two sets of thermal relaxations exhibited in the dielectric spectra of the samples show that there are at least two sources of polarizations which contributed to the total dielectric

response. The calculated values of E_a are 0.29 and 0.77 eV for $\text{Bi}_{1-x}\text{Ba}_x\text{FeO}_3$ (where $x = 0.05$ and 0.3) samples.

It is remarkable to see that the dielectric constant decreases with substitution of La doping concentrations ($x = 0.05, 0.1, 0.2,$ and 0.3) in all measured frequency ranges. Compared to the parent BiFeO_3 , at low frequency, the dielectric constant is higher than that of BiFeO_3 when it is doped with La ions. The decrease in dielectric constant values with increasing La-substituted corresponds to the slight reduction of the average grain sizes in the microstructure. The dielectric constant shows maximum values at the lower frequencies for high temperatures. It is observed that the exponential-like increase in the loss tangent corresponds to decreasing frequency to the lower frequency region in $\text{Bi}_{0.95}\text{La}_{0.05}\text{FeO}_3$, $\text{Bi}_{0.9}\text{La}_{0.1}\text{FeO}_3$, and $\text{Bi}_{0.8}\text{La}_{0.2}\text{FeO}_3$ samples are due to the effect of dc conductivity. The values in the samples for $\text{Bi}_{1-x}\text{La}_x\text{FeO}_3$ (where $x = 0.05, 0.1,$ and 0.2) can be estimated to be 0.47, 0.40, and 0.32 eV, respectively. The dc conduction activation energy decreases with the increases in La doping levels which the lower conduction activation energy, the promotion of polarization at the interfacial grains is easy.

The dielectric properties for Sm-doped BiFeO_3 ceramics are similar to that observed in the dielectric properties of La-doped samples. It was found that the dielectric constant was enhanced by increasing the grain size. It was suggested that the dielectric relaxation behavior and the high dielectric response in this material system might be associated with both the hopping motions inside the grains and the Maxwell-Wagner polarization at the grain boundaries. The activation energy values obtained were 0.45 and 0.74 for Sm doping amounts of 5% and 10%. The decrease in

the bandwidth and the increase in polaron binding energy results in an increase in activation energy.

The gradual increases in the dielectric constant with increases in DC bias is observed in pure BiFeO₃ and Ba-doped BiFeO₃ ceramics from 100 to 10⁴ Hz. It is noted that ϵ' above 10⁴ Hz becomes reduced by an applied DC bias. In case of La and Sm substituted in Bi site, the dielectric properties were observed to be found different for pure BiFeO₃ and Ba-doped samples. The dielectric constant of La- and Sm-doped BiFeO₃ under 0–20 V DC bias decreases with increases in applied DC bias voltage, while the dielectric constant above 10⁴ Hz does not change with applied DC bias.

5.5 Current–voltage characteristics

The current density (J) as a function of the applied electric field (E) at room temperature for the pure BiFeO₃ and doped ceramics display non-Ohmic behaviours. It is shown that the leakage current density increases with increases in the electric field for all conditions, while the E_b value increases with further increases of Ba doping. The nonlinear coefficient value (α) for a specific region of these curves provides information about the conduction mechanism involved in that region. The nonlinear coefficient of pure BiFeO₃ obtained was 2.31 indicating that the SCLC is dominant for undoped BiFeO₃ samples. In the case of Ba-doped samples, SCLC conduction occurs in region I and the α value increases in region II and region III. The α value was found to be between 1 and 2 for La- and Sm-doped samples, suggesting the co-existence of Ohmic as well as SCLC behaviour. With increasing

electric fields (region III) the mechanisms are probably related to either the Poole–Frenkel conduction mechanism or the Schottky emission mechanism.

5.6 Suggestion for future work

(1) Investigation of the stoichiometry of BiFeO₃-based ceramics using the energy dispersive spectroscopy (EDS) is required to confirm the fractions of the constituent elements of Fe, Bi, Ba, La, Sm, and O ions in the prepared samples.

(2) Simulation of the ionic occupancy and distribution of Bi³⁺, Ba²⁺, La³⁺ and Sm³⁺ ions in the A-site of the perovskite structure provides important information which leads to a better understanding of the optical, magnetic, dielectric, and electrical properties of the materials.

(3) The doping concentrations affect the structure of the BiFeO₃-based ceramics, and the Ba, La, and Sm doping concentrations require more energy to obtain an image of the modified BiFeO₃.

The logo of Sakon Nakhon Vejjajit Rajabhat University is a circular emblem. It features a central figure of a person standing on a pedestal, flanked by two stylized figures. Above the central figure is a large, ornate letter 'H'. The entire emblem is set against a background of a stylized lotus flower with multiple petals. The text 'มหาวิทยาลัยเทคโนโลยีสุรนารี' is written in Thai script around the bottom of the emblem.

REFERENCES

มหาวิทยาลัยเทคโนโลยีสุรนารี

REFERENCES

- Al-Douri, A. J., Al-Shakily, F., Alnajjar, A. A., and Alias, M. F. (2011). The role of dopant concentration on conductivity and mobility of CdTe thin films. **Advances in Condensed Matter Physics**. 2011: 1-7.
- Arora, M., and Kumar, M. (2014). Electron spin resonance probed enhanced magnetization and optical properties of Sm doped BiFeO₃ nanoparticles. **Materials Letters**. 137: 285-288.
- Arora, M., and Kumar, M. (2015). Structural, magnetic and optical properties of Ce substituted BiFeO₃ nanoparticles. **Ceramics International**. 41: 5705-5712.
- Asokan, K., Jan, J., Chiou, J., Pong, W., Tsai, M., Shih, H., Chen, H., Hsueh, H., Chuang, C., and Chang, Y. (2001). Electronic structures of Ba_{1-x}Ca_xTiO₃ studied by x-ray absorption spectroscopy and theoretical calculation. **Journal of Physics: Condensed Matter**. 13: 11087-11095.
- Basu, S., Pal, M., and Chakravorty, D. (2008). Magnetic properties of hydrothermally synthesized BiFeO₃ nanoparticles. **Journal of Magnetism and Magnetic Materials**. 320: 3361-3365.

- Béa, H., Bibes, M., Cherifi, S., Nolting, F., Warot-Fonrose, B., Fusil, S., Herranz, G., Deranlot, C., Jacquet, E., and Bouzehouane, K. (2006). Tunnel magnetoresistance and robust room temperature exchange bias with multiferroic BiFeO₃ epitaxial thin films. **Applied Physics Letters**. 89: 242114-242116.
- Beniwal, A., Bangruwa, J. S., Walia, R., and Verma, V. (2016). A systematic study on multiferroics Bi_{1-x}Ce_xFe_{1-y}Mn_yO₃: Structural, magnetic and electrical properties. **Ceramics International**. 42: 10373-10379.
- Besmel, R., Ghaffari, M., Shokrollahi, H., Chitsazan, B., and Karimi, L. (2011). Influence of milling time on the structural, microstructural and magnetic properties of mechanically alloyed Ni₅₈Fe₁₂Zr₁₀Hf₁₀B₁₀ nanostructured/amorphous powders. **Journal of Magnetism and Magnetic Materials**. 323: 2727-2733.
- Biasotto, G., Simões, A. Z., Foschini, C., Zaghete, M., Varela, J. A., and Longo, E. (2011). Microwave-hydrothermal synthesis of perovskite bismuth ferrite nanoparticles. **Materials Research Bulletin**. 46: 2543-2547.
- Biasotto, G., Simões, A. Z., Foschini, C. R., Antônio, S. G., Zaghete, M. A., and Varela, J. A. (2011). A novel synthesis of perovskite bismuth ferrite nanoparticles. **Processing and Application of Ceramics**. 5: 171-179.
- Bibes, M., and Barthélémy, A. (2008). Towards a magnetoelectric memory. **Nature Materials**. 7: 425-426.
- Brzozowski, E., Castro, M., Foschini, C., and Stojanovic, B. (2002). Secondary phases in Nb-doped BaTiO₃ ceramics. **Ceramics International**. 28: 773-777.

- Catalan, G., and Scott, J. F. (2009). Physics and applications of bismuth ferrite. **Advanced Materials**. 21: 2463-2485.
- Chen, Z., Li, Y., Wu, Y., and Hu, J. (2012). Hydrothermal synthesis and mechanism and property study of La-doped BiFeO₃ crystallites. **Journal of Materials Science: Materials in Electronics**. 23: 1402-1408.
- Cheng, G., Ruan, Y., Liu, W., and Wu, X. (2015). Effect of local structural distortion on magnetic and dielectric properties in BiFeO₃ with Ba, Ti co-doping. **Physica B: Condensed Matter**. 468: 81-84.
- Comyn, T. P., Kanguwe, D. F., He, J., and Brown, A. P. (2008). Synthesis of bismuth ferrite lead titanate nano-powders and ceramics using chemical co-precipitation. **Journal of the European Ceramic Society**. 28: 2233-2238.
- Costa, M., Pires Jr, G., Terezo, A., Graca, M., and Sombra, A. (2011). Impedance and modulus studies of magnetic ceramic oxide Ba₂Co₂Fe₁₂O₂₂(Co₂Y) doped with Bi₂O₃. **Journal of Applied Physics**. 110: 034107-034107-7.
- Dai, H., Li, T., Chen, Z., Liu, D., Xue, R., Zhao, C., Liu, H., and Huang, N. (2016). Studies on the structural, electrical and magnetic properties of Ce-doped BiFeO₃ ceramics. **Journal of Alloys and Compounds**. 672: 182-189.
- Dai, Z., Fujita, Y., and Akishige, Y. (2011). Dielectric properties and heating effect of multiferroic BiFeO₃ suspension. **Materials Letters**. 65: 2036-2038.
- Daniel, J., and Härdtl, K. (1976). Defect chemistry and electrical conductivity of doped barium titanate ceramics: Part I, electrical conductivity at high temperature of donor-doped barium titanate ceramics. **Philips Research Report**. 31: 487-504.

- Dong, G., Tan, G., Luo, Y., Liu, W., Ren, H., and Xia, A. (2014). Investigation of Tb-doping on structural transition and multiferroic properties of BiFeO₃ thin films. **Ceramics International**. 40: 6413-6419.
- Deng, X., Huang, J., Zhang, Y., Cai, W., and Fu, C. (2015). Effect of Ba substitution on microstructure, dielectric and ferroelectric properties of BiFeO₃ ceramics. **Ferroelectrics**. 478: 11-17.
- Desu, S. B., and Payne, D. A. (1990). Interfacial segregation in perovskites: III, microstructure and electrical properties. **Journal of the American Ceramic Society**. 73: 3407-3415.
- Dhir, G., Uniyal, P., and Verma, N. (2014). Effect of particle size on multiferroism of barium-doped bismuth ferrite nanoparticles. **Materials Science in Semiconductor Processing**. 27: 611-618.
- Drofenik, M. (1999). Grain size and conductivities anomaly in donor-doped barium titanate. **Acta Chimica Slovenica**. 46: 355-364.
- Du, Y., Cheng, Z. X., Dou, S. X., Shahbazi, M., and Wang, X. L. (2010). Enhancement of magnetization and dielectric properties of chromium-doped BiFeO₃ with tunable morphologies. **Thin Solid Films**. 518: e5-e8.
- Dzik, J., Bernard, H., Osińska, K., Lisińska-Czekaj, A., and Czekaj, D. (2011). Synthesis, structure and dielectric properties of Bi_{1-x}Nd_xFeO₃. **Archives of Metallurgy and Materials**. 56: 1119-1125.
- Eerenstein, W., Mathur, N., and Scott, J. F. (2006). Multiferroic and magnetoelectric materials. **Nature**. 442: 759-765.

- Fang, L., Liu, J., Ju, S., Zheng, F., Dong, W., and Shen, M. (2010). Experimental and theoretical evidence of enhanced ferromagnetism in sonochemical synthesized BiFeO₃ nanoparticles. **Applied Physics Letters**. 97: 242501-242501-3.
- Fang, L., Shen, M., Yang, J., and Li, Z. (2006). Reduced dielectric loss and leakage current in CaCu₃Ti₄O₁₂/SiO₂/CaCu₃Ti₄O₁₂ multilayered films. **Solid State Communications**. 137: 381-386.
- Freitas, V. F., Dias, G. S., Protzek, O. A., Montanher, D. Z., Catellani, I. B., Silva, D. M., Cótica, L. F., and Dos Santos, I. A. (2013). Structural phase relations in perovskite-structured BiFeO₃-based multiferroic compounds. **Journal of Advanced Ceramics**. 2: 103-111.
- Gao, T., Chen, Z., Zhu, Y., Niu, F., Huang, Q., Qin, L., Sun, X., and Huang, Y. (2014). Synthesis of BiFeO₃ nanoparticles for the visible-light induced photocatalytic property. **Materials Research Bulletin**. 59: 6-12.
- Gautam, A., and Rangra, V. (2010). Effect of Ba ions substitution on multiferroic properties of BiFeO₃ perovskite. **Crystal Research and Technology**. 45: 953-956.
- Ghosh, S., Dasgupta, S., Sen, A., and Maiti, H. S. (2005). Low temperature synthesis of bismuth ferrite nanoparticles by a ferrioxalate precursor method. **Materials Research Bulletin**. 40: 2073-2079.
- Godara, P., Agarwal, A., Ahlawat, N., and Sanghi, S. (2015). Crystal structure refinement, dielectric and magnetic properties of Sm modified BiFeO₃ multiferroic. **Journal of Molecular Structure**. 1097: 207-213.
- Gong, H., Wang, X., Zhang, S., Wen, H., and Li, L. (2014). Grain size effect on electrical and reliability characteristics of modified fine-grained BaTiO₃

- ceramics for MLCCs. **Journal of the European Ceramic Society**. 34: 1733-1739.
- Guo, M., Wu, T., Liu, T., Wang, S.-X., and Zhao, X.-Z. (2006). Characterization of $\text{CaCu}_3\text{Ti}_4\text{O}_{12}$ varistor-capacitor ceramics by impedance spectroscopy. **Journal of Applied Physics**. 99: 4113-4118.
- Gupta, H., Kumar Singh, M., and Tiwari, L. (2002). Lattice dynamic investigation of raman and infrared wavenumbers at the zone center of orthorhombic RFeO_3 ($\text{R} = \text{Tb, Dy, Ho, Er, Tm}$) perovskites. **Journal of Raman Spectroscopy**. 33: 67-70.
- Gupta, T. (2010). **Copper interconnect technology**. New York: Springer Science & Business Media.
- Hill, N. A. (2000). Why are there so few magnetic ferroelectrics?. **Journal of Physical Chemistry B**. 104: 6694-6709.
- Hou, L., Zuo, K., Sun, Q., Ren, Z., Zeng, Y., and Li, X. (2013). Effects of external magnetic field on the morphology and magnetic property of BiFeO_3 particles prepared by hydrothermal synthesis. **Applied Physics Letters**. 102: 082901-082901-4.
- Huang, F., Wang, Z., Lu, X., Zhang, J., Min, K., Lin, W., Ti, R., Xu, T., He, J., and Yue, C. (2013). Peculiar magnetism of BiFeO_3 nanoparticles with size approaching the period of the spiral spin structure. **Scientific Reports**. 3: 2907-2913.
- Hunpratub, S., Thongbai, P., Maensiri, S., Yamwong, T., and Yimnirun, R. (2009). Dielectric relaxations and dielectric response in multiferroic BiFeO_3 ceramics. **Applied Physics Letters**. 94: 062904-062904-3.

Ismailza, I.G. (1966). X-ray diffraction study of phase transitions in bismuth ferrite.

Doklady Akademii Nauk SSSR. 170: 85-87.

Ilić, N. I., Bobić, J. D., Stojadinović, B. S., Džunuzović, A. S., Petrović, M. M. V., Dohčević-Mitrović, Z. D., and Stojanović, B. D. (2016). Improving of the electrical and magnetic properties of BiFeO₃ by doping with yttrium.

Materials Research Bulletin. 77: 60-69.

Ianculescu, A., Mocanu, Z., Curecheriu, L., Mitoseriu, L., Padurariu, L., and Truşcă, R. (2011). Dielectric and tunability properties of La-doped BaTiO₃ ceramics.

Journal of Alloys and Compounds. 509: 10040-10049.

Jia, D.-C., Xu, J.-H., Ke, H., Wang, W., and Zhou, Y. (2009). Structure and multiferroic properties of BiFeO₃ powders. **Journal of the European Ceramic Society.** 29: 3099-3103.

Jun, Y.-K., Moon, W.-T., Chang, C.-M., Kim, H.-S., Ryu, H. S., Kim, J. W., Kim, K. H., and Hong, S.-H. (2005). Effects of Nb-doping on electric and magnetic properties in multi-ferroic BiFeO₃ ceramics. **Solid State Communications.** 135: 133-137.

Kawae, T., Teraguchi, Y., Kumeda, M., and Morimoto, A. (2009). Improved leakage and ferroelectric properties of Mn and Ti codoped BiFeO₃ thin films. **Applied Physics Letters.** 94: 112904-112904-3.

Kumar, M. M., Palkar, V., Srinivas, K., and Suryanarayana, S. (2000). Ferroelectricity in a pure BiFeO₃ ceramic. **Applied Physics Letters.** 76: 2764-2766.

Kaur, M., Yadav, K., and Uniyal, P. (2015). Investigations on multiferroic, optical and photocatalytic properties of lanthanum doped bismuth ferrite nanoparticles. **Advanced Materials Letters.** 6: 895-901.

- Khassaf, H., Ibanescu, G., Pintilie, I., Misirlioglu, I., and Pintilie, L. (2012). Potential barrier increase due to Gd doping of BiFeO₃ layers in Nb: SrTiO₃-BiFeO₃-Pt structures displaying diode-like behavior. **Applied Physics Letters**. 100: 252903-252903-4.
- Khomchenko, V., Kiselev, D., Kopcewicz, M., Maglione, M., Shvartsman, V., Borisov, P., Kleemann, W., Lopes, A., Pogorelov, Y., and Araujo, J. (2009). Doping strategies for increased performance in BiFeO₃. **Journal of Magnetism and Magnetic Materials**. 321: 1692-1698.
- Khomchenko, V., Paixao, J., Shvartsman, V., Borisov, P., Kleemann, W., Karpinsky, D., and Kholkin, A. (2010). Effect of Sm substitution on ferroelectric and magnetic properties of BiFeO₃. **Scripta Materialia**. 62: 238-241.
- Khomchenko, V., Shvartsman, V., Borisov, P., Kleemann, W., Kiselev, D., Bdikin, I., Vieira, J., and Kholkin, A. (2009). Effect of Gd substitution on the crystal structure and multiferroic properties of BiFeO₃. **Acta Materialia**. 57: 5137-5145.
- Kingery, W. D. (1960). **Introduction to ceramics**. New York: Wiley.
- Kolte, J., Salame, P. H., Daryapurkar, A., and Gopalan, P. (2015). Impedance and AC conductivity study of nano crystalline, fine grained multiferroic bismuth ferrite (BiFeO₃), synthesized by microwave sintering. **AIP Advances**. 5: 097164-097164-11.
- Kubel, F., and Schmid, H. (1990). Structure of a ferroelectric and ferroelastic monodomain crystal of the perovskite BiFeO₃. **Acta Crystallographica Section B: Structural Science**. 46: 698-702.

- Kumar, A., and Varshney, D. (2012). Crystal structure refinement of $\text{Bi}_{1-x}\text{Nd}_x\text{FeO}_3$ multiferroic by the Rietveld method. **Ceramics International**. 38: 3935-3942.
- Kumar, N., Kaushal, A., Bhardwaj, C., and Kaur, D. (2010). Effect of La doping on structural, optical and magnetic properties of BiFeO_3 thin films deposited by pulsed laser deposition technique. **Optoelectronics and Advanced Materials**. 4: 1497-1502.
- Lazenka, V., Zhang, G., Vanacken, J., Makoed, I., Ravinski, A., and Moshchalkov, V. (2012). Structural transformation and magnetoelectric behaviour in $\text{Bi}_{1-x}\text{Gd}_x\text{FeO}_3$ multiferroics. **Journal of Physics D: Applied Physics**. 45: 125002-125002-7.
- Lee, D., Kim, M. G., Ryu, S., Jang, H. M., and Lee, S. G. (2005). Epitaxially grown La-modified BiFeO_3 magnetoferroelectric thin films. **Applied Physics Letters**. 86: 222903-222903-3.
- Lee, K., and Manthiram, A. (2006). Investigation of $\text{Nd}_{0.6}\text{Sr}_{0.4}\text{Co}_{1-y}\text{M}_y\text{O}_{3-\delta}$ ($\text{M} = \text{Fe}$ and Mn) as cathode materials for intermediate temperature solid oxide fuel cells. **Advances in Electronic and Electrochemical Ceramics**. 179: 131-138.
- Li, G., Smith Jr, R., Inomata, H., and Arai, K. (2001). Preparation techniques and ionic transport properties of Ceria-based electrolytes. **Ionic and mixed conducting ceramics: proceedings of the international symposium**. 28: 36-40.
- Li, Y., Sritharan, T., Zhang, S., He, X., Liu, Y., and Chen, T. (2008). Multiferroic properties of sputtered BiFeO_3 thin films. **Applied Physics Letters**. 92: 132908-132908-3.
- Lipson, H. (1979). Elements of X-ray diffraction. **Contemporary Physics**. 20: 87-88.

- Liu, G.-Z., Wang, C., Wang, C.-C., Qiu, J., He, M., Xing, J., Jin, K.-J., Lu, H.-B., and Yang, G.-Z. (2008). Effects of interfacial polarization on the dielectric properties of BiFeO₃ thin film capacitors. **Applied Physics Letters**. 92: 122903-122903-3.
- Liu, J., Fang, L., Zheng, F., Ju, S., and Shen, M. (2009). Enhancement of magnetization in Eu doped BiFeO₃ nanoparticles. **Applied Physics Letters**. 95: 022511-022511-3.
- Liu, J., Lu, Y., Liu, J., Yang, X., and Yu, X. (2010). Investigation of near infrared reflectance by tuning the shape of SnO₂ nanoparticles. **Journal of Alloys and Compounds**. 496: 261-264.
- Liu, L., Fan, H., Fang, P., and Jin, L. (2007). Electrical heterogeneity in CaCu₃Ti₄O₁₂ ceramics fabricated by sol-gel method. **Solid State Communications**. 142: 573-576.
- Liu, Y., and Zuo, R. (2012). Tunable morphology and optical absorption of bismuth ferrite synthesized by sol-gel-hydrothermal method. **Journal of Materials Science: Materials in Electronics**. 23: 2276-2281.
- Lotey, G. S., Dhir, G., and Verma, N. (2013). Effect of reduced size and Ba doping on multiferroic properties of BiFeO₃ nanoparticles. **Proceeding of International Conference on Recent Trends in Applied Physics and Material Science: RAM 2013**. 1536: 969-970.
- Lu, S. Z., and Qi, X. (2014). Magnetic and dielectric properties of nanostructured BiFeO₃ prepared by sol-gel method. **Journal of the American Ceramic Society**. 97: 2185-2194.

- Mahbub, R., Fakhrul, T., Islam, M. F., Hasan, M., Hussain, A., Matin, M., and Hakim, M. (2015). Structural, dielectric, and magnetic properties of Ba-doped multiferroic bismuth ferrite. **Acta Metallurgica Sinica (English Letters)**. 28: 958-964.
- Makhdoom, A., Akhtar, M., Khan, R., Rafiq, M., Hasan, M., Sher, F., and Fitch, A. (2013). Association of microstructure and electric heterogeneity in BiFeO₃. **Materials Chemistry and Physics**. 143: 256-262.
- Makhdoom, A., Akhtar, M., Rafiq, M., and Hassan, M. (2012). Investigation of transport behavior in Ba doped BiFeO₃. **Ceramics International**. 38: 3829-3834.
- Marques, V., Ries, A., Simoes, A., Ramirez, M., Varela, J. A., and Longo, E. (2007). Evolution of CaCu₃Ti₄O₁₂ varistor properties during heat treatment in vacuum. **Ceramics International**. 33: 1187-1190.
- Maurya, D., Thota, H., Garg, A., Pandey, B., Chand, P., and Verma, H. (2008). Magnetic studies of multiferroic Bi_{1-x}Sm_xFeO₃ ceramics synthesized by mechanical activation assisted processes. **Journal of Physics: Condensed Matter**. 21: 1-6.
- Mishra, R., Pradhan, D. K., Choudhary, R., and Banerjee, A. (2008). Dipolar and magnetic ordering in Nd-modified BiFeO₃ nanoceramics. **Journal of Magnetism and Magnetic Materials**. 320: 2602-2607.
- Muneeswaran, M., Dhanalakshmi, R., and Giridharan, N. (2015). Effect of Tb substitution on structural, optical, electrical and magnetic properties of BiFeO₃. **Journal of Materials Science: Materials in Electronics**. 26: 3827-3839.

- Murugan, R., Ramakumar, S., and Janani, N. (2011). High conductive yttrium doped Li La₃Zr₂O₁₂ cubic lithium garnet. **Electrochemistry Communications**. 13: 1373-1375.
- Naganuma, H. (2011). **Multifunctional Characteristics of B-site Substituted BiFeO₃ Films**. Shanghai: Ferroelectric –Physical effects.
- Neaton, J., Ederer, C., Waghmare, U., Spaldin, N., and Rabe, K. (2005). First-principles study of spontaneous polarization in multiferroic BiFeO₃. **Physical Review B**. 71: 1-9.
- Palai, R., Katiyar, R., Schmid, H., Tissot, P., Clark, S., Robertson, J., Redfern, S., Catalan, G., and Scott, J. (2008). β phase and γ - β metal-insulator transition in multiferroic BiFeO₃. **Physical Review B**. 77: 014110-014111.
- Pandit, P., Satapathy, S., and Gupta, P. (2011). Effect of La substitution on conductivity and dielectric properties of Bi_{1-x}La_xFeO₃ ceramics: An impedance spectroscopy analysis. **Physica B: Condensed Matter**. 406: 2669-2677.
- Park, T.-J., Papaefthymiou, G. C., Viescas, A. J., Moodenbaugh, A. R., and Wong, S. S. (2007). Size-dependent magnetic properties of single-crystalline multiferroic BiFeO₃ nanoparticles. **Nano Letters**. 7: 766-772.
- Pattanayak, S., Choudhary, R., and Pattanayak, D. (2014). A comparative study of structural, electrical and magnetic properties rare-earth (Dy and Nd)-modified BiFeO₃. **Journal of Materials Science: Materials in Electronics**. 25: 3854-3861.

- Pattanayak, S., Parida, B., Das, P. R., and Choudhary, R. (2013). Impedance spectroscopy of Gd-doped BiFeO₃ multiferroics. **Applied Physics A**. 112: 387-395.
- Patterson, A. (1939). The Scherrer formula for X-ray particle size determination. **Physical Review**. 56: 978-982.
- Peng-Ting, L., Xiang, L., Li, Z., Jin-Hua, Y., Xing-Wang, C., Zhi-Hong, W., Yu-Chuan, W., and Guang-Heng, W. (2014). La-doped BiFeO₃: Synthesis and multiferroic property study. **Chinese Physics B**. 23: 047701-047701-6.
- Pradhan, A., Zhang, K., Hunter, D., Dadson, J., Loiutts, G., Bhattacharya, P., Katiyar, R., Zhang, J., Sellmyer, D. J., and Roy, U. (2005). Magnetic and electrical properties of single-phase multiferroic BiFeO₃. **Journal of Applied Physics**. 093903-093903-4.
- Pradhan, S., Das, J., Rout, P., Mohanta, V., Das, S., Samantray, S., Sahu, D., Huang, J., Verma, S., and Roul, B. (2010). Effect of holmium substitution for the improvement of multiferroic properties of BiFeO₃. **Journal of Physics and Chemistry of Solids**. 71: 1557-1564.
- Prakash, T., Ramasamy, S., and Murty, B. (2011). Effect of DC bias on electrical conductivity of nanocrystalline α -CuSCN. **AIP Advances**. 1: 022107-022107-7.
- Priya, A. S., Banu, I. S., and Anwar, S. (2016). Influence of Dy and Cu doping on the room temperature multiferroic properties of BiFeO₃. **Journal of Magnetism and Magnetic Materials**. 401: 333-338.

- Priyadharsini, P., Pradeep, A., Sathyamoorthy, B., and Chandrasekaran, G. (2014). Enhanced multiferroic properties in La and Ce co-doped BiFeO₃ nanoparticles. **Journal of Physics and Chemistry of Solids**. 75: 797-802.
- Putjuso, T., Manyum, P., Yimmirun, R., Yamwong, T., Thongbai, P., and Maensiri, S. (2011). Giant dielectric behavior of solution-growth CuO ceramics subjected to dc bias voltage and uniaxial compressive stress. **Solid State Sciences**. 13: 158-162.
- Qian, F., Jiang, J., Guo, S., Jiang, D., and Zhang, W. (2009). Multiferroic properties of Bi_{1-x}Dy_xFeO₃ nanoparticles. **Journal of Applied Physics**. 106: 4312-4318.
- Rai, R., Mishra, S. K., Singh, N., Sharma, S., and Kholkin, A. L. (2011). Preparation, structures, and multiferroic properties of single-phase BiRFeO₃, R = La and Er ceramics. **Current Applied Physics**. 11: 508-512.
- Ramachandran, B., Dixit, A., Naik, R., Lawes, G., and Rao, M. R. (2012). Weak ferromagnetic ordering in Ca doped polycrystalline BiFeO₃. **Journal of Applied Physics**. 111: 023910-023910-6.
- Ramírez, M., Bueno, P. R., Varela, J. A., and Longo, E. (2006). Non-Ohmic and dielectric properties of a Ca₂Cu₂Ti₄O₁₂ polycrystalline system. **Applied Physics Letters**. 89: 212102-212102-3.
- Reddy, V. A., Pathak, N., and Nath, R. (2012). Particle size dependent magnetic properties and phase transitions in multiferroic BiFeO₃ nano-particles. **Journal of Alloys and Compounds**. 543: 206-212.
- Riaz, S., Shah, S., Akbar, A., Atiq, S., and Naseem, S. (2015). Effect of Mn doping on structural, dielectric and magnetic properties of BiFeO₃ thin films. **Journal of Sol-Gel Science and Technology**. 74: 329-339.

- Rout, J., and Choudhary, R. (2015). Effect of multiple substitutions on structural, electrical and magnetic characteristics of thermo-mechanically activated BiFeO₃ ceramics. **Journal of Materials Science: Materials in Electronics**. 26: 2905-2912.
- Sakar, M., Balakumar, S., Saravanan, P., and Bharathkumar, S. (2015). Compliments of confinements: substitution and dimension induced magnetic origin and band-bending mediated photocatalytic enhancements in Bi_{1-x}Dy_xFeO₃ particulate and fiber nanostructures. **Nanoscale**. 7: 10667-10679.
- Sanjoom, K., Pengpat, K., Eitssayeam, S., Rujijanagul, G., and Jarupoom, P. (2013). Dielectric properties of modified BiFeO₃ ceramics. **2013 Joint IEEE International Symposium on Applications of Ferroelectric and Workshop on Piezoresponse Force Microscopy (ISAF/PFM)**. 201-204.
- Sanjoom, K., and Rujijanagul, G. (2013). Effects of process parameter and excess Bi₂O₃ on phase formation and electrical properties of BiFeO₃ ceramics. **Ferroelectrics**. 454: 51-56.
- Sen, K., Singh, K., Gautam, A., and Singh, M. (2012). Dispersion studies of La substitution on dielectric and ferroelectric properties of multiferroic BiFeO₃ ceramic. **Ceramics International**. 38: 243-249.
- Shami, M. Y., Awan, M., and Anis-ur-Rehman, M. (2011). Phase pure synthesis of BiFeO₃ nanopowders using diverse precursor via co-precipitation method. **Journal of Alloys and Compounds**. 509: 10139-10144.
- Sharma, P., Varshney, D., Satapathy, S., and Gupta, P. (2014). Effect of Pr substitution on structural and electrical properties of BiFeO₃ ceramics. **Materials Chemistry and Physics**. 143: 629-636.

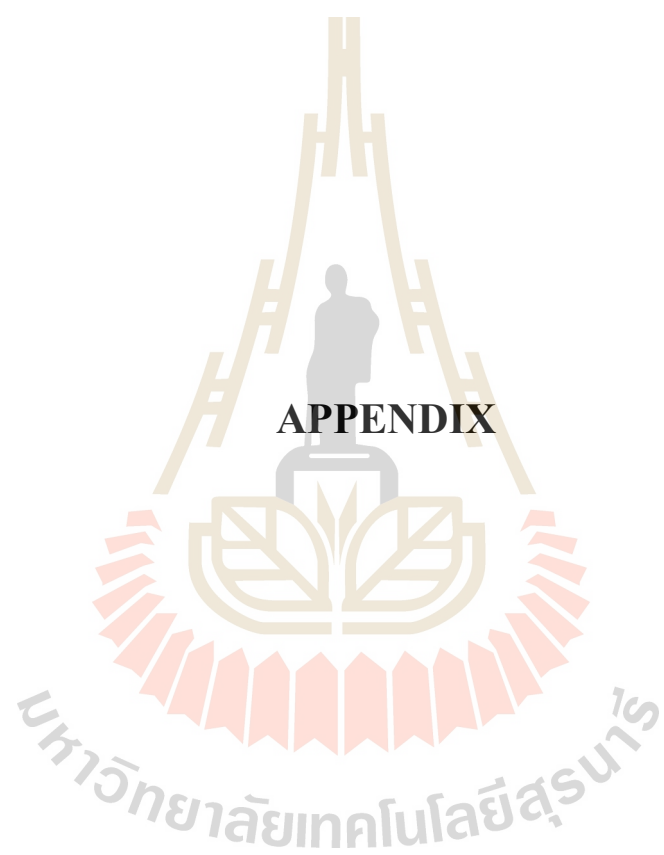
- Shokrollahi, H. (2013). Magnetic, electrical and structural characterization of BiFeO₃ nanoparticles synthesized by co-precipitation. **Powder Technology**. 235: 953-958.
- Singh, M. K., Prellier, W., Singh, M., Katiyar, R. S., and Scott, J. (2008). Spin-glass transition in single-crystal BiFeO₃. **Physical Review B**. 77: 144403-144403-3.
- Siwach, P., Singh, J., Singh, H., Varma, G., and Srivastava, O. (2008). Spray pyrolysis deposited multiferroic BiFeO₃ films. **Journal of Applied Physics**. 105: 07D916-907D918.
- Song, G., Zhang, H., Wang, T., Yang, H., and Chang, F. (2012). Effect of Sm, Co codoping on the dielectric and magnetoelectric properties of BiFeO₃ polycrystalline ceramics. **Journal of Magnetism and Magnetic Materials**. 324: 2121-2126.
- Srivastav, S. K., and S Gajbhiye, N. (2012). Low temperature synthesis, structural, optical and magnetic properties of bismuth ferrite nanoparticles. **Journal of the American Ceramic Society**. 95: 3678-3682.
- Srivastava, A., Singh, H., Awana, V., and Srivastava, O. (2013). Enhancement in magnetic and dielectric properties of La and Pr co substituted BiFeO₃. **Journal of Alloys and Compounds**. 552: 336-344.
- Suresh, P., and Srinath, S. (2013). Effect of La substitution on structure and magnetic properties of sol-gel prepared BiFeO₃. **Journal of Applied Physics**. 113: 17D920-917D923.
- Suresh, P., and Srinath, S. (2013). Observation of high coercivity in multiferroic lanthanum doped BiFeO₃. **Journal of Alloys and Compounds**. 554: 271-276.

- Thakur, S., Pandey, O., and Singh, K. (2014). Structural and optical properties of $\text{Bi}_{1-x}\text{A}_x\text{FeO}_3$ ($\text{A} = \text{Sr}, \text{Ca}; 0.40 \leq x \leq 0.55$). **Journal of Molecular Structure**. 1074: 186-192.
- Thongbai, P., Jumptam, J., Putasaeng, B., Yamwong, T., Amornkitbamrung, V., and Maensiri, S. (2014). Effects of La^{3+} doping ions on dielectric properties and formation of Schottky barriers at internal interfaces in a $\text{Ca}_2\text{Cu}_2\text{Ti}_4\text{O}_{12}$ composite system. **Journal of Materials Science: Materials in Electronics**. 25: 4657-4663.
- Thu Huong, N., Lee, S., Atabaev, T. S., Kurisu, M., and Hong, N. H. (2015). Rare Earth-Doped BiFeO_3 Thin Films: Relationship between Structural and Magnetic Properties. **Advances in Condensed Matter Physics**. 2015: 1-5.
- Tian, Z., Yuan, S., Wang, X., Zheng, X., Yin, S., Wang, C., and Liu, L. (2009). Size effect on magnetic and ferroelectric properties in $\text{Bi}_2\text{Fe}_4\text{O}_9$ multiferroic ceramics. **Journal of Applied Physics**. 106: 103912-103912-4.
- Uniyal, P., and Yadav, K. (2008). Study of dielectric, magnetic and ferroelectric properties in $\text{Bi}_{1-x}\text{Gd}_x\text{FeO}_3$. **Materials Letters**. 62: 2858-2861.
- Valant, M., Axelsson, A.-K., and Alford, N. (2007). Peculiarities of a solid-state synthesis of multiferroic polycrystalline BiFeO_3 . **Chemistry of Materials**. 19: 5431-5436.
- Van Den Brink, J., and Khomskii, D. I. (2008). Multiferroicity due to charge ordering. **Journal of Physics: Condensed Matter**. 20: 434217-434222.
- Vedrinskii, R., Kraizman, V., Novakovich, A., Demekhin, P. V., and Urazhdin, S. (1998). Pre-edge fine structure of the 3d atom K X-ray absorption spectra and

- quantitative atomic structure determinations for ferroelectric perovskite structure crystals. **Journal of Physics: Condensed Matter**. 10: 9561-9580.
- Vijayanand, S., Potdar, H., and Joy, P. (2009). Origin of high room temperature ferromagnetic moment of nanocrystalline multiferroic BiFeO₃. **Applied Physics Letters**. 94: 182507-182509.
- Wagner, K. W. (1913). The theory of imperfect perfect dielectrics. **Annalen der Physik (Leipzig)**. 40: 817-855.
- Wang, D., Goh, W., Ning, M., and Ong, C. (2006). Effect of Ba doping on magnetic, ferroelectric, and magnetoelectric properties in multiferroic BiFeO₃ at room temperature. **Applied Physics Letters**. 88: 2907-2909.
- Wang, J., Neaton, J., Zheng, H., Nagarajan, V., Ogale, S., Liu, B., Viehland, D., Vaithyanathan, V., Schlom, D., and Waghmare, U. (2003). Epitaxial BiFeO₃ multiferroic thin film heterostructures. **Science**. 299: 1719-1722.
- L. Wang, Z. Wang, K.-J. Jin, J.-Q. Li, H.-X. Yang, C. Wang, R.-Q. Zhao, H.-B. Lu, H.-Z. Guo, G.-Z. Yang. (2013). Effect of the thickness of BiFeO₃ layers on the magnetic and electric properties of BiFeO₃/La_{0.7}Sr_{0.3}MnO₃ heterostructures. **Applied Physics Letters**. 102: 242902-242902-5.
- Wang, L., Xu, J.-B., Gao, B., Chang, A.-M., Chen, J., Bian, L., and Song, C.-Y. (2013). Synthesis of BiFeO₃ nanoparticles by a low-heating temperature solid-state precursor method. **Materials Research Bulletin**. 48: 383-388.
- Wang, X., Zhang, Y. G., and Wu, Z. (2010). Magnetic and optical properties of multiferroic bismuth ferrite nanoparticles by tartaric acid-assisted sol-gel strategy. **Materials Letters**. 64: 486-488.

- Waugh, M. D. (2010). Design solutions for DC bias in multilayer ceramic capacitors. **Electronic Engineering Times**. 34-36.
- Wu, Y.-J., Chen, X.-K., Zhang, J., and Chen, X.-J. (2013). Magnetic enhancement across a ferroelectric–paraelectric phase boundary in $\text{Bi}_{1-x}\text{Sm}_x\text{FeO}_3$. **Physica B: Condensed Matter**. 411: 106-109.
- Xi, X., Wang, S., Liu, W., Wang, H., Guo, F., Wang, X., Gao, J., and Li, D. (2014). Enhanced magnetic and conductive properties of Ba and Co co-doped BiFeO_3 ceramics. **Journal of Magnetism and Magnetic Materials**. 355: 259-264.
- Yan, F., Lai, M.-O., Lu, L., and Zhu, T.-J. (2010). Enhanced multiferroic properties and valence effect of Ru-doped BiFeO_3 thin films. **The Journal of Physical Chemistry C**. 114: 6994-6998.
- Yang, C.-H., Kan, D., Takeuchi, I., Nagarajan, V., and Seidel, J. (2012). Doping BiFeO_3 : approaches and enhanced functionality. **Physical Chemistry Chemical Physics**. 14: 15953-15962.
- Yang, C., Jiang, J.-S., Qian, F.-Z., Jiang, D.-M., Wang, C.-M., and Zhang, W.-G. (2010). Effect of Ba doping on magnetic and dielectric properties of nanocrystalline BiFeO_3 at room temperature. **Journal of Alloys and Compounds**. 507: 29-32.
- Yin, L., Sun, Y., Zhang, F., Wu, W., Luo, X., Zhu, X., Yang, Z., Dai, J., Song, W., and Zhang, R. (2009). Magnetic and electrical properties of $\text{Bi}_{0.8}\text{Ca}^{0.2}\text{Fe}_{1-x}\text{Mn}_x\text{O}_3$ ($0 \leq x \leq 0.5$). **Journal of Alloys and Compounds**. 488: 254-259.

- Zhang, J., Wu, Y.-J., Chen, X.-K., and Chen, X.-J. (2013). Structural evolution and magnetization enhancement of $\text{Bi}_{1-x}\text{Tb}_x\text{FeO}_3$. **Journal of Physics and Chemistry of Solids**. 74: 849-853.
- Zhang, J., Zheng, P., Wang, C., Zhao, M., Li, J., and Wang, J. (2005). Dielectric dispersion of $\text{CaCuTi}_4\text{O}_{12}$ ceramics at high temperatures. **Applied Physics Letters**. 87: 142901-142901-3.
- Zhang, Q., Zhu, X., Xu, Y., Gao, H., Xiao, Y., Liang, D., Zhu, J., Zhu, J., and Xiao, D. (2013). Effect of La^{3+} substitution on the phase transitions, microstructure and electrical properties of $\text{Bi}_{1-x}\text{La}_x\text{FeO}_3$ ceramics. **Journal of Alloys and Compounds**. 546: 57-62.
- Zhang, S., Lu, M., Wu, D., Chen, Y., and Ming, N. (2005). Larger polarization and weak ferromagnetism in quenched BiFeO_3 ceramics with a distorted rhombohedral crystal structure. **Applied Physics Letters**. 87: 262907-262907-3.
- Zhang, S., Luo, W., Wang, D., and Ma, Y. (2009). Phase evolution and magnetic property of $\text{Bi}_{1-x}\text{Dy}_x\text{FeO}_3$ ceramics. **Materials Letters**. 63: 1820-1822.
- Zhang, Y.-J., Zhang, H.-G., Yin, J.-H., Zhang, H.-W., Chen, J.-L., Wang, W.-Q., and Wu, G.-H. (2010). Structural and magnetic properties in $\text{Bi}_{1-x}\text{R}_x\text{FeO}_3$ ($x = 0-1$, $\text{R} = \text{La}, \text{Nd}, \text{Sm}, \text{Eu}$ and Tb) polycrystalline ceramics. **Journal of Magnetism and Magnetic Materials**. 322: 2251-2255.



APPENDIX

APPENDIX

PUBLICATION AND PRESENTATION

A. 1 List of publications

Yotburut, B., Yamwong, T., Thongbai, P., and Maensir, S. (2013) Synthesis and characterization of coprecipitation-prepared La-doped BiFeO₃ nanopowders and their bulk dielectric properties. **Japanese Journal of Applied Physics**. 53. 06JG13.

A. 2 List of oral presentations

Yotburut, B., Yamwong, T., Thongbai, P., and Maensir, S. (2014) Electrical and nonlinear current-voltage characteristics of multiferroic La-doped BiFeO₃ ceramics. In **The 12th International Nanotech Symposium & Nano-Convergence Expro**. Coex, seoul, Korea.

Yotburut, B., Yamwong, T., Thongbai, P., and Maensir, S. (2014) Synthesis and characterization of multiferroic Sm-doped BiFeO₃ nanopowders and its bulk dielectric properties. **The 9th Asian Meeting in Ferroelectrics (AMF-9) and the 9th Asian Meeting on Electroceramics (AMEC-9) (AMF-AMEC 2014)**. Shanghai International convention center. Shanghai, China.

A. 3 List of poster presentations

Yotburut, B., Yamwong, T., Thongbai, P., and Maensir, S. (2013) Synthesis and characterization of coprecipitation-prepared La-doped BiFeO₃ nanopowders and

their bulk dielectric properties. In 26th International Microprocessor and Nanotechnology Conference. Royton Sapporo, Hokkaido, Japan.

Yotburut, B., Yamwong, T., and Maensir, S. (2013) Dielectric and nonlinear current-voltage characteristics of La-doped BiFeO₃ ceramics. In **The 2nd conference on Natural Science for Master and PhD Students (CASEAN 2013)**. Phnom Penh, Cambodia.



CURRICULUM VITAE

Name Miss Benjaporn Yotburut

Date of Birth April 2, 1988

Place of Birth 273 Moo 3 Tambol boonnakpattana, Muang Didtrict,
Lampang Province, 52000, Thailand.

Education

2007 - 2011 University of Phayao, Phayao, Thailand.
B. Ed. Science-Physics.

2011 - 2016 Suranaree University of Technology, Nakhon Ratchasima,
Thailand, Ph.D. Physics.

มหาวิทยาลัยเทคโนโลยีสุรนารี